

Design and mechanism of thermally activated delayed fluorescent (TADF) and efficient room temperature phosphorescent (RTP) molecules

Dissertation

Zur Erlangung des Grades

“Doktor der Naturwissenschaften”

am Fachbereich Chemie, Pharmazie und Geowissenschaften der

Johannes Gutenberg-Universität in Mainz



JOHANNES GUTENBERG
UNIVERSITÄT MAINZ

Dehai Dou

Geboren in Anhui Province, China

Mainz, 2023

Dekan:

1. Berichterstatter:

2. Berichterstatter:

Tag der mündlichen Prüfung:

Die vorliegende Arbeit wurde in der Zeit von April 2020 bis September 2023 am Max-Planck-Institut für Polymerforschung in Mainz unter der Betreuung von Prof. Dr. Martin Baumgarten und Prof. Dr. Paul W.M. Blom durchgeführt.

Dedicated to my family and fiancée

Affidavit

I hereby declare that I completed the dissertation independently and without any external support. Except for the places mentioned and referenced in the thesis, no external sources were used.

Furthermore, I confirm that this thesis has not yet been submitted as part of another examination process neither in identical nor in similar form.

Ort, Datum:

Unterschrift:

Abstract

In recent years pure organic photoluminescent materials have been shown to possess great potential for applications in the fields of sensors, optoelectronic devices, bio-imaging, data encryption, etc.. Especially thermally activated delayed fluorescent (TADF) and room temperature phosphorescent (RTP) materials received extensive attention from researchers around the world. Currently, organic electroluminescent devices based on TADF materials have achieved some success in small-size displays, but blue materials still suffer from device transport imbalance and low device lifetime. For RTP materials, the triplet state excitons are very susceptible to the influence of the external environment. Efficient and stable room temperature phosphorescent materials that are purely organic have been a challenge. The main studies of this thesis is divided into 3 parts which are summarized as follows:

Firstly, TADF and RTP materials need a fast intersystem crossing (ISC) process and a small singlet triplet splitting (ΔE_{ST}). Model emitters were designed and synthesised with simultaneous fluorescence, delayed fluorescence, and room temperature phosphorescence. It was proven experimentally and theoretically that multiple excited states are involved in the luminescence process. By adjusting the molecular structure, emitters with RTP quantum yield of more than 30% were obtained. Secondly, we designed and studied molecules for achieving phosphorescence emission in neat films. By changing the intramolecular steric hindrance, the phosphorescence radiation lifetime can be improved, also enhancing the quantum yield of phosphorescence emission in neat films. Our experimental data show that lifetimes up to 40 ms and phosphorescence quantum yields of 6.3% are achievable in neat films. All molecules have a lifetime of over 30 ms under ambient conditions. Thirdly, the introduction of fluorine atoms at the donor lowers the HOMO and LUMO energies but also affects the packing pattern of the molecules. Molecules without fluorine atoms pack more tightly compared to molecules with fluorine atoms. The molecules with tighter molecular packing achieved nearly trap-free electron transport in blue emitting molecules. We have gained a deep understanding of how to design trap-free blue luminescent materials.

Zusammenfassung

In den letzten Jahren hat sich gezeigt, dass rein organische photolumineszente Materialien ein großes Potenzial für Anwendungen in den Bereichen Sensoren, optoelektronische Geräte, Bio-Imaging, Datenverschlüsselung usw. besitzen. Insbesondere thermisch aktivierte verzögerte fluoreszierende (TADF) und bei Raumtemperatur phosphoreszierende (RTP) Materialien haben bei Forschern in aller Welt große Aufmerksamkeit erregt. Derzeit haben organische Elektrolumineszenz-Bauelemente auf der Grundlage von TADF-Materialien einen gewissen Erfolg in kleinen Displays erzielt, aber blaue Materialien leiden immer noch unter einem Transportungleichgewicht und einer geringen Lebensdauer der Bauelemente. Bei RTP-Materialien sind die Exzitonen im Triplett-Zustand sehr anfällig für den Einfluss der äußeren Umgebung. Effiziente und stabile, bei Raumtemperatur phosphoreszierende Materialien, die rein organisch sind, stellen eine Herausforderung dar. Die Hauptstudien dieser Arbeit sind in 3 Teile unterteilt, die im Folgenden zusammengefasst werden:

Erstens benötigen TADF- und RTP-Materialien einen schnellen Intersystem-Crossing-Prozess (ISC) und eine geringe Singulett-Triplett-Aufspaltung (ΔE_{ST}). Es wurden Modell-Emitter mit gleichzeitiger Fluoreszenz, verzögerter Fluoreszenz und Phosphoreszenz bei Raumtemperatur entwickelt und synthetisiert. Es wurde experimentell und theoretisch nachgewiesen, dass mehrere angeregte Zustände an dem Lumineszenzprozess beteiligt sind. Durch Anpassung der Molekülstruktur konnten Emitter mit einer RTP-Quantenausbeute von mehr als 30 % erzielt werden. Zweitens entwarfen und untersuchten wir Moleküle zur Erzielung von Phosphoreszenzemissionen in reinen Filmen. Durch Veränderung der intramolekularen sterischen Hinderung kann die Lebensdauer der Phosphoreszenzstrahlung verbessert werden, was auch die Quantenausbeute der Phosphoreszenzemission in reinen Filmen erhöht. Unsere experimentellen Daten zeigen, dass in reinen Filmen Lebensdauern von bis zu 40 ms und Phosphoreszenz-Quantenausbeuten von 6,7 % erreicht werden können. Alle Moleküle haben unter Umgebungsbedingungen eine Lebensdauer von über 30 ms. Drittens senkt die Einführung von Fluoratomen am Donor die HOMO- und LUMO-Energien, beeinflusst aber auch das Packungsmuster der Moleküle. Moleküle ohne Fluoratome packen dichter als Moleküle mit Fluoratomen. Die Moleküle mit dichterem Molekülpackung erreichten einen nahezu fallfreien Elektronentransport in blau emittierenden Molekülen. Wir haben ein tiefes Verständnis dafür gewonnen, wie man fallfreie blaue Leuchtstoffe entwickelt.

Contents

Chapter 1. Introduction	1
1.1 General background	1
1.2 Molecular excitation and relaxation	2
1.3 Fluorescence (FL)	2
1.3.1 Kasha's rule and Franck–Condon principle	3
1.3.2 Stokes shift	4
1.3 Delayed fluorescence (DF)	5
1.3.1 Triplet–triplet annihilation	6
1.3.2 Hybridized local and charge-transfer	8
1.3.2 Thermally activated delayed fluorescence (TADF)	10
1.4 Room temperature phosphorescence (RTP)	14
1.4.1 Phosphorescent quantum yield and phosphorescent lifetime	15
1.4.2 Methods for improving RTP efficiency	15
1.5 Applications of pure organic RTP	28
1.5.1 Anti-counterfeiting encryption	28
1.5.2 Sensors	30
1.5.3 Bioimaging	33
1.6 Conclusions	35
1.7 References	35
Chapter 2. Simultaneous delayed fluorescence and phosphorescence in organic emitters employing multiple excited states	39
2.1 Abstract	39
2.2 Introduction	39
2.3 Synthesis	41
2.4 Optical properties	42
2.4 Limitation of the two-state model	45
2.5 Involvement of upper triplet state in the model emitter	46
2.6 Theoretical molecular simulations	50
2.7 A three-state model	52
2.8 Multi-color emissive system by Förster resonance energy transfer	55
2.9 Application for efficient RTP materials development	60
2.10 Summary	67
2.11 Synthetic details	68
2.12 Supplementary note 1: Two-state system modelling	72

2.13 References	80
Chapter 3. Steric hindrance induced through space charge transfer for achieving room temperature phosphorescence in amorphous neat film	86
Abstract.....	86
3.1 Introduction	86
3.2 Synthesis.....	87
3.3 Optical properties.....	88
3.4 Density functional theory (DFT) calculations.....	97
3.5 Transient excited state absorption (TESA).....	98
3.6 Time-resolved anti-counterfeiting application.....	101
3.7 Summary	102
3.8 Synthetic details.....	103
3.9 References	109
Chapter 4. Cleverly designed molecules influence molecular stacking to eliminate charge carrier trapping.....	111
4.1 Introduction	111
4.2 Synthesis.....	112
4.3 Optical properties.....	113
4.4 Electrochemical properties.....	115
4.5 Density functional theory (DFT) calculations.....	117
4.6 Crystal structure analysis.....	118
4.7 Electron transport	120
4.8. Summary	122
4.9 Synthetic details.....	123
4.10 References	133
Chapter 5. Conclusion and Outlook	135
Appendix	138
Appendix-I Experimental section and analytical techniques	138
Appendix-II NMR spectra.....	142
List of Publication	164
Curriculum Vitae	165
Acknowledgments.....	166

Abbreviations

Å	angstrom
ΔE	energy gap
μ_h	hole mobility
μ_e	electron mobility
μs	microsecond
AcOH	acetic acid
a. u.	arbitrary unit
B3LYP	Becke, three-parameter, Lee-Yang-Parr
CV	cyclic voltammetry
<i>d</i>	doublet (NMR signal)
<i>dd</i>	doublet of doublets (NMR signal)
DCM	dichloromethane
DF	delayed fluorescence
DFT	density functional theory
DMF	N,N-dimethylformamide
EA	electron affinity
eV	electron volt
Fc	ferrocene
FL	fluorescence
FWHM	full width at half maximum
h	hour
HRMS	high resolution mass spectrometry
HOMO	highest occupied molecular orbital
ICT	intramolecular charge transfer
IE	ionization energy
ITO	indium tin oxide
ISC	intersystem crossing
LUMO	lowest unoccupied molecular orbital
<i>m</i>	multiplet (NMR signal)
ms	millisecond

MR	multi-resonant
NBS	N-bromosuccinimide
NIR	near infrared
nm	nanometer
ns	nanosecond
OLEDs	organic light emitting diodes
PL	photoluminescence
ppm	parts per million
ps	picosecond
r.t.	room temperature
RISC	reverse intersystem crossing
RTP	room temperature phosphorescence
s	singlet (NMR signal)
t	triplet (NMR signal)
TADF	thermally activated delayed fluorescence
THF	tetrahydrofuran
UV-vis-NIR	ultraviolet-visible-near infrared
V	volt

Chapter 1. Introduction

1.1 General background

Optoelectronic materials are attracting more and more attention, due to their application in bioimaging,¹ information storage,² sensing devices,³ organic light-emitting diodes,⁴ and digital encryption.⁵ The traditional inorganic luminescent materials are no longer able to fulfill the needs of rapidly developing optical displays due to their opaqueness and processing difficulties. In contrast, organic photoluminescent materials are more structurally diverse, colorful, and easier to process. Luminescence is the process whereby excitons in the excited state of a molecule transfer back under radiation to the ground state. The luminescence is mainly divided into fluorescence and phosphorescence, where singlet state excitons usually undergo radiative decay to the ground state via fluorescence emission. The triplet excitons can return to the singlet state via reversed intersystem crossing (RISC) if their energies are close, and the singlet excitons decay to the ground state as delayed fluorescence emission. Triplet state excitons radiatively decay via phosphorescence emission or nonradiative decay producing heat. While prompt fluorescence emission is a very fast process in the nanosecond regime of 10^{-9} to 10^{-7} s,⁶ phosphorescence emission is a much slower process on the order of 10^{-3} s⁷ due to the fact that electrons in the triplet state clearly have not the same spin direction as in the ground state and do not satisfy the Pauli exclusion principle.⁸ The decay of the radiation from the triplet state is forbidden by the decay rule of quantum mechanics, therefore other vibrational states have to be considered.⁹

The conventional fluorescent materials have only the singlet state that can radiatively decay to the ground state at room temperature, and phosphorescence can only be observed at low temperatures, limiting the application of fluorescent materials. Room temperature phosphorescence (RTP) means that at room temperature, the triplet state can decay under radiation to the ground state and thus emit phosphorescence. Current compounds with room temperature phosphorescence properties mainly contain precious metal organometallic complexes, which are costly, toxic and therefore not suited for large-scale applications.¹⁰ In contrast, pure organic room-temperature phosphorescent materials are low cost, easily processable and have a wide range of uses. High-performance pure organic room-temperature phosphorescent materials have great potential for future applications.

1.2 Molecular excitation and relaxation

In molecular spectroscopy, the Jablonski diagram is a diagram illustrating the electronic states and vibrational energy levels of a molecule and the transitions between them.¹¹ As shown in **Figure 1.1**, the process of photon emission from excitons is mainly divided into fluorescence emission and phosphorescence emission. The excitation of a molecule to the singlet state is a very fast process ($\sim 10^{-15}$ s), and the excitons in the singlet state and the electrons in the ground state remain in spin pairs. Higher-energy singlet excitons decay to S_1 by internal conversion and vibrational relaxation, and the exciton emits fluorescence by radiative excursion to the ground state, a process permitted by the rules of quantum-mechanical excursion selection. If there is a large amount of vibrational energy level coupling between S_1 and the triplet state, the exciton can cross to the triplet state through intersystem crossing, and at the same time the exciton in the triplet state will return to S_1 through RISC. The spin direction of the triplet electron is different from that of the excited ground state electron and the excited ground state electron does not reverse the electron spin direction during the excitation process, which is the reason why the electron in the ground state can't be directly excited to the triplet state. The process of direct return of excitons from the triplet state to the ground state is called phosphorescent emission.

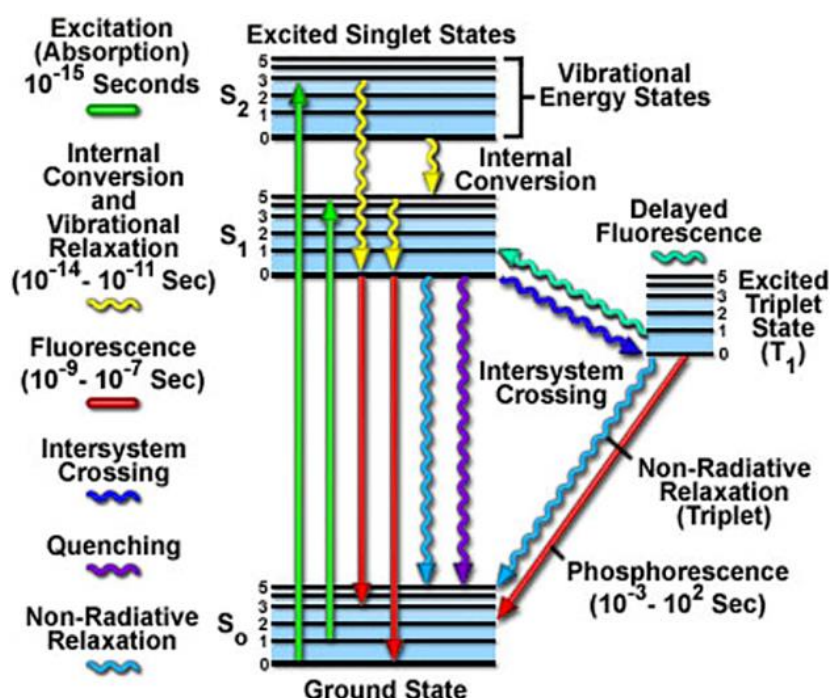


Figure 1.1 Jablonski energy diagram for illustrating fluorescence and photoluminescence processes.¹¹

1.3 Fluorescence (FL)

The basic principle of fluorescence generation is shown in **Figure 1.2**. Electrons jump from the ground state (S_0) to the single excited state ($S_n, n > 0$) after absorbing energy. The valence band electron in one of the vibrational energy levels of the higher-energy singlet excited state (S_n) vibrationally relaxes to the lowest vibrational energy level and then to S_1 by internal conversion. S_1 returns to the S_0 by radiative decay, a very fast process that takes $10^{-9} \sim 10^{-7}$ s.⁶

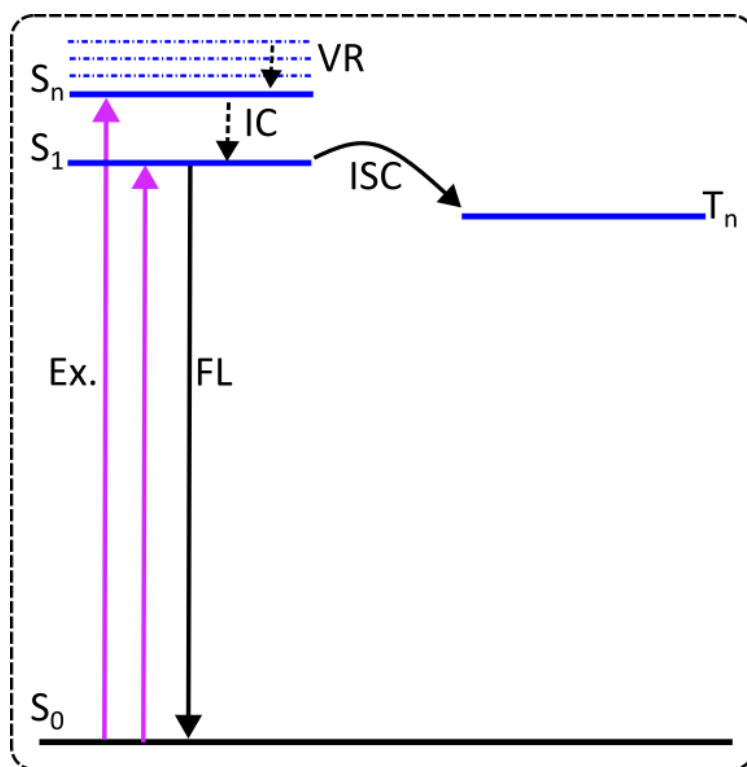


Figure 1.2 The schematic diagram of fluorescence emission. Excitation (Ex.), Fluorescence (FL), vibration relaxation (VR), internal conversion (IC), and intersystem crossing (ISC).

1.3.1 Kasha's rule and Franck–Condon principle

Kasha's rule was proposed by the American spectroscopist Michael Kasha in 1950.¹² As mentioned earlier, once a ground state molecule absorbs a photon, the electron is excited to a higher electronic energy level S_n ($n > 0$), as shown in **Figure 1.2**. The exciton decays to S_1 through IC and VR, and then radiates a photon and emits fluorescence. However, since the rate of IC and VR is typically between $10^{-14} \sim 10^{-12}$ s, much faster than the fluorescence emission rate, this means that the fluorescence emission is expected to come only from the lowest excited state S_1 , and therefore when the excitation wavelength is within the absorption range of the material, the emission wavelength is independent of the excitation wavelength. Kasha's rule can be explained by the Franck-Condon factor for the electron vibrational

transitions (**Figure 1.3a**).¹³ The strength of an electronic vibrational transition is proportional to the square of the overlap integral between the vibrational wave functions of the initial and final states of the transition. This means that the greater the overlap, the faster the molecule undergoes transitions from a higher to a lower energy level. The overlap between pairs is greatest when the energy of the two vibrational levels is close or when the vibration-free level (where the vibrational quantum number v is zero) of the electronic state coupled through the transition is close.¹³ On the contrary, in some cases anti-Kasha's Rule occurs due to their ultrafast radiative rate or large S_2 - S_1 energy.¹² For example, for azulene, its maximum absorption and emission exists between S_0 and S_2 energy, due to the large difference in energy levels between S_1 and S_2 of azulene (see **Figure 1.3b** and **c**).

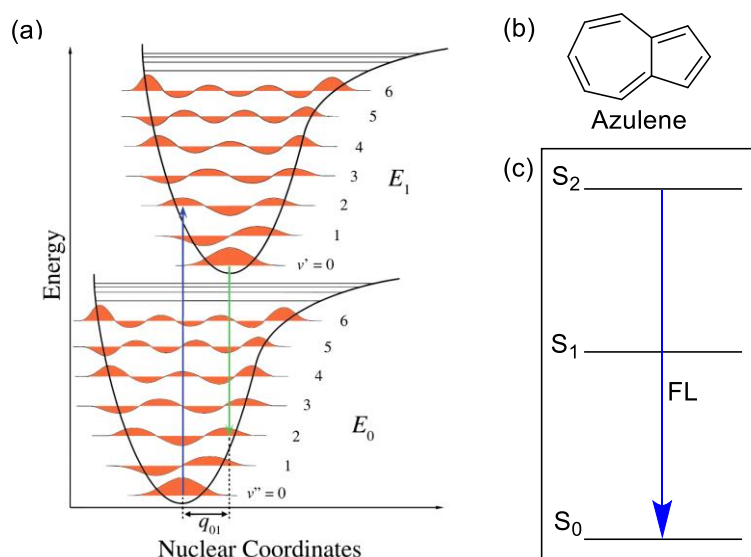


Figure 1.3 (a) Franck–Condon principle energy diagram. (b) Molecule structure of azulene. (c) Diagram of the anti-Kasha's rule.

1.3.2 Stokes shift

The Stokes shift was discovered by the Irish physicist Stokes in 1950.¹⁴ As shown in **Figure 1.4**, if there is no energy loss during absorption and emission, the molecular fluorescence spectrum should be mirror symmetric with the absorption spectrum, but in reality the emission wavelength of fluorescence is always greater than the wavelength of the excitation. The difference between the energy of the maximum fluorescence wavelength and the maximum absorption wavelength is called the Stokes shift. There are two main causes of Stokes displacement. The first is that the molecule in the excited state loses some of its energy through internal conversion or vibrational relaxation to S_1 before emitting fluorescence.

The second is that when the exciton radiative decays from S_1 back to S_0 , not all of it decays directly to the lowest vibrational energy level of S_0 , but mostly from the highest vibrational energy level of S_0 back to the lowest vibrational energy level of S_0 through vibrational relaxation, with further loss of vibrational energy.¹⁴

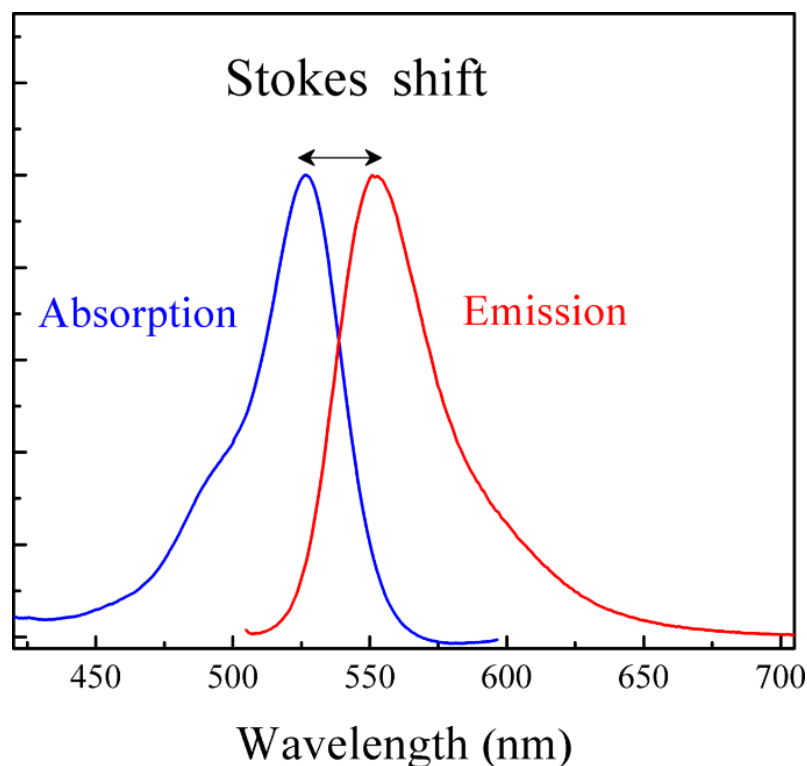


Figure 1.4 Diagram of the Stokes shift between absorption and emission light spectra.

1.3 Delayed fluorescence (DF)

In recent years, the enormous potential of delayed fluorescence in organic light-emitting diodes (OLEDs) has attracted a lot of attention. Based on theory, with conventional fluorescent molecules, only 25% of the singlet excitons can induce fluorescence emission (S_1 - S_0), while 75% of the triplet excitons are consumed in other forms, such as thermal energy. Considering the optical output coupling efficiency (20%), the theoretical maximum external quantum efficiency (EQE) of the fluorescent material in a device is 5%. The effective use of triplet excitons is therefore key to improving the efficiency of OLED devices. There are two ways to enhance the exciton utilisation, the first being phosphorescent materials, but as phosphorescent materials have a relatively long luminous life-time, they are more susceptible to environmental factors and are also more expensive due to the use of rare earth metals. The second is delayed fluorescence, which can achieve 100% in-conversion efficiency while being insensitive to environmental quenching, so delayed fluorescence has higher potential for

application. There are currently three strategies to achieve delayed fluorescence: triplet–triplet annihilation, hybridized local and charge-transfer, thermally activated delayed fluorescence.

1.3.1 Triplet–triplet annihilation

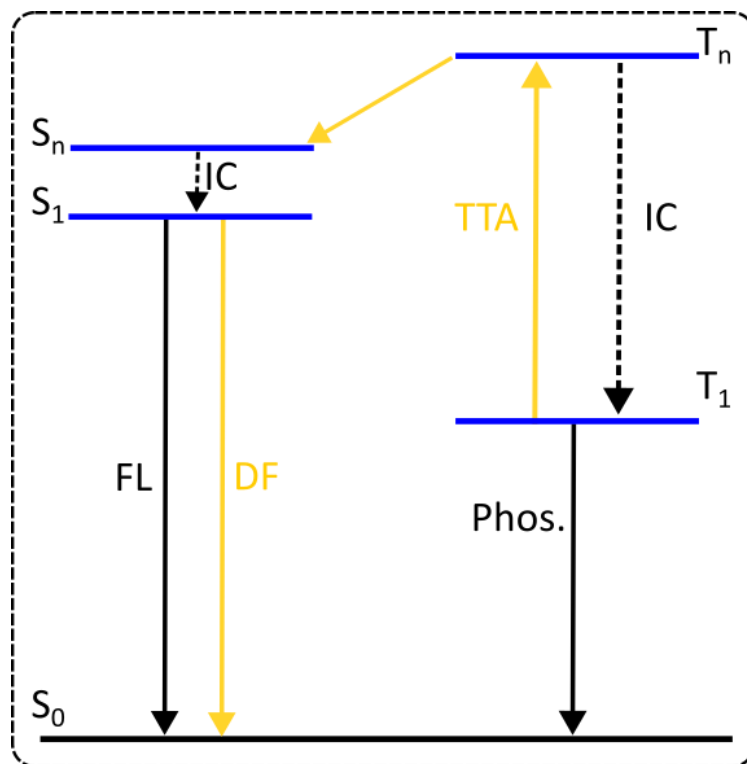


Figure 1.5 The schematic diagram of triplet–triplet annihilation.¹⁵

Triplet-triplet annihilation (TTA) is the process of capturing triplet excitons while generating delayed fluorescence. As shown in **Figure 1.5**, the triplet states of two adjacent excited molecules combine to form a higher triplet state, and the newly formed triplet state returns to the singlet state via RISC. TTA-type delayed fluorescence was first found in pyrene. TTA has limitations in producing delayed fluorescence while improving the efficiency of OLED devices. Neglecting losses that may quench single and triplet states to varying degrees, the maximum efficiency of the TTA in producing singlet state is only 37.5% based on spin statistics. This also means that in TTA-type materials, a maximum of 62.5% of singlet excitons can be utilized. Taking into account the 20% optical output coupling efficiency, the maximum EQE of an OLED device is 12.5% when using a TTA-type material as the light-emitting layer. On the other hand, in order to obtain an efficient TTA process, a high concentration of triplet excitons is required in a device, which results in unavoidable device efficiency roll-off and short device lifetime.¹⁵

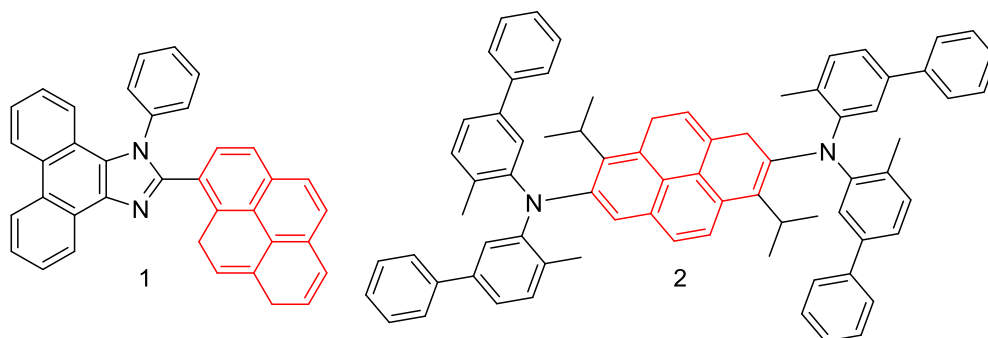


Figure 1.6 Molecular structures of pyrene-based TTA emitters **1-2**.^{16,17}

Lu and colleagues developed a blue TTA emitter based on a pyrene structure (1) shown in **Figure 1.6**. The emitter in the neat film exhibited 57% photoluminescence quantum yield (PLQY).¹⁶ The non-doped OLED of emitter 1 exhibited pure blue emission with CIE coordinates of (0.15, 0.14) and an EQE of 5.11%, while the device exhibited low roll-off, with EQE stable above 5.0 % at luminance of 300-3000 cd m⁻² and an EQE of 4.76 % at ultra-bright luminance of 10000 cd m⁻². Recently, Wei et al. synthesized blue TTA emitter (2) by using pyrene as the core chromophore modified with two dinaphthylamine units.¹⁷ The PLQY of the film doped into the 9,10-di(2-naphthyl)anthracene (AND)¹⁷ host was 64%. A maximum EQE of 6.25% and CIE coordinates of (0.13, 0.16) were achieved in the doped devices.

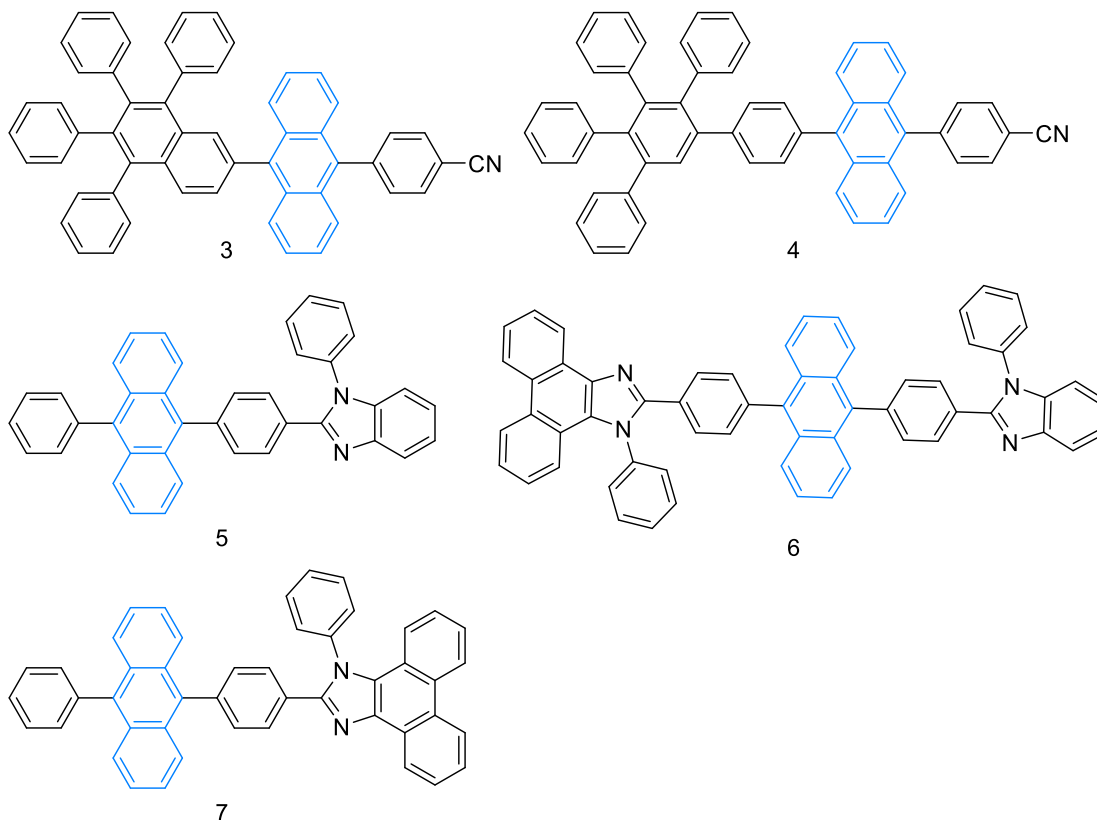


Figure 1.7 Molecular structures of anthracene-based TTA emitters **3-7**.^{18,19}

In addition to pyrene, anthracene has a rigid planar surface and good carrier mobility as shown in **Figure 1.7**, Anthracene also has a high PLQY and good thermal stability.^{18,19} Therefore, anthracene is also a common group for efficient TTA emitters. As shown by Promarak et al. two deep blue emitters (3 and 4) based on an anthracene skeleton were prepared by introducing highly spatially-site resistive 2,3,4-tetraphenylnaphthalene (TPN) and 2,3,4,5-tetraphenyl-1,1'-biphenyl (TPB).¹⁸ The maximum fluorescence emission peak of compound 3 is 446 nm. Interestingly, due to the perfect anthracene dimerization of compound 4, the fluorescence peak exhibits a red shift (462 nm), while exhibiting 97% PLQY. In the non-doped device, the maximum EQE for compound 4 is 6.25% with CIE coordinates of (0.13, 0.16). Benzimidazole (BI) and phenanthroimidazole (PI) have been shown to be an effective functional part of the design of various TTA emitters. Lee et al. designed three blue emitters by introducing BI and PI into the anthracene backbone (5-7).¹⁹ The emission peaks of the three compounds were red-shifted by 8-24 nm in neat films compared to in solution. The PLQY of compounds 5-7 were 70.3%, 52.7%, and 30%, respectively. In particular, the non-doped device based on emitter 6 exhibited a high EQE of 8.41% with CIE coordinates of (0.15, 0.15).¹⁹

1.3.2 Hybridized local and charge-transfer

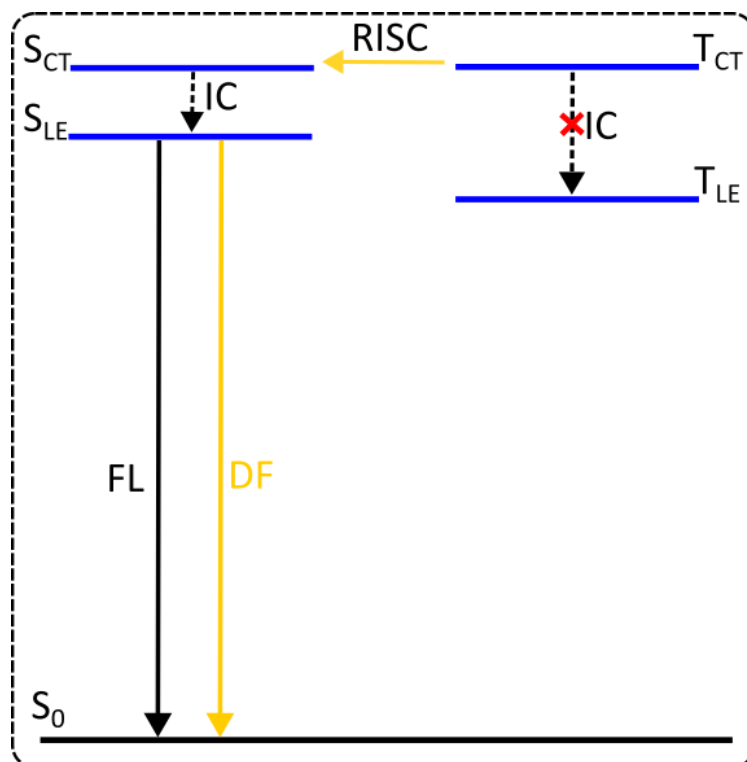


Figure 1.8. The schematic diagram of hybridized local and charge-transfer.¹⁵ Charge transfer (CT). Local excited (LE)

Hybridized local and charge-transfer (HLCT) is another effective strategy for delayed fluorescence using triplet state excitons.¹⁵ As shown in **Figure 1.8**, in this system, the excitons located in the upper excited states above the S_1 and T_1 states are called hot excitons and the RISC process occurs between the hot excitons, that is, between the upper excited states. The typical HLCT molecule consists of D and A parts, so a well-regulated dihedral angle of D-A can modulate the characteristics and energy level arrangement of the excited states, thus facilitating the radiative decay and RISC processes. Thus, the performance of HLCT molecules is highly dependent on the capabilities of the donor, acceptor, and π -spacer.

In 2014, Ma's group reported a series of HLCT molecules with high exciton utilization efficiency and full-color range emission.²⁰ Photophysical studies and DFT analysis show that the CT component in the HLCT state can be enhanced by reducing the twist angles and increasing the electron absorption capacity of these twisted D-A molecules. The structure of molecules 8-13 are shown in **Figure 1.9**. OLEDs with these HLCT-state materials as emitters show excellent EL performance and high exciton utilization efficiency values (up to 90%).

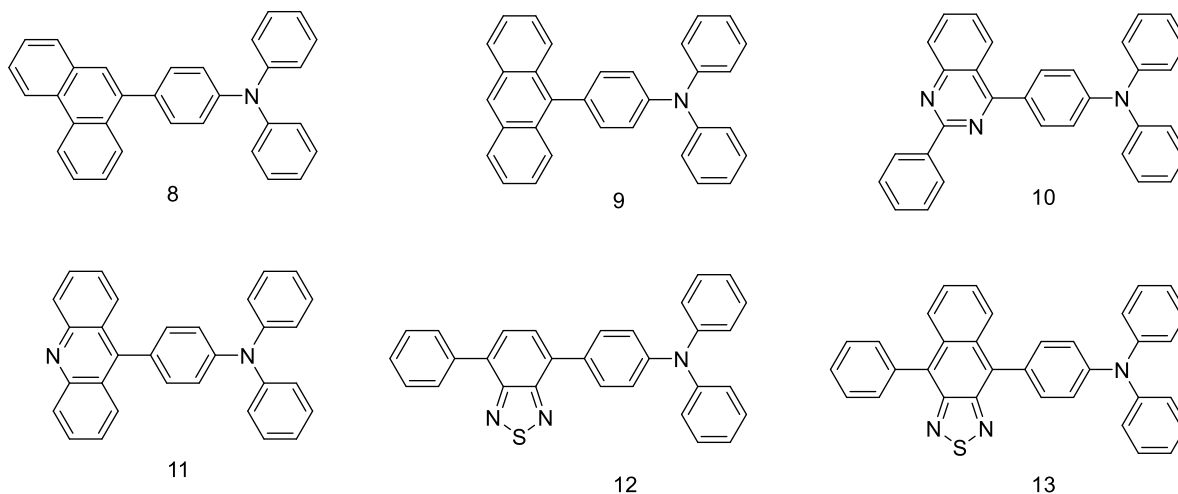


Figure 1.9 Molecular structures of HLCT emitters 8-13.²⁰

1.3.2 Thermally activated delayed fluorescence (TADF)

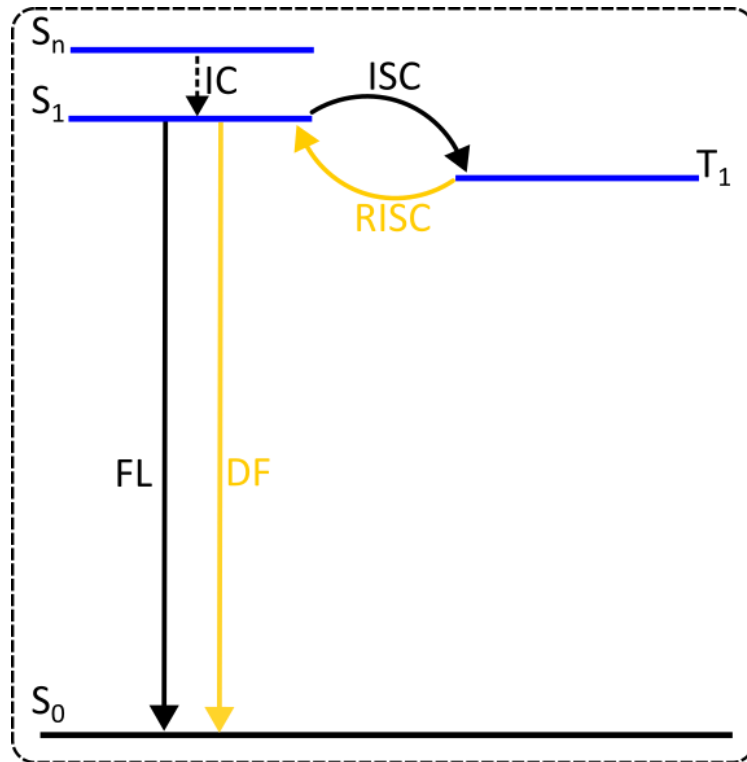


Figure 1.10. The schematic diagram of thermally activated delayed fluorescence.

Exciton energy transfer and utilization in the thermally activated delayed fluorescence (TADF) emitter is shown in **Figure 1.10**. Singlet excitons have two possible energy decay routes in addition to the non-radiative decay: fluorescence radiation from S_1 to S_0 , and ISC from S_1 to T_1 , while triplet excitons can be converted to the singlet state via RISC if the energy difference between S_1 and T_1 is small (< 0.2 eV), which then emits delayed fluorescence. RISC is a key step in delayed fluorescence using triplet excitons emission, and a small S_1 - T_1 energy split (ΔE_{ST}) is required to achieve a competitive RISC rate (k_{RISC}). It is generally recognized that $\Delta E_{ST} < 0.2$ eV is favourable for an efficient RISC process. Here, the k_{RISC} can be expressed in equation 1:²¹

$$k_{RISC} = A \exp \left[-\frac{\Delta E_{ST}}{k_B T} \right] \quad (1)$$

where A is the frequency factor, k_B is Boltzmann's constant and T is absolute temperature.

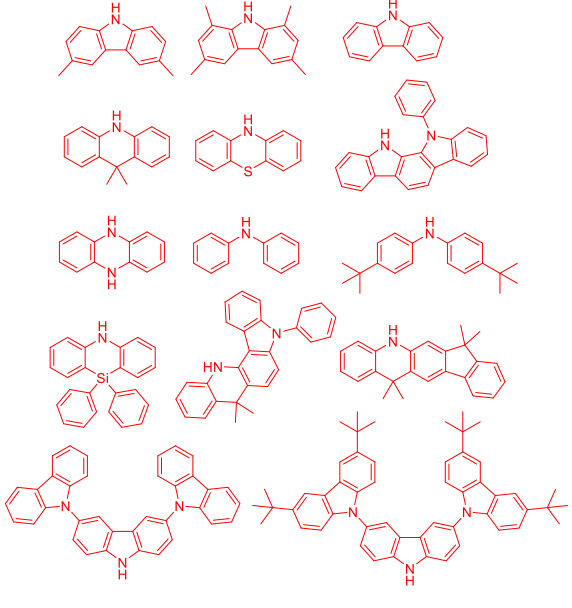
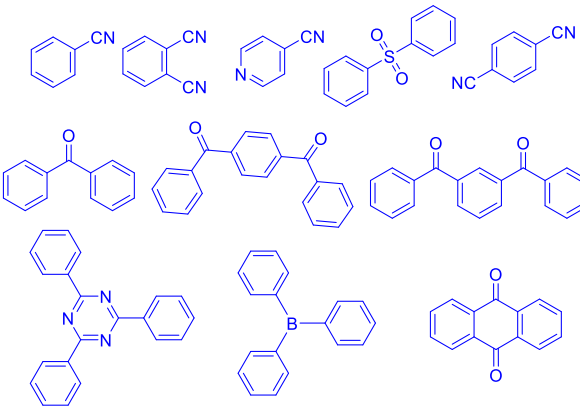
The ΔE_{ST} can be expressed in equation 2:²²

$$\Delta E_{ST} = 2 \iint \phi_H(r_1) \phi_L(r_2) \frac{1}{|r_2 - r_1|} \phi_H(r_2) \phi_L(r_1) dr_1 dr_2 \quad (2)$$

where $(r_2 - r_1)$ denotes the distance between the centres of distribution of the HOMO and LUMO electrons.

Since S_1 and T_1 of the TADF molecule can be interconverted by ISC and RISC, close to 100% internal quantum efficiency (IQE) can be achieved during the electroluminescence of the TADF emitter by collecting singlet and triplet excitons. To date, three design strategies have been proposed, such as highly twisted donor-acceptor (D-A) structures, exciplex systems, and multi-resonant (MR) effect-induced TADF. The typical donors include carbazole, dimethyldihydroacridine, diphenylamine, dihydrophenazine, etc., and typical acceptors include groups such as benzonitrile, phthalonitrile, benzophenone, triphenylboron and triphenyltriazine etc., and the structures are summarised in **Table 1.1**.

Table 1.1 Common donor and acceptor moieties for TADF.

Donor	Acceptor
	

According to equation 2, if the distributions of HOMO and LUMO are spatially separated the ΔE_{ST} will be small. An effective way to spatially separate donor and acceptor parts in the molecules to obtain non overlapping HOMO and LUMO distribution is through a highly twisted D-A structure, where the HOMO is strongly localized on D and the LUMO on the A. Charge transfer (CT) states are excited states formed by electron transfer between D and A. In 2011, Adachi's group first reported the pure aromatic compound 14, with efficient TADF properties and a maximum EQE of 5.3% at low current densities.²³ In 2012, they reported another molecule, 15, which exhibited an EQE of 19.3% in doped devices.²⁴ In

addition to the strategy of using highly distorted D-A structures to reduce the overlap between HOMO and LUMO, this can be achieved by increasing the dihedral angle between D and A, or by introducing spacer groups to separate the π -conjugation between D and A.²⁵ For example, molecule 16 has a weak TADF activity due to the small dihedral angle between the phenylcarbazole and the triphenyltriazine. However, the introduction of the methyl groups at carbazole or the central benzene ring (17-19) increases the dihedral angle due to the spatial repulsion between D and A, resulting in an efficient TADF effect.

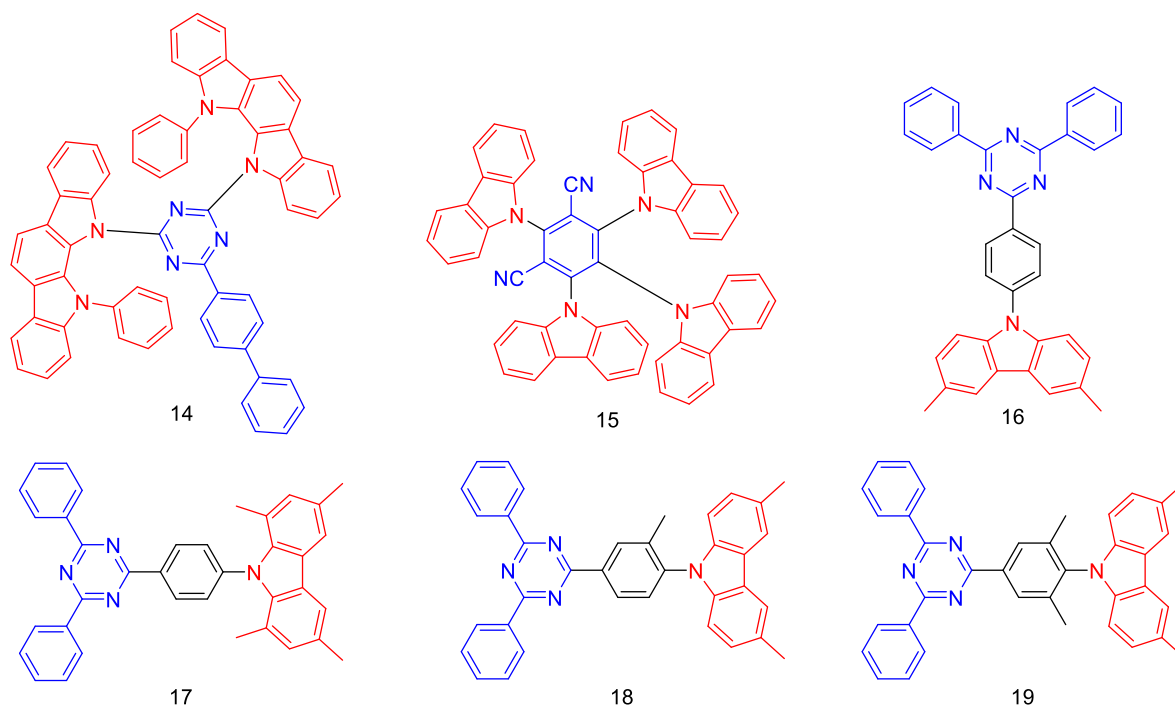


Figure 1.11 Molecular structures of TADF emitters **14-19**.^{23,24,25}

The k_{RISC} increases when HOMO and LUMO orbitals are spatially separated. However, as the spatial separation increases, it leads to a decrease in the intensity of the transition oscillator (f), which reduces the PLQY of the emitter and the EL efficiency of the device. In addition, the CT state molecule produces a large structural relaxation in the excited state, resulting in a broad emission spectrum with a large Stokes shift and low colour purity. The development of narrow-emission TADF is therefore crucial. Generally, the larger the change in structure between the S_0 and S_1 states of the emitter, the more vibrational transitions (0-1, 0-2, 0-3 ect.) contribute, resulting in a larger full width at half maxima (FWHM) of the emission spectrum and larger Stokes shift. In contrast, when the structural change between the S_0 and S_1 states is small, the emission spectrum becomes narrow.

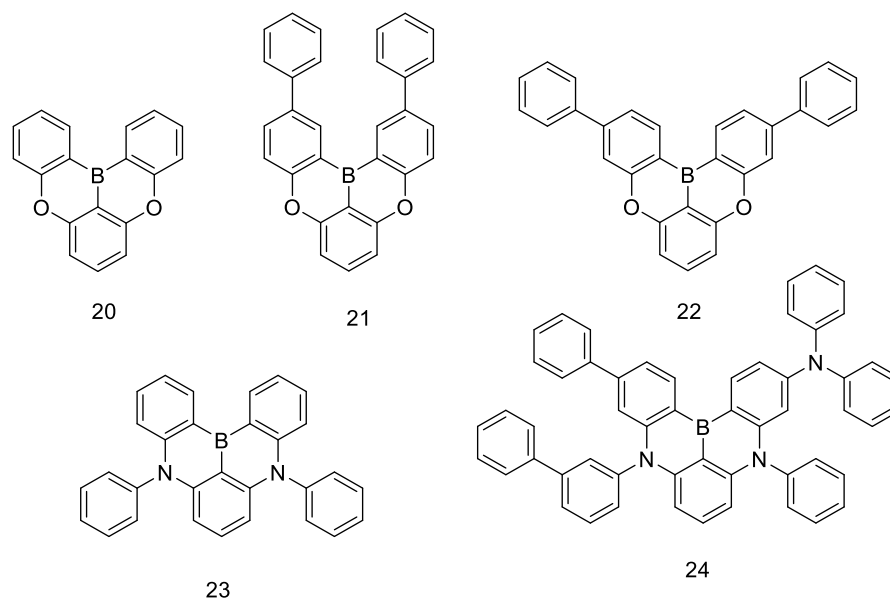


Figure 1.12 Molecular structures of TADF emitters **20-24**.^{26,27}

In 2015, Hatakeyama et al. reported a series of B/O-embedded MR-TADF molecules 20-22.²⁶ In this molecular design, the HOMO is predominantly localised on the electron donating atoms (O, N) and the carbon (C) atoms in ortho/sub positions with respect to them, whereas the LUMO is distributed on the central electron withdrawing atoms (B) of the neighbouring benzene ring and on the C atoms in their ortho/sub positions. Thus, the opposite magnetic resonance effect can be utilised to separate HOMO and LUMO into different atomic molecules without the need to construct a pre-distorted D-A structure. Compound 20 exhibited UV emission in dichloromethane (DCM) with a PL maximum at 398 nm and FWHM of 34 nm. Compounds 21 and 22, substituted with phenyl groups at different positions, also showed narrow emission. However, compared to 20, their PL exhibits a red shift of about 12 nm. In addition to the oxygen atom, the nitrogen atom is also used in MR-TADF. In 2016, Hatakeyama et al. reported two molecules, 23 and 24, and proposed a narrowband TADF design strategy with MR effects.²⁷ The donating electron atoms (nitrogen) are regularly arranged in the ortho positions of the dense polycyclic aromatic backbone with respect to the withdrawing electron atom (boron), thus, the HOMO can be induced to localize to three of the six carbons of the benzene ring and the LUMO to the other three, providing a small ΔE_{ST} (23 is 0.18 eV, 24 is 0.14eV).²⁷ The narrowband ultrapure blue emission peaks at 462 and 470 nm were achieved for 23 and 24, with FWHM of 33 and 34 nm in DCM and high PLQY of 89% and 85%, respectively. TADF-OLEDs using 23 and 24 as emitters (1 wt% doping in 3,3-di(9H-carbazol-9-yl)-1,1-biphenyl (mCBP)) achieved maxima EQE of up to

13.5% and 20.2%. MR-TADF materials are attracting more and more attention at the forefront of research into organic light-emitting materials, both from a chemical and physical point of view. It is believed that MR-TADF materials/systems will undoubtedly make a significant contribution to the core technology of ultra-wide colour OLED displays in the near future.

1.4 Room temperature phosphorescence (RTP)

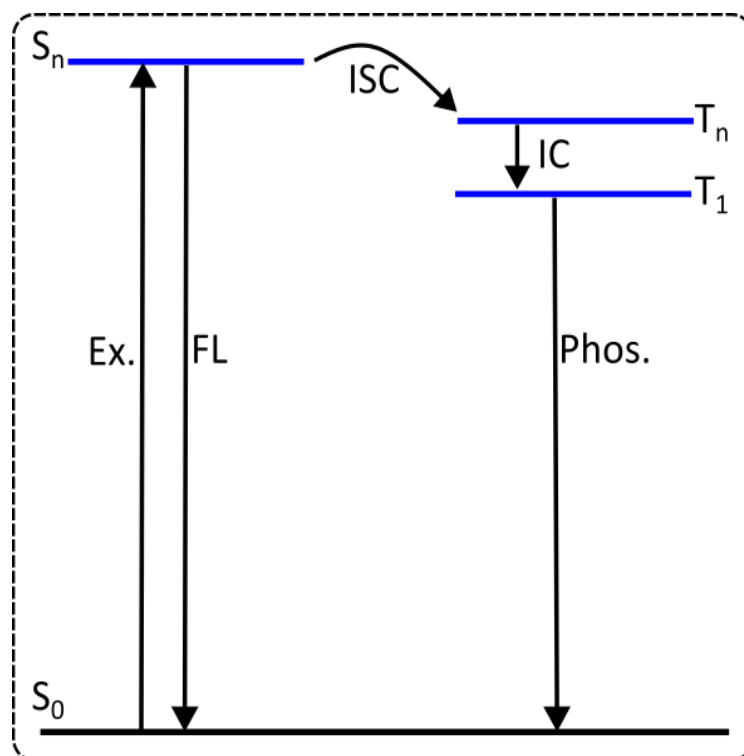


Figure 1.13 The schematic diagram of phosphorescence emission. Excitation (Ex.), Fluorescence (FL), Phosphorescence (Phos.), internal conversion (IC), and intersystem crossing (ISC).²⁸

The basic principle of phosphorescence generation is shown in **Figure 1.13**. Electrons jump from the ground state (S_0) to the singlet excited state (S_n) after absorbing energy, electrons through ISC to the triplet excited state (T_n), and then relax through IC to T_1 . The final return to the S_0 from T_1 is in the form of radiative decay. Phosphorescent molecules are particularly sensitive to environmental factors, such as molecular aggregation, temperature, and oxygen, etc. Therefore, phosphorescence was generally observed at low temperature and/or under inert gases. This means that phosphorescent molecules are difficult to process for applications such as bioimaging, organic light-emitting diodes, and data encryption, etc. Early RTP materials were basically inorganic materials or organometallic complexes containing noble metals, which are usually expensive, toxic, and environmentally inhospitable. In

contrast, pure organic RTP materials have the advantages of low cost, wide variety, biocompatibility, and processability.

1.4.1 Phosphorescent quantum yield and phosphorescent lifetime

Phosphorescence quantum yield is the proportion of absorbed photons used for phosphorescence radiation decay. It can be used to describe the phosphorescence ability of a material or the intensity of phosphorescence.²⁸ Phosphorescence is the photon emitted by the process from $T_1 \rightarrow S_0 + h\nu$, where the triplet state quantum yield (Φ_T) is calculated as:

$$\Phi_T = \frac{k_{ISC}}{k_{ISC} + k_F + k_{nr.F} + \sum k_{FQ}} \quad (1)$$

The phosphorescence quantum yield (Φ_P) can be calculated as:

$$\Phi_P = \Phi_T \times \frac{k_P}{k_P + k_{nr.P} + \sum k_{PQ}} = \frac{k_{ISC}}{k_{ISC} + k_F + k_{nr.F} + \sum k_{FQ}} \times \frac{k_P}{k_P + k_{nr.P} + \sum k_{PQ}} \quad (2)$$

where k_F is the fluorescence decay rate from S_1 to S_0 state; k_{ISC} is the intersystem crossing (ISC) rate from S_1 to T_1 , k_P is the phosphorescence decay rate from T_1 to S_0 state; $\sum k_{PQ}$ and $\sum k_{FQ}$ denote the sum of the rate constants of all bimolecular bursts during fluorescence and phosphorescence, respectively; $k_{nr.F}$ and $k_{nr.P}$ denote the rate constants of the non-radiative decay of fluorescence and phosphorescence, respectively.²⁸

The phosphorescence lifetime (τ_p) is the time taken for the phosphorescence intensity to decay to $1/e$ of its original value, which is the average time for the exciton to return from the excited state of the triplet to ground state (S_0). The τ_p can be calculated as:

$$\tau_p = \frac{1}{(k_P + k_{nr.P} + k_q)} \quad (3)$$

where τ_p is the intrinsic phosphorescence lifetime, k_q is the quenching rate of the triplet excited state by quenching species.²⁸

1.4.2 Methods for improving RTP efficiency

To obtain highly efficient RTP for pure organic molecules, three requirements should be satisfied according to the equations of phosphorescence quantum yield: 1) efficient ISC to fill a sufficient number of triplet excitons, 2) fast phosphorescent decay from T_1 to S_0 , and 3) suppression or decrease of the non-radiative decay and quenching processes of T_1 .²⁸

1.4.2.1 Efficient ISC

In photoluminescence, ISC is an important process to produce triplet excitons, but in organic light emitters, the spin orientation of the singlet to triplet state electrons is flipped, resulting in a low flipping efficiency. The k_{ISC} constant can be expressed in equation 4:²⁸

$$k_{ISC} = \frac{2\pi}{\hbar} |\langle S | \hat{H}_{SOC} | T \rangle|^2 \sqrt{\frac{\pi}{\lambda k_B T}} \exp \left[-\frac{(\Delta E_{ST} - \lambda)^2}{4\lambda k_B T} \right] \quad (4)$$

where \hbar is the reduced Planck's constant; $\langle S | \hat{H}_{SOC} | T \rangle$ is the spin-orbit coupling (SOC) element of the matrix between the singlet and triplet states; T is the temperature; λ is the total reorganization energy; k_B is the Boltzmann constant; ΔE_{ST} is the energy gap between the involved singlet and triplet states.

The ISC rate can be estimated qualitatively by EL-Sayed's rule,²⁹ if the transition between the singlet and triplet states involves a change in molecular orbital type, then the ISC rate is relatively large. Effective ISC occurs only from $^1n\pi^*$ to $^3\pi\pi^*$ and $^1\pi\pi^*$ to $^3n\pi^*$, in that case molecular transition orbitals p_x and p_y have a large overlap. The difference is that it's forbidden from $^1\pi\pi^*$ to $^3\pi\pi^*$ and $^1n\pi^*$ to $^3n\pi^*$ (as shown in **Figure 1.14**), because the transition orbitals overlap is smaller.

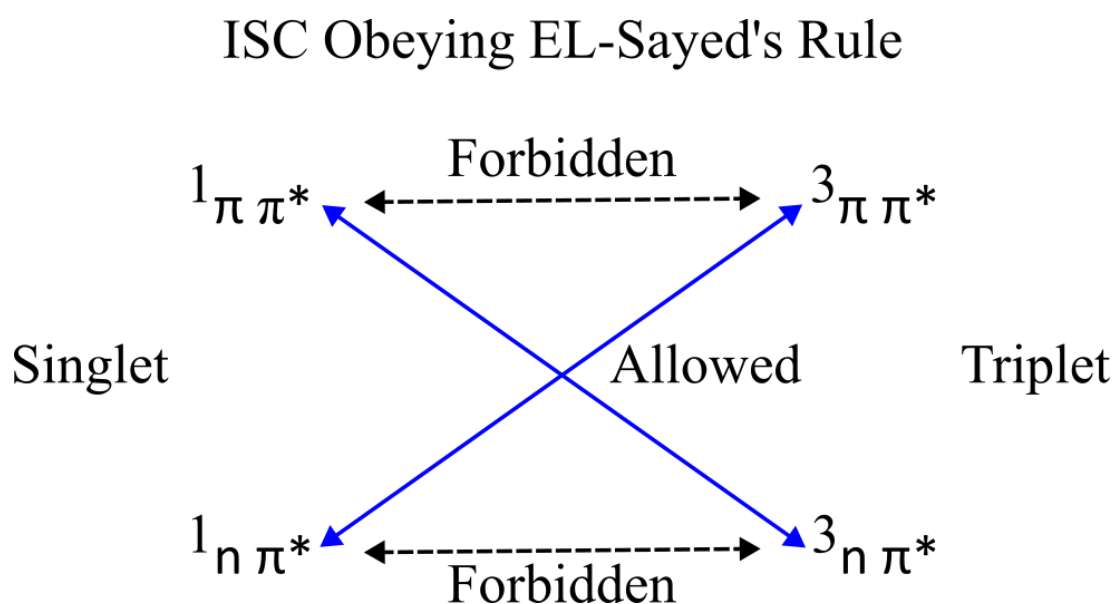


Figure 1.14 El-Sayed's rules.²⁹

SOC is the major mechanism to induce spin-flip transition reversal. The wave functions and coupling magnitudes of the singlet and triplet excited states in the SOC process can be expressed by the following equations:

$$\Psi_{SO} = \Psi_T + \lambda\Psi_S \quad (5)$$

$$\lambda = E_{SO} / (E_S - E_T) = H_e \mu_s / (E_S - E_T) \quad (6)$$

where Ψ_{SO} the mixed wave function for singlet and triplet excited states spin orbits; Ψ_S and E_S denote the wave function and energy of the singlet excited state, respectively; Ψ_T and E_T denote the wave function and energy of the triplet excited state, respectively; λ represents the factor of the coupling between the singlet and triplet states; E_{SO} is the spin orbital coupling energy; H_e is the magnetic field generated by the motion of electrons in the orbit; μ_s is the magnetic moment generated from the electron spin.

1.4.2.1.1 Heavy-atom effect

The multifunctional molecular design strategy for ISC enhancement is based on the use of heavy atoms. As described earlier, SOC is the main mechanism that facilitates ISC. As shown in equations 5 and 6, SOC is proportional to E_{SO} , which is proportional to the 4th order of atomic number, so as the atomic number increases, SOC and ISC increase as well. The heavy atoms are normally used in pure organic materials such as chlorine, bromine, iodine, sulfur, and selenium.

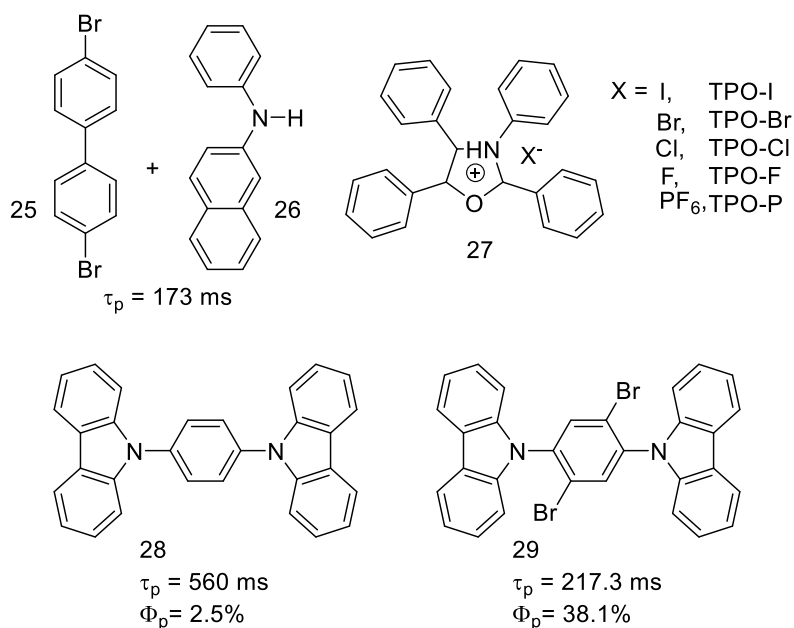


Figure 1.15 Molecules containing heavy atoms.^{30,31,32}

In 2016, Wang's group achieved a phosphorescence lifetime of 173 ms through doping the molecule 26 (N-phenyl-1-naphthylamine) into a 25 (4,4'-dibromobiphenyl) crystal containing heavy atoms, the structure is shown in **Figure 1.15**.³⁰ In 2018, Tang's group proposed to use external heavy atoms via anion- π^+ interactions, and the positively charged

aromatic ring (27) exhibited strong room temperature phosphorescence due to external heavy atoms via anion- π^+ interactions, the structure shown in **Figure 1.15**.³¹ In 2019, Huang's group designed two molecules 28 (9,9'-(1,4-phenylene)bis-9H-carbazole) and 29 (9,9'-(2,5-dibromo-1,4-phenylene)bis(9H-carbazole)) shown in **Figure 1.15**. By introducing two bromine atoms to the molecule, the phosphorescence quantum yield was increased from 2.5% to 38.1% compared to the molecule without the bromine atom.³²

1.4.2.1.2 Lone-pair electron incorporation

According to El-Sayed's rule (**Figure 1.14**), since the $^1\pi\pi^*$ to $^3\pi\pi$ transition is forbidden, this will therefore result in a smaller SOC and thus a smaller k_{ISC} . So by introducing groups or atoms with rich electrons, the S_1 of the organic molecule is dominated by $^1n\pi^*$ and the T_n close to S_1 in energy is dominated by $^3\pi\pi^*$, increasing the SOC and k_{ISC} .

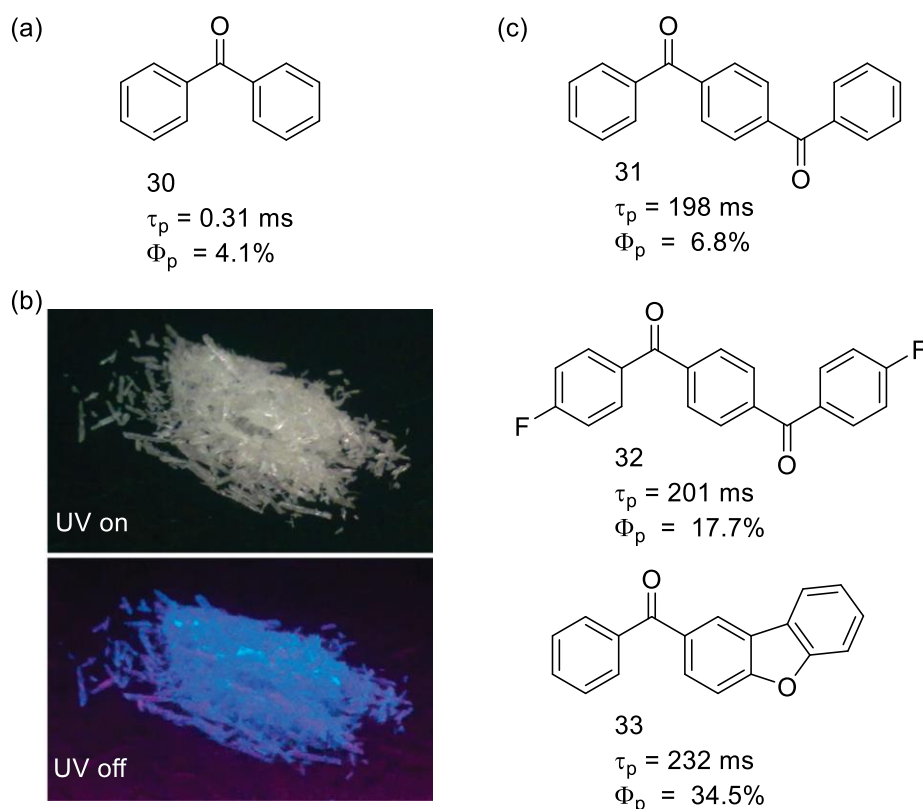


Figure 1.16 (a) and (c) Electron-rich molecules that emit phosphorescence at room temperature. (b) Photographs of crystals of 30 taken under laboratory lighting and UV illumination at room temperature. Copyright 2010, American Chemical Society.^{33,34}

In 2010, Tang's group investigated the phosphorescent properties of benzophenone (30) in single crystals. As shown in **Figure 1.16** long-lived phosphorescence was still visible

at room temperature after illumination.³³ In 2016, Tang's group designed a series of room-temperature phosphorescent molecules based on 30, where oxygen atoms containing lone pairs of electrons affected the phosphorescence lifetime and quantum yield of the molecules, with the 33 phosphorescence quantum yield reaching 34.5%.³⁴

1.4.2.1.3 Molecular aggregation

For organic room temperature phosphorescent molecules, the triplet state is relatively easy to be quenched after molecular aggregation. However, if the molecules are stacked in a specific way, e.g. H-aggregation, π - π stacking and n - π stacking, the triplet excitons are stabilised to some extent, leading to ultra-long room-temperature phosphorescence. This is due to the large number of electron interactions that result in overlap between exciton orbitals when molecules are aggregated, generating more ISC channels and increasing the ISC and RTP efficiency of the aggregates.

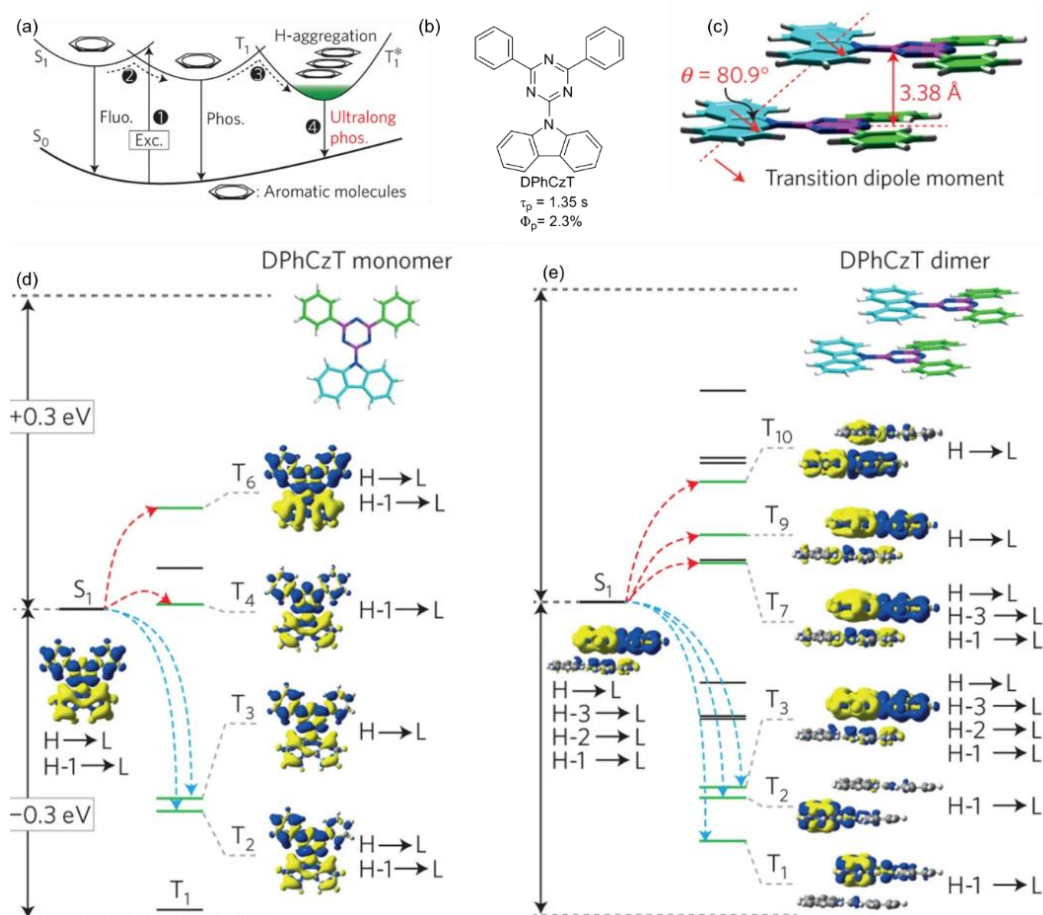


Figure 1.17 (a) Mechanism of H-aggregation for phosphorescence enhancement. (b) Diphenyl-carbazolyl-triazine (DPhCzT) structure, Φ_p , and phosphorescent lifetime at room temperature. (c) Single-crystal structures of DPhCzT. (d) and (e) The TD-DFT-calculated energy levels, isosurface

and main orbital configurations of a DPhCzT monomer and its coplanar dimer at singlet (S_n) and triplet (T_n) states. Copyright 2015, Nature Publishing Group.³⁵

In 2015, Huang's group reported a room-temperature phosphorescent molecule (DPhCzT, shown in **Figure 1.17**) with 2.3% for Φ_p and 1.35s for τ_p in the crystal.³⁵ It has been calculated that in the dimer, the molecule adds many ISC channels, which is the reason for such a long room temperature phosphorescence lifetime.

1.4.2.1.4 Smaller Energy-gap

According to equation 4, k_{ISC} can be accelerated by molecular design to shrink ΔE_{ST} typically after the addition of the acceptor and donor units, the molecule produces an internal charge transfer (1CT and 3CT) that acts as an intermediate state for minimising ΔE_{ST} . Although a smaller ΔE_{ST} accelerates ISC, and also results in higher k_{ISC} values, when the ΔE_{ST} is too small, the reverse ISC (RISC) process occurs, giving rise to TADF, and there is competition between TADF and RTP at this point, so the ΔE_{ST} needs to be within a reasonable range when designing the molecules.

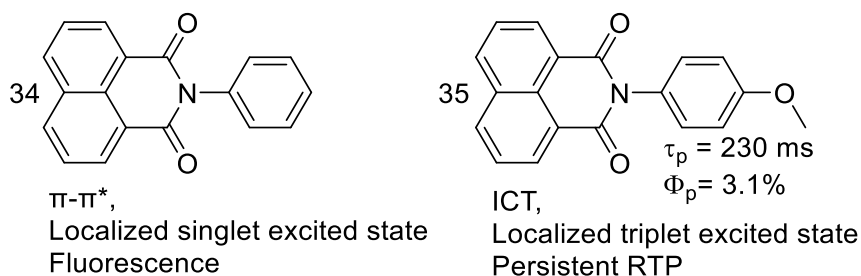


Figure 1.18 Molecule structure of **34**, **35** based on naphthalimide.³⁶

In 2016, Zhang's group investigated naphthalimide based **34** and **35**, shown in **Figure 1.18**.³⁶ The phenyl-naphthalimide **34** showed a localized singlet state and exhibited only fluorescence. After the introduction of the methoxy group **35** had an intramolecular charge transfer, the molecule exhibited a localized triplet state with a phosphorescence lifetime of 230 ms and a quantum yield of 3.1%. In 2017, Yang's group designed a new purely organic emitter 2,3-bis(4-(10H-phenoxazin-10-yl)phenyl)quinoxaline (DBQPXZ, shown in **Figure 1.19**).³⁷ Although, ΔE_{ST} is only 0.0863 eV, DBQPXZ has both TADF and RTP properties. In the crystalline state, its phosphorescent lifetime is 3.2 ms at room temperature. Interestingly, when the temperature is below 170 K, T_1 barely returns to S_1 and the T_1 to S_0 decay dominates

the process. When the temperature is above 170 K, the TADF emission is the dominant component.

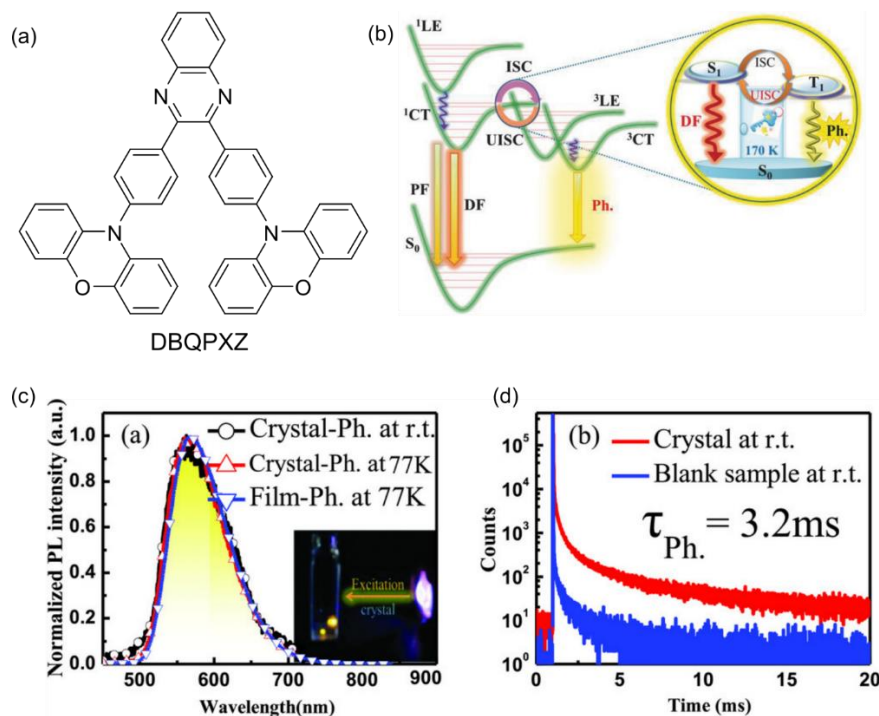


Figure 1.19 (a) Molecule structure of DBQPXZ. (b) Schem for thermal-controlled triplet recycling through reverse intersystem crossing and phosphorescence radiation for DBQPXZ. (c) Normalized phosphorescence and (d) transient PL decay spectra of DBQPXZ. Copyright 2017, Wiley-VCH.³⁷

1.4.2.2 Suppression or decrease of k_{nr} and k_q

As described in the formulae for phosphorescence quantum yield and phosphorescence lifetime, in addition to increase k_{ISC} as mentioned above, it is also crucial to suppress or reduce k_{nr} (nonradiative transitions) and k_q (the quenching rate of the triplet excited state by quenching species) in order to obtain high phosphorescence quantum yields and long phosphorescence lifetimes. Common methods used to reduce k_{nr} and k_q include: matrix rigidification, embedding in polymer, host–guest complexation, and crystallization.

1.4.2.2.1 Rigidification in a polymer matrix

Compared to small molecules, polymers have a larger molecular weight and long chains that can lead to entanglement and a high degree of rigidity, making them ideal candidates for the observation of phosphorescence in organic emitters. Polymers can not only act as rigid substrates to suppress the molecular vibrations and rotations of phosphors like a lattice, but also reduce the quenching effect of oxygen and moisture in the surrounding environment, allowing the triplet state excitonic compounds of organics to survive sufficiently

long for emission at room temperature. The reduction of k_{nr} and k_q via polymerization is usually achieved by dilution of a small RTP molecule into a polymer, such as polymethyl methacrylate (PMMA) or polyvinyl alcohol (PVA).

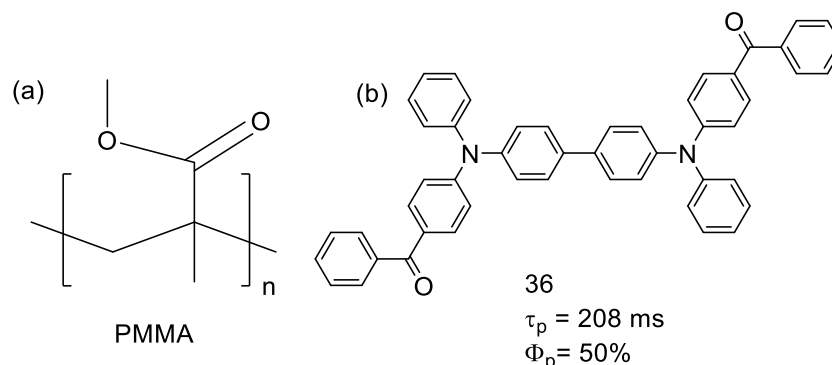


Figure 1.20 (a) Molecule structure of PMMA. (b) RTP emitter **36**.³⁸

In 2013, Baldo's group reported that an organic molecule **36** (shown in the **Figure 1.20**) dispersed into PMMA, showed highly efficient dual fluorescence and phosphorescence emission at room temperature, the estimated Φ_P was as high as 50% with a slow decay lifetime of 208 ms.³⁸

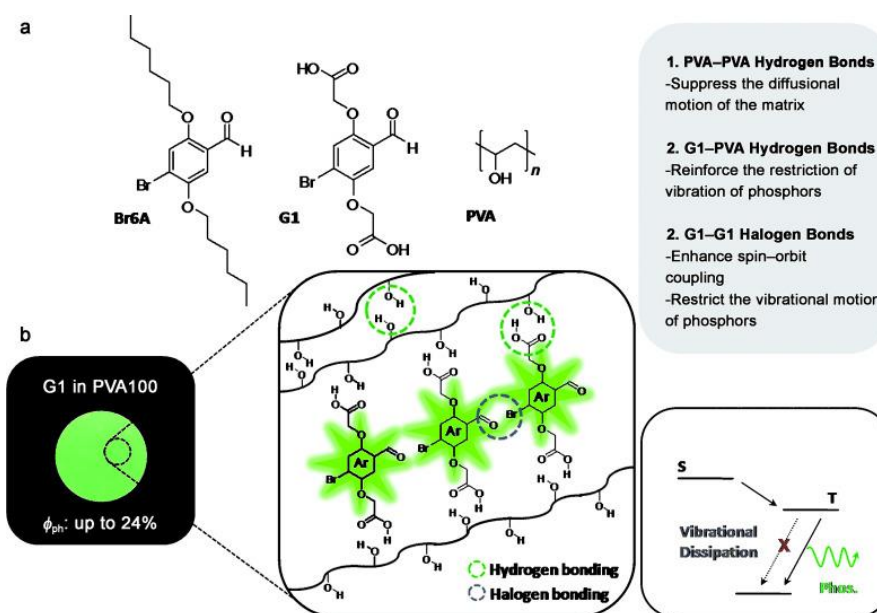


Figure 1.21 (a) Chemical structures of Br6A, G1, and PVA. (b) Phosphorescence image of G1 embedded in PVA100 under UV light ($\lambda=365$ nm) and schematic illustration of phosphorescence processes in the G1–PVA composite. Copyright 2014, Wiley-VCH.³⁹

In 2014, Kim's group proposed an immobilisation method to suppress vibrations between the phosphor and the substrate.²¹ As shown in the **Figure 1.21**, strong hydrogen

bonds are formed between the emitter and the PVA, inhibiting the movement of the molecules.³⁹ They chose two materials, Br6A and G1, with bromobenzoic acid as the core. The Br6A-doped PVA80 films produced green phosphorescence at room temperature, but the phosphorescence quantum yield is only 2.2%, much lower than the 13% of G1-doped PVA80. The authors also investigated the effect of different degrees of polymerisation of the polymers (PVA100 and PVA80) on the inhibition of molecular motion. PVA100 has 25% more hydrogen bonding sites than PVA80. By using PVA100, the green phosphorescent quantum yield of G1 reached 24%.

1.4.2.2.2 Matrix rigidification

In addition to doping the emitters into the polymer to inhibit molecular motion, a rigid host is another way to achieve inhibition of k_{nr} and k_q . The common rigid hosts are: metal-organic frameworks (MOF), organic crystals, silica, etc.

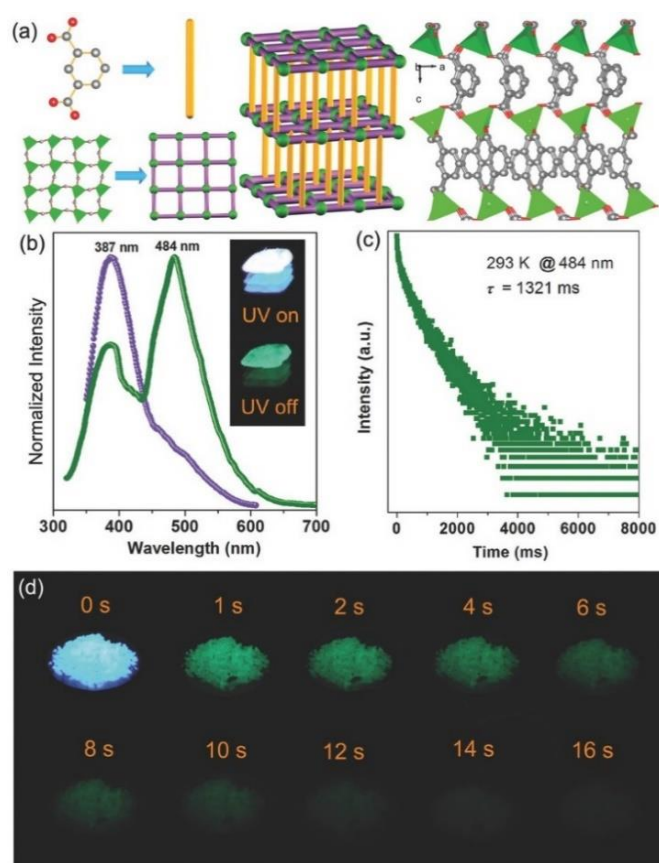


Figure 1.22 (a) Crystal structure of Zn-IPA. (b) Photoluminescence spectra of Zn-IPA in crystalline state (purple line is fluorescence and green line is phosphorescence). Insets show the corresponding photographs taken before and after the excitation source is turned off. (c) Time-resolved emission decay curve (484 nm) for Zn-IPA under ambient conditions. (d) Photographs of the long-lived RTP

Zn-IPA material taken at different time intervals before and after turning off the UV excitation (365 nm) under ambient conditions. Copyright 2016, Wiley-VCH.⁴⁰

Metal-organic frameworks are inorganic-organic hybrid materials that generally have a relatively rigid structure. Through molecular design, organic phosphorescent groups are coordinated to metal ions, which can be confined to the MOF material due to the stronger coordination interactions to reduce the k_{nr} and k_q . In 2016, Yang's group reported the first MOF-based RTP materials. They chose isophthalic acid (IPA), which exhibits both fluorescence and phosphorescence dual emission and can be coordinated with metals as a ligand. After coordination with Zn^{2+} to produce MOF(Zn-IPA), the crystal phosphorescence lifetime at room temperature is 1321 ms, and the afterglow emission can be recognized in the time range 0–16 s after removing the UV excitation (shown in **Figure 1.22**).⁴⁰

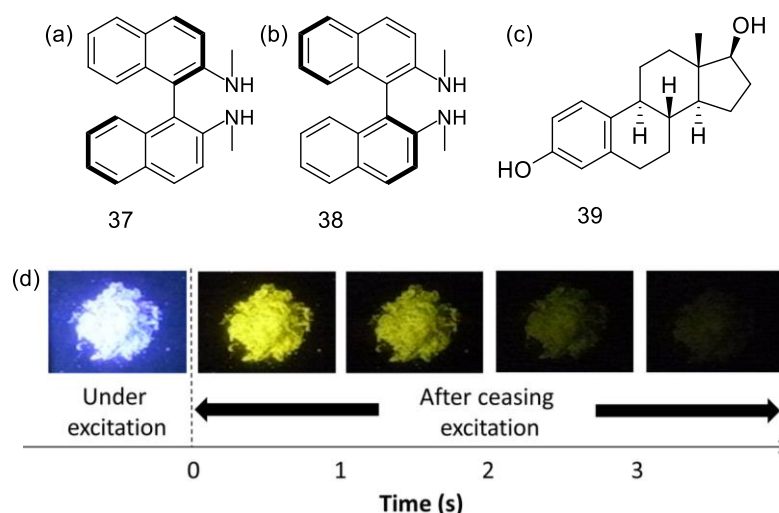


Figure 1.23 (a) Chemical structure of 37. (b) Chemical structure of 38. (c) Chemical structure of 39. (d) Changes in the luminescence of 0.3% (mass fraction) (R)-DMBDA-doped β -estradiol powders under excitation and after ceasing the excitation. Copyright 2016, American Chemical Society.⁴¹

In 2016, Vacha's group reported circularly polarised RTP from metal-free and heavy-atom-free chiral aromatics with afterglow emission properties in air.⁴¹ The enantiomer of N,N'-dimethyl-1,1'-binaphthyl-2,2'-diamine (37 and 38, shown in **Figure 1.23**) doped into 39 produced blue fluorescence and yellow persistent RTP in air. The lifetime and quantum yield of the yellow persistent RTP in the air were 0.67 s and 2.3%, respectively. Clear yellow emission remained after ceasing the excitation.

1.4.2.2.3 Host–guest complexation

Another effective way to inhibit the movement of molecules, apart from matrix rigidification and polymerization, is host–guest complexation. Phosphorescent molecules as the guest and rigid materials as the host, stiffen the structure of phosphorescent molecules to avoid excessive concentrations that could lead to self-quenching and extinction.

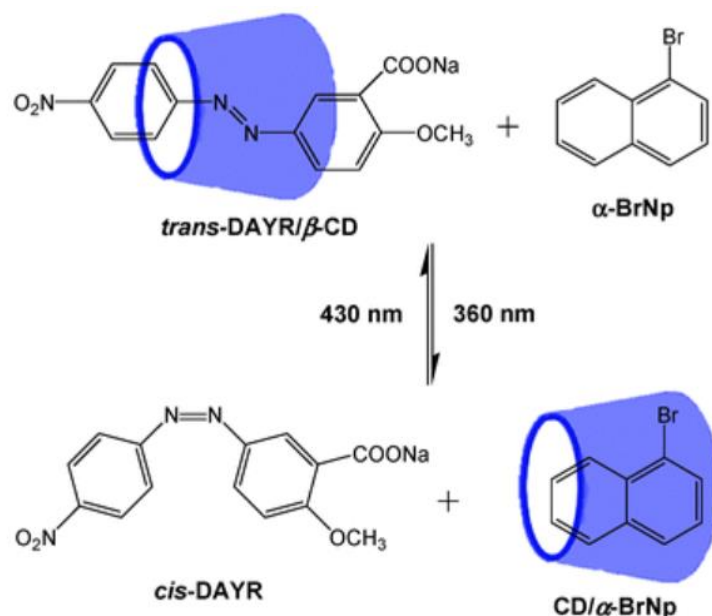


Figure 1.24 The reversible inclusion of β -CD/DAYR/ α -BrNp ternary system. Copyright 2011, The Royal Society of Chemistry.⁴²

In 2011, Tian's group reported a room temperature phosphorescent system based on β -cyclodextrin (β -CD), α -bromonaphthalene (α -BrNp), and sodium 2-hydroxy-5-((4-nitrophenyl)diazenyl)benzoate (DAYR) (**Figure 1.24**).⁴² The trans-DAYR can preferentially form an inclusive pseudo-rotaxane with β -CD. Under light (UV = 360 nm), DAYR changes from a trans structure to a cis structure and β -CD includes α -BrNp to generate RTP emission. The phosphorescence lifetime at room temperature is 0.53 ms. The structural change is reversible under different wavelengths of illumination

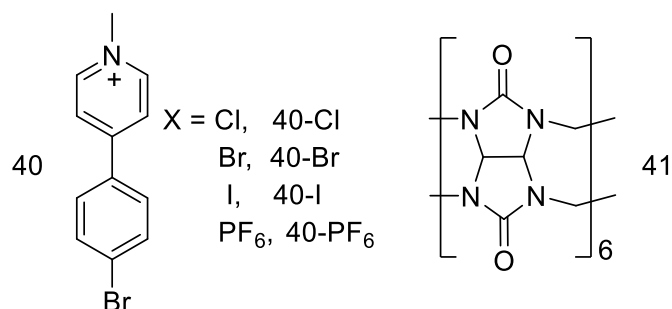


Figure 1.25 Molecular structures of 40 and 41.²⁸

In 2019, Liu's group reported enhanced phosphorescence effects of organic single molecules through supramolecular assembly of complexation between host cucurbit[6]uril (41) and guest (4-(4-bromophenyl)-N-methylpyridinium (40, X= Cl, Br, I, and PF₆) (shown in **Figure 1.25**). The phosphorescence quantum yields of 40-Cl, 40-Br, and 40- PF₆ are 2.6%, 4.6% and 0.4% respectively. Remarkably, the quantum yield of 40-I is as high as 24.1%. The complex 40/41 (X= Cl, Br, I, and PF₆) is formed when 40 complexes with 41. Due to the tight encapsulation of 41, the quantum yields were increased to varying degrees compared to the pure guest, where 40-Cl/41 increased to 81.2% and 40-Br/41 increased to 72.9%. The quantum yield of 40-I/41 is reduced to 3.0% compared to the pure guest because 40-I can form charge-transfer complexes, which lead to quenching of the luminescence.²⁸

1.4.2.2.4 Crystallization

Crystallization is the most common method of reducing molecular vibrations, and due to the close packing of crystals, it is effective in reducing molecular vibrations while keeping the material free from external factors such as oxygen. However, this does not apply to all phosphorescent materials. For some planar structured luminescent materials, after crystallisation, the π -orbitals between molecules overlap, leading to trilinear-state - trilinear-state annihilation, which weakens the phosphorescence. In 2015, the group reported effective crystal emission from a group of aromatic acids and esters free of metals and heavy atoms. The terephthalic acids (TPA) exhibit very low photoluminescence efficiency in solution and in the amorphous state due to vibrations and rotations. However, the crystalline powder exhibits intense deep blue light emission (388 nm) and an RTP lifetime of 0.16 ms, as shown in **Figure 1.26**.⁴³ The other two derivatives of benzodicarboxylic acid (shown in **Figure 1.26**): isophthalic acid (IPA) and tetrafluoroterephthalic acid (TFTPA), are also almost non-luminous in solution (only a single peak), but in crystals show a shoulder at higher wavelength in addition to the fluorescence peak, which is attributed to the RTP. The phosphorescence lifetimes of isophthalic acid and tetrafluoroterephthalic acid are 289.86 ms and 17.93 ms, respectively. Moreover, a long green afterglow lasting for several seconds is detected for IPA crystals after photoexcitation is stopped, as shown in **Figure 1.26**.

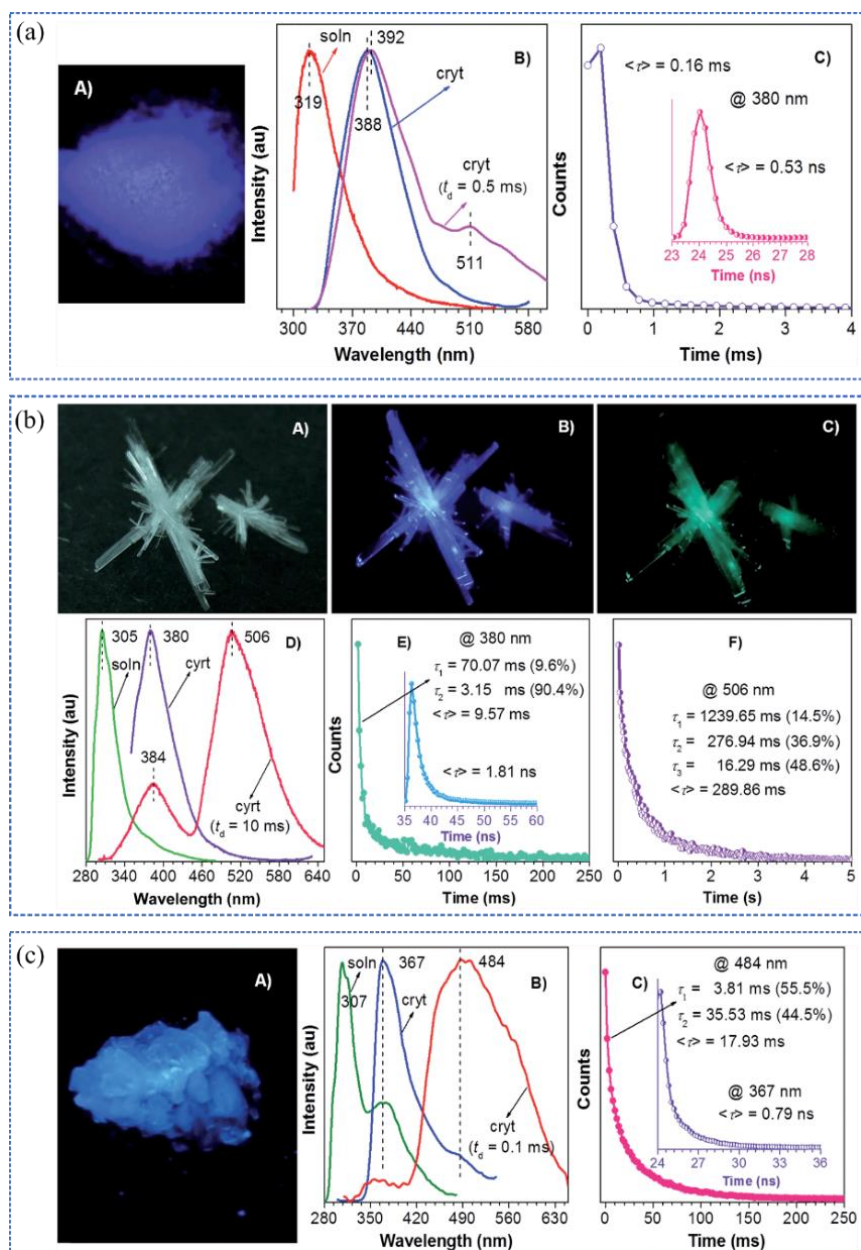


Figure 1.26 (a) The terephthalic acid (TPA) section: (A) Photograph of crystalline powders of TPA taken under 365 nm UV light. (B) PL spectra of TPA solution (20 μ M in ethanol) and crystalline powders with t_d of 0 and 0.5 ms. (C) Emission decay curves of crystalline powders of TPA monitored at 380 nm. (b) The isophthalic acid (IPA) section: Photographs of IPA crystals under (A) room light, (B) 365 nm UV light and (C) just after stopping UV light. (D) PL spectra of IPA solution (20 μ M in ethanol) and crystals with t_d of 0 and 10 ms. (E) Emission decay curves of IPA crystals monitored at (E) 380 and (F) 506 nm. (c) The tetrafluoroterephthalic acid (TFTPA) section: Photograph of TFTPA crystals under 365 nm UV light. (B) PL spectra of TFTPA solution (20 μ M in ethanol) and crystals with t_d of 0 and 0.1 ms. (C) Emission decay curves of TFTPA crystals monitored at 484 and 367 nm (inset). Copyright 2015, The Royal Society of Chemistry.⁴³

1.5 Applications of pure organic RTP

Based on the unique luminescent properties of pure organic RTP materials, and their low cost, ease of preparation and good processability, they are used in a wide range of applications such as anti-counterfeiting encryption, displays, sensor, bio-imaging .ect.²⁸

1.5.1 Anti-counterfeiting encryption

Organic RTP materials have a long lifetime, which allows them to hold more information than fluorescent molecules, thus enabling multiple information encryption. As mentioned above, the luminescence of organic RTP materials is influenced by the aggregation of molecules and therefore the appropriate encryption method should be used for each material. Solid powders and printing are commonly used.

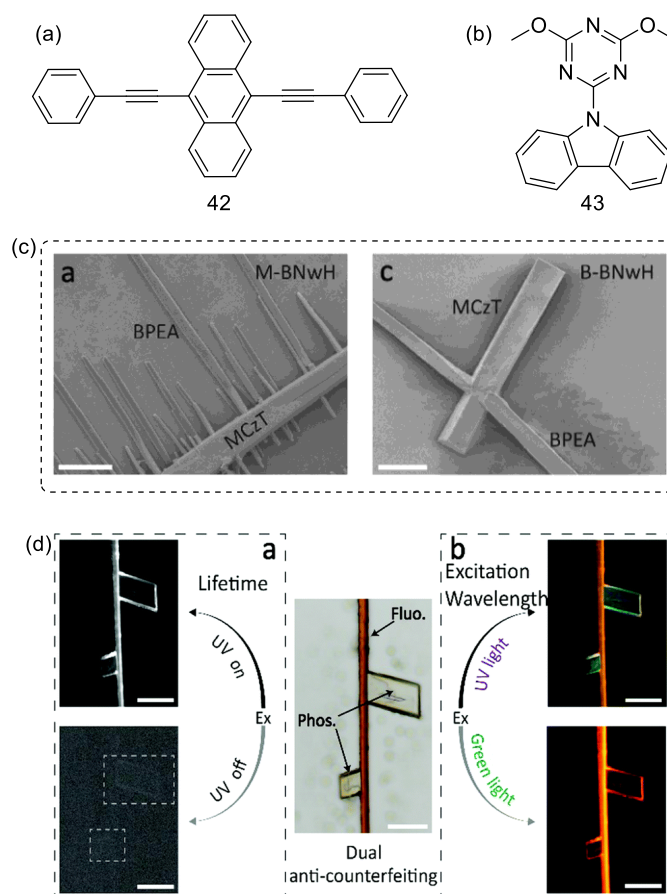


Figure 1.27 (a) and (b) are the molecular structures of 42 (BPEA) and 43(MCzT), respectively. (c) SEM image of an M-BNwH and B-BNwH. (d) Dual-anti-counterfeiting application of B-BNwHs. The black-white fluorescence micrography images of MCzT nanostructures under UV on and off. The micrography image of B-BNwHs under UV off were taken at 0.5 s after turning off the excitation

(right). The fluorescence microscopy images of the heterostructure excited by UV light (330–380 nm) and green light (510–560 nm). The scale bars of all are 10 μm (left). Copyright 2019, The Royal Society of Chemistry.⁴⁴

In 2019, Ann's group prepared two types of branched organic heterostructures M-BNwHs ($C_{\text{BPEA}}/C_{\text{MCzT}} = 1:4$) and B-BNwHs ($C_{\text{BPEA}}/C_{\text{MCzT}} = 1:1$) by co-assembling fluorescent material 42 (9,10-bis(phenylethynyl)-anthracene, BPEA) and a pure organic phosphorescent material 43 (9-(4,6-dimethoxy-1,3,5-triazin-2-yl)-9H-carbazole, MCzT) and adjusting the concentrations of the two components (shown in **Figure 1.27**).⁴⁴ The authors use B-BNwHs as a sample to demonstrate a dual anti-counterfeiting application (shown in **Figure 1.27**). Time-resolved luminescence of the B-BNwHs pass enables the first level of anti-counterfeiting. The fluorescence of the skeletal material disappears rapidly after the excitation light source is switched off, while the branches show a continuous luminescence for a few seconds. In addition, the colour of the branches changes from blue to red when the excitation source is adjusted from UV to green light. A second level of anti-counterfeiting is therefore achieved. This method is both easy to observe and difficult to counterfeit due to the special phosphorescent material used.

In 2020, Yang's group discovered a time-varying afterglow colour in the single-component organic molecular crystal 4,4'-bis(N-carbazolyl)-1,1'-biphenyl (pCBP) (shown in **Figure 1.28**).⁴⁵ In dual-coded anti-counterfeiting (shown in **Figure 1.28**), there is a cryptographic pattern "2" with the crystal pCBP that is not visible under the UV light source due to interference from methyl 3-(10-(4-methoxyphenyl)anthracen-9-yl)benzoate (cDPA). When the UV light source is switched off, a blue "2" pattern becomes visible and the colour changes from blue to orange within 1 second. In addition, crystalline pCBP can be used to construct a 4D code for data encryption. The pattern is prepared using elements 2, 0, 1, and 9 (in positions A, B, C, and D respectively). After switching off the light, the scanner moves from position A to position D and reads the blue "2" at 0.0 s, the blue "0" at 0.1 s and the purple "1" at 0.5 s, and the orange "9" at 1 s.

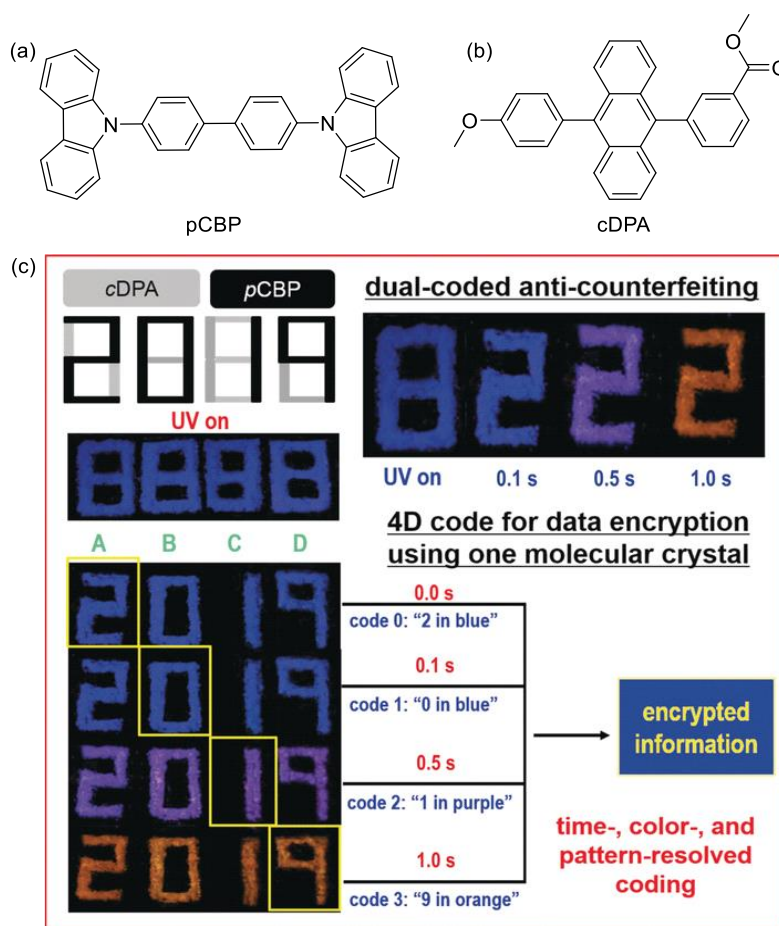


Figure 1.28 (a) and (b) are the molecular structures of pCBP and cDPA, respectively. (c) Dual-coded anticounterfeiting and 4D coding models for data encryption with time-dependent afterglow color changes of pCBP. Copyright 2020, Wiley-VCH.⁴⁵

1.5.2 Sensors

According to Equation 4 (please refer to 1.4.2.1), the temperature has a significant impact on the luminous efficiency and lifetime of room temperature phosphorescence, so organic RTP materials can be used for temperature sensing applications. The triplet exciton is also sensitive to changes in the external environment, such as water and oxygen. Therefore, RTP materials can also be used for these external detections.

In 2020, Huang's group demonstrated that organic afterglow can be enhanced by thermally activated processes and exhibits anomalous tri-mode emission at room temperature from the radiative decay of S_1 , T_1 , and T_1^* (stabilized triplet state).⁴⁶ In the crystal, DCzB exhibits tri-mode emission with peaks at 475 nm, 495 nm, 525 nm, and 570 nm and lifetimes of 240 ms, 234 ms, and 231 ms respectively. The 475 nm is attributed to fluorescence and TADF, 495 nm to phosphorescence, and 525 nm and 570 nm to organic ultralong room

temperature phosphorescence (OURTP). At the same time, DCzB shows great potential for color displays and visual detection at certain temperatures. As shown in **Figure 1.29**, the DCzB pattern of an "8", excited by a UV lamp (365 nm), appears blue at different temperatures, and when the UV lamp is switched off, the pattern changes from a lime green afterglow emission at 300K to a yellow-green afterglow emission at 77K.

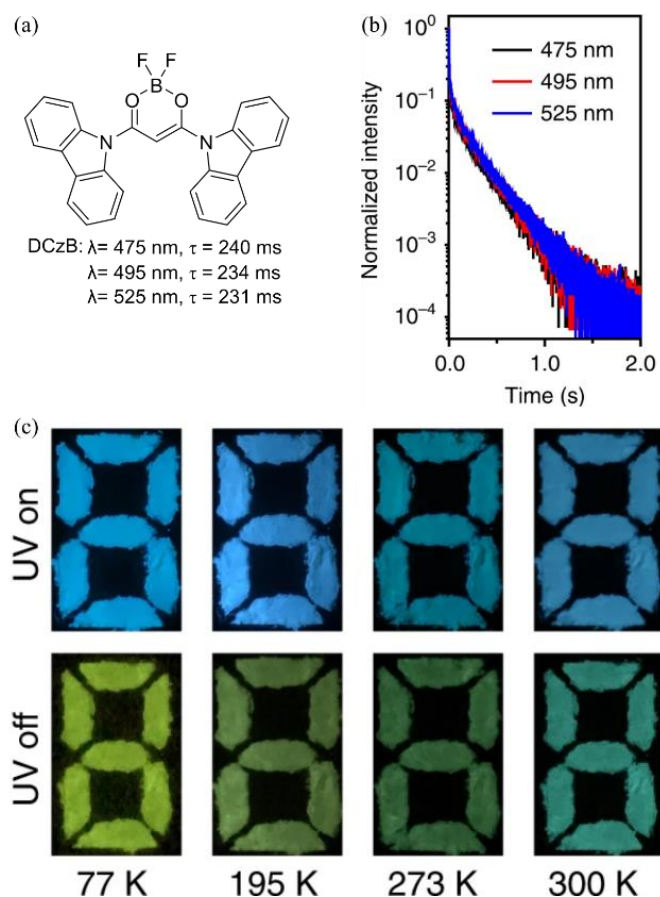


Figure 1.29 (a) The molecular structure of DCzB. (b) Afterglow decay profiles of the 475, 495, and 525 nm emission bands of DCzB crystal excited at 380 nm at room temperature. (c) Photographs of the pattern before (UV on) and after (UV off) the turning off of the 365 nm UV lamp at 77, 195, 273, and 300 K. Copyright 2020, Nature Publishing Group.⁴⁶

In 2009, Fraser's group reported a series of compounds (P1, P2, and P3) (shown in **Figure 1.30**) coupled with iodide-substituted difluoroboron dibenzoylmethane and poly(lactic acid) (PLA).⁴⁷ They exhibited significant long afterglow emission under oxygen-free conditions. The modulation of fluorescence and long afterglow luminescence is achieved by controlling the number of iodine atoms in the polymer by modulating the chain length of the polymer. As the chain length of the polymer increases, the fluorescence emission peak is red-shifted, indicating that ΔE_{ST} increases with increasing chain length. The ratio between the

fluorescence and the long afterglow luminous intensity of polymer P1 in thin films has a linear relationship with the oxygen concentration, which is why it can be used as a turn-on type sensor at low oxygen concentrations. Polymer P2 exhibits a more balanced dual emission of fluorescence and phosphorescence and is prepared as nanoparticles (98 nm diameter) by nanoprecipitation, while the nanoparticles exhibit good biocompatibility and high oxygen sensitivity for bioimaging mouse tumor sites at different oxygen concentrations. Red areas are microvasculature, blue areas are hypoxic tumor tissue.

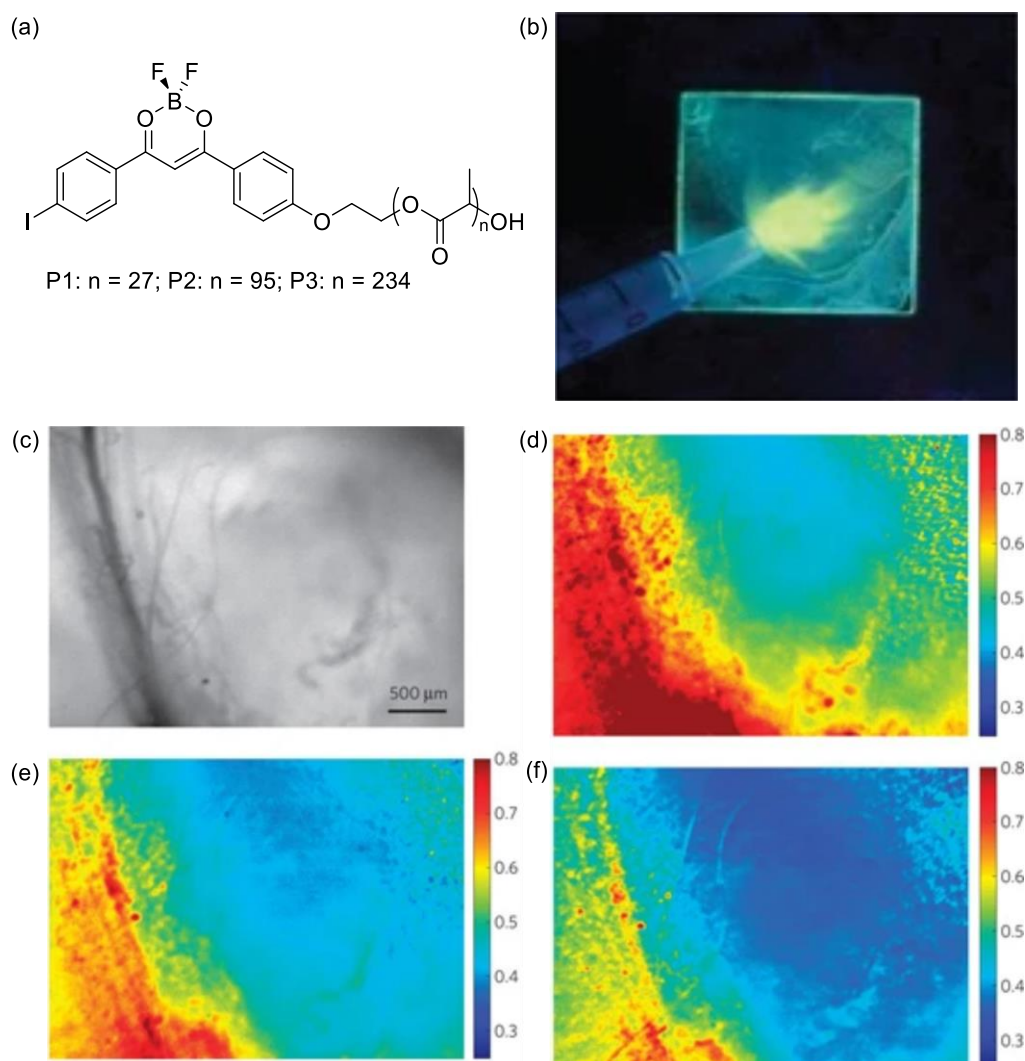


Figure 1.30 (a) The molecular structures of P1, P2, and P3. (b) Image showing yellow phosphorescence emission under a N₂ gas stream for a spin-cast P1 film under ultraviolet excitation. (Yellow phosphorescence turns on immediately on gas contact. Blue-green background: weak P1 fluorescence.) c-f is the in vivo imaging of nanoparticles in the tumor region of the mouse. (c) Bright-field; (d) BNP fluorescence/phosphorescence ratio while breathing carbogen—95% O₂; (e) Room air—21% O₂; (f) Nitrogen—0% O₂. Copyright 2020, Nature Publishing Group.⁴⁷

1.5.3 Bioimaging

Organic RTP materials have a long luminescence lifetime and can effectively reduce the effects of autofluorescence and background signals in organisms, thus achieving a high signal-to-noise ratio during bioimaging. The long-lived emission images are easy to capture and can be acquired using relatively inexpensive detection equipment. At the same time, pure organic RTP materials can avoid the biological toxicity associated with precious metals and are biocompatible, making them promising for use in high-resolution bioimaging techniques.

In 2017, Tang's group used the unique permeabilizing and amphiphilic properties of saponins to deliver fluorescent nanoparticles and pure organic phosphorescent nanocrystals (NCs) (44, shown in **Figure 1.31**) encapsulated into cells.⁴⁸ Remarkably, this method can successfully deliver nanoparticles to cells in less than 5 minutes. The pure organic phosphorescent nanocrystals also showed a long lifetime of up to 100 ms in HeLa cells, shown in **Figure 1.31**, which is four orders of magnitude better than conventional dyes (hexaphenylsilole, 45) and background autofluorescence. This result suggests that organic RTP molecules are promising candidates for achieving high-resolution bioimaging without background interference.

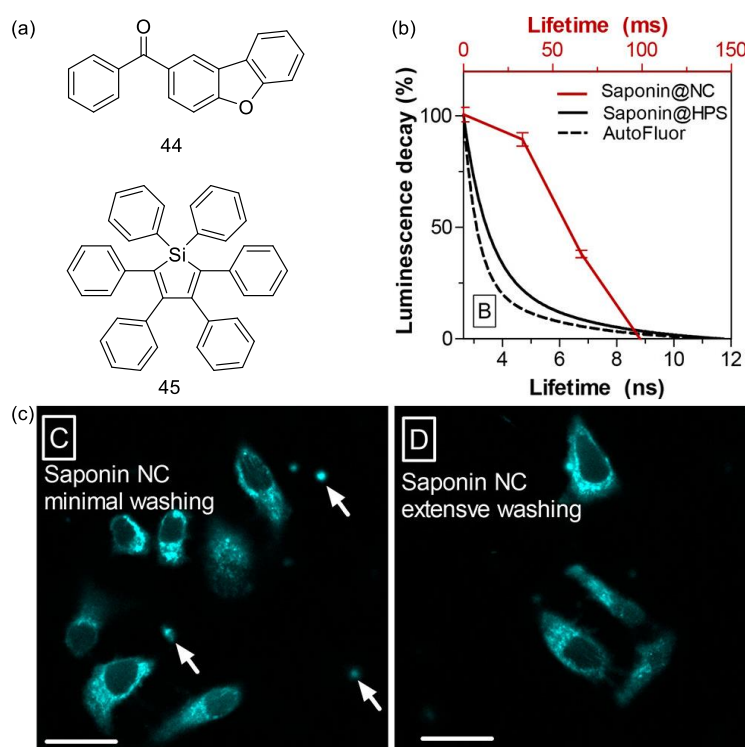


Figure 1.31 (a) Molecular structures of 44 and 45. (b) Normalized luminescence decay comparison between saponin@NCs, 45, and cellular autofluorescence in HeLa cells. (c) confocal laser scanning

microscope images of HeLa cells after 5 min incubation with 1 $\mu\text{g/mL}$ of saponin @NCs. Scale bar = 20 μm for all images.⁴⁸

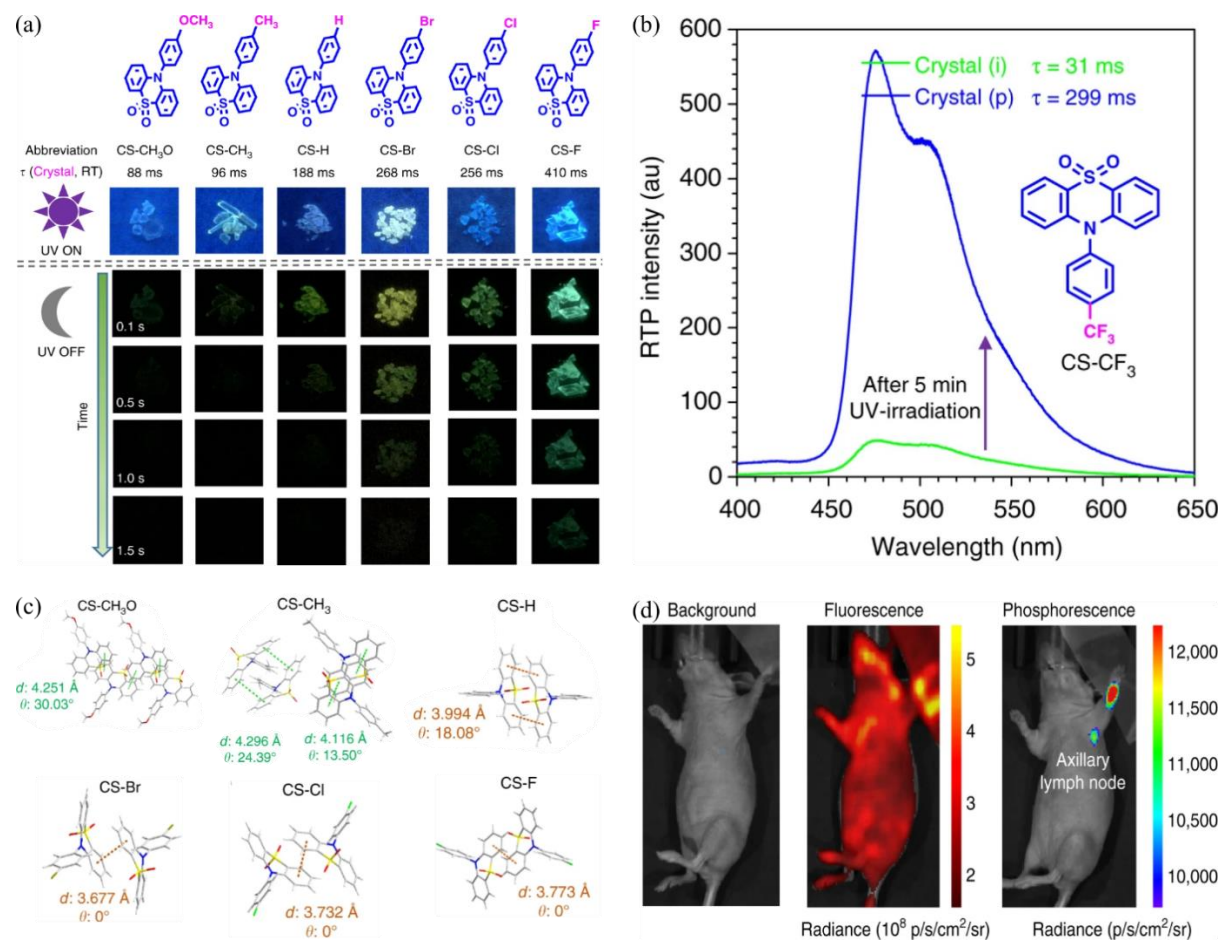


Figure 1.32 (a) Molecular structures of CS-CH₃O, CS-CH₃, CS-H, CS-Br, CS-Cl, and CS-F, and their corresponding phosphorescence lifetimes in crystals at room temperature. (b) The room temperature phosphorescence spectra of CS-CF₃ crystal before and after 365 nm UV irradiation for 3 min. (c) Crystal structures of CS-CH₃O, CS-CH₃, CS-H, CS-Br, CS-Cl, and CS-F. (d) Ultralong phosphorescence and fluorescence imaging of lymph node in living mice 1 h after the intradermal injection of CS-F nanoparticles into the forepaw of mice. Copyright 2018, Nature Publishing Group.⁴⁹

In 2018, Li's group developed a series of phenothiazine-5,5-dioxide derivatives (CS-CH₃O, -CH₃, -H, -Br, -Cl, and -F) (shown in **Figure 1.32**).⁴⁹ All compounds showed RTP properties in single crystals with lifetimes ranging from 88-410 ms. After analysis of the electrostatic potential calculations and crystal structures, the authors concluded that in solids, strong π - π interactions between molecules can promote persistent RTP. Interestingly, the CS-CF₃ crystals showed a unique reversible photo phosphorescence effect, with a change in molecular stacking under UV light and a phosphorescence lifetime longer than before the

ultraviolet illumination (shown in **Figure 1.32**). At the same time molecules with electron-absorbing substituents have stronger π - π interactions leading to longer-lived RTPs than molecules with donating electron substituents. The long phosphorescence lifetime of CS-F makes it possible to use CS-F nanoparticles for in vivo imaging. One hour after nanoparticle injection into mice, phosphorescence was still detectable in bioluminescence mode 10 seconds after removal of the light source after one minute of UV light irradiation (shown in **Figure 1.32**).⁴⁹

1.6 Conclusions

Phosphorescence is a different process as compared to fluorescence. Phosphorescence has a slow emission, which in practice excludes the effects of autofluorescence, and is sensitive to oxygen. RTP emitters are therefore widely used in applications such as oxygen sensors, anti-counterfeit printing, and bio-imaging. Equations (2) and (3) show that there are two main factors in achieving efficient RTP. The first is that phosphorescence depends heavily on the rate of ISC, so increasing ISC is essential. It can be achieved via the introduction of elements containing lone pairs of electrons or heavy atoms. The second is to reduce the non-radiative decay rate of the triplet state. Doping of a rigid polymer matrix with room temperature phosphorescent materials and crystal packaging can effectively suppress non-radiative transitions. In the last few decades, various RTP materials have been designed and synthesized and the mechanisms of phosphorescent emission have been investigated. However, high-performance all-organic RTP materials remain a formidable challenge. To develop high performance RTP materials with excellent τ_p and Φ_p values for different applications, it is essential to actively explore the design rules and luminescence mechanisms of RTP molecules.

1.7 References

1. Li, Z. *et al.* Ultra-small fluorescent inorganic nanoparticles for bioimaging. *J. Mater. Chem. B* **2**, 2793–2818 (2014).
2. Yu, J. *et al.* Recent advances in optical and optoelectronic data storage based on luminescent nanomaterials. *Nanoscale* **12**, 23391–23423 (2020).
3. Ku, M., Hwang, J. C., Oh, B. & Park, J.-U. Smart Sensing Systems Using Wearable Optoelectronics. *Adv. Intell. Syst.* **2**, 1900144 (2020).
4. Sun, D. *et al.* Thermally Activated Delayed Fluorescent Dendrimers that Underpin High-Efficiency Host-Free Solution-Processed Organic Light-Emitting Diodes. *Adv. Mater.* **34**, 1–11

- (2022).
5. Ye, W. *et al.* Confining isolated chromophores for highly efficient blue phosphorescence. *Nat. Mater.* **20**, 1539–1544 (2021).
 6. Peng, Q., Yi, Y., Shuai, Z. & Shao, J. Toward quantitative prediction of molecular fluorescence quantum efficiency: Role of Duschinsky rotation. *J. Am. Chem. Soc.* **129**, 9333–9339 (2007).
 7. Li, Y. *et al.* Reduced Intrinsic Non-Radiative Losses Allow Room-Temperature Triplet Emission from Purely Organic Emitters. *Adv. Mater.* **33**, 2101844 (2021).
 8. Xviii, P. & Braams, C. M. On the influence motion. *Physica* **29**, 431–440 (1952).
 9. Chen, R. *et al.* Promoting singlet/triplet exciton transformation in organic optoelectronic molecules: Role of excited state transition configuration. *Sci. Rep.* **7**, 1–11 (2017).
 10. Theiss, T. *et al.* Room-Temperature Phosphorescence from Pd(II) and Pt(II) Complexes as Supramolecular Luminophores: The Role of Self-Assembly, Metal-Metal Interactions, Spin-Orbit Coupling, and Ligand-Field Splitting. *J. Am. Chem. Soc.* **145**, 3937–3951 (2022)
 11. Varano Casasanta, C. Pioneers in Optics: Alexander Jablonski (1898–1980). *Micros. Today* **30**, 46–46 (2022).
 12. Del Valle, J. C. & Catalán, J. Kasha's rule: A reappraisal. *Phys. Chem. Chem. Phys.* **21**, 10061–10069 (2019).
 13. Thompson, M. J. & Messina, M. A Quantitative Explanation of the Dynamics Underlying the Franck-Condon Principle: A Mostly Classical Viewpoint. *J. Chem. Educ.* **96**, 1171–1177 (2019).
 14. Santos, E. M. *et al.* Design of Large Stokes Shift Fluorescent Proteins Based on Excited State Proton Transfer of an Engineered Photobase. *J. Am. Chem. Soc.* **143**, 15091–15102 (2021).
 15. Yang, Z. *et al.* Recent advances in organic thermally activated delayed fluorescence materials. *Chem. Soc. Rev.* **46**, 915–1016 (2017).
 16. Shan, T. *et al.* Highly efficient and stable pure blue nondoped organic light-emitting diodes at high luminance based on phenanthroimidazole-pyrene derivative enabled by triplei-triplet annihilation. *Dye. Pigment.* **142**, 189–197 (2017).
 17. Hu, S. *et al.* High-efficiency and long-lifetime deep-blue organic light-emitting diode with a maximum external quantum efficiency of 20.6% and CIEy of 0.04. *Dye. Pigment.* **205**, 110548 (2022).
 18. Nalaoh, P. *et al.* A Dimeric π -Stacking of Anthracene Inducing Efficiency Enhancement in Solid-State Fluorescence and Non-Doped Deep-Blue Triplet–Triplet Annihilation Organic Light-Emitting Diodes. *Adv. Opt. Mater.* **9**, 2100500 (2021).
 19. Jiang, H., Tao, P. & Wong, W. Y. Recent Advances in Triplet-Triplet Annihilation-Based Materials and Their Applications in Electroluminescence. *ACS Mater. Lett.* 822–845 (2023) doi:10.1021/acsmaterialslett.2c01070.

20. Nalaoh, P. *et al.* A Hybridized Local and Charge-Transfer Excited State for Highly Efficient Fluorescent OLEDs: Molecular Design, Spectral Character, and Full Exciton Utilization. *Adv. Opt. Mater.* **2**, 892–901 (2021).
21. Singh, J., Shakeel, U., Ompong, D. & Ram, K. S. Intersystem and Reverse-Intersystem Crossings in Organic Light-Emitting Diodes. *J. Phys. Chem. Lett.* **13**, 6177–6180 (2022).
22. Chen, T. *et al.* Understanding the Control of Singlet-Triplet Splitting for Organic Exciton Manipulating: A Combined Theoretical and Experimental Approach. *Sci. Rep.* **5**, 1–11 (2015).
23. Endo, A. *et al.* Efficient up-conversion of triplet excitons into a singlet state and its application for organic light emitting diodes. *Appl. Phys. Lett.* **98**, 2009–2012 (2011).
24. Uoyama, H., Goushi, K., Shizu, K., Nomura, H. & Adachi, C. Highly efficient organic light-emitting diodes from delayed fluorescence. *Nature* **492**, 234–238 (2012).
25. Cui, L. S. *et al.* Controlling Singlet–Triplet Energy Splitting for Deep-Blue Thermally Activated Delayed Fluorescence Emitters. *Angew. Chemie - Int. Ed.* **56**, 1571–1575 (2017).
26. Kim, H. J. & Yasuda, T. Narrowband Emissive Thermally Activated Delayed Fluorescence Materials. *Adv. Opt. Mater.* **10**, 2201714 (2022).
27. Hatakeyama, T. *et al.* Ultrapure Blue Thermally Activated Delayed Fluorescence Molecules: Efficient HOMO-LUMO Separation by the Multiple Resonance Effect. *Adv. Mater.* **28**, 2777–2781 (2016).
28. Zhao, W., He, Z. & Tang, B. Z. Room-temperature phosphorescence from organic aggregates. *Nat. Rev. Mater.* **5**, 869–885 (2020).
29. Baba, M. Intersystem crossing in the $1n\pi^*$ and $1\pi\pi^*$ states. *J. Phys. Chem. A* **115**, 9514–9519 (2011).
30. Wei, J. *et al.* Induction of Strong Long-Lived Room-Temperature Phosphorescence of N - Phenyl-2-naphthylamine Molecules by Confinement in a Crystalline Dibromobiphenyl Matrix . *Angew. Chemie* **128**, 15818–15822 (2016).
31. Wang, J. *et al.* A facile strategy for realizing room temperature phosphorescence and single molecule white light emission. *Nat. Commun.* **9**, 1–9 (2018).
32. Shi, H. *et al.* Highly Efficient Ultralong Organic Phosphorescence through Intramolecular-Space Heavy-Atom Effect. *J. Phys. Chem. Lett.* **10**, 595–600 (2019).
33. Wang, C. R., Gong, Y. Y., Yuan, W. Z. & Zhang, Y. M. Crystallization-induced phosphorescence of pure organic luminogens. *Chinese Chem. Lett.* **27**, 1184–1192 (2016).
34. Zhao, W. *et al.* Rational Molecular Design for Achieving Persistent and Efficient Pure Organic Room-Temperature Phosphorescence. *Chem* **1**, 592–602 (2016).
35. An, Z. *et al.* Stabilizing triplet excited states for ultralong organic phosphorescence. *Nat. Mater.* **14**, 685–690 (2015).
36. Chen, X. *et al.* Versatile Room-Temperature-Phosphorescent Materials Prepared from N-

- Substituted Naphthalimides: Emission Enhancement and Chemical Conjugation. *Angew. Chemie - Int. Ed.* **55**, 9872–9876 (2016).
37. Yu, L. *et al.* Pure Organic Emitter with Simultaneous Thermally Activated Delayed Fluorescence and Room-Temperature Phosphorescence: Thermal-Controlled Triplet Recycling Channels. *Adv. Opt. Mater.* **5**, 1–8 (2017).
 38. Reineke, S., Seidler, N., Yost, S., Prins, F., Tisdale, W., Baldo, M. Highly efficient, dual state emission from an organic semiconductor. *Appl. Phys. Lett.* **103**, 093302 (2013).
 39. Kwon, M. S., Lee, D., Seo, S., Jung, J. & Kim, J. Tailoring Intermolecular Interactions for Efficient Room-Temperature Phosphorescence from Purely Organic Materials in Amorphous Polymer Matrices. *Angew. Chemie - Int. Ed.* **53**, 11177–11181 (2014).
 40. Yang, X. & Yan, D. Strongly Enhanced Long-Lived Persistent Room Temperature Phosphorescence Based on the Formation of Metal–Organic Hybrids. *Adv. Opt. Mater.* **4**, 897–905 (2016).
 41. Hirata, S. & Vacha, M. Circularly Polarized Persistent Room-Temperature Phosphorescence from Metal-Free Chiral Aromatics in Air. *J. Phys. Chem. Lett.* **7**, 1539–1545 (2016).
 42. Ma, X., Cao, J., Wang, Q. & Tian, H. Photocontrolled reversible room temperature phosphorescence (RTP) encoding β -cyclodextrin pseudorotaxane. *Chem. Commun.* **47**, 3559–3561 (2011).
 43. Gong, Y. *et al.* Crystallization-induced dual emission from metal- and heavy atom-free aromatic acids and esters. *Chem. Sci.* **6**, 4438–4444 (2015).
 44. Yang, C. *et al.* Controllable co-assembly of organic micro/nano heterostructures from fluorescent and phosphorescent molecules for dual anti-counterfeiting. *Mater. Horizons* **6**, 984–989 (2019).
 45. Wang, J. X. *et al.* Time-Dependent Afterglow Color in a Single-Component Organic Molecular Crystal. *Angew. Chemie - Int. Ed.* **59**, 10032–10036 (2020).
 46. Jin, J. *et al.* Thermally activated triplet exciton release for highly efficient tri-mode organic afterglow. *Nat. Commun.* **11**, 1–9 (2020).
 47. Zhang, G., Palmer, G. M., Dewhirst, M. W. & Fraser, C. L. A dual-emissive-materials design concept enables tumour hypoxia imaging. *Nat. Mater.* **8**, 747–751 (2009).
 48. Nicol, A. *et al.* Ultrafast Delivery of Aggregation-Induced Emission Nanoparticles and Pure Organic Phosphorescent Nanocrystals by Saponin Encapsulation. *J. Am. Chem. Soc.* **139**, 14792–14799 (2017).
 49. Yang, J. *et al.* The influence of the molecular packing on the room temperature phosphorescence of purely organic luminogens. *Nat. Commun.* **9**, 1–10 (2018).

Chapter 2. Simultaneous delayed fluorescence and phosphorescence in organic emitters employing multiple excited states

2.1 Abstract

Triplet dynamics plays a key role in room temperature phosphorescence (RTP) and thermally activated delayed fluorescence (TADF). In this work, we report a model emitter with three emission components: prompt fluorescence (PF) in nanoseconds, delayed fluorescence in microseconds, and RTP in milliseconds, with the emission spectrum from ultraviolet to deep blue. We experimentally and theoretically verify that a higher triplet excited state T_2 is involved in facilitating simultaneous PF, TADF, and RTP. The reverse intersystem crossing (rISC) from T_2 to S_1 contributes to the TADF, while the radiative transition from T_1 to the ground state is the origin of the long-lived RTP. By transferring the energy of multiple excited states to a series of conventional fluorescence emitters, a multi-color emissive system within the entire visible wavelength range has been realized, with the photoluminescence decay ranging from 10^{-9} s to 10^{-1} s. By slightly tuning the energy difference between these excited states in the model molecule a highly efficient organic luminescent material with only PF and RTP emission has been obtained with an RTP quantum yield above 30%.

2.2 Introduction

Exciton kinetics have significant impact on the efficiency and operational stability of optoelectronic devices based on organic semiconductors.¹⁻⁶ In purely organic emitters, triplets are normally non-radiative or with low radiative rates, because it is spin forbidden. However, 75% of excitons formed under electron-hole recombination in electrically driven light-emitting devices are triplets.⁷ Two strategies have been developed to harvest these non-radiative triplets for efficient organic light-emitting diodes (OLEDs). By using the heavy atom effect from iridium or platinum with a high atomic number, the intersystem crossing (ISC) and the resulting triplet radiation have been significantly enhanced, giving rise to efficient phosphorescence at room temperature.⁸⁻¹⁰ Another strategy is minimizing the energy splitting between the singlet and triplet states ΔE_{ST} , to realize efficient reverse intersystem crossing (rISC) with the assistance of the thermal energy (~ 0.026 eV) at room temperature, termed as

thermally activated delayed fluorescence (TADF).^{11,12} Recently, there have also been reports of direct triplet emission in purely organic emitters as room temperature phosphorescence (RTP), achieved by fixing organic emitters in a polymer matrix or crystals to reduce the non-radiative relaxation from triplets.^{13–16} Because there is no need of rare and expensive heavy metal ingredients, TADF and RTP emissions from purely organic emitters have gained tremendous scientific attention in recent years.^{14,17–21}

For purely organic emitters, the prompt fluorescence (PF) originating from the spin-allowed singlet radiative transition has an emission lifetime on the nanoseconds timescale, resulting in a typical singlet radiative rate $k_{r,S}$ in the range of 10^{10} - 10^8 s⁻¹.^{22,23} The TADF from the ISC-rISC cycling normally has a longer decay lifetime of 10^{-7} - 10^{-5} s, because of the involvement of spin-flip processes and nuclear geometry changes.^{11,24} In the case of RTP, the direct triplet radiation is very slow, with rates in the range of 1 - 10^3 s⁻¹.^{13,14,19,25} Therefore, the transient emission behavior of purely organic emitters is kinetically determined by the involved processes in a coupled manner.^{12,24,26} Because the kinetic rates related to TADF and RTP differ by several orders of magnitude, simultaneous PF, TADF and RTP from a single emitter is a rare and unexpected occurrence.²⁷

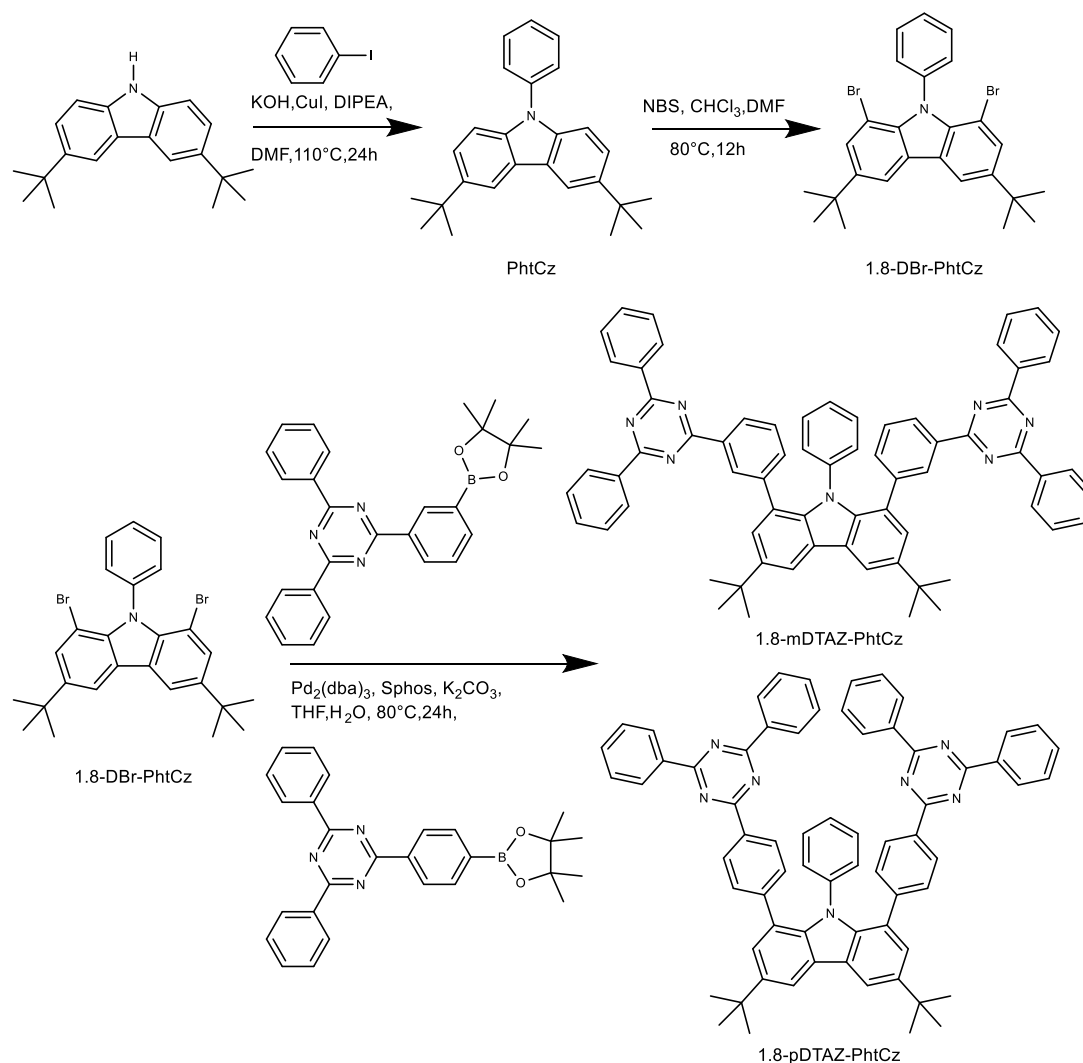
The transient photophysical properties for TADF and RTP emitters have been widely investigated and are typically modelled with a two-excited state model, in which two excited states – a singlet S_1 and a triplet state T_1 –are involved.^{13,26} Though an additional higher-lying triplet state T_2 energetically below S_1 while higher than T_1 has been theoretically addressed²⁰, there is a lack of direct experimental evidence. Therefore, a thorough understanding of the impact of the higher-lying triplet state on the photophysical properties is still absent. Due to smaller energy difference S_1 - T_2 as compared to S_1 - T_1 , the rISC rate between S_1 - T_2 is higher than the rate between S_1 - T_1 . For TADF emitter design, a faster rISC rate will reduce the triplet concentration under a constant current density, which will enhance the operational stability for electroluminescent devices based on TADF emitters.²⁸ Furthermore, according to the Fermi's golden rule, a higher ISC rate is anticipated between S_1 - T_2 , as compared to S_1 - T_1 , because of the relatively smaller energy difference, which can be used to enhance the phosphorescence quantum yield by RTP materials design. Therefore, the experimental investigation of the higher-lying triplet state and its impact on photophysical properties is of

general significance for organic luminescent materials design in general and as well as for the development of electroluminescent devices.

In this work, we show that with only two excited states, it is impossible to achieve PF in nanoseconds (ns), TADF in microseconds (μ s), and RTP in milliseconds (ms) simultaneously from a single emissive system. In the present study, we firstly report a model emitter 3,6-di-tert-butyl-1,8-bis(3-(4,6-diphenyl-1,3,5-triazin-2-yl)phenyl)-9-phenyl-9H-carbazole (1,8-mDTAZ-PhtCz), with photoluminescence (PL) signatures of PF, TADF and RTP decay. Using the emitter 1,8-mDTAZ-PhtCz as a model system, we experimentally and theoretically verify by transient absorption (TA) spectroscopy together with molecular simulations that a higher-lying triplet state T_2 is involved. The transient emissive behavior can be described and fitted with a three-state model, with the upper triplet state T_2 contributing to the TADF property while the T_1 state being responsible for the RTP emission. Based on the model emitter, color tunable systems have been realized via Förster resonance energy transfer (FRET) to conventional fluorescent emitters, with the emission decay from the ns to second region. One derivative have been synthesized by further modifying the chemical structure of the model molecule, named as 3,6-di-tert-butyl-1,8-bis(4-(4,6-diphenyl-1,3,5-triazin-2-yl)phenyl)-9-phenyl-9H-carbazole (1,8-pDTAZ-PhtCz). Highly efficient PF/RTP emitter 1,8-pDTAZ-PhtCz has been achieved, with the RTP quantum yield higher than 30%.

2.3 Synthesis

The synthesis of 1,8-mDTAZ-PhtCz and 1,8-pDTAZ-PhtCz are described in **Scheme 2.1**. 3,6-di-tert-butyl-9-phenyl-9H-carbazole (PhtCz) is obtained by coupling tert-butyl carbazole and iodobenzene. 1,8-dibromo-3,6-di-tert-butyl-9-phenyl-9H-carbazole (1,8-DBr-PhtCz) is obtained by bromination of PhtCz with 1-bromo-2,5-pyrolidinedione (NBS). Suzuki coupling of 1,8-DBr-PhtCz with 2,4-diphenyl-6-(3-(4,4,5,5-tetramethyl-1,3,2-dioxaborolan-2-yl)phenyl)-1,3,5-triazine (received from commercial sources) gave the final 1,8-mDTAZ-PhtCz. Suzuki coupling of 1,8-DBr-PhtCz with 2,4-diphenyl-6-(4-(4,4,5,5-tetramethyl-1,3,2-dioxaborolan-2-yl)phenyl)-1,3,5-triazine (received from commercial sources) yielded the corresponding 1,8-pDTAZ-PhtCz. The structures of intermediates and the target product were unambiguously characterized by nuclear magnetic resonance (NMR) spectra, high-resolution mass spectra (HRMS), and finally by X-ray diffraction analysis from suitable crystals.



Scheme 2.1 Synthetic routes for the 1,8-mDTAZ-PhtCz and 1,8-pDTAZ-PhtCz.

2.4 Optical properties

The extinction coefficient of 1,8-mDTAZ-PhtCz in toluene as plotted versus wavelength of the optical absorption is shown in **Figure 2.1a**. The strong absorption band at 330-360 nm is attributed to the π - π^* transitions.²⁹ Strong PL emission from the emitter was observed, spanning from the ultraviolet to deep blue region, presented in **Figure 2.1a** and **2b**. The fluorescence is solvent polarity dependent, as summarized in **Table 2.1**, indicating the charge transfer (CT) nature of the emissive dipoles.^{30,31} The absolute photoluminescence quantum yield (PLQY) of highly diluted 1,8-mDTAZ-PhtCz in a rigid polymer matrix polystyrene (PS) was determined as 36.1% in air and 51.1% in nitrogen. The difference of PLQY in ambient and nitrogen atmosphere indicates the involvement of triplets during the

emissive process. The delayed PL spectrum spans from the ultraviolet to the deep blue region as well, shown in **Figure 2.1c**.

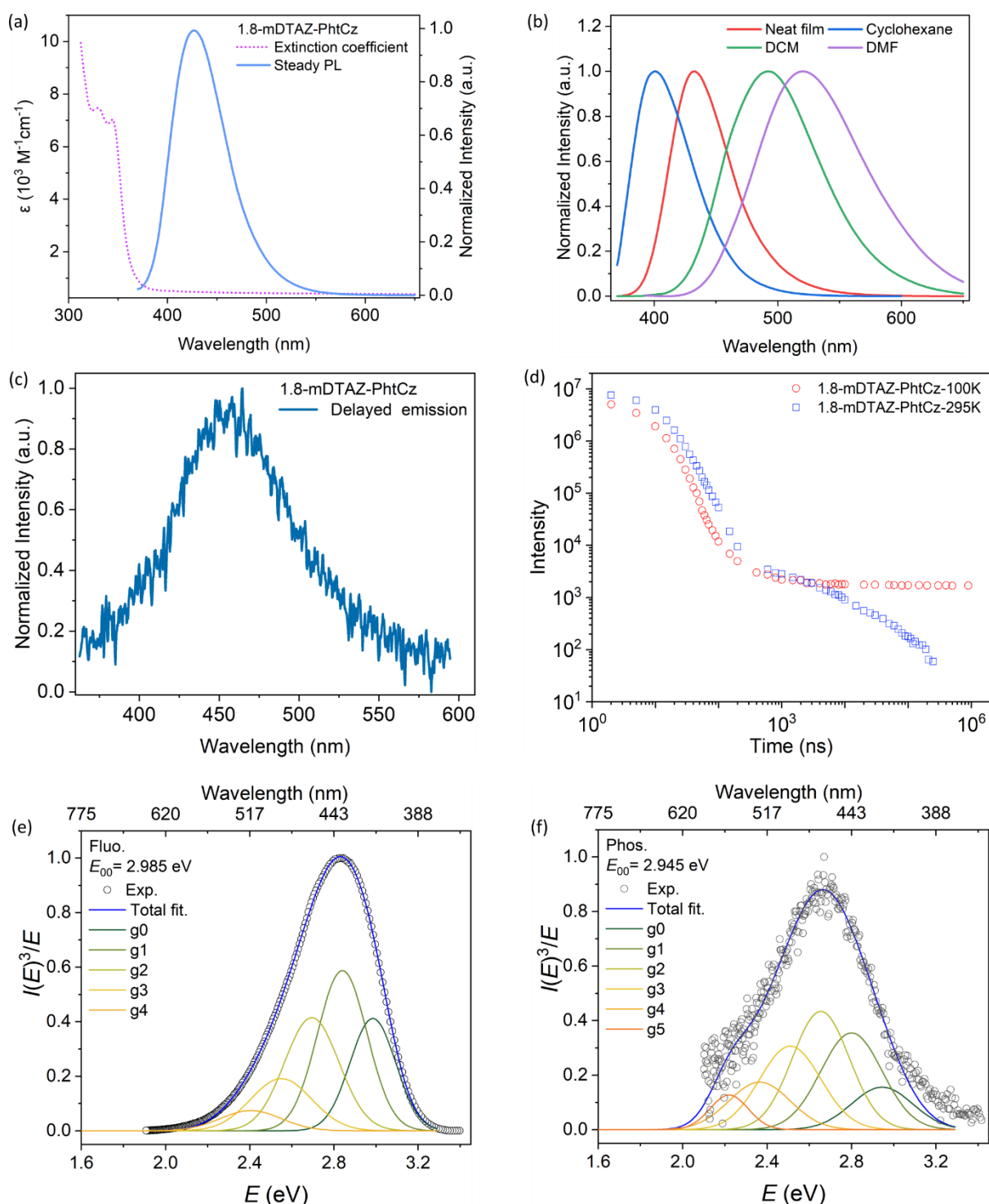


Figure 2.1 (a) Steady state UV-Vis absorption and PL emission spectra in toluene. (b) Steady-state PL spectra in different solvents and neat film of 1,8-mDTAZ-PhtCz. (c) PL spectrum with a delay of 200 μ s after the laser excitation. Measured in a rigid polymer matrix. (d) Temperature dependency of

transient emission decay of 1,8-mDTAZ-PhtCz film doped in PMMA (2 wt%). (e) Lineshape analysis of fluorescence spectra. (f) Lineshape analysis of phosphorescence spectra.

Reducing the temperature to 100 K, the delayed emission within the μs range is then taken over by the long-lived phosphorescence without significant intensity decrease in the μs range, as shown in **Figure 2.1d**, indicating the involvement of TADF emission. The singlet and triplet energies were determined according to the lineshape analysis from the fluorescence and delayed spectrum. The lineshape analysis is done based on the consideration that the different vibronic energy states in the ground state for organic emitters can be described with a small energy difference. The Franck–Condon factors describing the transition probabilities to different vibronic states (i.e. different Gaussian shape fitting components) follow a Poisson progression, which leads to the relation between the emission spectral lineshape and energetic states involved.³² Such a lineshape analysis has been used for the precise determination of energy levels for TADF and RTP emitters.^{13,33} As shown in **Figure 2.1e** and **2.1f**, it is determined as 2.985 eV and 2.945 eV for the model emitter S_1 and T_1 , respectively. Therefore, the singlet-triplet splitting ΔE_{ST} is determined to be 0.04 eV, indicating the possibility of TADF emission with such a small ΔE_{ST} . The key photophysical properties are summarized in **Table 2.1**.

Table 2.1. Key photophysical properties for developed luminescent materials.

Sample	λ_{Abs} (nm) ^a	λ_{FL} (nm) ^a	λ_{FL} (nm) ^b	λ_{FL} (nm) ^c	λ_{FL} (nm) ^d	λ_{FL} (nm) ^e	λ_{FL} (nm) ^f	λ_{PH} (nm) ^b	E_{S1} (eV)	E_{T1} (eV)	Φ (Air/N ₂) (%) ^g
1,8-mDTAZ-PhtCz	330/345	425	427	410	433	493	521	458	2.985	2.945	36.1/51.1

(a) In toluene. (b) Doped in poly(methyl methacrylate) (PMMA) with 2 wt%. (c) In cyclohexane. (d) Neat film. (e) In DCM. (f) In DMF. (g) Doped in PS with 2 wt%.

As shown in **Figure 2.2a**, after stopping the UV irradiation, the intensity of the photoluminescence gradually decreased and remained present up to 42 s, indicating ultra-long afterglow phosphorescence emission in 1,8-mDTAZ-PhtCZ crystals at room temperature. The long-lived PL of the 1,8-mDTAZ-PhtCz crystal is related to the packing mode. The crystal structure of 1,8-mDTAZ-PhtCz is shown in **Figure 2.2b** and **2.2c**. In the single crystal, the TAZ groups are packed in a relative plane configuration, which might result from the strong intramolecular confinement from hydrogen bonds (2.48-2.54 Å). Meanwhile, the torsion angle Θ_2 between the *N*-phenyl ring and the tert-butylcarbazole is 63°, close to the torsion

angles between phenyl-triazine and tert-butylcarbazole (Θ_1 : 55° , Θ_3 : 58°) (**Figure 2.2b**). Such a twisted configuration leads to a distortion between the donor and acceptor moieties. The intermolecular packing in the single crystal is presented in **Figure 2.2c**. The triazine planes from the two molecules are packed with a vertical distance of 3.35 \AA , with a shift angle of 48.79° . Molecules are packed in a monoclinic style, with the detailed crystal parameters summarized in **Table 2.7**. These weak intramolecular and intermolecular interactions in crystals significantly reduce the molecular movements, giving rise to the long-lived triplet emission in crystals.³⁴

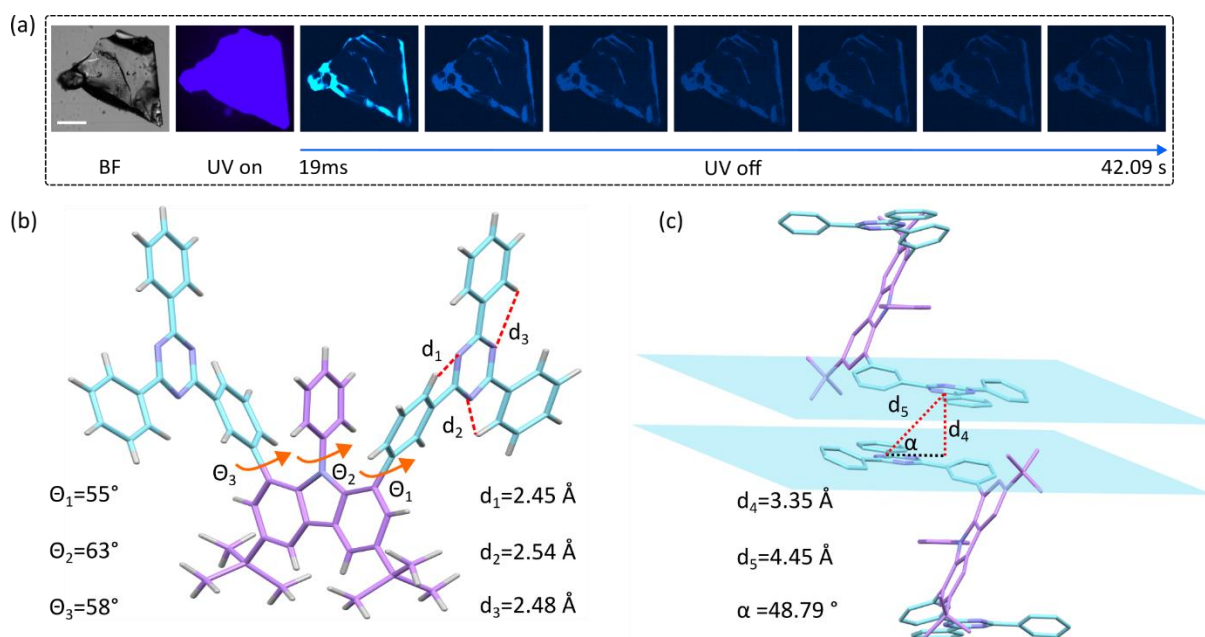


Figure 2.2 (a) Ultralong afterglow emission from the model emitter 1,8-mDTAZ-PhtCz crystal. (b) Intramolecular interactions in the single crystal. (c) Molecular packing behavior in a unit cell.

2.4 Limitation of the two-state model

We further turned to study the exciton kinetics of the emitter 1,8-mDTAZ-PhtCz. Pronounced PF decay, TADF and RTP emissions have been observed by time-correlated single photon counting (TCSPC) measurements, which will be discussed in the following section. The transient PL kinetics of purely organic emitters with PF and TADF emission has been modeled with a two-state system, with only a singlet excited state S_1 and a triplet state T_1 .^{26,35} This was in collaboration with Yungui Li (Max Planck Institute for Polymer Research, Mainz). We firstly used the two-state model to fit the emission kinetics, with details explained in the Supplementary note 1. By scanning ISC and rISC rates, and taking the singlet and triplet lifetime in a physically meaningful range, as shown in **Figure S2.1-S2.6**, we can

obtain numerical solutions for the coupled rate equations determined by the two-state model. However, mathematically, only two components with different orders of decay lifetime can be resolved with such a two-state model. Physically, one can interpret the numerical results in the following way. To maintain the long-lived RTP emission in ms, the intrinsic triplet lifetime τ_T in the two-state model should be comparable to that value. Simultaneously, to obtain delayed fluorescence with lifetime in μs , the rate k_{rISC} should be in the range of 10^6 s^{-1} . Since the rISC and RTP come from the same source T_1 in the two-state model, if k_{rISC} is orders of magnitude higher than the triplet radiative rate ($\sim 1/\tau_T$), triplets will mainly convert to singlets via rISC, leading to vanishing of RTP with pronounced TADF emission. In the other case when k_{rISC} is of the same order of $1/\tau_T$, only one delayed component can be observed with a delayed lifetime comparable to τ_T , though both TADF and RTP contribute to the delayed PL. Finally, if k_{rISC} is orders lower than $1/\tau_T$, only the long-lived RTP can be resolved, while the TADF emission is negligible. This is the normal case for RTP emitters when ΔE_{ST} is much larger than the thermal energy. The change of k_{ISC} and τ_S can only change the PF lifetime and the intensity of the delayed PL emission. In summary, based on the two-state model, the triplet state can only contribute to one delayed PL signal, though the lifetime of the delayed component can be varied over several orders of magnitude. It is impossible to obtain two delayed components with lifetimes in the μs and ms simultaneously, based on the two-state model with a single triplet state.

2.5 Involvement of upper triplet state in the model emitter

To reveal the mechanism behind the simultaneous occurrence of TADF and RTP, we then used TA spectroscopy to monitor the excited state kinetics in the model emitter 1,8-mDTAZ-PhtCz. This was in collaboration with Yungui Li (Max Planck Institute for Polymer Research, Mainz). The ns-TA spectra in degassed solution are shown in **Figure 2.3a** within the UV-VIS range. A pronounced long-lived excited state absorption (ESA) signal from the nanosecond to microsecond timescale is observed.

A forward evolving factor analysis (EFA) based on the UV-VIS ns-TA dataset indicates that there are three principal components contributing to the ns-TA signal (**Figure 2.3b**).^{36,37} We therefore use three components to fit the ns-TA data by the multivariate curve resolution alternating least square (MCR-ALS) algorithm, in which the experimental dataset are decomposed into associated spectra and concentration profiles of the principal

components.³⁸ In this soft-hard modelling process, the only constrain condition is that the concentration for each component is non-negative, which is of course physically robust.

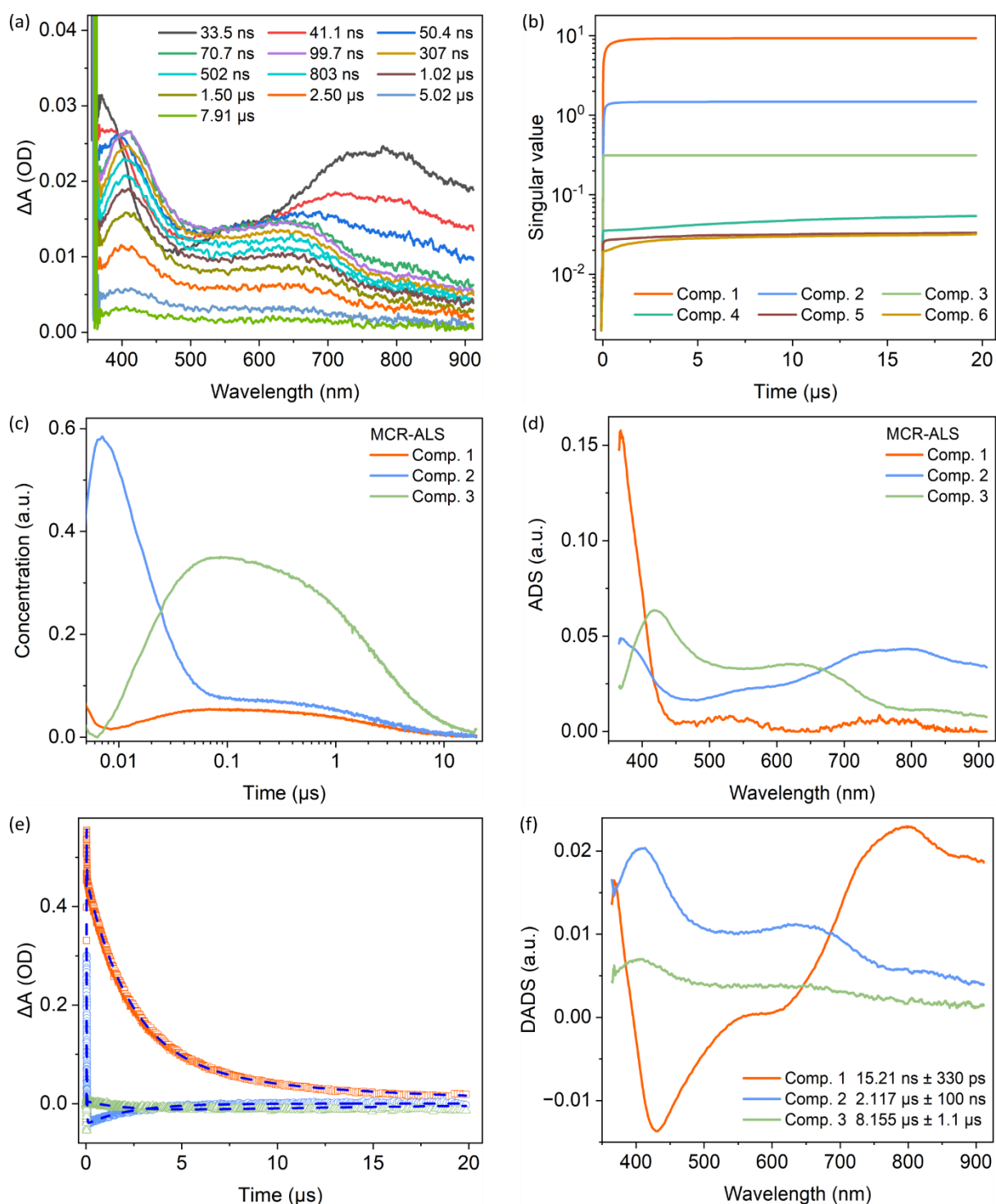


Figure 2.3 (a) Experimental ns-TA spectra of the degassed solution at specific delay times in the UV-VIS range. (b) Forward EFA of the ns-TA data. (c) Concentration evolution and (d) associated spectra

of the principal components from MCR-ALS fitting. (e) Kinetic fitting by the global analysis with three components based on a parallel scheme. (f) DADS from the global analysis.

The decomposed concentration profiles and associated spectra are shown in **Figure 2.3c** and **Figure 2.3d**, respectively. From the concentration evolution, it is known that the component 2 has a fast intensity decay within the early ~ 50 ns, while the other two components have an intensity increase process, followed by a gradual concentration decrease in the microsecond region. The associated spectra for these components indicate the absorptive feature of these components in the UV-VIS range.

A global analysis based on the parallel model is then carried out to further uncover the physical sources of these components.³⁹ As shown in **Figure 2.3e**, the experimental kinetic decays can be fitted nicely with three components within the investigated timescale. The decay associated difference spectra (DADS) for these components are presented in **Figure 2.3f**. It shows that there is a fast component with the decay lifetime about 15 ns, indicating that it is a singlet state. The DADS1 has singlet features at <400 nm and 700-900 nm decay, which corresponding to the fast signal change within the first ~ 100 ns, shown in **Figure 2.3a**. The DADS2 has triplet features with ESA peaks at 400 nm and 700 nm, with a decay lifetime of ~ 2.1 μ s. The component 3 has very similar DADS with component 2, as the normalized DADS shown in **Figure 2.4**. However, the decay lifetime for the third component is ~ 8.2 μ s, longer than the second component. The existence of two long-lived components is consistent with the EFA and MCR-ALS analysis. Furthermore, because the similarity of the DADS and long lifetime in microseconds for component 2 and 3, it indicates that these two are triplet states with very similar energy levels but different decay lifetimes.

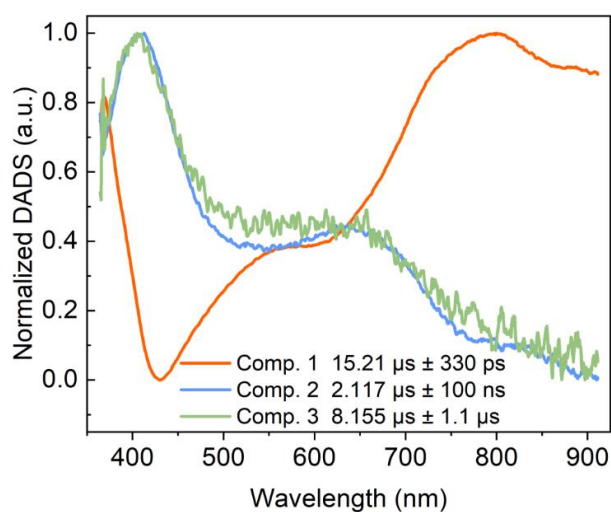


Figure 2.4 Normalized DADS for global analysis with a parallel model for 3 components of the model emitter 1,8-mDTAZ-PhtCz.

The comparison of ns-TA measurements in degassed and aerated solutions is shown in **Figure 2.5**. The long-lived ESA features at 400 nm and 600 nm in degassed solution is quenched by oxygen with the decay lifetime to a few hundred nanoseconds. Such a measurement indicates the triplet contribution within the wavelength region, consistent with the MCR-ALS and global analysis. As for 800 nm and 900 nm, similar quenching behavior is noted for the long-lived signal, while the short-lived decay is preserved in aerated solution, indicating the combined singlet and triplet contributions, which is consistent with DADS from the global analysis.

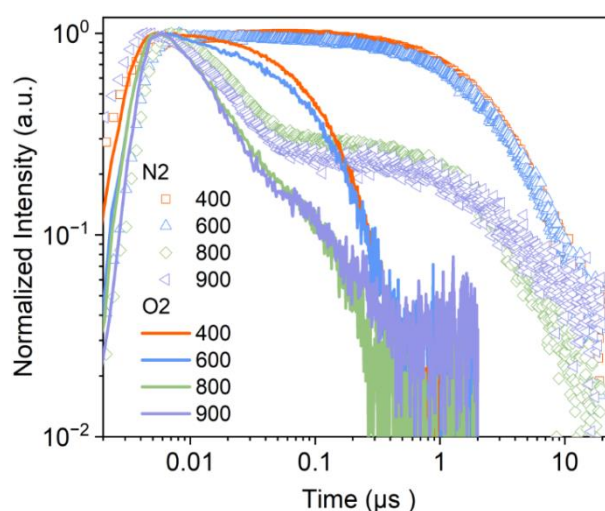


Figure 2.5 Oxygen sensitivity of ns-TA in degassed and aerated solutions of the model emitter 1,8-mDTAZ-PhtCz.

As a comparison, a global analysis based on the parallel model with only two components is done for the same dataset, with the DADS and kinetics fitting shown in **Figure 2.6**. Such a model can nicely fit the early experimental decays, while failing to fit the long-lived signals. Such a comparison demonstrates that there is indeed another long-lived components in the microsecond scale, justifying the treatment of three principal components in the previous data analysis. In conclusion, from the ns-TA measurements, we observed a singlet and two triplets contributing to the exciton dynamics in 1,8-mDTAZ-PhtCz, while the two triplet states have similar energy levels but different decay lifetimes.

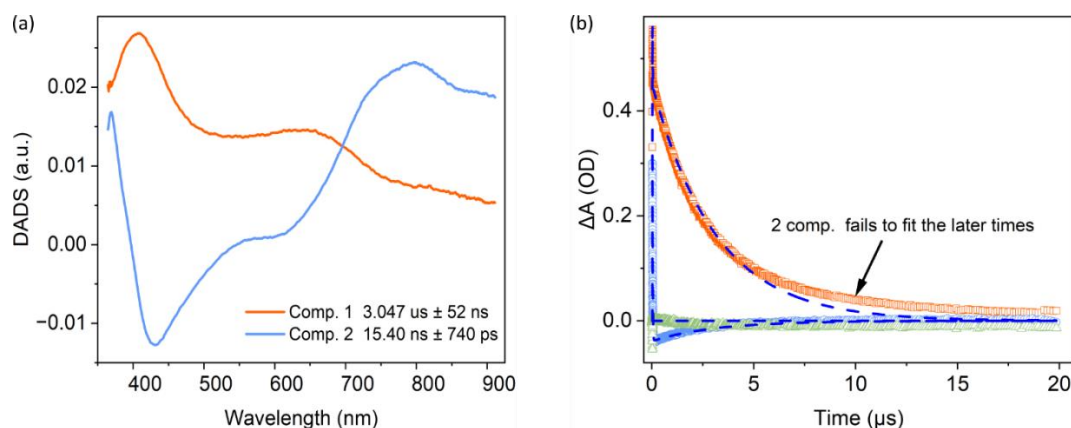


Figure 2.6 Global analysis with a parallel model for 2 components of 1,8-mDTAZ-PhtCz. (a) DADS; (b) Experimental and fitted kinetics, in which the long-lived signals are failed to fit.

2.6 Theoretical molecular simulations

To further elucidate the excited states of 1,8-mDTAZ-PhtCz, we performed molecular simulations to calculate their excited state energies, including Time-Dependent Density Functional Theory (TDDFT) with three different functionals, hybrid functional B3LYP, omega-tuned range-separated hybrid functionals ω T-CAM-B3LYP and ω T- ω B97xd, and the Restricted Open-shell Kohn–Sham method (ROKS)^{40,41} with the LC- ω PBE08 functional. For all the calculations, the 6-311g (d,p) basis set are applied. This was in collaboration with Wenlan Liu and Dennis Andrienko (Max Planck Institute for Polymer Research, Mainz). The simulation results are summarized in **Table 2.2**. All the three TDDFT methods underestimate the optical energy gaps, while the ROKS method predicted the excitation energies of the lowest singlet (S_1) and the two lowest triplet states (T_1 and T_2) perfectly consistent with the experimental ns-TA results. The ground state and excited state electron distributions are shown in **Figure 2.7**. The excitation energy of the first excited state is 3.493 eV (354 nm), close to the maximum absorption peak at 345 nm, shown in **Figure 2.1a** and **Table 2.1**.

Table 2.2 ROKS, DFT and TD-DFT simulation results for the model emitter (1,8-mDTAZ-PhtCz).

	ROKS	B3LYP	ω T-CAM-B3LYP	ω T- ω B97xd
Absorption	3.493 eV	3.087 eV	3.099 eV	3.180 eV
S_1	2.978 eV	2.700 eV	2.604 eV	2.650 eV
T_2	2.953 eV	2.790 eV	2.768 eV	2.820 eV
T_1	2.912 eV	2.613 eV	2.585 eV	2.634 eV

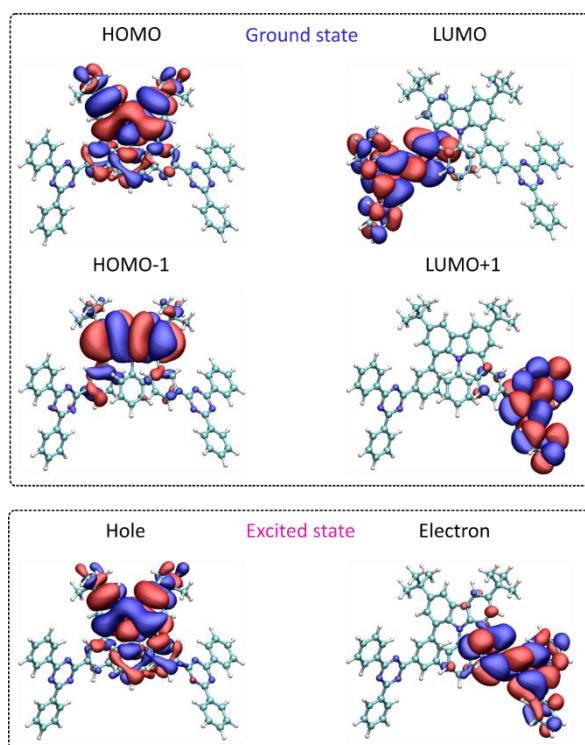


Figure. 2.7 Ground state and excited state electron distributions based on restricted ROKS for the model emitter.

The simulated energy levels for the different excited states are shown in **Figure 2.8a**. The calculated singlet state is 2.978 eV, based on the relaxed molecular configuration after photon excitation. The electron cloud distribution in **Figure 2.8b** indicates that the singlet state has a pronounced charge-transfer (CT) feature, consistent with the experimental observations summarized in **Table 2.1**. The simulated energy level of S_1 is close to the experimentally determined value of 2.985 eV, summarized in **Table 2.1**. The calculated energy level for T_1 is 2.912 eV, which is also close to the experimental result of 2.945 eV. Moreover, another triplet state T_2 with higher energy at 2.953 eV has been resolved, which is slightly lower than the simulated energy level of S_1 .

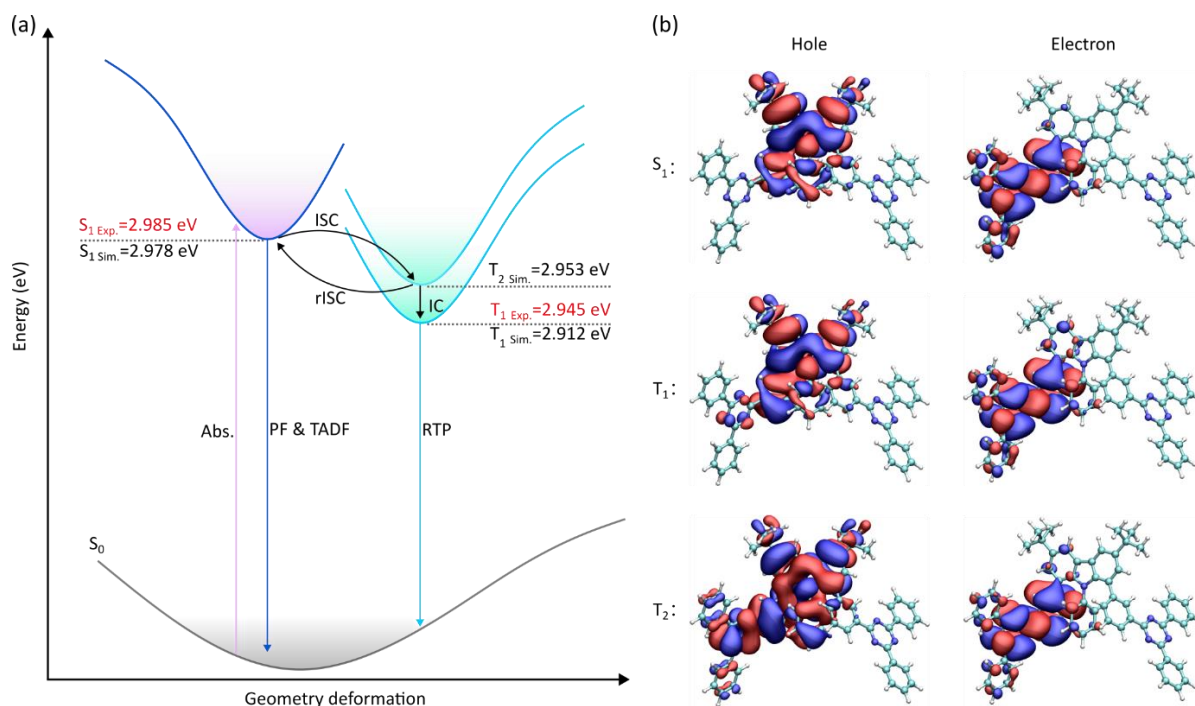


Figure 2.8 (a) Energy diagrams. (b) The hole and electron states electron distributions.

As shown in **Figure 2.8b**, S_1 , T_1 , and T_2 of 1,8-mDTAZ-PhtCz consist of a mixture of locally excited (LE) and CT states. The hole and electron wave functions of the S_1 and T_1 states are mainly located at the carbazole donor and phenyl-triazine acceptor, respectively. However, T_1 exhibits more LE character compared to S_1 . In contrast, the hole state of the T_2 is located on the carbazole donor and phenyl-triazine acceptor, while the electron state is mainly located on the phenyl-triazine acceptor, which means that the T_2 state accounts for more LE contributions.

The energy difference between S_1 and T_2 is ~ 0.025 eV, comparable to the thermal energy at room temperature. The energy level simulation indicates that efficient rISC can happen from T_2 to S_1 . Also, since the energy splitting between S_1 and T_2 is smaller than S_1 - T_1 , ISC is more likely to happen between S_1 and T_2 , according to the Fermi's golden rule. Combined with the TA analysis in the previous section, we can then assign the two long-lived triplet states to T_2 and T_1 , respectively.

2.7 A three-state model

Based on the previous TA analysis and molecular simulations, we propose a three-state model to describe the exciton kinetics in the model emitter with three components. The specific model for the emitter 1,8-mDTAZ-PhtCz is shown in **Figure 2.8**. This was in

collaboration with Yungui Li (Max Planck Institute for Polymer Research, Mainz). ISC and rISC are mainly happening between S_1 and T_2 , which is similar to the two-state model for TADF emitters. Part of T_2 will relax to T_1 by internal conversion (IC), while the T_1 state contributes to the phosphorescence. Non-radiative losses are assumed from S_1 with rate $k_{nr,S}$ and T_1 with non-radiative rate $k_{nr,T}$. Since the radiative relaxation is competing with the non-radiative processes, the S_1 lifetime τ_S is kinetically defined as $1/(k_{r,S} + k_{nr,S})$, while the T_1 lifetime τ_T as $1/(k_{r,T} + k_{nr,T})$. In this kinetic model, one can describe the exciton kinetics with the following rate equations for S_1 density n_{S1} (Eq. 1), T_2 density n_{T2} (Eq. 2), and T_1 density n_{T1} (Eq. 3), respectively:

$$\frac{dn_{S1}}{dt} = -\frac{n_{S1}}{\tau_{S1}} - k_{ISC}n_{S1} + k_{rISC}n_{T2} \quad (1)$$

$$\frac{dn_{T2}}{dt} = k_{ISC}n_{S1} - k_{rISC}n_{T2} - k_{IC}n_{T2} \quad (2)$$

$$\frac{dn_{T1}}{dt} = -\frac{n_{T1}}{\tau_{T1}} + k_{IC}n_{T2} - k_{TTA}n_{T1}^2 \quad (3)$$

For S_1 and the upper triplet level T_2 , we skip the effect of the singlet-singlet, singlet-triplet, and triplet-triplet annihilation (TTA) for simplification. The TTA effect is assumed to only impact the long-lived T_1 state. In this model, the transient PL decay is the sum of the simultaneous radiative relaxation of S_1 and T_1 .

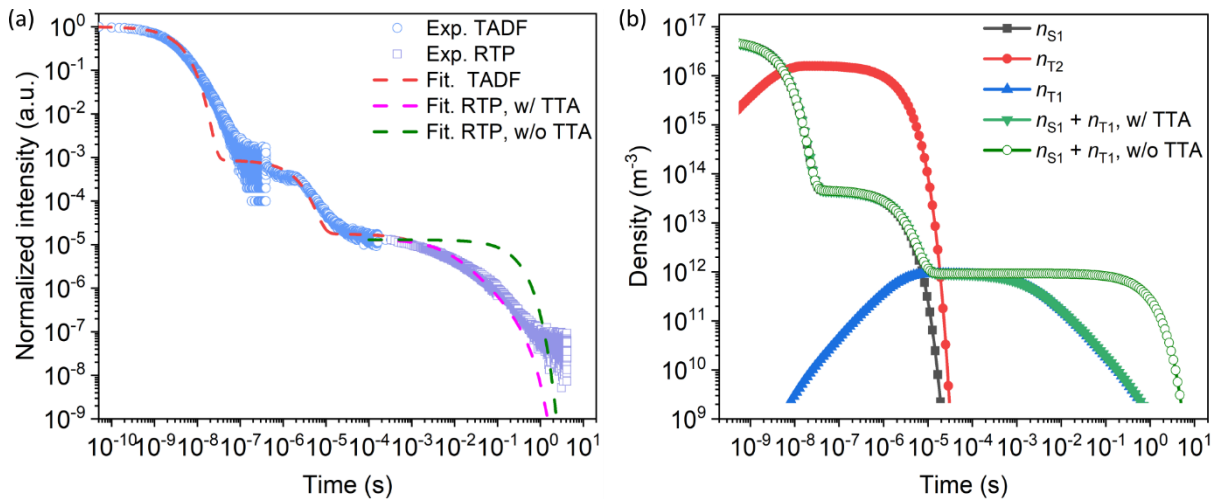


Figure 2.9 (a) Normalized experimental transient PL intensity, fitted with the proposed three-state model. (b) Modelled exciton densities under the experimental excitation dose.

The transient PL decay of 1,8-mDTAZ-PhtCz has been studied by TCSPC measurements over the time range from ns to second region. To capture the full picture of the PL decay in different time domains, the repetition rate of the excitation laser was tuned to sequentially measure the PF in the ns region, delayed fluorescence in the μs region, and long-lived RTP emission in the ms to second region. Since the long-lived RTP spans a long-time window, to get a reasonable signal-to-noise ratio, the excitation laser was working in a burst mode. A number of pulses in 1 MHz repetition rate was used to accumulate sufficient emissive T_1 , then the long-lived emission was detected with the laser off. In such a case, it is possible that the accumulated long-lived triplets are quenched because of annihilation. The detailed laser settings for the TCSPC measurements can be found in the experimental section.

The entire transient PL decay is shown in **Figure 2.9a**. After the PF with a lifetime in ns, a pronounced TADF feature with lifetime in μs was observed. Furthermore, a very long-lived RTP emission of hundreds of ms was detected. The exciton density evolution can be obtained by fitting the experimental decay numerically based on the three-state model with Eqs. 1-3. The fitting parameters are summarized in **Table 2.3**. For 1,8-mDTAZ-PhtCz, the intrinsic lifetime of S_1 is ~ 6 ns, while the lifetime of T_1 is about 0.25 s. The lifetime of the T_2 state can be estimated by $1/k_{\text{rISC}}$, which is about 1.3 μs . The low IC rate between T_2 and T_1 might result from the relatively small Frank-Condon factor, because of the orbital difference, as shown in **Figure 2.8b**.

Table 2.3 Kinetic modelling parameters for transient PL decay.

τ_{S_1}	k_{ISC}	k_{rISC}	k_{IC}	τ_{T_1}	k_{TTA}
(s)	(s^{-1})	(s^{-1})	(s^{-1})	(s)	($\text{m}^{-3}\text{s}^{-1}$)
6.0×10^{-9}	6.0×10^7	7.5×10^5	30	0.25	1.5×10^{-18}

The exciton density evolution for each excited state is plotted in **Figure 2.9b**, with the initial singlet density determined by the excitation laser intensity.^{26,42} Because the singlet lifetime is only ~ 6 ns, the decay of PF till hundreds of ns results from the direct relaxation of S_1 to the ground state. The delayed fluorescence within 10^{-7} to 10^{-5} s mainly comes from rISC from the T_2 to S_1 state. The slow radiation of T_1 contributes to the long-lived RTP emission from 10^{-4} to 10 s. Because of annihilation effects, the effective RTP lifetime is shortened, as shown in **Figure 2.9a**.

Multi-level models with a higher-lying triplet state have already been developed for TADF emitters, however, without considering triplet annihilation effects.^{44,45} The reason for this omission is that typically for TADF emitters the T1 lifetime is in μs region due to the efficient rISC process.^{44,45} In contrast, in our model emitter the T1 lifetime is in the range of hundreds of ms, resulting in much higher triplet densities and therefore enhanced triplet annihilation processes as TTA. Because of the occurrence of triplet annihilation effects, the analytical expressions derived for the conventional multi-level model cannot be used,⁴⁴ and only numerical modelling can be adopted to describe the transient photoluminescence of our model emitter, as shown in **Fig. 2.9**.

2.8 Multi-color emissive system by Förster resonance energy transfer

Based on the fascinating photophysical properties of the model emitter 1,8-mDTAZ-PhtCz, we here demonstrate that by utilizing the energy of these multiple excited states, it is possible to obtain emissive systems with multi-color emission within a window from ns to ms region. This was in collaboration with Qiqi Yang (Max Planck Institute for Polymer Research, Mainz). As for 1,8-mDTAZ-PhtCz, the energy state for S₁, T₂, and T₁ are high, so the energy can effectively transfer to the singlet state of doped fluorescent emitters by Förster resonance transfer. The energy transfer diagram in such a system with multiple excited states is shown in **Figure 2.10a**. We selected some conventional fluorescent emitters as an example, including the blue emitter 2,5,8,11-tetra-tert-butylperylene (TBPe), green emitter 9,10-bis[N,N-di-(*p*-tolyl)-amino]anthracene (TTPA), super yellow poly(*p*-phenylene-vinylene) polymer (SYPPV) and red emitter 4-(dicyanomethylene)-2-tert-butyl-6-(1,1,7,7-tetramethyljulolidin-4-yl-vinyl)-4H-pyran (DCJTB). Their chemical structures are shown in **Figure 2.11**. It is possible to further extend into the deep red or even NIR region by mixing emitters with lower energy gaps. In the framework of FRET, the energy transfer rate increases with the distance decrease between the donor and acceptor, as well as their spectral overlap.⁴⁵

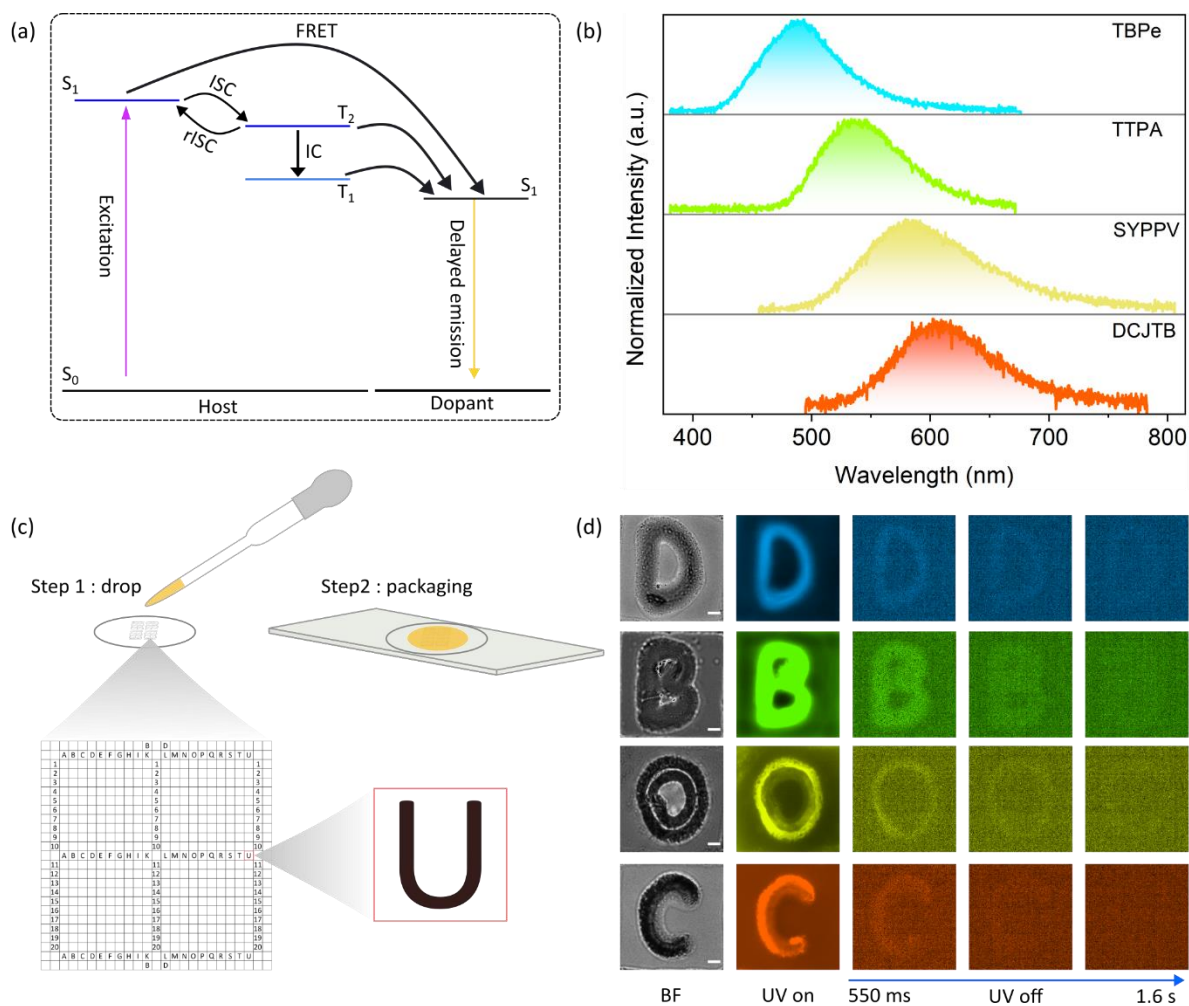


Figure 2.10 (a) The energy diagram to obtain multi-color PF-TADF-RTP systems. (b) Delayed emission at 200 μs with different dopants. (c) Schematic presentation of the preparation of microscopic imaging samples. (d) Time-resolved microscopy images with tunable delayed emission color by doping different conventional fluorescent emitters. The letters D, B, O, and C are doped with TBPe, TTPA, SYPPV, and DCJTb, respectively. The scale bar is 5 μm . BF means bright field.

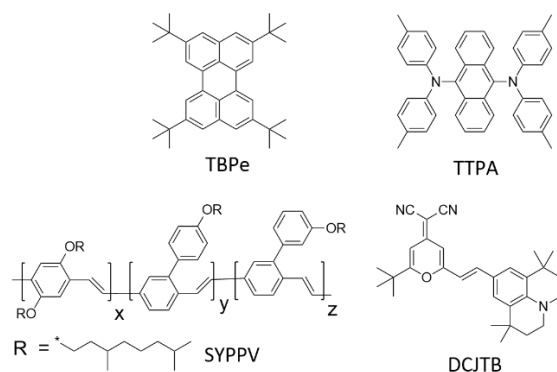


Figure 2.11 Chemical structures of conventional fluorescent dopants.

As plotted in **Figure 2.12**, there is significant spectral overlap between the absorption of the dopant emitters and the delayed PL spectra of 1,8-mDTAZ-PhtCz. When increasing the dopant concentration, the emission originating from the donor is gradually reduced, as shown in **Figure 2.13**. The distance between the acceptor and donor emitter decreases by increasing the dopant concentration, leading to a higher FRET rate. Complete energy transfer is achieved when the emission from 1,8-mDTAZ-PhtCz is fully quenched. In this case, simultaneous FRET happens from S_1 , T_2 , and T_1 of 1,8-mDTAZ-PhtCz to the singlet state of dopant emitters, leading to the observation of PF, TADF and RTP from the dopant. The delayed emission spectra with different dopants at 200 μ s are shown in **Figure 2.10b**. As shown in **Figure 2.14**, by mixing conventional fluorescent emitters, we can obtain an emissive system within the entire VIS range with delayed emission covering ns to second region.

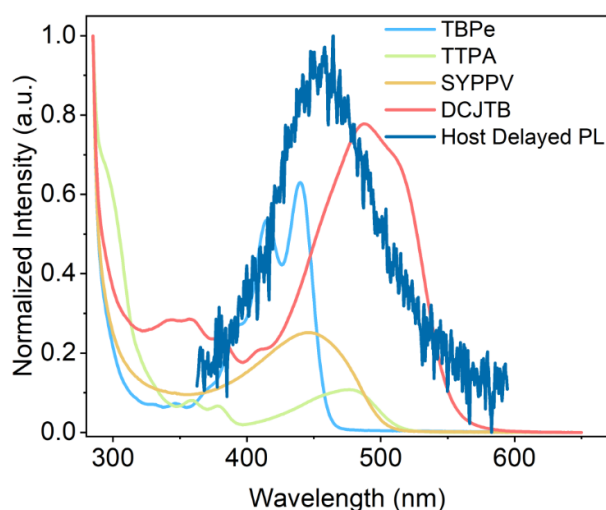


Figure 2.12 Spectra overlap between the dopant absorption and 1,8-mDTAZ-PhtCz delayed emission spectra.

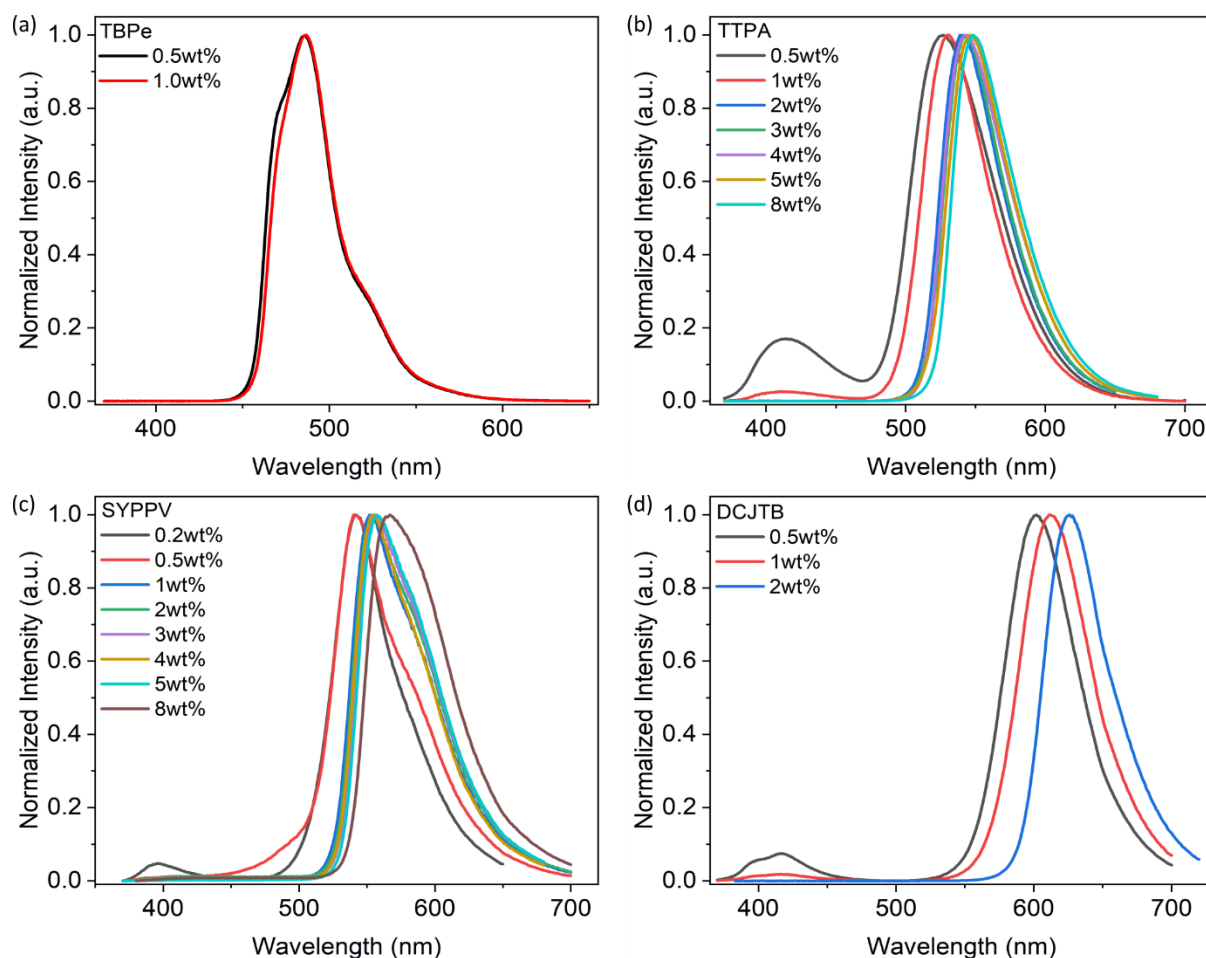


Figure 2.13 Steady state Fluorescence spectra of emitter-doped in PMMA. (a) TBPe; (b) TTPA; (c) SYPPV; (d) DCJTB. The emitters are doped in PMMA with a concentration as PMMA: 1,8-mDTAZ-PhtCz: dopant = 1: 2wt%: x wt%.

The multi-color emissive system has quite some potential applications, such as bio-imaging or data encryption. We here show a demo for time-resolved microscopy as a proof-of-concept. The sample preparation with pre-defined microscopic patterns is schematically illustrated in **Figure 2.10c**. The letters *D*, *B*, *O*, and *C* in a pre-engraved coverslip were casted with a mixture of 1,8-mDTAZ-PhtCz and various dopants in a PMMA matrix. A gradual PL decay with different emission colors can be observed after the UV excitation. As presented in **Figure 2.10d**, delayed emission till ~ 1.6 s is still observable. Due to the simultaneous emission of PF, TADF and RTP from the same luminescent material system, it is possible to select a delayed time window to capture the image from the sample. Furthermore, as shown in **Figure 2.15**, when using luminescent systems with different emissive colors in one pattern, by selecting different detection wavelength and time window, only the area with a specific

color within the exposure time windows can be detected. Therefore, such a color tunable luminescent system from blue, green, yellow to red, together with the simultaneous PF, TADF and RTP emission can potentially be applied for bio-imaging and data encryption.

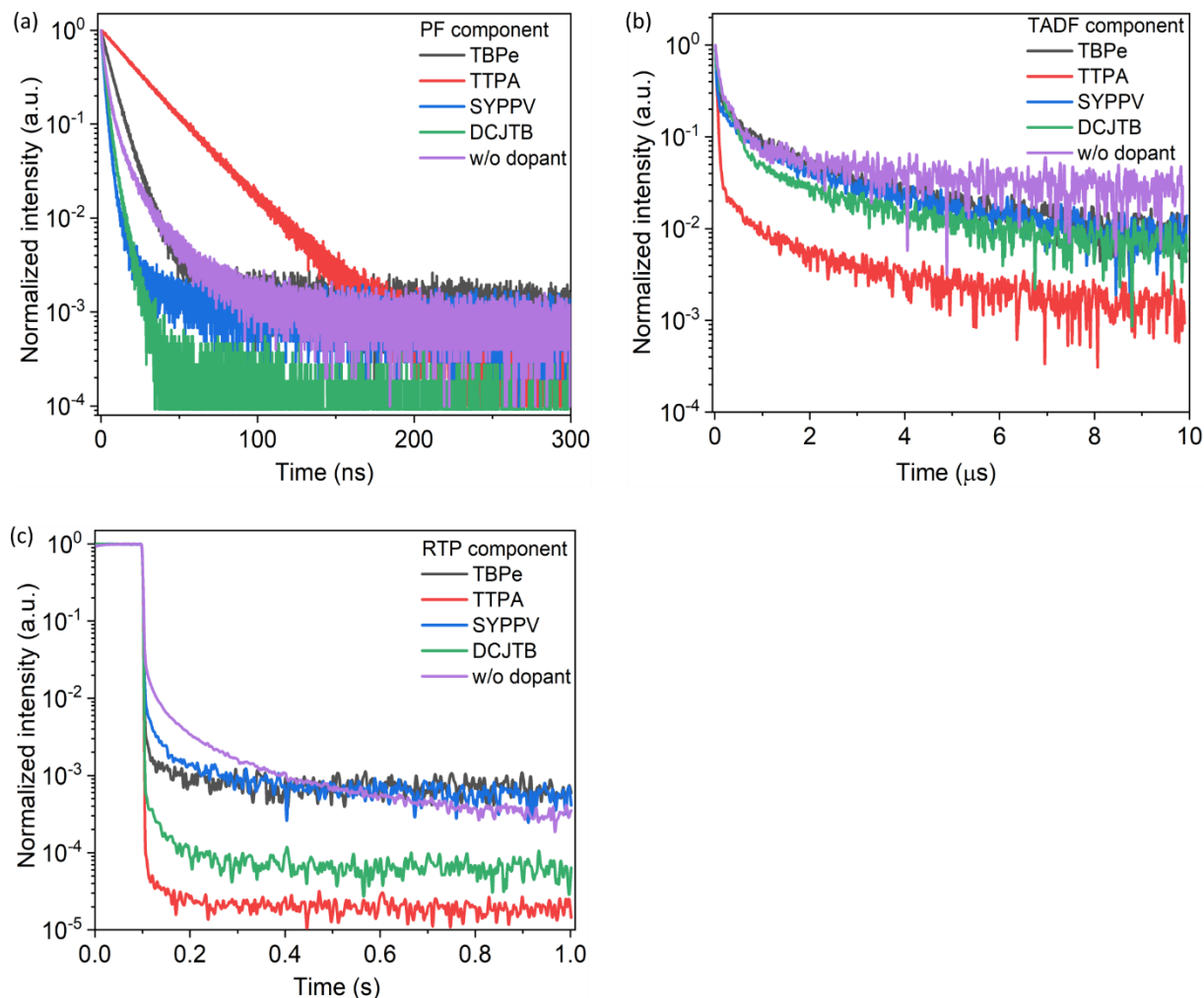


Figure 2.14 Multi-color PF-TADF-RTP emission via FRET from nanosecond to second regions. (a) PF component in ns region. (b) TADF component in μ s region. (c) RTP component in ms region.

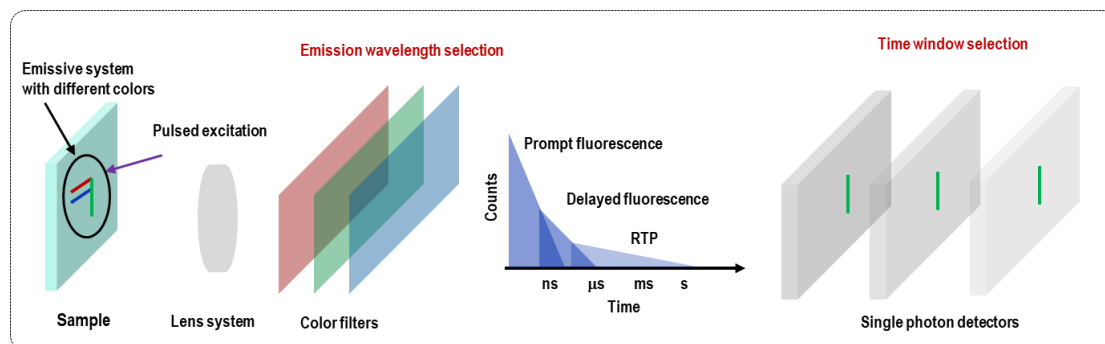


Figure 2.15 Schematic illustration on time-dependent and emissive wavelength-dependent microscopy imaging application.

2.9 Application for efficient RTP materials development

The existence of the additional higher-lying triplet state with energy lower than the singlet state makes it possible to develop efficient organic luminescent materials. A new derivative 1,8-pDTAZ-PhtCz with its chemical structure shown in **Figure 2.16a**, has been obtained based on the model emitter 1,8-mDTAZ-PhtCz, with a slightly tuned energy difference between these excited states (S_1 , T_2 and T_1) by increasing the conjugation length between the donor and acceptor.

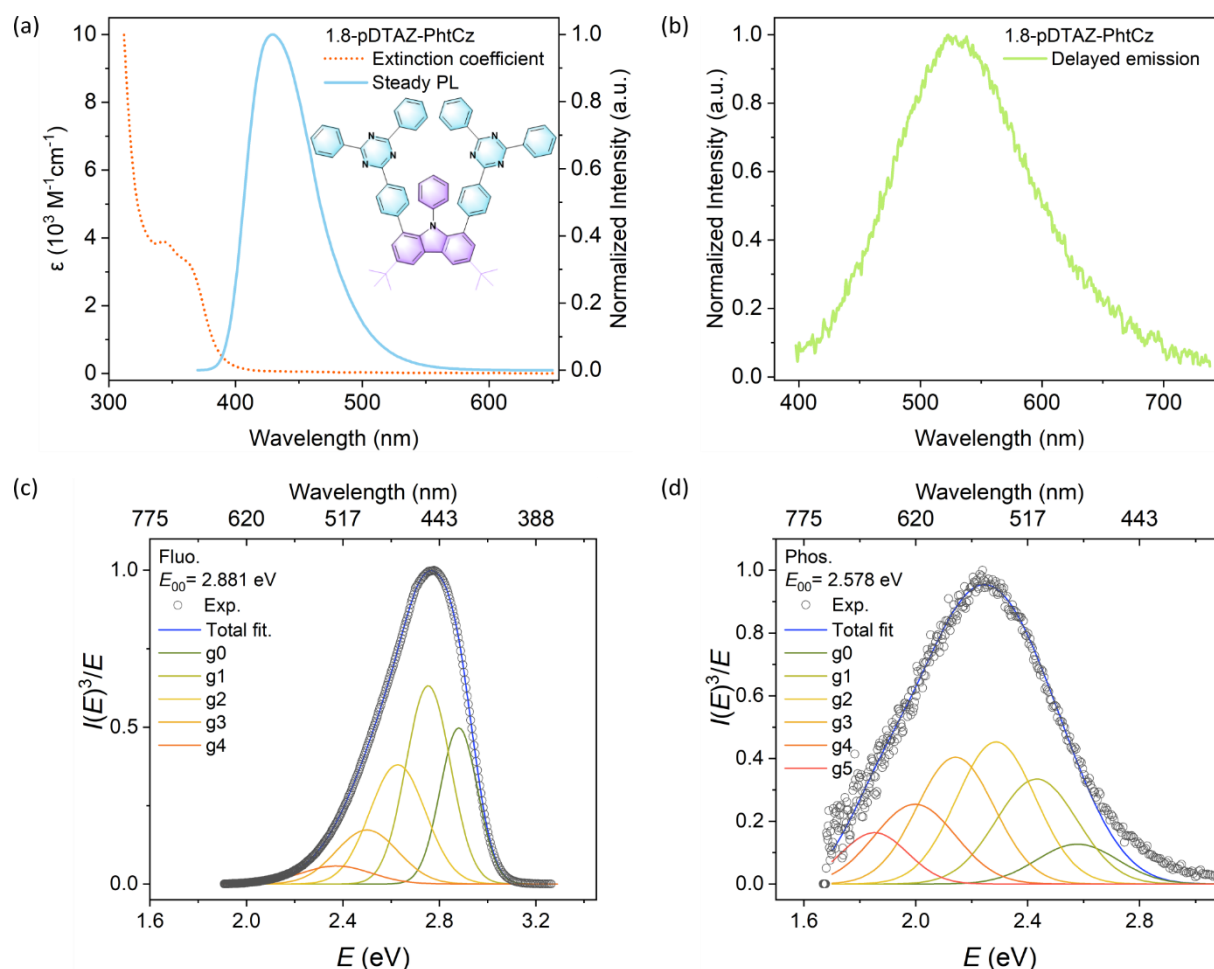


Figure 2.16 (a) Steady state UV-Vis absorption and PL emission spectra in toluene, Inset: Chemical structures of 1,8-pDTAZ-PhtCz. (b) PL spectrum with a delay of 200 μ s after the laser excitation. Measured in a rigid polymer matrix in nitrogen atmosphere. (c) Lineshape analysis of fluorescence spectra. (d) Lineshape analysis of phosphorescence spectra.

As shown in **Figure 2.16a** and **2.16b**, the absorption onset is 400 nm, while the fluorescence and delayed emission spectral peaks are at 430 nm and 523 nm, respectively. The energy levels for singlet S_1 2.881 eV and triplet T_1 2.578 eV are shown in **Figure 2.16c-**

2.16d and **Table 2.4**, respectively, determined by lineshape analysis of its fluorescence and phosphorescence spectra. Because of a reduction of the triplet energy levels, a larger ΔE_{ST} of 0.3 eV between S_1 - T_1 is noted for 1,8-pDTAZ-PhtCz. As a result, the TADF effect is suppressed, with only pronounced RTP emission with a high quantum yield exceeding 30%. The detailed photophysical properties for 1,8-pDTAZ-PhtCz are summarized in **Table 2.4**.

Table 2.4 Key photophysical properties for 1,8-pDTAZ-PhtCz.

Sample	λ_{Abs} (nm) ^a	λ_{FL} (nm) ^a	λ_{PH} (nm) ^b	λ_{PH} (nm) ^b	E_{S1} (eV)	E_{T1} (eV)	Φ (Air/N ₂) (%) ^c
1,8-pDTAZ-PhtCz	344/362	430	441	523	2.881	2.578	56.0/ 89.6

(a) In toluene.

(b) Doped in poly(methyl methacrylate) (PMMA) with 2 wt%.

(c) Doped in PS with 2 wt%.

For 1,8-pDTAZ-PhtCz, the fluorescence and phosphorescence transient PL decays are shown in **Figure 2.17**. The fitting parameters are shown in **Table 2.5**. The fluorescence lifetime of S_1 is 5.2 ns, while the phosphorescence lifetime of T_1 is about 118.7 ms. As shown in **Table 2.3** and **Table 2.5**, compound 1,8-pDTAZ-PhtCz has a slightly higher ISC rate than 1,8-mDTAZ-PhtCz.

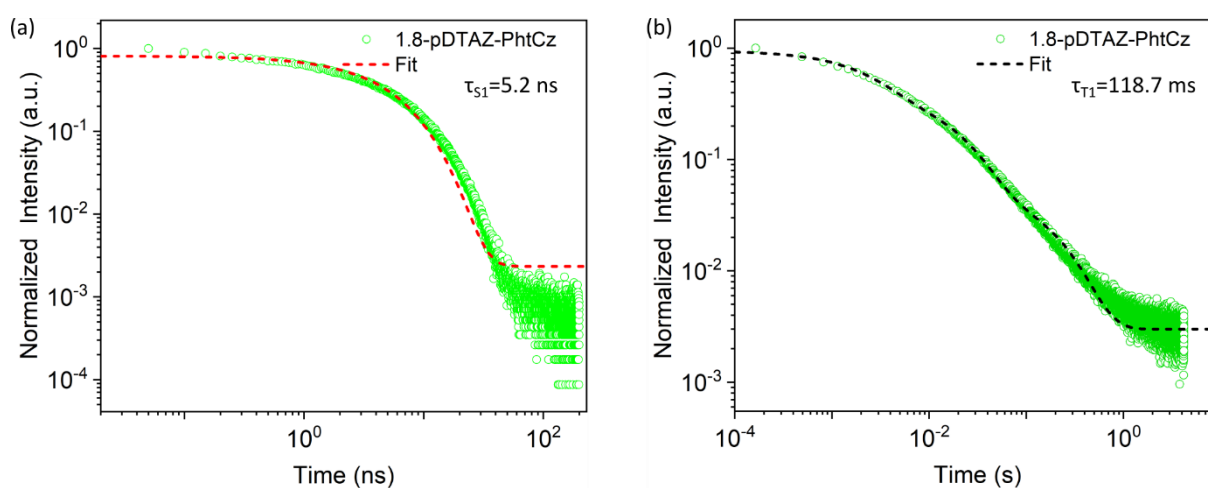


Figure 2.17 (a) Normalized fluorescence decay transients of 1,8-pDTAZ-PhtCz, fitted with the monoexponential function. (b) Normalized phosphorescence decay transients of 1,8-pDTAZ-PhtCz, fitted with the triexponential function.

Table 2.5. Kinetic modelling parameters for transient PL decay of 1,8-pDTAZ-PhtCz.

τ_{S1}	k_{ISC}	k_{ISC}	τ_{T1}
(s)	(s^{-1}) ^a	(s^{-1}) ^b	(ms)
5.2×10^{-9}	6.5×10^7	8.5×10^7	118.7

$$k_{ISC} = \phi_{ISC} / \tau_{S1}. \text{ (a) } k_{nr.PF} = 0, \phi_{nr.PF} = 0, \phi_{ISC} = 1 - \phi_{PF}, \text{ (b) } k_{nr.PH} = 0, \phi_{nr.PH} = 0, \phi_{ISC} = \phi_{PH}.$$

As shown in **Figure 2.18a**, for molecules 1,8-pDTAZ-PhtCz, the diphenyltriazine group tended towards a planar conformation due to strong intramolecular hydrogen bonding constraints. The torsion angle between the triazine molecule and the tert-butylcarbazole in 1,8-pDTAZ-PhtCz is almost identical to that in 1,8-mDTAZ-PhtCz. In the crystal unit of 1,8-pDTAZ-PhtCz, two molecules are closely stacked and show a head-t-tail staggered arrangement. As shown in **Figure 2.18b**, the closest distance from the tert-butyl carbazolyl to the N-phenyl ring of the other molecule is 3.91 Å. The detailed crystal parameters summarized in **Table 2.7**. As shown in **Figure 2.18c**, in single crystals the molecules 1,8-pDTAZ-PhtCz, like the molecule 1,8-mDTAZ-PhtCz, exhibit ultra-long afterglow phosphorescence emission.

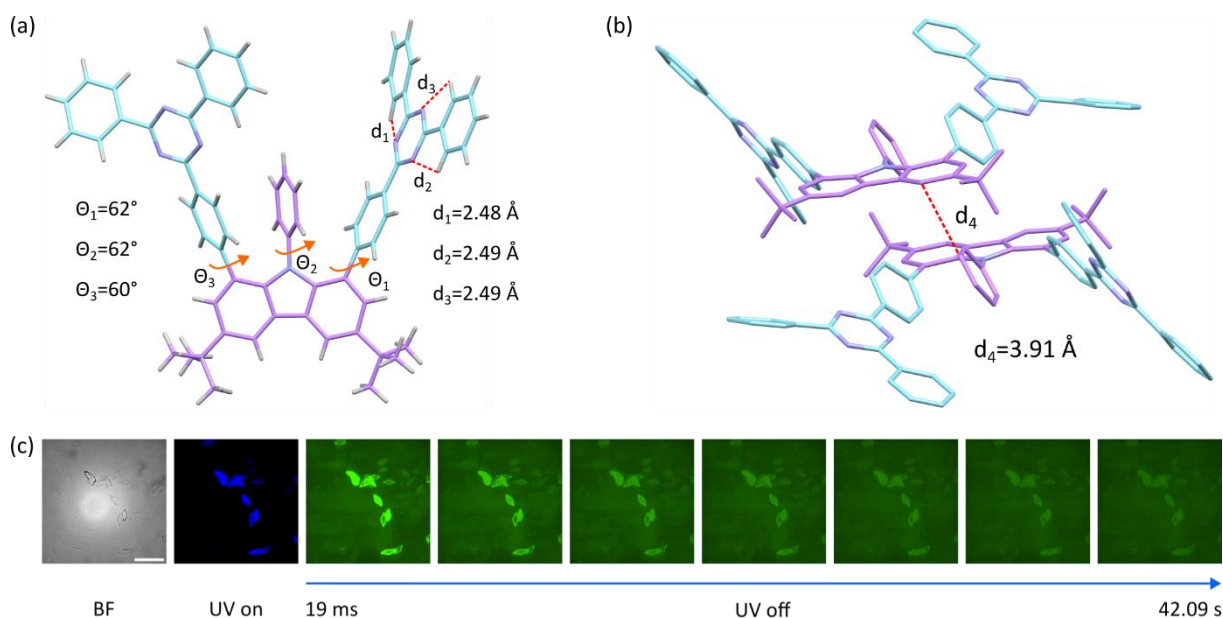


Figure 2.18 (a) Intramolecular interactions in the single crystal. (b) Molecular packing behavior in a unit cell. (c) Ultralong afterglow emission from the model emitter 1,8-pDTAZ-PhtCz crystal.

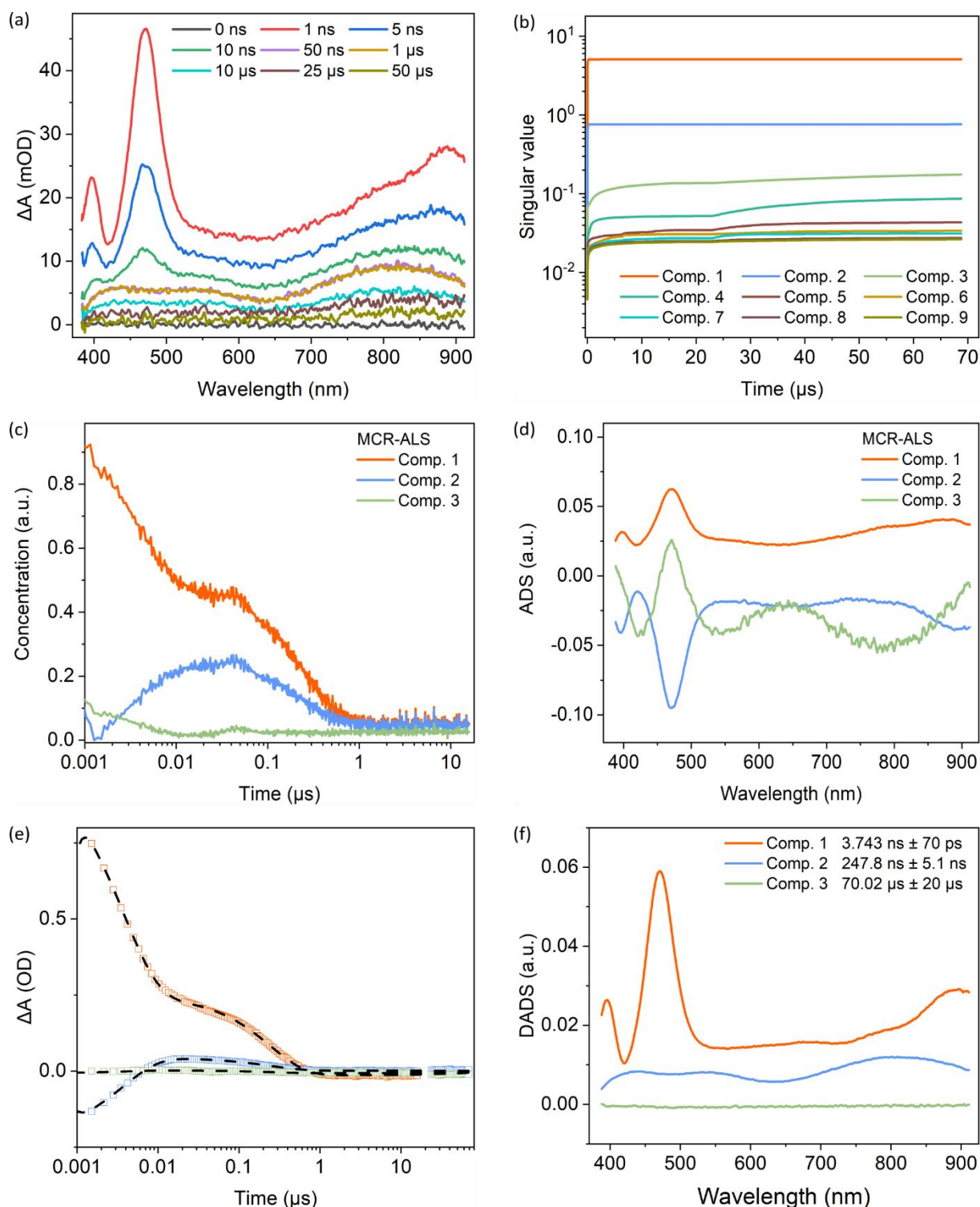


Figure 2.19 Experimental ns-TA spectra of 1,8-pDTAZ-PhtCz in degassed toluene. (a) Specific ns-TA spectra in the UV-VIS range. (b) Forward EFA of the ns-TA data. (c) Concentration evolution and (d) associated spectra of the principal components from MCR-ALS fitting. (e) Kinetic fitting by the global analysis with 3 components based on a parallel scheme. (f) DADS from the global analysis.

The ns-TA spectroscopy is shown in **Figure 2.19a** for 1,8-pDTAZ-PhtCz in degassed toluene. Pronounced ESA from singlets is observed, within the time scale of ns region. Afterwards, long-lived ESA within the time window of 20-50 μ s has been still observed. The EFA to determine the principal components of the ns-TA data, shown in **Figure 2.19b**, indicates that there are three principal components, which is the same for the model emitter 1,8-mDTAZ-PhtCz.

Furthermore, the ns-TA spectra for 1,8-pDTAZ-PhtCz in degassed toluene are fitted by the MCR-ALS method, shown in **Figure 2.19c** and **2.19d**. It is noted that the first and second components are correlated. The first component has a decay lifetime in the ns region, correlated with the concentration increase of the second component. The second component is decaying within the μ s region, while the increase of the concentration of the third component is related to the concentration decrease of the second component. The MCR-ALS fitting and forward EFA analysis indicates that a singlet and two triplet states are involved in the dynamics of this derivative. Thus, similar exciton dynamics have been resolved in the ns-TA spectra as compared to the model emitter 1,8-mDTAZ-PhtCz.

However, based on a parallel scheme, it is difficult to distinguish the second and third component by the global analysis. This is indicated by the large uncertainty of decay lifetime and the similar or mirror-like DADS for the second and third components, as shown in **Figure 2.19e** and **2.19f**. The possible reason could be the small energy difference between T_2 and T_1 , or similar lifetime in degassed solvent for these triplet states. The two triplet states can be resolved in a better manner whenever measured in aerated solvents, due to a different quenching behavior of the two triplet states with oxygen molecules. The detailed analysis for ns-TA data in solvents with oxygen has been summarized in **Figure 2.20**.

Nevertheless, the transient PL and ns-TA spectroscopy measurements indicate the existence of an additional upper triplet state for 1,8-pDTAZ-PhtCz. However, with relatively larger energy difference between singlet and triplet states, only RTP emission can be obtained without TADF contribution. The quantum yield of the RTP emission for 1,8-pDTAZ-PhtCz is more than 30%.

It is noted that the RTP quantum yield in purely organic PF/RTP emitters is normally less than 10% because of relatively low ISC rates and/or intrinsically slow triplet decay. The newly developed derivative of the model emitter is 2-3 times higher than conventional purely

organic emitters, as compared to reported purely organic RTP emitters with carbazole as the donor summarized in **Table 2.6**.^{16,46,55–57,47–54} Compared to dual emission PF/RTP materials with two excited states (S_1 and T_1), there should be at least three excited states involved for materials with simultaneous PF/DF/RTP emission. Therefore, the current work will pave a new avenue for developing purely organic RTP materials by tuning the relative energy difference between S_1 and T_2/T_1 states.

Table 2.6 The RTP parameters of reported organic emitters without heavy atoms based on carbazole as the donor.

Emitters	RTP lifetime	Phosphorescence quantum yield	Wavelength for RTP decay	Reference
Cz-DBF	650 ms	14.3%	550 nm	Nat. Commun. 10 , 1595 (2019)
DPhCzT	1.06 s	1.25%	530 nm	Nat. Mater. 14 , 685–690 (2015)
DECzT	1.28 s	0.6 %	529 nm	
4-BACz	558 ms	6.9%	549 nm	J. Mater. Chem. C. 7 , 9095–9101 (2019)
CzBP	518 ms (in crystal)	1.4%	570 nm	Adv. Mater. 27 , 6195–6201 (2015)
CBA	540 ms	n.a	550 nm	Chem. Commun. 51 , 10381–10384 (2015)
CPM	748 ms	3.17%	530 nm	Adv. Mater. 29 , 1606829 (2017)
m-MCBA	795 ms	2.1 %	600 nm	Angew. Chemie - Int. Ed. 57 , 7997–8001 (2018)
TCz-F	727 ms	7.4 %	556 nm	Nat. Commun. 11 , 2617 (2020)
PhCz	646 ms	0.7 %	530 nm	Adv. Mater. 29 , 1701244 (2017)
m-PBCM	710 ms (in recrystallized solids)	5.7 %	n.a.	Adv. Mater. 31 , 1807222 (2019)
p-PBCM	311 ms (in recrystallized solids)	9.8 %	n.a.	
o-PBCM	344ms (in recrystallized solids)	10.2 %	n.a.	
CX	150 ms (in crystal)	n.a.	n.a.	Chem. Sci. 9 , 3782–3787 (2018)
PTCz	810 ms (in crystal)	5.1 %	n.a.	Adv. Opt. Mater. 9 , 2001549 (2021)
CzBz	321 ms	2.18 %	n.a.	J. Phys. Chem. C. 125 , 16350–16357 (2021).

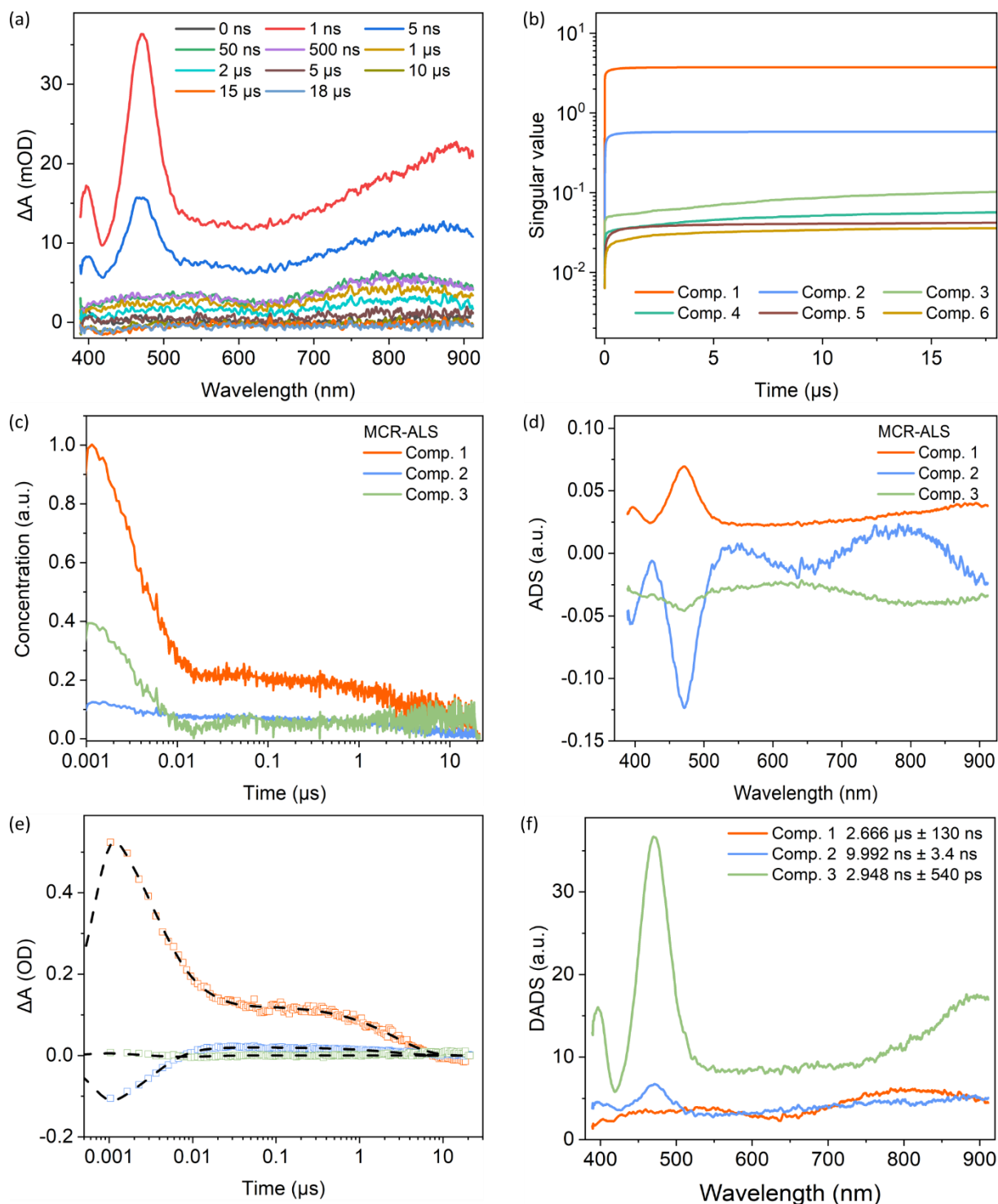


Figure 2.20 Experimental ns-TA spectra of 1,8-pDTAZ-PhtCz in aerated toluene. (a) Specific ns-TA spectra in the UV-VIS range. (b) Forward EFA of the ns-TA data. (c) Concentration evolution and (d) associated spectra of the principal components from MCR-ALS fitting. (e) Kinetic fitting by the global analysis with 3 components based on a parallel scheme. (f) DADS from the global analysis.

The higher-lying triplet state can be potentially meaningful for TADF emitter design as well. Because the T_2 level is higher than T_1 and therefore a relative smaller ΔE_{ST} between T_2 and S_1 , the rISC rate from T_2 to S_1 should be faster than that from T_1 to S_1 . Thus, it is possible to enhance the rISC rate for TADF emitters with shorter triplet lifetime and lower triplet density in the device, which is of vital importance for operational stable organic light-emitting diodes.²⁸ The numerical modelling on exciton kinetics and experimental verification by transient photoluminescence and TA spectroscopic methods in the current work can shine light on future TADF designs and photophysical studies.

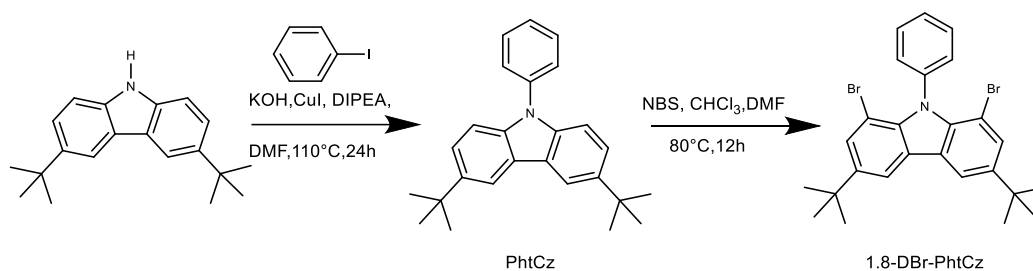
Vice versa, the higher-lying triplet state can be potentially meaningful for TADF emitter design as well. Because the T_2 level is higher than T_1 the resulting smaller ΔE_{ST} between T_2 and S_1 , as compared to T_1 and S_1 , the rISC rate from T_2 to S_1 should be faster than that from T_1 to S_1 . Thus, it is possible to enhance the rISC rate for TADF emitters with shorter triplet lifetime and lower triplet density in the device, which is of vital importance for operational stable organic light-emitting diodes.²⁸ There are papers which theoretically consider intermediates state for TADF emitters, however, at this moment, there is still a lack of experimental confirmation.²⁰ The numerical modelling on exciton kinetics and experimental verification by transient photoluminescence and transient-absorption spectroscopic methods in the current work can shine light on future TADF designs and photophysical studies.

2.10 Summary

In summary, we demonstrated that multiple excited states are involved to obtain PF, TADF, and RTP from a single emitter. For emitters with only T_1 and S_1 , it is not possible to simultaneously obtain efficient TADF and RTP with orders of decay lifetime difference. Specifically, for the emitter 1,8-mDTAZ-PhtCz developed in this work, the emission spectrum covers from UV to deep blue range. We experimentally and theoretically confirmed that another upper triplet state T_2 is involved in the emissive process. We demonstrated that it is possible to obtain multi-color emission by doping with different fluorescent emitters via Förster resonance energy transfer. The doped multi-color system still exhibits transient emission spanning 8-9 orders of time scale. Such an emissive system makes it possible to select different time windows and wavelength regions for microscopic applications. By tuning the relative energy difference between these exciton levels, we obtained highly efficient

organic luminescent materials with only prompt fluorescence and RTP emission, while the RTP quantum yield can reach more than 30%. We anticipate that this work can enhance the fundamental understanding on the photon generation from the purely organic emitters, and therefore the manipulation of the emission behavior either under optical or electrical excitation.

2.11 Synthetic details



Scheme 2.2 Synthetic routes for the PhtCz and 1,8-DBr-PhtCz.

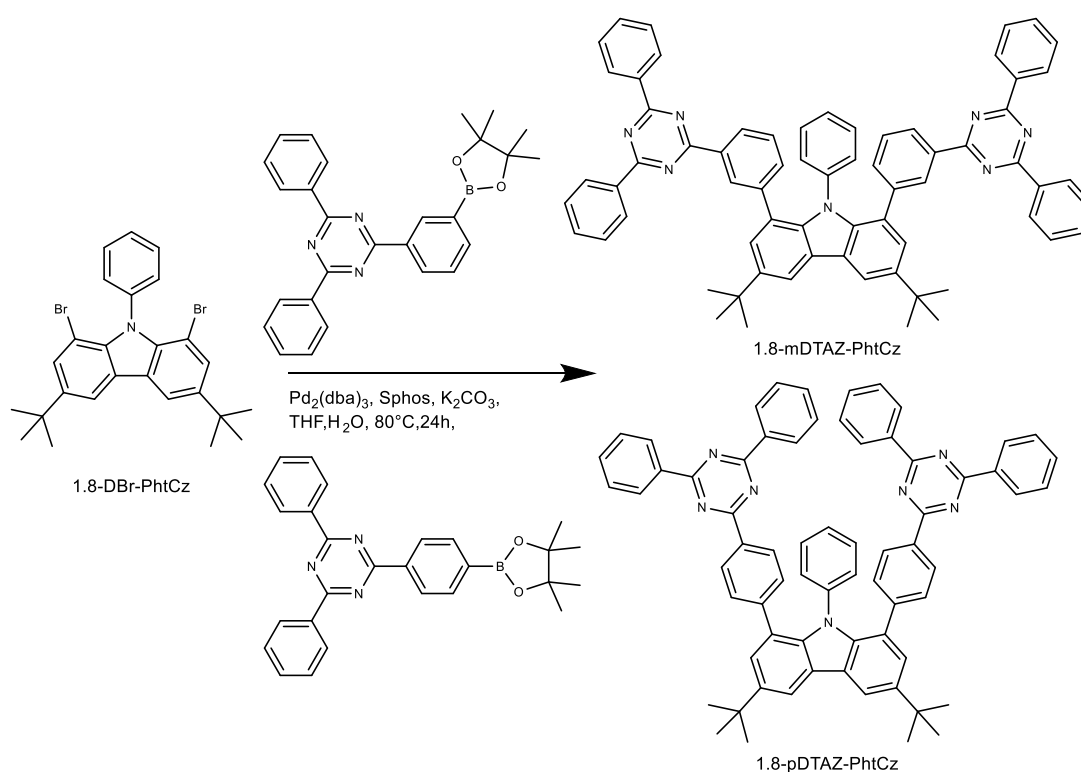
3,6-Di-tert-butyl-9-phenyl-9H-carbazole (PhtCz).

A mixture of iodobenzene (0.61 g, 30 mmol), 3,6-di-tert-butyl carbazole (0.28 g, 10 mmol), copper(I) iodide (0.19 g, 1 mmol), N, N-diisopropylethylamine (0.05 g, 0.4 mmol) and potassium hydroxide (1.1 g, 20 mmol) were added in N, N-dimethylformamide (100 mL). The reaction was carried out under nitrogen atmosphere at 110 °C for 24 hours. After cooling down to room temperature, the mixture was poured into 100 mL water, and extracted with dichloromethane (DCM) three times. The organic layer was then dried over anhydrous Na₂SO₄. The crude product was purified by column chromatography to give a white solid compound (yield: 84%). ¹H NMR (700 MHz, CDCl₃) δ 8.18 (d, J = 1.9 Hz, 2H), 7.62 – 7.58 (m, 4H), 7.48 (dd, J = 8.7, 1.9 Hz, 2H), 7.45 (td, J = 6.8, 2.2 Hz, 1H), 7.38 (d, J = 8.6 Hz, 2H), 1.50 (d, J = 1.1 Hz, 18H). ¹³C NMR (176 MHz, CDCl₃) δ 142.93, 139.42, 138.36, 129.88, 127.10, 126.92, 123.71, 123.48, 116.35, 109.33, 34.88, 32.18. High-resolution mass spectrometry (HRMS) (APCI) m/z: calcd for C₂₆H₂₉N: 355.2300; found: 355.2299.

1,8-Dibromo-3,6-di-tert-butyl-9-phenyl-9H-carbazole (1,8-DBr-PhtCz).

3,6-Di-tert-butyl-9-phenyl-9H-carbazole (1.5 g, 0.42 mmol), NBS (1.5 g, 8.6 mmol), DMF (60 mL) and CHCl₃ (40 mL) were added into a 250 mL flask. The mixture was stirred at 80 °C in the dark for 12 h. After cooling to room temperature, the mixture was poured into 100 mL water, and extracted with DCM for three times. The organic layer was washed with

brine and then dried over anhydrous Na_2SO_4 . The solution was filtered and concentrated by a rotary evaporator. The crude product was purified by column chromatography to give a white solid product. (yield: 75%). ^1H NMR (700 MHz, CDCl_3) δ 8.09 (dd, $J = 1.9, 0.9$ Hz, 2H), 7.64 (dd, $J = 1.8, 0.9$ Hz, 2H), 7.58 – 7.53 (m, 1H), 7.50 – 7.45 (m, 4H), 1.47 (d, $J = 1.2$ Hz, 18H). ^{13}C NMR (176 MHz, CDCl_3) δ 144.78, 138.41, 137.15, 132.77, 130.28, 129.34, 128.02, 125.58, 115.51, 103.92, 34.79, 31.94. High-resolution mass spectrometry (HRMS) (APCI) m/z : calcd for $\text{C}_{26}\text{H}_{27}\text{Br}_2\text{N}$: 511.0510; found: 511.0508.



Scheme 2.3 Synthetic routes for the 1,8-mDTAZ-PhtCz and 1,8-pDTAZ-PhtCz.

3,6-Di-tert-butyl-1,8-bis(3-(4,6-diphenyl-1,3,5-triazin-2-yl)phenyl)-9-phenyl-9H-carbazole (1,8-mDTAZ-PhtCz).

A mixture of 1,8-DBr-PhtCz (0.15 g, 0.29 mmol) and commercially available 2,4-diphenyl-6-(3-(4,4,5,5-tetramethyl-1,3,2-dioxaborolan-2-yl)phenyl)-1,3,5-triazine (0.26 g, 0.61 mmol), $\text{Pd}_2(\text{dba})_3$ (0.027 g, 0.029 mmol), SPhos (0.049 g, 0.12 mmol) and K_2CO_3 (0.16 g, 1.16 mmol) were dissolved in a mixture of THF and water in an argon atmosphere. The mixture was heated to 80°C and stirred for 24 h. After cooling to room temperature, the mixture was washed with brine and then extracted with DCM. Afterwards, the mixture was dried over anhydrous Na_2SO_4 . The solution was filtered and then concentrated by a rotary

evaporator. The product was purified by column chromatography. (yield: 45%). ^1H NMR (700 MHz, CD_2Cl_2) δ 8.68 – 8.66 (m, 8H), 8.38 (d, $J = 2.0$ Hz, 2H), 8.32 (d, $J = 7.8$ Hz, 2H), 8.06 (s, 1H), 7.53 (d, $J = 7.3$ Hz, 13H), 7.43 (d, $J = 2.0$ Hz, 3H), 7.17 (s, 3H), 6.68 (s, 2H), 6.12 (s, 3H), 1.56 (s, 18H). ^{13}C NMR (176 MHz, CD_2Cl_2) δ 171.64, 143.00, 140.48, 139.66, 137.81, 136.64, 133.80, 132.82, 129.16, 128.99, 127.98, 127.77, 127.67, 126.64, 126.51, 124.75, 115.96, 35.06, 32.21. High-resolution mass spectrometry (HRMS) (APCI) m/z : calcd for $\text{C}_{68}\text{H}_{55}\text{N}_7$: 969.4519; found: 969.4504.

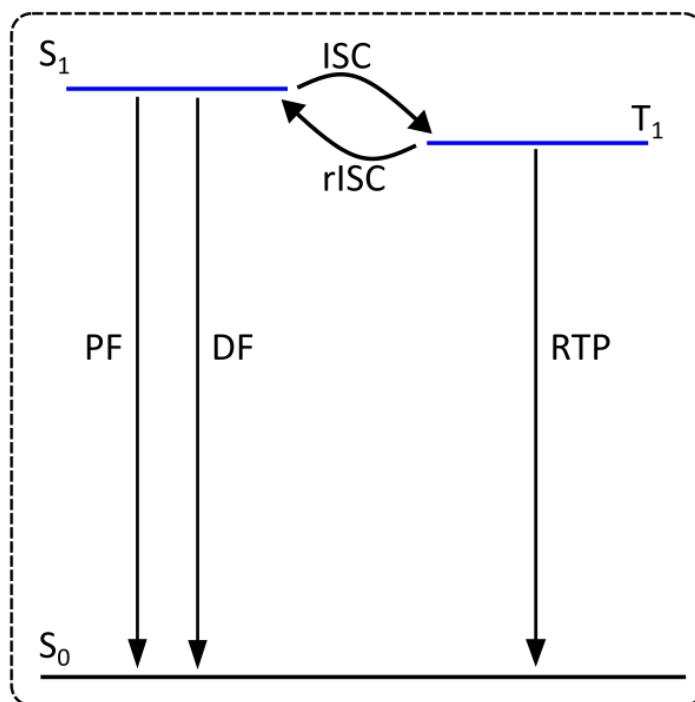
3,6-Di-tert-butyl-1,8-bis(4-(4,6-diphenyl-1,3,5-triazin-2-yl)phenyl)-9-phenyl-9H-carbazole (1,8-pDTAZ-PhtCz).

A mixture of 1,8-DBr-PhtCz (0.15 g, 0.29 mmol) and commercially available 2,4-diphenyl-6-(4-(4,4,5,5-tetramethyl-1,3,2-dioxaborolan-2-yl)phenyl)-1,3,5-triazine (0.26 g, 0.61 mmol), $\text{Pd}_2(\text{dba})_3$ (0.027 g, 0.029 mmol), SPhos (0.049 g, 0.12 mmol) and K_2CO_3 (0.16 g, 1.16 mmol) were dissolved in a mixture of THF and water in an argon atmosphere. The mixture was heated to 80 °C and stirred for 24 h. After cooling to room temperature, the mixture was washed with brine and then extracted with DCM. Afterwards, the mixture was dried over anhydrous Na_2SO_4 . The solution was filtered and then concentrated by a rotary evaporator. The product was purified by column chromatography. (yield: 48%). ^1H NMR (400 MHz, CD_2Cl_2) δ 8.76 – 8.69 (m, 8H), 8.36 – 8.27 (m, 6H), 7.65 – 7.55 (m, 11H), 7.54 (t, $J = 1.8$ Hz, 1H), 7.40 (d, $J = 2.0$ Hz, 2H), 7.17 – 7.09 (m, 4H), 6.74 – 6.66 (m, 2H), 6.64 – 6.51 (m, 3H), 1.54 (s, 18H). ^{13}C NMR (101 MHz, CD_2Cl_2) δ 171.90, 171.86, 144.97, 143.09, 139.89, 137.95, 136.72, 133.94, 132.84, 130.14, 129.80, 129.19, 129.01, 127.92, 127.89, 127.57, 126.87, 126.37, 124.90, 116.13, 35.04, 32.16. High-resolution mass spectrometry (HRMS) (APCI) m/z : calcd for $\text{C}_{68}\text{H}_{55}\text{N}_7$: 969.4519; found: 969.4512.

Table 2.7. Crystal data and structure refinement for 1,8-mDTAZ-PhtCz and 1,8-pDTAZ-PhtCz.

	1,8-mDTAZ-PhtCz	1,8-pDTAZ-PhtCz
Empirical formula	C ₇₂ H ₆₃ Cl ₈ N ₇	C ₆₈ H ₅₅ N ₇
Moiety formula	C ₆₈ H ₅₅ N ₇ , 4(CH ₂ Cl ₂)	C ₆₈ H ₅₅ N ₇
CCDC	2236406	2287999
Formula weight/ g/mol	1309.89	970.19
Temperature	120(2) K	120(2) K
Crystal system	Monoclinic	Triclinic
Space group name, number	C 2/c, (15)	P -1, (2)
a/ Å	17.6557(15)	9.6915(3)
b/ Å	17.4013(8)	16.8118(4)
c/ Å	22.2560(17)	17.3312(5)
α/°	/	75.474(2)
β/°	108.245(6)	79.839(2)
γ/°	/	73.930(2)
Volume/ Å ³	6494.0(8)	2609.29(13)
Density (calculated)/ mg/m ³	1.340	1.235
Absorption coefficient/ mm ⁻¹	0.396	0.564
Crystal size / mm ³	0.060 x 0.120 x 0.900	0.070 x 0.070 x 0.160
Wavelength, radiation type	0.71073 Å, MoKα	1.54178 Å, CuKα
Theta range for data collection	2.531 to 28.067°	5.606 to 67.934°
Index ranges	-22<=h<=23 -22<=h<=22 -29<=h<=29	-11<=h<=11 -20<=h<=20 -20<=h<=20
Reflections collected	17827	29054
Independent reflections	7771 [R(int) = 0.0373]	8982 [R(int) = 0.0297]
Goodness-of-fit on F ²	1.082	1.060
R ₁ , wR ₂ [I>2σ(I)]	0.0775, 0.1854	0.0620, 0.1456
R ₁ , wR ₂ [all data]	0.1153, 0.2163	0.0835, 0.1662
Largest diff. peak and hole/ eÅ ⁻³	0.712 and -0.819	0.376 and -0.259

2.12 Supplementary note 1: Two-state system modelling



Scheme S2.1. A two-state model for simultaneous PF, TADF, and RTP emission from a single emitter.

In the two-state model, as shown in **Scheme S2.1**, the singlet density n_S and triplet density n_T as a function of time (t) can be described by two coupled ordinary differential equations (Coupled-ODEs):

$$\frac{dn_S}{dt} = -\frac{n_S}{\tau_S} - k_{\text{ISC}}n_S + k_{\text{rISC}}n_T \quad (\text{Equation S1})$$

$$\frac{dn_T}{dt} = -\frac{n_T}{\tau_T} + k_{\text{ISC}}n_S - k_{\text{rISC}}n_T \quad (\text{Equation S2})$$

In the above equations, n_S and n_T denote the singlet and triplet lifetime. Here, the bimolecular annihilation effect is not included. This is reasonable when the exciton density is low. For emitters with both TADF from singlet and RTP radiation from triplet, the transient PL decay is therefore the sum of n_S and n_T as a function of time:

$$n = n_S + n_T \quad (\text{Equation S3})$$

The non-radiative losses in singlets or triplets, contributes to the exciton lifetime:

$$\tau_{(S,T)} = \frac{1}{k_r + k_{nr}} \quad (\text{Equation S4})$$

We here solve these equations numerically. We started to assume an arbitrary low singlet exciton density as the initial condition. Such a treatment can make sure that the annihilation effect is not involved, so the rate equations are physically robust. The shape of the solution for Equation S1-S4 can be used to determine how many components can be observed in such a two-state system.

For the given Coupled ODEs, six parameters are involved. One can drop the physical meaning for these parameters firstly, but just comparing the difference of the numerical solution to determine the solution properties of equations S1-S3.

Observing the form of equation S1 and S2, one can see that $1/\tau_S$ and k_{ISC} have the same effect on the decay rate of n_S (thus: dn_S/dt), and $1/\tau_T$ and k_{TISC} have the same effect on the decay rate of n_T (dn_T/dt). In other words, whenever the difference between $1/\tau_S$ and k_{ISC} , $1/\tau_T$, and k_{TISC} is large enough, such as more than 1 order difference, the term with a larger absolute number will dominate while the smaller term can be cancelled. Specifically for Equation S2, this mathematical effect gives rise to an effect that only one term either $1/\tau_T$ or k_{TISC} can dominate. Thus, only one major component will contribute to the decrease of n_T in the solution form. Physically, this effect means that triplets from a single energy level can only either contributes to one major process, either TADF with lifetime in 10^{-6} s or RTP emission with lifetime in 1 s.

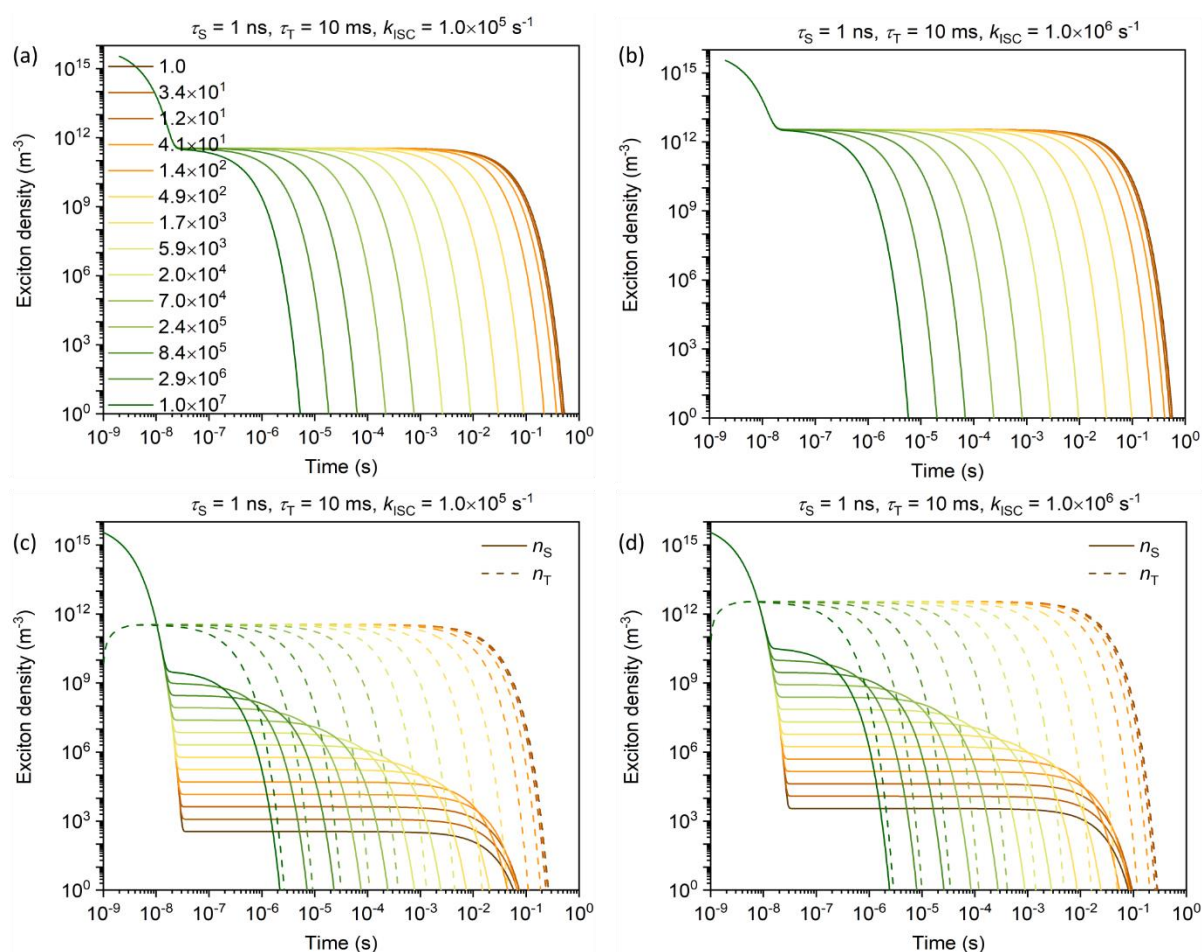


Figure S2.1 Exciton density modelling with a two-state system. The τ_S is assumed to be 1 ns and τ_T 10 ms. The ISC rate is 10^5 s^{-1} for (a) and (c), while it is 10^6 s^{-1} for (b) and (d). For each plot, the rISC rate is swept from 1 to 10^7 s^{-1} in the logarithmic scale. Top row: the emission decay (n_S+n_T); bottom row: emissive singlet and triplet density contributing to the entire PL decay.

The mathematical analysis can be demonstrated by scanning the kinetic parameters involved. Since it is known that the singlet lifetime for TADF emitters can be varied from 10^{-9} to 10^{-7} s range, while the long-lived RTP emission can have lifetime from 10^{-3} to 1 s, the solution for equations S1-S3 can be obtained with different combinations of kinetic parameters. The detailed analysis will be done in the following.

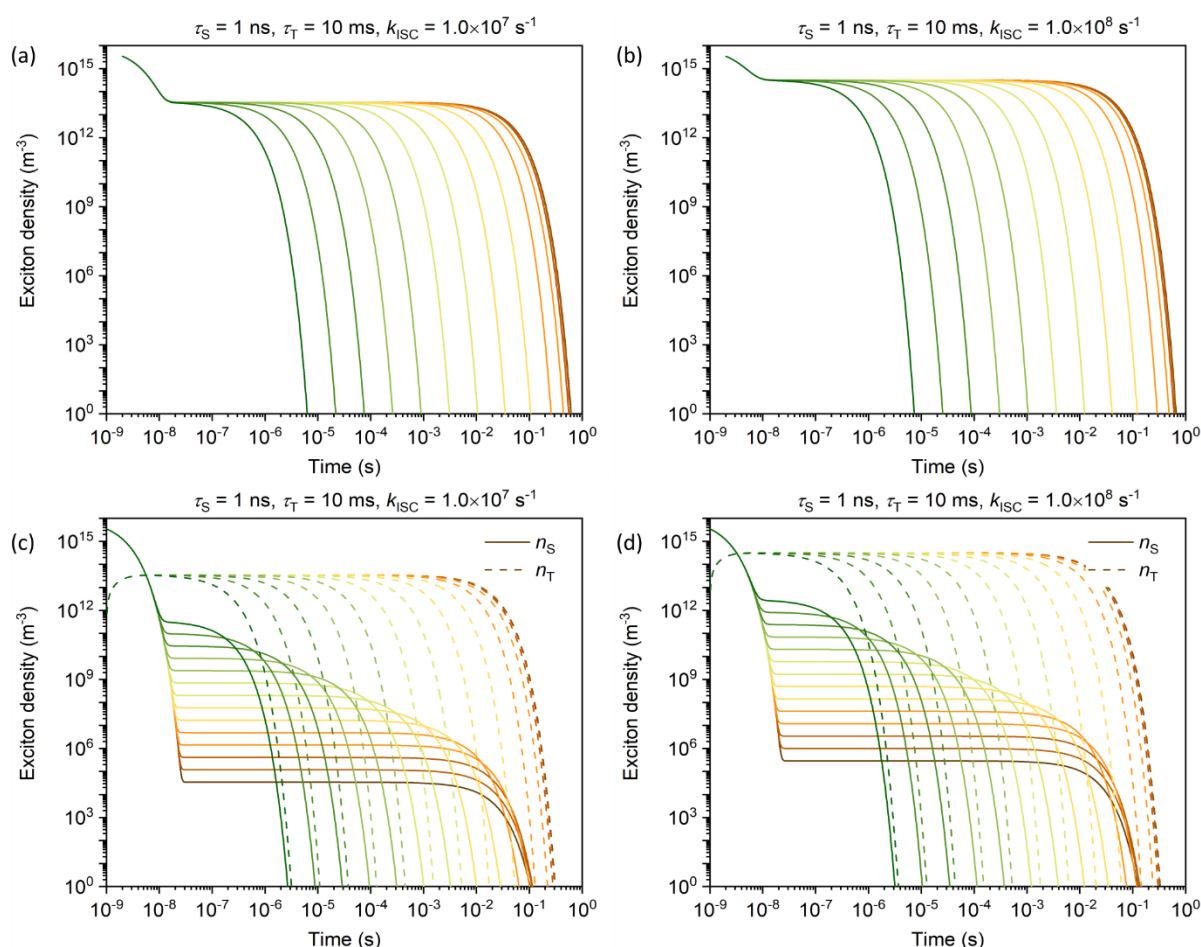


Figure S2.2 Exciton density modelling with a two-state system. The τ_S is assumed to be 1 ns and τ_T 10 ms. The ISC rate is in 10^7 s^{-1} (a) and (c), while it is 10^8 s^{-1} in (b) and (d). For each plot, the rISC rate is swept from 1 to 10^7 s^{-1} in the logarithmic scale. Top row: the sum of emissive exciton density (n_S+n_T); bottom row: emissive singlet and triplet density contributing to the PL decay.

The contribution of each excited state can be examined by separating the singlet and triplet evolution, as shown in the bottom rows in **Figure S2.1-S2.3**. When $1/\tau_T$ is comparable or larger than k_{rISC} , the long-lived decay intensity and lifetime is mainly determined by the triplet radiation as phosphorescence. Within the rate range when $1/\tau_T > k_{\text{rISC}}$, the change of k_{rISC} plays a negligible role on the PL decay. The TADF emission is vanished, leading to the observation of one delayed PL component as phosphorescence. When k_{rISC} increasing to a range which is comparable to $1/\tau_T$, the delayed emission from singlets via rISC contributes to direct triplet emission. TADF emission starts to play a role for the total PL decay. However, in this specific case, since $1/\tau_T$ and k_{rISC} is on the same order, still only one delayed component can be resolved.

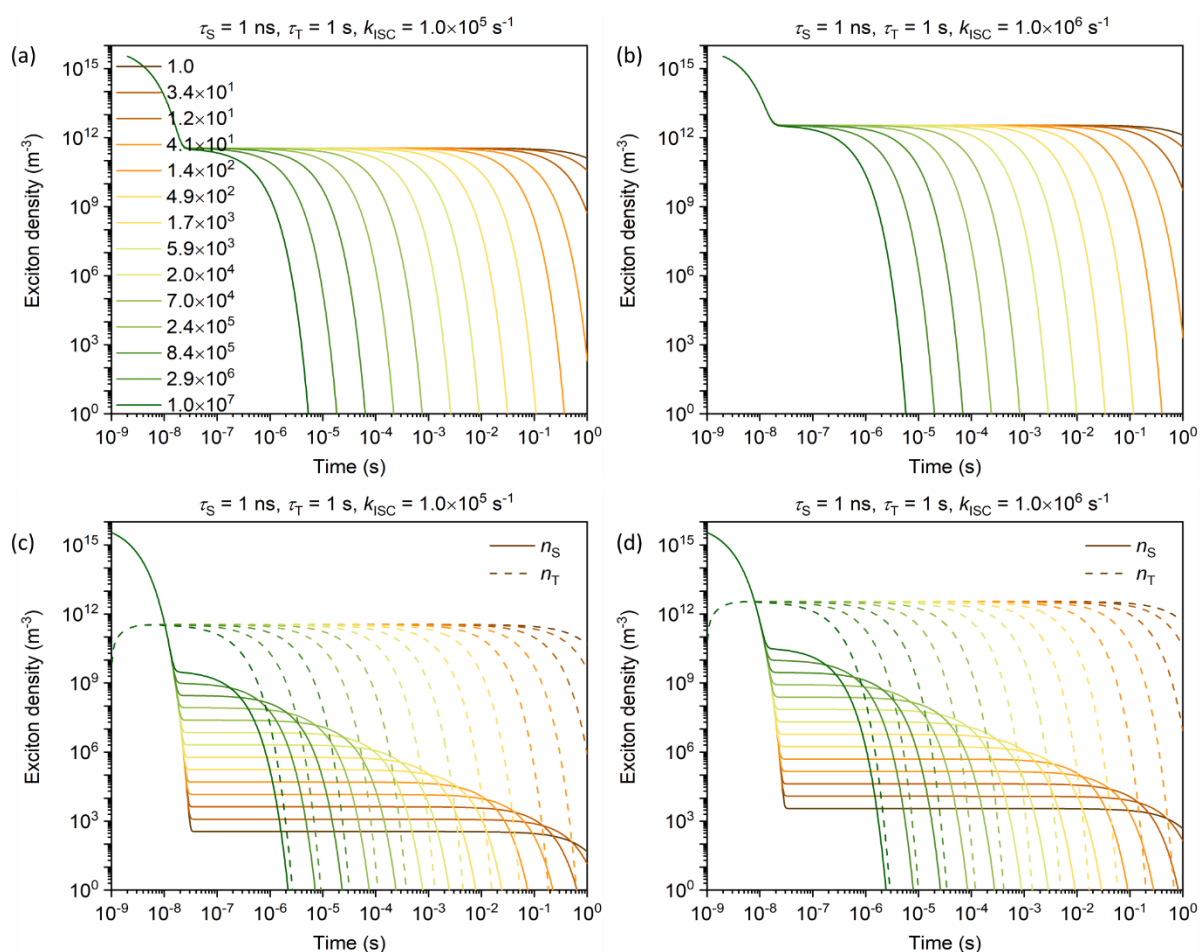


Figure S2.3 Exciton density modelling with a two-state system. The τ_S is assumed to be 1 ns and τ_T 1 s. The ISC rate is 10^5 s^{-1} in (a) and (c), while it is 10^6 s^{-1} in (b) and (d). For each plot, the rISC rate is swept from 1 to 10^7 s^{-1} in the logarithmic scale. Top row: the sum of emissive exciton density (n_S+n_T); bottom row: emissive singlet and triplet density contributing to the PL decay.

As shown in **Figure S2.3** and **S2.4**, when increasing the ISC rate while fixing the other parameters, the delayed PL intensity is increased. The delayed PL is composed with phosphorescence and TADF. The proportion of TADF is determined by the rISC rate.

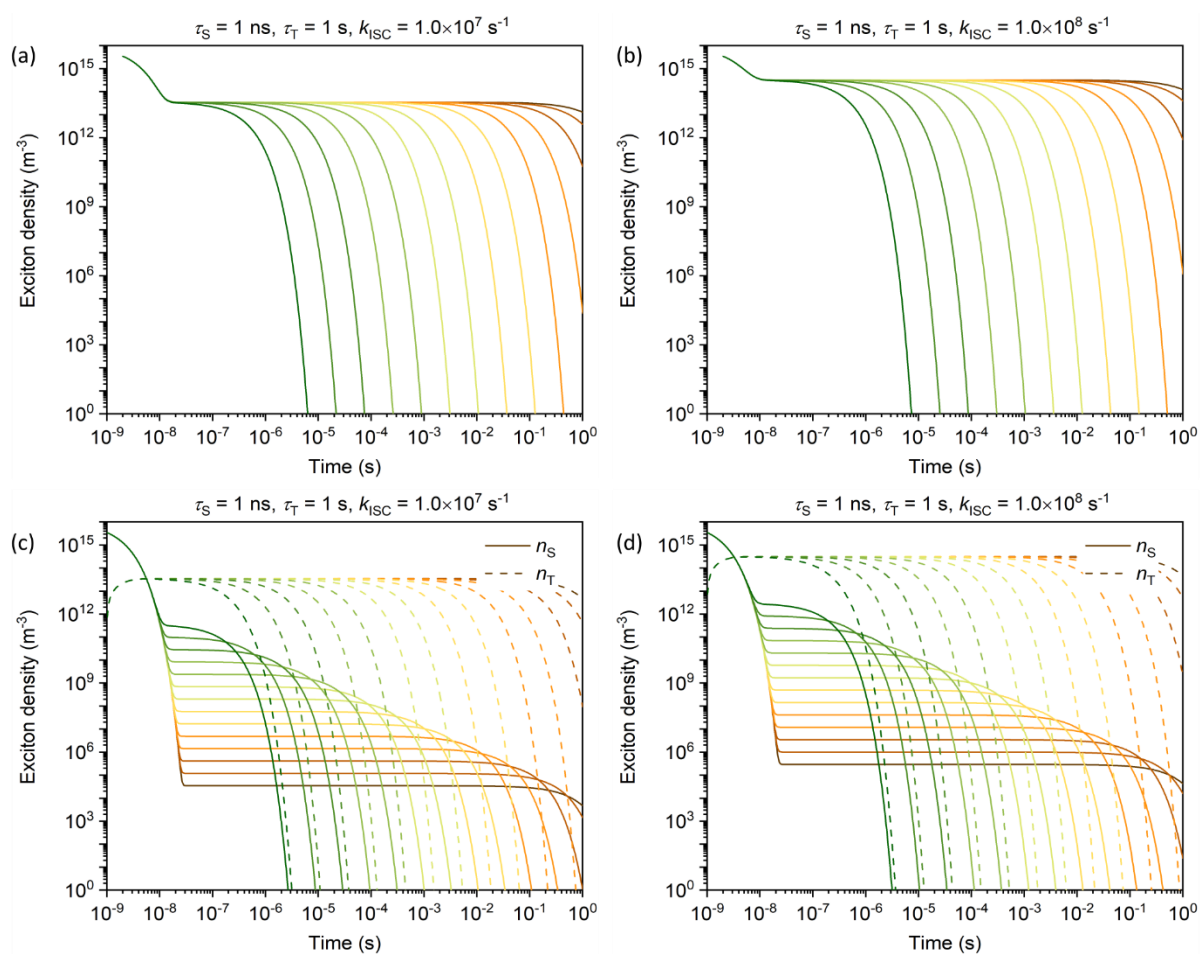


Figure S2.4 The PL decay kinetics modelled by the total exciton density with a two-state system. The τ_S is assumed to be 1 ns and τ_T 1 s. The ISC rate is 10^7 s^{-1} in (a) and (c), while it is 10^8 s^{-1} in (b) and (d). For each plot, the rISC rate is swept from 1 to 10^7 s^{-1} (line color from brown to green) in the logarithmic scale. Top row: the sum of emissive exciton density (n_S+n_T); bottom row: emissive singlet and triplet density contributing to the PL decay.

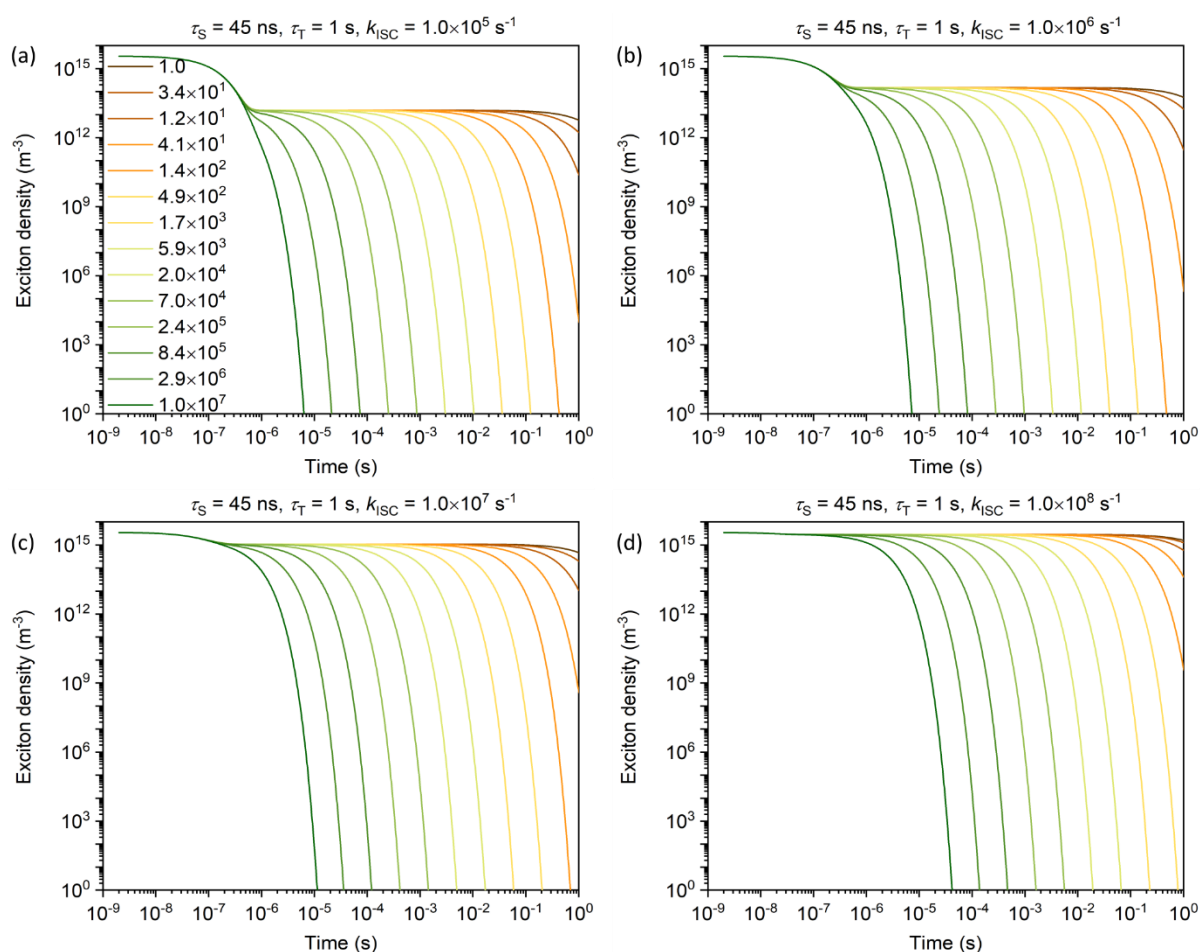


Figure S2.5 The total PL decay modelling by a two-state system. The τ_S is assumed to be 45 ns and τ_T 1 s. with different rates of ISC and rISC. The ISC rate is 10^5 s^{-1} in (a), 10^6 s^{-1} in (b), 10^7 s^{-1} in (c) and 10^8 s^{-1} in (d), respectively. For each panel, the rISC rate is swept from 1 to 10^7 s^{-1} in the logarithmic scale.

As shown in **Figure S2.5** and **S2.6**, when increasing the singlet lifetime and fixing the other parameters in a two-state model, the contribution of prompt fluorescence gradually increases. Again, raising the ISC rate will result in higher contribution of delayed emission. However, the delayed emission lifetime is dependent either on the triplet lifetime or rISC rate. The long-lived component lifetime is either determined by the rISC rate or the intrinsic triplet lifetime. Nevertheless, only one delayed PL component can be observed.

Overall, it is demonstrated that for organic emitters with one singlet and one triplet excited state, it is only possible to have two components in the PL transient decay: one is prompt fluorescence and another delayed emission either from TADF and/or RTP. It is possible that TADF and RTP contributes simultaneously to the delayed emission, but the decay lifetime of TADF and RTP is on the same order. Otherwise, the process of either TADF

or RTP process which has a higher transition rate will dominate, making the other process playing a negligible role. Therefore, with the two-state model, it is impossible to describe emission systems with three components with orders of decay lifetime difference.

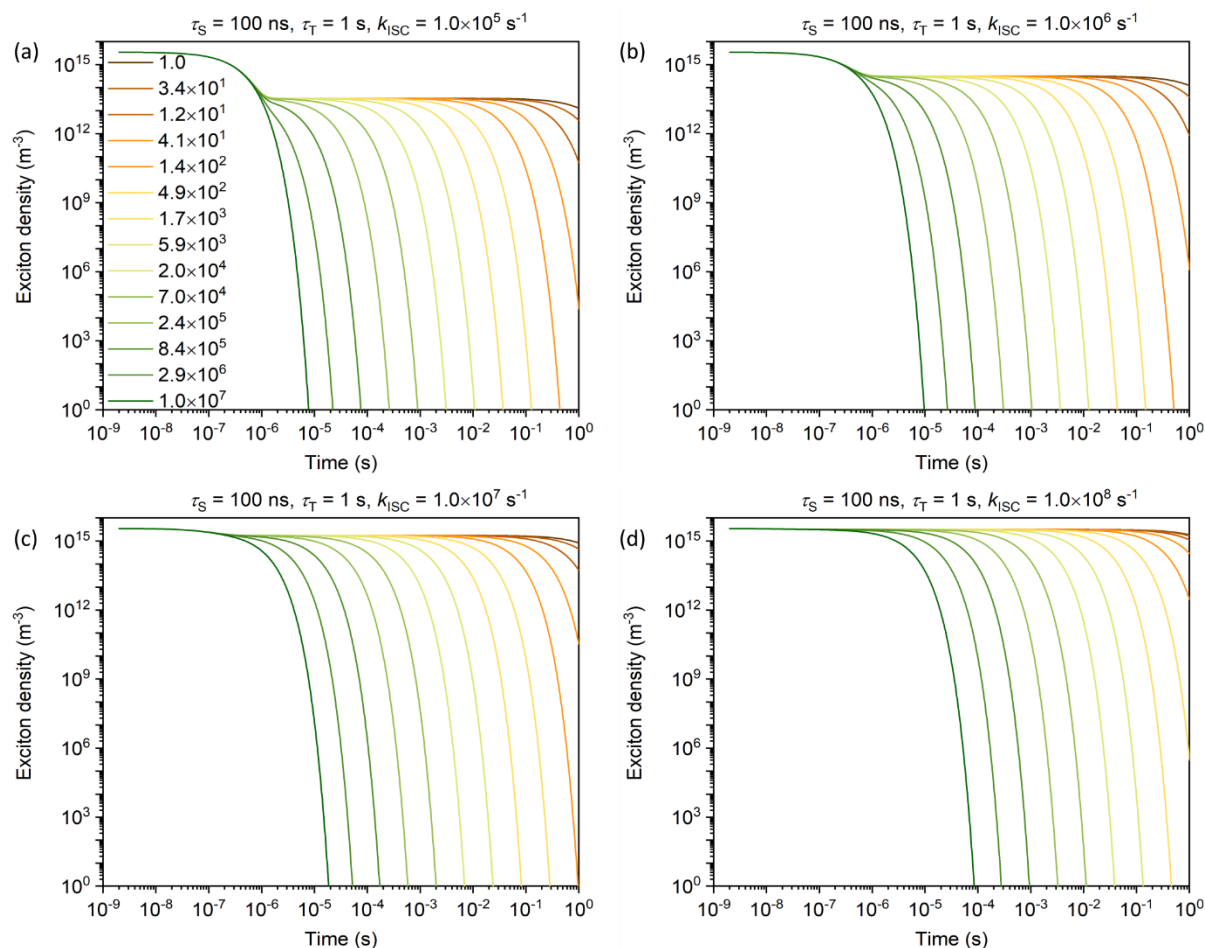


Figure S2.6 The total PL decay modeling by a two-state system. The τ_S is assumed to be 100 ns and τ_T 1 s. with different rates of ISC and rISC. The ISC rate is 10^5 s^{-1} in (a), 10^6 s^{-1} in (b), 10^7 s^{-1} in (c), and 10^8 s^{-1} in (d), respectively. For each panel, the rISC rate is swept from 1 to 10^7 s^{-1} in the logarithmic scale.

2.13 References

1. Reineke, S., Walzer, K. & Leo, K. Triplet-exciton quenching in organic phosphorescent light-emitting diodes with Ir-based emitters. *Phys. Rev. B* **75**, 125328 (2007).
2. Baldo, M. A., Adachi, C. & Forrest, S. R. Transient analysis of organic electrophosphorescence. II. Transient analysis of triplet-triplet annihilation. *Phys. Rev. B* **62**, 10967–10977 (2000).
3. Firdaus, Y. *et al.* Long-range exciton diffusion in molecular non-fullerene acceptors. *Nat. Commun.* **11**, 5220 (2020).
4. Baldo, M. A., Holmes, R. J. & Forrest, S. R. Prospects for electrically pumped organic lasers. *Phys. Rev. B - Condens. Matter Mater. Phys.* **66**, 353211–3532116 (2002).
5. Furukawa, T., Nakanotani, H., Inoue, M. & Adachi, C. Dual enhancement of electroluminescence efficiency and operational stability by rapid upconversion of triplet excitons in OLEDs. *Sci. Rep.* **5**, 8429 (2015).
6. Reineke, S. *et al.* White organic light-emitting diodes with fluorescent tube efficiency. *Nature* **459**, 234–238 (2009).
7. Van der Zee, B., Li, Y., Wetzelaer, G. A. H. & Blom, P. W. M. Efficiency of Polymer Light-Emitting Diodes: A Perspective. *Adv. Mater.* **34**, 2108887 (2022).
8. Baldo, M. A. *et al.* Highly efficient phosphorescent emission from organic electroluminescent devices. *Nature* **395**, 151–154 (1998).
9. Thompson, M. The Evolution of Organometallic Complexes in Organic Light-Emitting Devices. *MRS Bull.* **32**, 694–701 (2007).
10. Reineke, S., Thomschke, M., Luessem, B. & Leo, K. White organic light-emitting diodes: Status and perspective. *Rev. Mod. Phys.* **85**, 1245–1293 (2013).
11. Uoyama, H., Goushi, K., Shizu, K., Nomura, H. & Adachi, C. Highly efficient organic light-emitting diodes from delayed fluorescence. *Nature* **492**, 234–238 (2012).
12. Wong, M. Y. & Zysman-Colman, E. Purely Organic Thermally Activated Delayed Fluorescence Materials for Organic Light-Emitting Diodes. *Adv. Mater.* **29**, 1605444

- (2017).
13. Li, Y. *et al.* Reduced Intrinsic Non-Radiative Losses Allow Room-Temperature Triplet Emission from Purely Organic Emitters. *Adv. Mater.* **33**, 2101844 (2021).
 14. Zhang, G., Palmer, G. M., Dewhurst, M. W. & Fraser, C. L. A dual-emissive-materials design concept enables tumour hypoxia imaging. *Nat. Mater.* **8**, 747–751 (2009).
 15. Bolton, O., Lee, K., Kim, H. J., Lin, K. Y. & Kim, J. Activating efficient phosphorescence from purely organic materials by crystal design. *Nat. Chem.* **3**, 205–210 (2011).
 16. An, Z. *et al.* Stabilizing triplet excited states for ultralong organic phosphorescence. *Nat. Mater.* **14**, 685–690 (2015).
 17. Louis, M. *et al.* Blue-Light-Absorbing Thin Films Showing Ultralong Room-Temperature Phosphorescence. *Adv. Mater.* **31**, 1807887 (2019).
 18. Gmelch, M., Thomas, H., Fries, F. & Reineke, S. Programmable transparent organic luminescent tags. *Sci. Adv.* **5**, eaau7310 (2019).
 19. Reineke, S. & Baldo, M. A. Room temperature triplet state spectroscopy of organic semiconductors. *Sci. Rep.* **4**, 3797 (2015).
 20. Hu, Y. X. *et al.* Efficient selenium-integrated TADF OLEDs with reduced roll-off. *Nat. Photonics* **16**, 803–810 (2022).
 21. Hatakeyama, T. *et al.* Ultrapure Blue Thermally Activated Delayed Fluorescence Molecules: Efficient HOMO-LUMO Separation by the Multiple Resonance Effect. *Adv. Mater.* **28**, 2777–2781 (2016).
 22. Peng, Q., Yi, Y., Shuai, Z. & Shao, J. Toward quantitative prediction of molecular fluorescence quantum efficiency: Role of Duschinsky rotation. *J. Am. Chem. Soc.* **129**, 9333–9339 (2007).
 23. Rörich, I. *et al.* Temperature dependence of the photo- and electroluminescence of poly(p -phenylene vinylene) based polymers. *J. Mater. Chem. C* **6**, 10569–10579 (2018).
 24. Dias, F. B., Penfold, T. J. & Monkman, A. P. Photophysics of thermally activated

- delayed fluorescence molecules. *Methods Appl. Fluoresc.* **5**, 012001 (2017).
25. Ye, W. *et al.* Confining isolated chromophores for highly efficient blue phosphorescence. *Nat. Mater.* **20**, 1539–1544 (2021).
 26. Thakur, K., Zee, B., Wetzelaer, G. A. H., Ramanan, C. & Blom, P. W. M. Quantifying Exciton Annihilation Effects in Thermally Activated Delayed Fluorescence Materials. *Adv. Opt. Mater.* **10**, 2101784 (2022).
 27. Long, Y. *et al.* Excited State Dynamics of Thermally Activated Delayed Fluorescence from an Excited State Intramolecular Proton Transfer System. *J. Phys. Chem. Lett.* **11**, 3305–3312 (2020).
 28. Li, Y. *et al.* Enhanced Operational Stability by Cavity Control of Single-Layer Organic Light-Emitting Diodes Based on Thermally Activated Delayed Fluorescence. *Adv. Mater.* **28**, 1-8 (2023).
 29. Shih, P. I. *et al.* Novel carbazole/fluorene hybrids: Host materials for blue phosphorescent OLEDs. *Org. Lett.* **8**, 2799–2802 (2006).
 30. Wei, Q. *et al.* Conjugation-Induced Thermally Activated Delayed Fluorescence (TADF): From Conventional Non-TADF Units to TADF-Active Polymers. *Adv. Funct. Mater.* **27**, 1605051 (2017).
 31. Chen, G. *et al.* Conjugation-Induced Rigidity in Twisting Molecules: Filling the Gap between Aggregation-Caused Quenching and Aggregation-Induced Emission. *Adv. Mater.* **27**, 4496–4501 (2015).
 32. Scholz, R. *et al.* Investigation of Thermally Activated Delayed Fluorescence from a Donor-Acceptor Compound with Time-Resolved Fluorescence and Density Functional Theory Applying an Optimally Tuned Range-Separated Hybrid Functional. *J. Phys. Chem. A* **124**, 1535–1553 (2020).
 33. Li, Y. *et al.* Organic Light-Emitting Diodes Based on Conjugation-Induced Thermally Activated Delayed Fluorescence Polymers: Interplay Between Intra- and Intermolecular Charge Transfer States. *Front. Chem.* **7**, 688 (2019).
 34. Yang, J. *et al.* The influence of the molecular packing on the room temperature phosphorescence of purely organic luminogens. *Nat. Commun.* **9**, 840 (2018).

35. Haase, N. *et al.* Kinetic Modeling of Transient Photoluminescence from Thermally Activated Delayed Fluorescence. *J. Phys. Chem. C* **122**, 29173–29179 (2018).
36. Aloïse, S. *et al.* The benzophenone S1(n,π^*) \rightarrow T1(n,π^*) states intersystem crossing reinvestigated by ultrafast absorption spectroscopy and multivariate curve resolution. *J. Phys. Chem. A* **112**, 224–231 (2008).
37. Beckwith, J. S., Rumble, C. A. & Vauthey, E. Data analysis in transient electronic spectroscopy—an experimentalist’s view. *Int. Rev. Phys. Chem.* **39**, 135–216 (2020).
38. Ruckebusch, C., Sliwa, M., Pernot, P., de Juan, A. & Tauler, R. Comprehensive data analysis of femtosecond transient absorption spectra: A review. *J. Photochem. Photobiol. C Photochem. Rev.* **13**, 1–27 (2012).
39. Van Stokkum, I. H. M., Larsen, D. S. & Van Grondelle, R. Global and target analysis of time-resolved spectra. *Biochim. Biophys. Acta - Bioenerg.* **1657**, 82–104 (2004).
40. Stein, T., Eisenberg, H., Kronik, L. & Baer, R. Fundamental Gaps in Finite Systems from Eigenvalues of a Generalized Kohn-Sham Method. *Phys. Rev. Lett.* **105**, 266802 (2010).
41. Kronik, L., Stein, T., Refaely-Abramson, S. & Baer, R. Excitation gaps of finite-sized systems from optimally tuned range-separated hybrid functionals. *J. Chem. Theory Comput.* **8**, 1515–1531 (2012).
42. Hasan, M. *et al.* Exciton–Exciton Annihilation in Thermally Activated Delayed Fluorescence Emitter. *Adv. Funct. Mater.* **30**, 2000580 (2020).
43. Tsuchiya, Y. *et al.* Molecular Design Based on Donor-Weak Donor Scaffold for Blue Thermally-Activated Delayed Fluorescence Designed by Combinatorial DFT Calculations. *Front. Chem.* **8**, 2–11 (2020).
44. Tsuchiya, Y. *et al.* Exact Solution of Kinetic Analysis for Thermally Activated Delayed Fluorescence Materials. *J. Phys. Chem. A* **125**, 8074–8089 (2021).
45. Kirch, A., Gmelch, M. & Reineke, S. Simultaneous Singlet-Singlet and Triplet-Singlet Förster Resonance Energy Transfer from a Single Donor Material. *J. Phys. Chem. Lett.* **10**, 310–315 (2019).
46. Zhao, W. *et al.* Boosting the efficiency of organic persistent room-temperature

- phosphorescence by intramolecular triplet-triplet energy transfer. *Nat. Commun.* **10**, 1595 (2019).
47. Zhang, T. *et al.* Hydrogen bonding boosted the persistent room temperature phosphorescence of pure organic compounds for multiple applications. *J. Mater. Chem. C* **7**, 9095–9101 (2019).
48. Gong, Y. *et al.* Achieving Persistent Room Temperature Phosphorescence and Remarkable Mechanochromism from Pure Organic Luminogens. *Adv. Mater.* **27**, 6195–6201 (2015).
49. Xue, P. *et al.* Luminescence switching of a persistent room-temperature phosphorescent pure organic molecule in response to external stimuli. *Chem. Commun.* **51**, 10381–10384 (2015).
50. Xie, Y. *et al.* How the Molecular Packing Affects the Room Temperature Phosphorescence in Pure Organic Compounds: Ingenious Molecular Design, Detailed Crystal Analysis, and Rational Theoretical Calculations. *Adv. Mater.* **29**, 1606829 (2017).
51. Xiong, Y. *et al.* Designing Efficient and Ultralong Pure Organic Room-Temperature Phosphorescent Materials by Structural Isomerism. *Angew. Chemie - Int. Ed.* **57**, 7997–8001 (2018).
52. Feng, H. T. *et al.* Tuning molecular emission of organic emitters from fluorescence to phosphorescence through push-pull electronic effects. *Nat. Commun.* **11**, 1–9 (2020).
53. Cai, S. *et al.* Visible-Light-Excited Ultralong Organic Phosphorescence by Manipulating Intermolecular Interactions. *Adv. Mater.* **29**, 1701244 (2017).
54. He, Z. *et al.* Achieving Persistent, Efficient, and Robust Room-Temperature Phosphorescence from Pure Organics for Versatile Applications. *Adv. Mater.* **31**, 1807222 (2019).
55. Mu, Y. *et al.* Mechano-induced persistent room-temperature phosphorescence from purely organic molecules. *Chem. Sci.* **9**, 3782–3787 (2018).
56. Ruan, Z. *et al.* Luminous Butterflies: Rational Molecular Design to Optimize Crystal Packing for Dramatically Enhanced Room-Temperature Phosphorescence. *Adv. Opt.*

- Mater.* **9**, 2001549 (2021).
57. Lai, L., Fang, B., Fan, M., Cheng, W. & Yin, M. Modulating Room-Temperature Phosphorescence through the Synergistic Effect of Heavy-Atom Effect and Halogen Bonding. *J. Phys. Chem. C* **125**, 16350–16357 (2021).
58. Weintraub, E., Henderson, T. M. & Scuseria, G. E. Long-range-corrected hybrids based on a new model exchange hole. *J. Chem. Theory Comput.* **5**, 754–762 (2009).
59. Grimme, S., Ehrlich, S. & Goerigk, L. Effect of the damping function in dispersion corrected density functional theory. *J. Comput. Chem.* **32**, 1456–1465 (2011).
60. Van Voorhis, T., Head-Gordon, M. A geometric approach to direct minimization. *Mol. Phys.* **100**, 1713–1721 (2002).
61. Hait, D. & Head-Gordon, M. Excited State Orbital Optimization via Minimizing the Square of the Gradient: General Approach and Application to Singly and Doubly Excited States via Density Functional Theory. *J. Chem. Theory Comput.* **16**, 1699–1710 (2020).
62. Humphrey, W., Dalke, A. & Schulten, K. VMD: Visual molecular dynamics. *J. Mol. Graph.* **14**, 33–38 (1996).

Chapter 3. Steric hindrance induced through space charge transfer for achieving room temperature phosphorescence in amorphous neat film

Abstract

Pure organic emitters with room temperature phosphorescence (RTP) in neat films have tremendous potential applications in display, sensing, etc. However, the annihilation of triplet state excitons in neat films leads to relatively short lifetimes, so rational molecular design is still challenging. Here, we report a strategy to improve the phosphorescence efficiency of neat films through steric hindrance effect-induced space charge transfer (TSCT). All molecules emit blue fluorescence and phosphorescence in neat films. Our experimental data show that lifetimes up to 40 ms and phosphorescence quantum yields of 6.3% are achievable in neat films. All molecules have a lifetime of over 30 ms under ambient conditions. Charge transfer has been demonstrated by transient absorption. The strategy developed here provides important insights into the realization of highly efficient organic phosphorescent materials in neat films.

3.1 Introduction

Room-temperature phosphorescence (RTP) from an organic material that is capable of fully utilizing the excited state energy and provide long-lived emission is highly desirable. In recent years, they have received considerable attention due to their extensive applications in displays, sensors, imaging, anti-counterfeiting, and encryption.¹⁻⁴ However, most of the RTP materials are formed by the coordination of metals and organic/inorganic materials, which is costly and toxic. Metal-free emitters with persistent RTP effects have rarely been reported. Highly efficient RTP organic emitters can reduce non-radiative decay by suppressing molecular motions (i.e., H-aggregation,⁵ host-guest composition,^{6,7} and polymer matrix^{8,9}) or the introduction of heavy atoms or heteroatoms to enhance intersystem crossing.^{1,3} However, long-lived triplet excitons may be quenched due to active vibration of the luminescent material or diffusion of excitons. Therefore, when RTP materials are doped into a rigid polymer matrix, the RTP effect is usually observed, whereas it is difficult to observe it in neat films. However, the difficulty of controlling the dose concentration in the

dopant system, inhomogeneity of the dopant film, and phase separation have hindered their further development. Long-lived RTP from neat films can effectively avoid these problems and is highly desirable for many applications. Nevertheless, organic emitters with long-lived phosphorescent emission in neat films are still rare.^{10,11} Therefore, the development of neat films of phosphorescent materials with long-lived emission remains a formidable challenge.

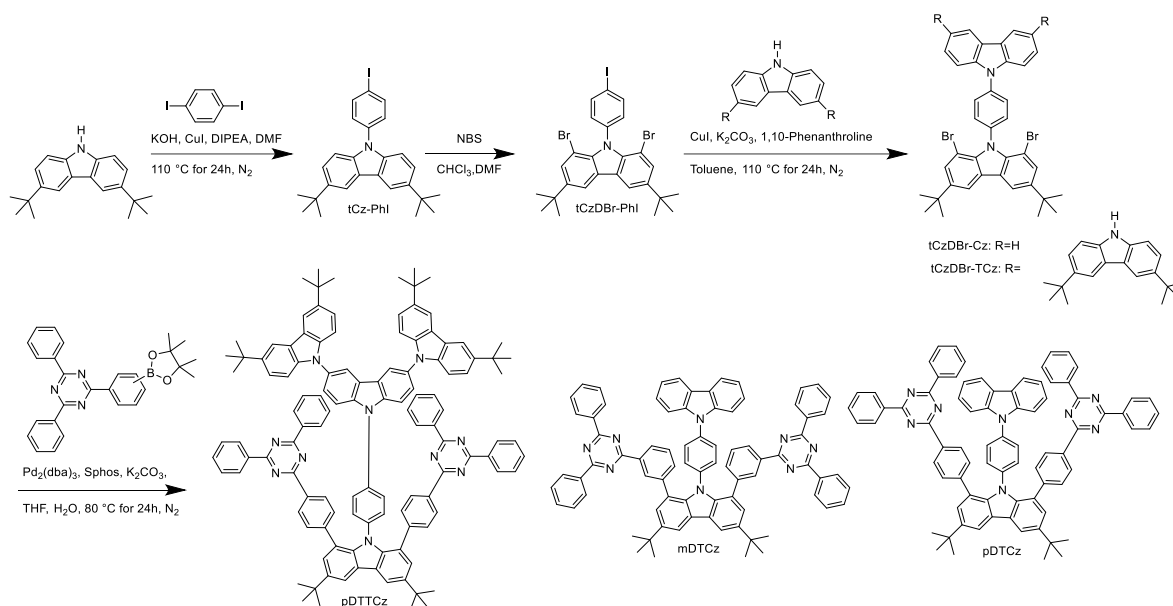
The ISC rate is a key factor in achieving efficient RTP.¹² The ability to obtain higher rates of ISC through bond charge transfer and space charge transfer between donor and acceptor has been demonstrated in thermally activated delayed fluorescence (TADF). In addition, among the molecules with space-charge charge transfer effect, the space-charge effect can greatly suppress the non-radiative decay of TSCT excited states.¹³ Based on this principle, it is possible to achieve efficient RTP emission in neat films via designing the molecules as acceptor-donor-acceptor π -stacks and obtaining efficient space charge transfer.

In this chapter, we present a general molecular design approach to develop RTP in neat films through space charge transfer. We designed three molecules with tert-butylcarbazole as a bridge, carbazole and tercarbazole as donors and triazines as acceptors: 9-(4-(9H-carbazol-9-yl)phenyl)-3,6-di-tert-butyl-1,8-bis(3-(4,6-diphenyl-1,3,5-triazin-2-yl) phenyl)-9H-carbazole (mDTCz), 9-(4-(9H-carbazol-9-yl)phenyl)-3,6-di-tert-butyl-1,8-bis(4-(4, 6-diphenyl-1,3,5-triazin-2- yl)phenyl)-9H-carbazole (pDTCz), and 3,3'',6,6''-tetra-tert-butyl-9'-(4-(3,6-di-tert-butyl-1,8-bis(4-(4,6-diphenyl-1,3,5-triazin-2- yl)phenyl)) phenyl)-9H-carbazol-9-yl)phenyl)-9'H-9,3': 6',9''-tercarbazole (pDTTCz). Experimental and theoretical studies reveal a face-to-face arrangement of donors and acceptors, with enhanced π - π interactions in the molecule as the triazine position moves from the meta to para phenylene connection. Excitingly, in ambient conditions, phosphorescence emission is exhibited in the pure film. Due to their long-lasting phosphorescent performance, pure films of these three molecules can potentially be used in the field of information encryption. Importantly, our approach may provide a much-needed solution for achieving ultra-long-lived RTP of organic molecules in pure films under ambient conditions.

3.2 Synthesis

The synthesis of these three compounds is described in **Scheme 3.1**. 3,6-Di-tert-butyl-9-(4-iodophenyl)-9H-carbazole (tCz-PhI) was synthesised from tert-butylcarbazole and 1,4-diiodobenzene by Ullmann reaction. After bromination, tCzDBr-PhI was obtained. The

coupling reaction of carbazole and tricarbazoles with tCzDBr-PhI provided the corresponding tCzDBr-Cz/tCzDBr-TCz, respectively. Suzuki coupling of tCzDBr-Cz/tCzDBr-TCz with 2,4-diphenyl-6-(4-(4,4,5,5-tetramethyl-1,3,2-dioxaborolan-2-yl)phenyl)-1,3,5-triazine gave the final pDTCz and pDTTCz. Suzuki coupling of tCzDBr-Cz with 2,4-diphenyl-6-(3-(4,4,5,5-tetramethyl-1,3,2-dioxaborolan-2-yl)phenyl)-1,3,5-triazine yielded the corresponding mDTCz. The structures of intermediates and the target product were unambiguously characterized by nuclear magnetic resonance (NMR) spectra, high-resolution mass spectra (HRMS), and finally by X-ray diffraction analysis from suitable crystals.



Scheme 3.1 Synthetic routes for the three compounds.

3.3 Optical properties

As shown in **Figure 3.1a, b, and c**, the ultraviolet-visible (UV-vis) absorption spectra of mDTCz, pDTCz, and pDTTCz at room temperature together with their fluorescence in different solvents (10^{-5} M) were recorded. In toluene, all three molecules exhibit broad absorptions in the 330-400 nm wavelength range attributed to π - π^* and charge transfer (from the carbazole/tert-butylcarbazole bridge/tricarbazole to the triazine acceptor) transitions.¹⁴

When dissolved in different solvents, the steady-state PL spectrum is red-shifted when the solvent polarity increases.¹⁵ Moreover, there is a gradual increase of the prompt fluorescence decay lifetime, as shown in **Figure 3.2**. The fitted prompt fluorescence lifetime for these materials in different solvents are summarized in **Table 3.1**. The polarity-dependent emission properties indicate the charge-transfer character of the excited states of these

compounds. The delayed emission at 200 μ s, which is treated as the phosphorescence spectra for these materials are plotted in **Figure 3.1d-f** for mDTCz, pDTCz, and pDTTCz, respectively. The singlet and triplet energy were determined according to the line-shape analysis from the fluorescence and delayed emission spectra, as shown in **Figure 3.2** and **Table 3.1**. The singlet-triplet splitting ΔE_{ST} of mDTCz, pDTCz, and pDTTCz are 0.10 eV, 0.11 eV, and 0.04 eV, respectively. The relatively small energy splitting ΔE_{ST} indicates the possibility of TADF emission from these luminescent materials.

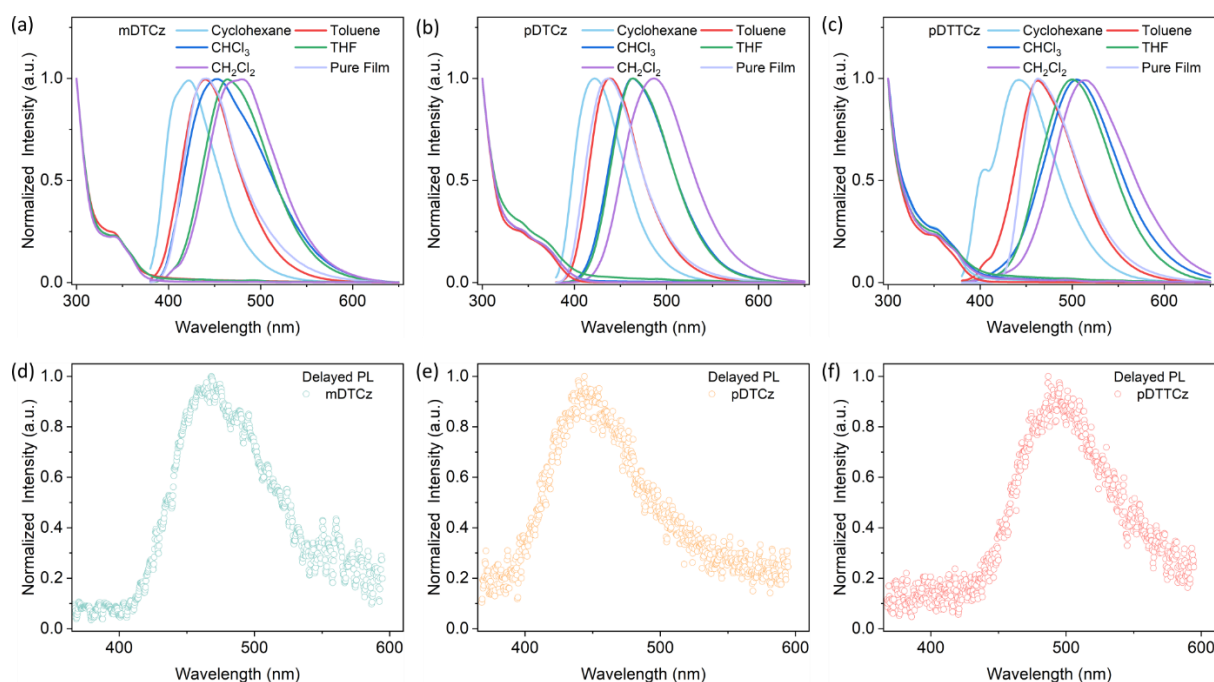


Figure 3.1 Ultraviolet-visible (UV-vis) absorption spectra in toluene and steady state PL emission. (a) mDTCz. (b) pDTCz. (c) pDTTCz. The PL spectrum with a delay of 200 μ s after the laser excitation. Measured in neat films. (d) mDTCz. (e) pDTCz. (f) pDTTCz.

Table 3.1 Photophysical properties of mDTCz, pDTCz, and pDTTCz.

Sample	$\lambda_{abs.}$	λ_{FL}	λ_{FL}	λ_{FL}	λ_{FL}	λ_{FL}	λ_{FL}	λ_{PL}	PLQY	Air/N ₂	S ₁ /T ₁
	(nm) ^a	(nm) ^b	(nm) ^a	(nm) ^c	(nm) ^d	(nm) ^e	(nm) ^f	(nm) ^f	(%) ^f		(eV)
mDTCz	341/357	421	438	453	464	483	441	470	43.8 / 48.0		2.90 / 2.80
pDTCz	340/367	422	438	463	463	487	437	443	50.3 / 54.9		2.92 / 2.81
pDTTCz	352/371	441	462	504	499	514	463	481	67.2 / 73.5		2.84 / 2.80

^a In toluene. ^b In cyclohexane. ^c In CHCl₃. ^d In THF. ^e In CH₂Cl₂. ^f In neat film.

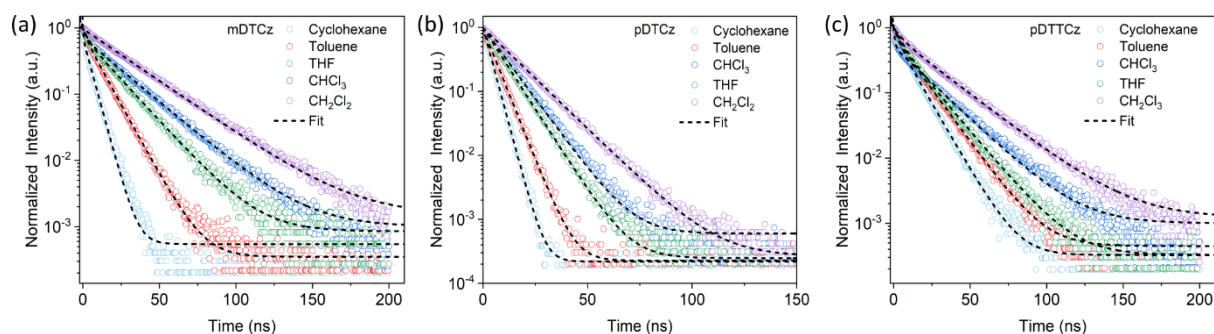


Figure 3.2 Fluorescence lifetime in different solutions. (a) mDTCz. (b) pDTCz. (c) pDTTCz.

The PL quantum yield (PLQY) of mDTCz, pDTCz, and pDTTCz were determined by integrating sphere under a nitrogen and ambient atmosphere. In the neat films, the PLQY is increased from 48.0% for mDTCz to 54.9% for pDTCz, and to 73.5% for pDTTCz (**Table 3.1**). This is due to the fact that in strongly bound exciplexes, the intramolecular motion of donors and acceptors is restricted, leading to the inhibition of non-radiative decay. The PLQY is slightly reduced when measured in ambient atmosphere, indicating the involvement of triplets.¹⁶

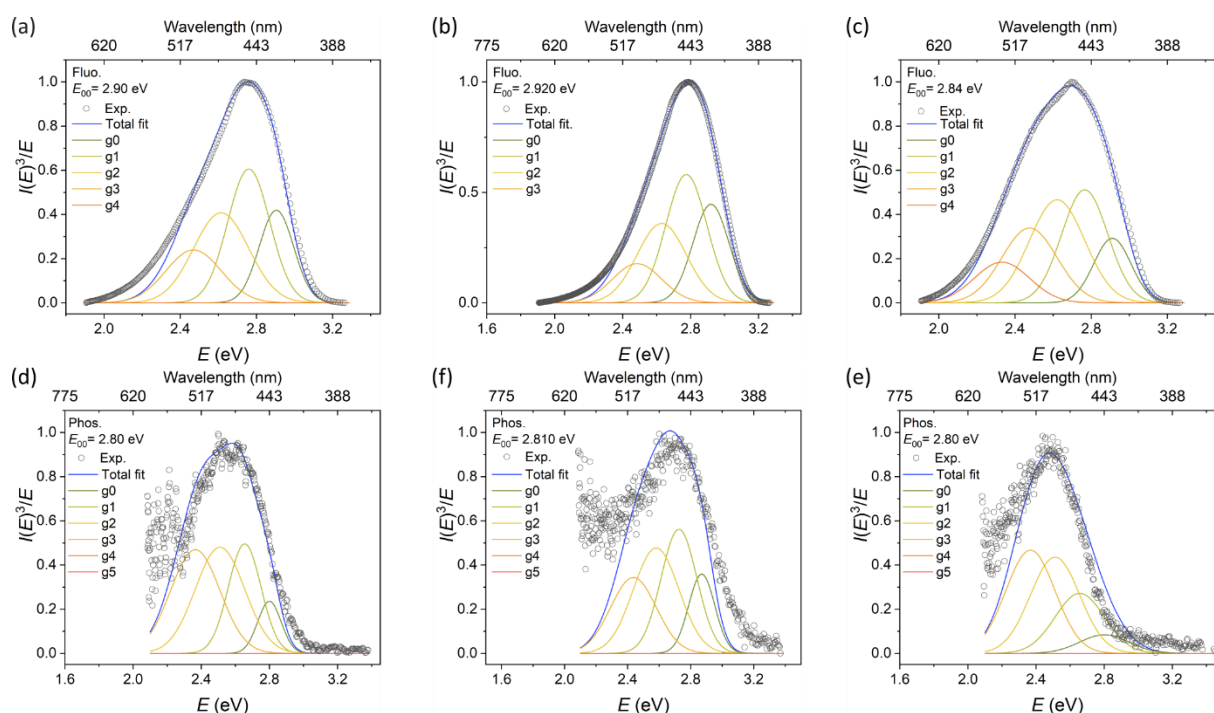


Figure 3.3 Lineshape analysis of fluorescence. (a) mDTCz. (b) pDTCz. (c) pDTTCz. Lineshape analysis of phosphorescence spectra. (d) mDTCz. (e) pDTCz. (f) pDTTCz.

The lineshape analysis is derived from quantum mechanics about electronic state transitions to determine the energy level of the excited state. In short, in the

Born–Oppenheimer approximation, each state factorizes into an electronic part and a vibrational part, while the radiative recombination rate can be generalized to a sum over different vibrational levels in the electronic ground state. For fluorescence and phosphorescence emission, the different vibronic energy states in the ground state can be described with a small energy difference, while the Franck–Condon factors describing the transition probabilities to different vibronic states (i.e. these Gaussian shape fitting components) follow a Poisson progression, which leads to the relation between spectral lineshape and energetic states involved. Such a lineshape analysis has been used for the precise determination of the energy levels for TADF and RTP emitters.¹⁷

Table 3.2 Fluorescence lifetime in different solutions of mDTCz, pDTCz, and pDTTCz.

Sample	τ_{PF} (ns) ^a	τ_{PF} (ns) ^b	τ_{PF} (ns) ^c	τ_{PF} (ns) ^d	τ_{PF} (ns) ^e
mDTCz	4.93	9.76	16.35	21.65	27.51
pDTCz	3.56	5.32	8.51	9.75	13.75
pDTTCz	9.78	12.60	13.81	18.63	23.02

^a In toluene. ^b In cyclohexane. ^c In CHCl₃. ^d In THF. ^e In CH₂Cl₂.

The intramolecular steric hindrance effect on the transient photophysical properties is further investigated for mDTCz, pDTCz, and pDTTCz. Firstly, the transient PL decay for these neat films prepared by the thermal evaporation on glass substrates is investigated. As shown in **Figure 3.4**, the transient PL decay in nitrogen atmosphere measured by time-correlated single-photon counting (TCSPC) indicates that there is prompt fluorescence (PF) in the nanosecond (ns) range, delayed fluorescence (DF) in the microsecond (μ s) range, and RTP emission in millisecond (ms) range. The decay lifetime by bi-exponential fitting is summarized in **Table 3.4**. For these three materials, the decay lifetime is \sim 8-10 ns for the PF, and \sim 0.83-1.11 μ s for the DF. The RTP decay lifetime is 34.3 ms, 36.5 ms, and 41.9 ms for mDTCz, pDTCz, and pDTTCz, respectively. It worth noting that the film prepared by the thermal evaporation is amorphous, as confirmed by XRD of neat films, shown in **Figure 3.6**. Because of pronounced molecular movements with the activation energy comparable to the thermal energy at room temperature, non-radiative molecular relaxations in forms of molecular vibrations or rotations can effectively quench the phosphorescence without rigid environmental confinement. Because of the steric hindrance effect employed in the molecules in this study, molecular rotations are significantly suppressed, contributing to the RTP

emission even in the neat amorphous film. The possible reason for slightly longer RTP lifetime in pDTTCz could also stem from a stronger steric hindrance effect, as compared to the derivatives mDTCz and pDTCz.

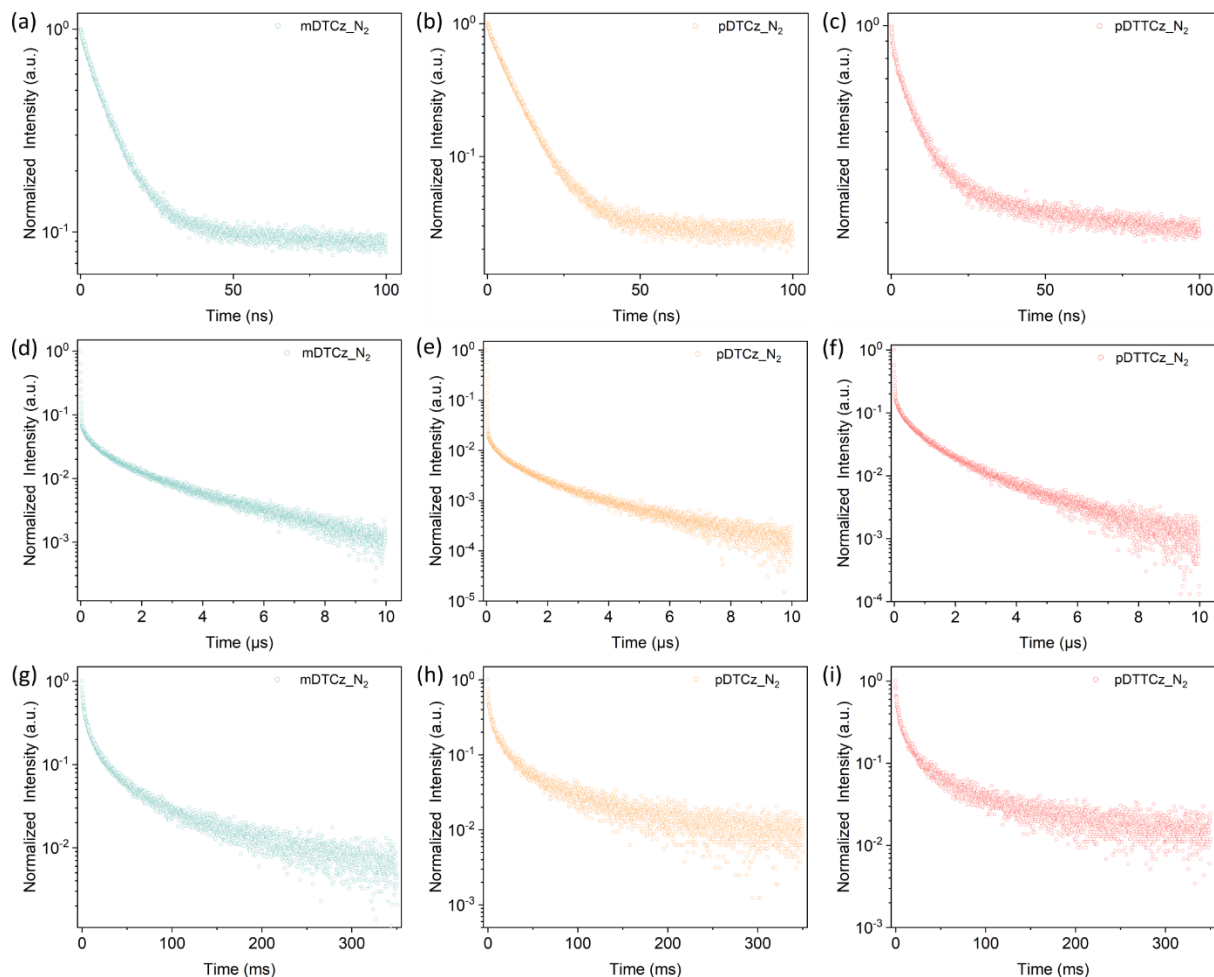


Figure 3.4 Transient PL decay in N_2 for developed materials for mDTCz (1st column), pDTCz (2nd column), and pDTTCz (3rd column) in amorphous neat film by thermal evaporation. (a, b, c) for prompt fluorescence in the ns range, (d, e, f) for delayed fluorescence in the μs range, and (g, h, i) for RTP phosphorescence in the ms range.

Table 3.3 Photophysical parameters at room temperature in neat film of mDTCz, pDTCz, and pDTTCz.

Sample	τ_{PF} (ns) Air/ N_2	τ_{DF} (μs) Air/ N_2	τ_{RTP} (ms) Air/ N_2
mDTCz	8.49 / 8.43	0.85 / 1.11	31.22 / 34.29
pDTCz	7.86 / 7.92	0.74 / 0.87	34.72 / 36.52
pDTTCz	9.75 / 9.82	0.81 / 0.83	37.49 / 41.94

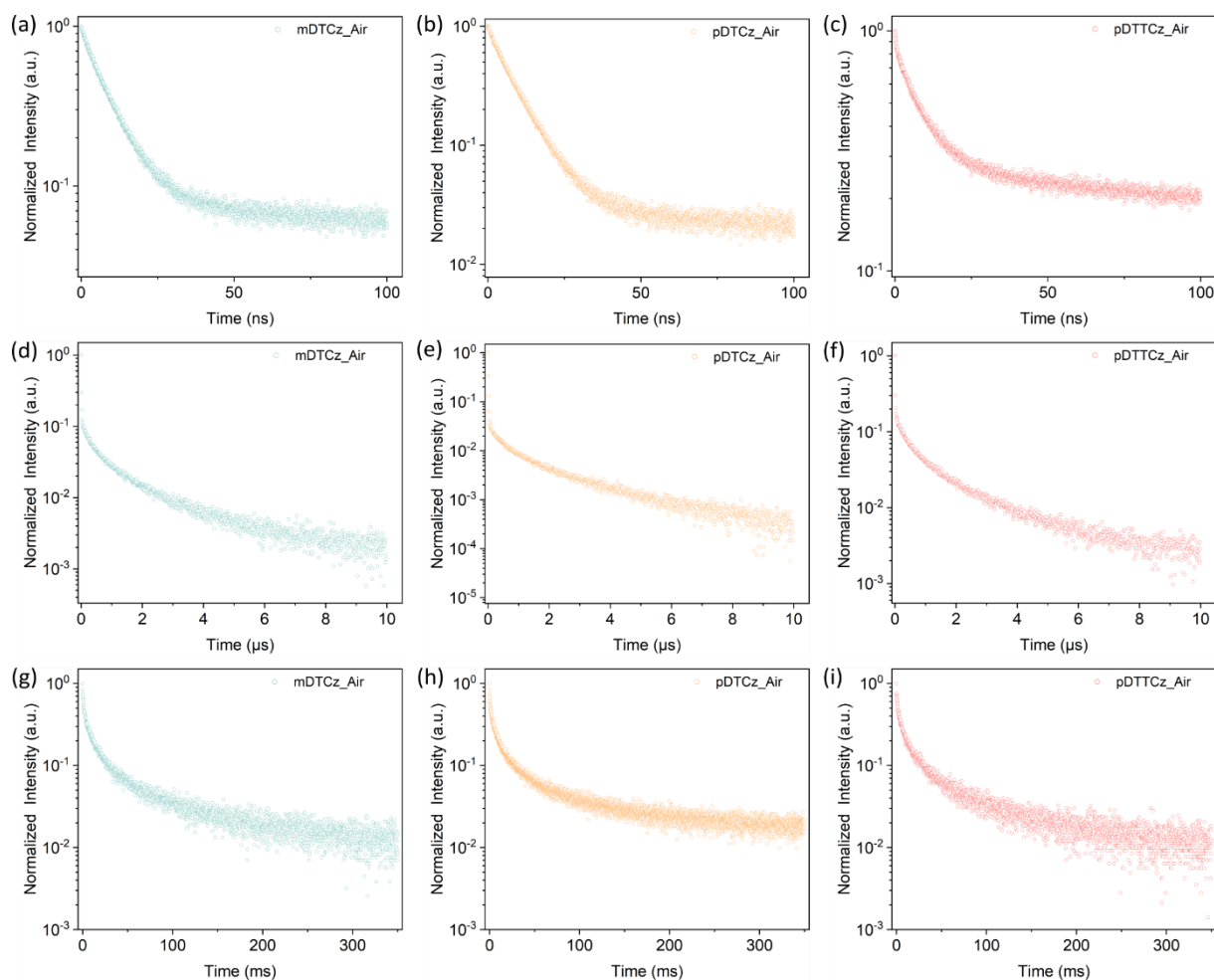


Figure 3.5 Transient PL decay in ambient atmosphere for developed materials for mDTCz (1st column), pDTCz (2nd column), and pDTTCz (3rd column) in amorphous neat film by thermal evaporation. (a, b, c) for prompt fluorescence in the ns range, (d, e, f) for delayed fluorescence in the μ s range and (g, h, i) for RTP phosphorescence in the ms range.

Furthermore, it is noted that DF and RTP emission can even be detected under ambient condition for mDTCz, pDTCz, and pDTTCz amorphous films. As shown in **Figure 3.5**, the pronounced RTP decay for these amorphous films in air can still be observed, with similar decay lifetime as measured in nitrogen, summarized in **Table 3.3**. The decay lifetime of DF and RTP emission for these amorphous film measured under ambient atmosphere is slightly reduced, as compared to these measurements in nitrogen. Nevertheless, the DF decay lifetime can still be as long as 0.85 μ s, 0.74 μ s, and 0.81 μ s, while the RTP decay lifetime is 31.2 ms, 37.4 ms and 37.5 ms for mDTCz, pDTCz, and pDTTCz amorphous films, respectively. It is found that the material mDTCz with less steric hindrance has the largest

reduction in the decay lifetime under ambient atmosphere as compared to that measured in nitrogen. In other words, for pDTCz and pDTTCz with more pronounced intramolecular steric hindrance, only a minor reduction in the decay lifetime has been observed.

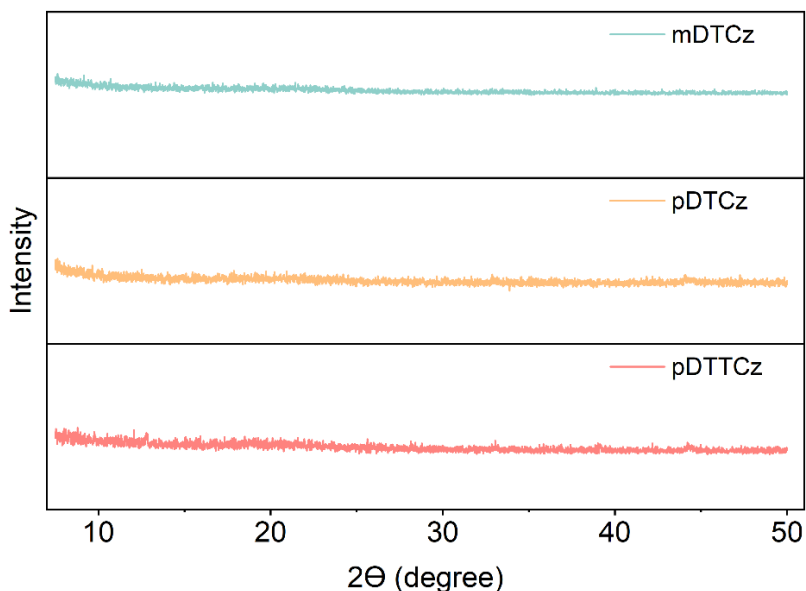


Figure 3.6 X-ray diffraction (XRD) pattern of the mDTCz, pDTCz, and pDTTCz in neat films.

To investigate the molecular ordering of mDTCz, pDTCz, and pDTTCz, we used X-ray analysis of suitable single crystals grown from THF, n-hexane, and toluene. The corresponding data are collected in **Table 3.5**. As shown in **Figure 3.7 a** and **d**, for pDTCz, the closest distance between the benzene ring attached to the nitrogen atom on the carbazole and the N or C of the acceptor triazine is very small, 3.142-3.206 Å. mDTCz and pDTCz crystallize in a triclinic crystal system with space group P1, all containing two molecules in the crystal unit. For mDTCz, in the crystal unit, the two molecules are closely stacked. Between the tert-butyl carbazolyl bridge and between the triazine rings, the π - π distances are 3.492 and 3.394 Å, respectively. (**Figure 3.7c**). As shown in **Figure 3.7 a**, since the tert-butyl carbazolyl bridge is attached to the meta-position of the triazine benzene ring, there is no edge-to-edge alignment of the carbazole and the triazine. The distances from the carbazole to the two triazine benzene rings are 3.681 and 3.808 Å, respectively. It can be seen from their space-filling structures that there is less overlap of the electron cloud between the triazine ring and the carbazole (**Figure 3.7b**), which means a weaker space charge transfer in the molecule. Specifically, the acceptor change from meta to para position at the connecting benzene ring, and gives rise to edge-edge alignment of the carbazole and triazine. This results in close

confocal π - π stacking of most of the atoms of the two fragments (3.2-3.8 Å) (**Figure 3.7d**). The increased π - π stacking from mDTCz to pDTCz can also be seen from their space-filling structures (**Figure 3.7e**). In the pDTCz crystal cell, the two molecules show a head-to-tail staggered arrangement, with the closest distance from the tert-butyl carbazolyl-bridge to the triazine ring of the other molecule being 3.475 Å, which means that there is close π -interaction between the donor and acceptor part enabling intermolecular through space charge transfer.

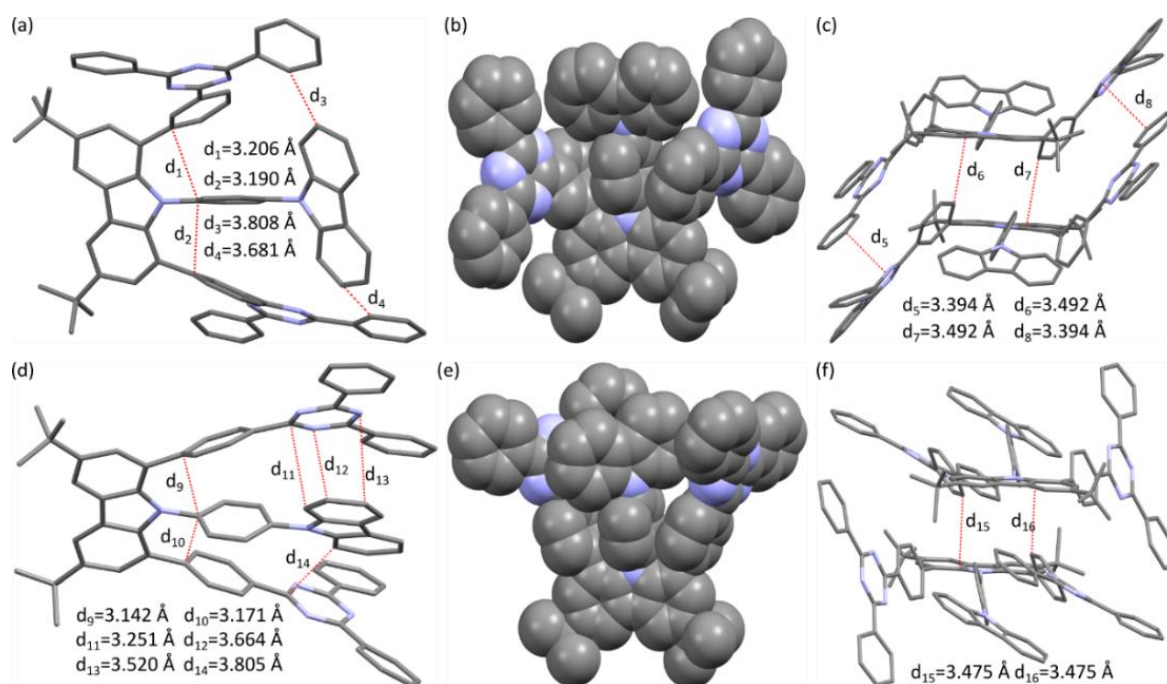


Figure 3.7 Illustration of the intramolecular interactions. (a) mDTCz. (d) pDTCz. Spacefill structure. (b) mDTCz. (e) pDTCz. Molecular packing behavior in a cell cell. (c) mDTCz. (f) pDTCz.

While pDTTCz, crystallized in a monoclinic crystal system with space group P2/n, containing four molecules in the crystal cell, showing a closest distance between two molecules of tercarbazole of 3.587 Å (**Figure 3.8c**). Similar to mDTCz and pDTCz, the closest distance between the benzene ring attached to the nitrogen atom of the tricarbazole and the acceptor is 3.142-3.206 Å. Interestingly, the benzene ring of the triazine is very close to the branched carbazole of the tricarbazoles. This makes it possible for more charge transfer to occur between them. This can also be seen from its space-filling structure.

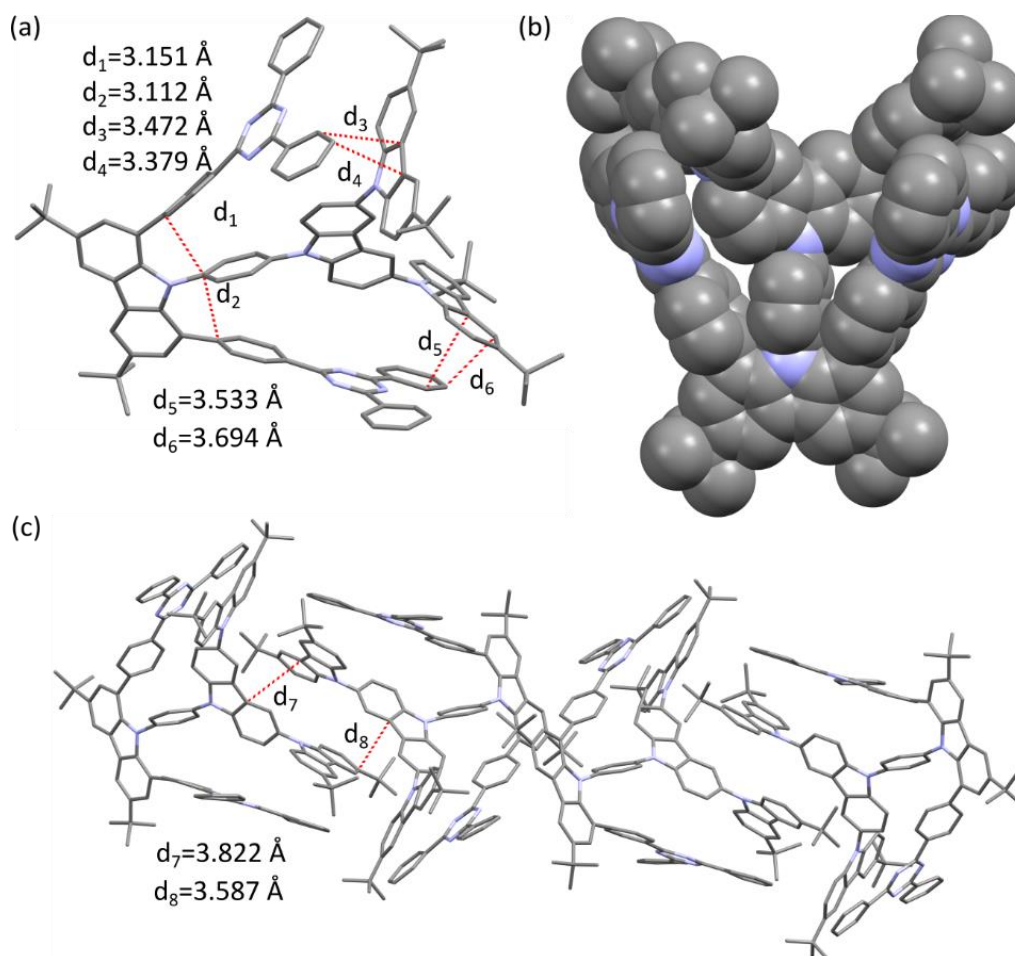


Figure 3.8 (a) Illustration of the intramolecular interactions of pDTTCz. (b) Spacefill structure of pDTTCz. (c) Molecular packing behavior in a cell of pDTTCz.

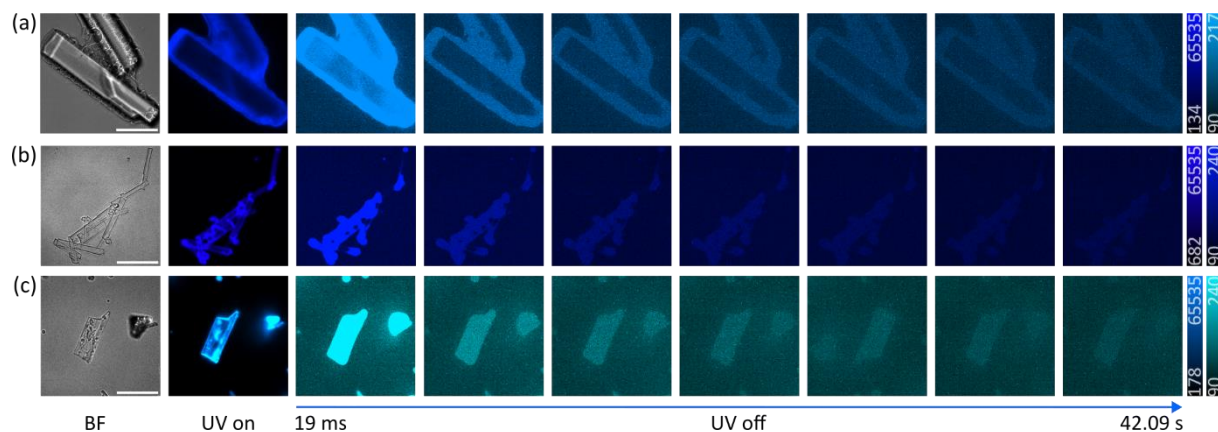


Figure 3.9 Photographs of crystalline taken during and after irradiation (390 nm) under N_2 conditions. The scale bar is $20 \mu\text{m}$. BF means bright field. (a) mDTTCz. (b) pDTTCz. (c) pDTTCz. Color bar: left (UV on), right (UV off).

As shown in **Figure 3.9**, after stopping the UV irradiation, the intensity of the photoluminescence gradually decreased and remained present up to 42 s, indicating ultra-long afterglow phosphorescence emission in mDTCz, pDTCz, and pDTTCz crystals at room temperature.

3.4 Density functional theory (DFT) calculations

To explain the relationship between the molecular structures and properties of the target molecules, theoretical calculations were performed with density functional theory (DFT) and time-dependent DFT (TD-DFT) under the 6-311G level for the ground states. The HOMO/LUMO distributions of mDTCz, pDTCz, and pDTTCz are shown in **Figure 3.10**. The HOMOs of mDTCz and pDTTCz were mainly distributed on the carbazole and tert-butyl carbazole bridges as the donor group. The difference is that for pDTTCz, the HOMO is distributed only on the tricarbazole moiety. This could be attributed to the stronger electron-donating ability of the tricarbazole. The LUMOs were distributed on the triazine parts as the acceptor group. From the distribution of HOMOs and LUMOs, there are possible space charge transfers and bond charge transfers for the three molecules. The complete separation of HOMOs / LUMOs of three compounds led to the small ΔE_{ST} (**Table 1**), indicating the potential TADF feature.¹⁸

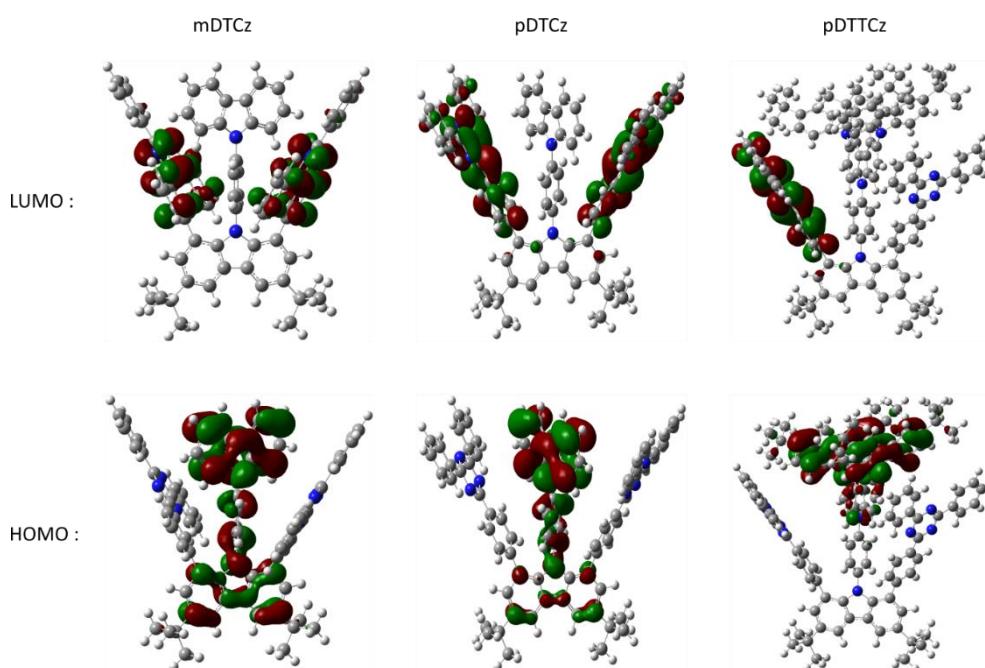


Figure 3.10 HOMO and LUMO distributions of mDTCz, pDTCz, and pDTTCz. DFT (B3LYP, 6-311G).

Table 3.4 The HOMO and LUMO levels of mDTCz, pDTCz, and pDTTCz. Calculations were carried out at the DFT/TD-DFT//B3LYP/6-311G level.

Sample	HOMO (eV)	LUMO (eV)	E_g (eV)	S_1 (eV)	T_1 (eV)	ΔE_{ST} (eV)
mDTCz	-5.44	-2.17	3.27	2.820	2.814	0.006
pDTCz	-5.42	-2.17	3.25	2.806	2.793	0.013
pDTTCz	-5.26	-2.27	2.99	2.663	2.662	0.001

3.5 Transient excited state absorption (TESA)

The charge transfer property of the excited states for the developed materials is further investigated by femtosecond transient absorption (fs-TA) spectroscopy. This was done in collaboration with Yungui Li (Max Planck Institute for Polymer Research, Mainz). The 2D transient absorption spectra (ΔA in false colors) for mDTCz, pDTCz, and pDTTCz solution in CHCl_3 are shown in **Figure 3.11a-c**, respectively. Pronounced excited state absorption (ESA) has been observed for all emitters. The long-lived ESA signal can be assigned to singlet and triplet absorption, from ~ 10 ps till the detection time window of ~ 8 ns. It is further found that there are fast decays from fs to ps range, which has been indicated in **Figure 3.11a-f**. To exclude possible experimental artifacts, the fast decay signal is also observed with a lower excitation laser intensity, as shown in **Figure 3.12**.

Table 3.5 Fast decay lifetime photophysical characterization of mDTCz, pDTCz, and pDTTCz.

Sample	τ (ps) ^a @550 nm	τ (ps) ^b @550 nm	τ (ps) ^b @1550 nm	τ (ps) ^c @550 nm	τ (ps) ^c @1550 nm
mDTCz	/	/	3.91	/	/
pDTCz	12.65	10.45	8.32	/	/
pDTTCz	87.92	10.34	19.11	/	/

^a In CHCl_3 , laser intensity 50 μW .

^b In CHCl_3 , laser intensity 100 μW .

^c In cyclohexane, laser intensity 100 μW .

/ : Indicates no fast decay process

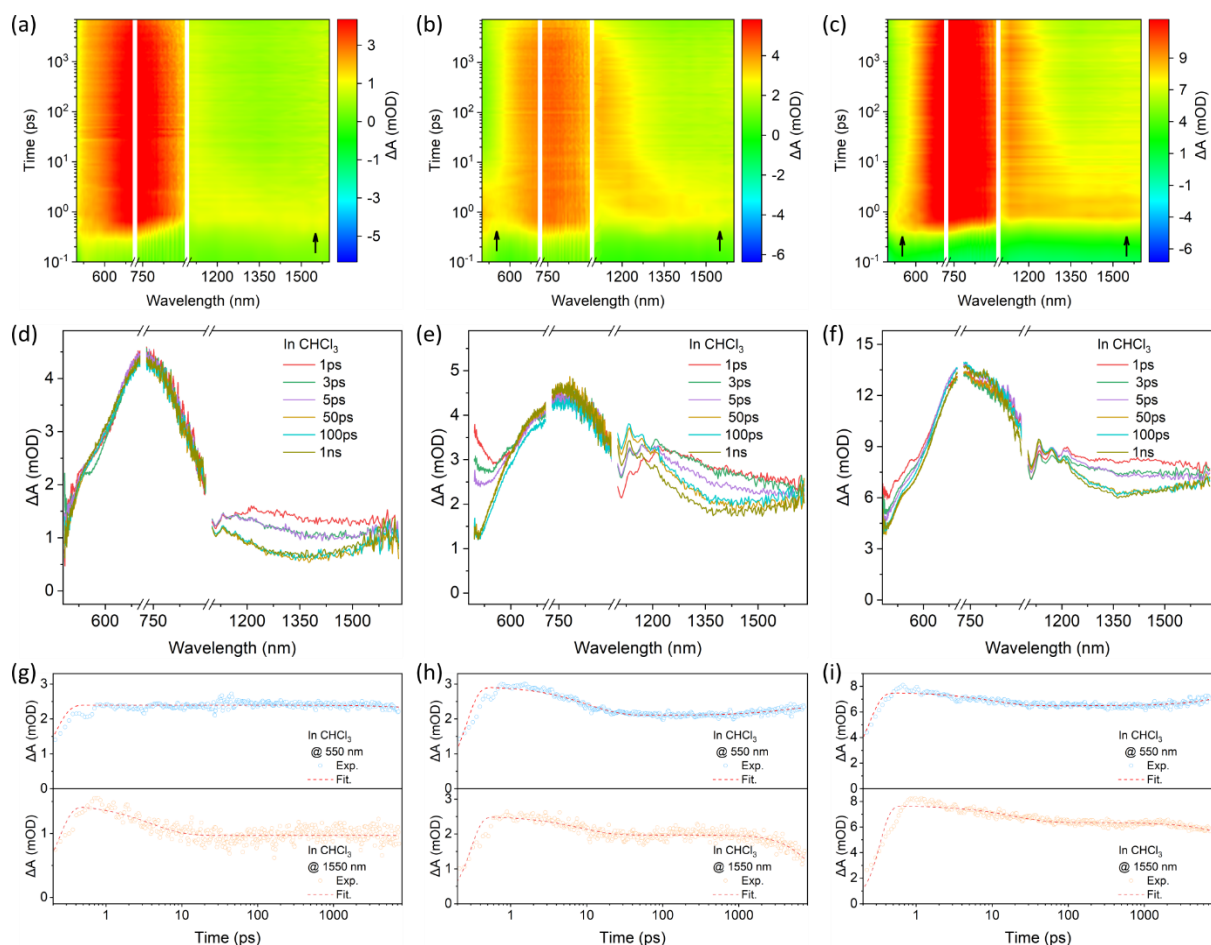


Figure 3.11 fs-TA spectroscopic characterization of the charge-transfer state for mDTCz (1st column), pDTCz (2nd column), and pDTTCz (3rd column). (a), (b), and (c) The 2D transient absorption spectra (ΔA in false colors) in CHCl_3 , excited by 100 μW laser at 360 nm. The arrow indicates the fast decay signals within the first picoseconds. (d), (e), and (f) Extracted spectra from transient spectra. (g), (h), and (i) are selected fs-TA decays at 550 nm and 1550 nm in CHCl_3 .

For all the emitters under study, fast decay signals have been observed both in the visible and NIR wavelength region in CHCl_3 . However, the fast decay component vanishes in the non-polar solvent cyclohexane, as shown in **Figure 3.13**. Considering the chemical structures of the materials under study, the fast decay component can be assigned to the charge transfer (CT) state relaxation. Compared to non-polar solvents, in polar solvents there is a high proportion of polar charge transfer states in the excited states of the molecules, resulting in charge transfer states that are easier to observe.

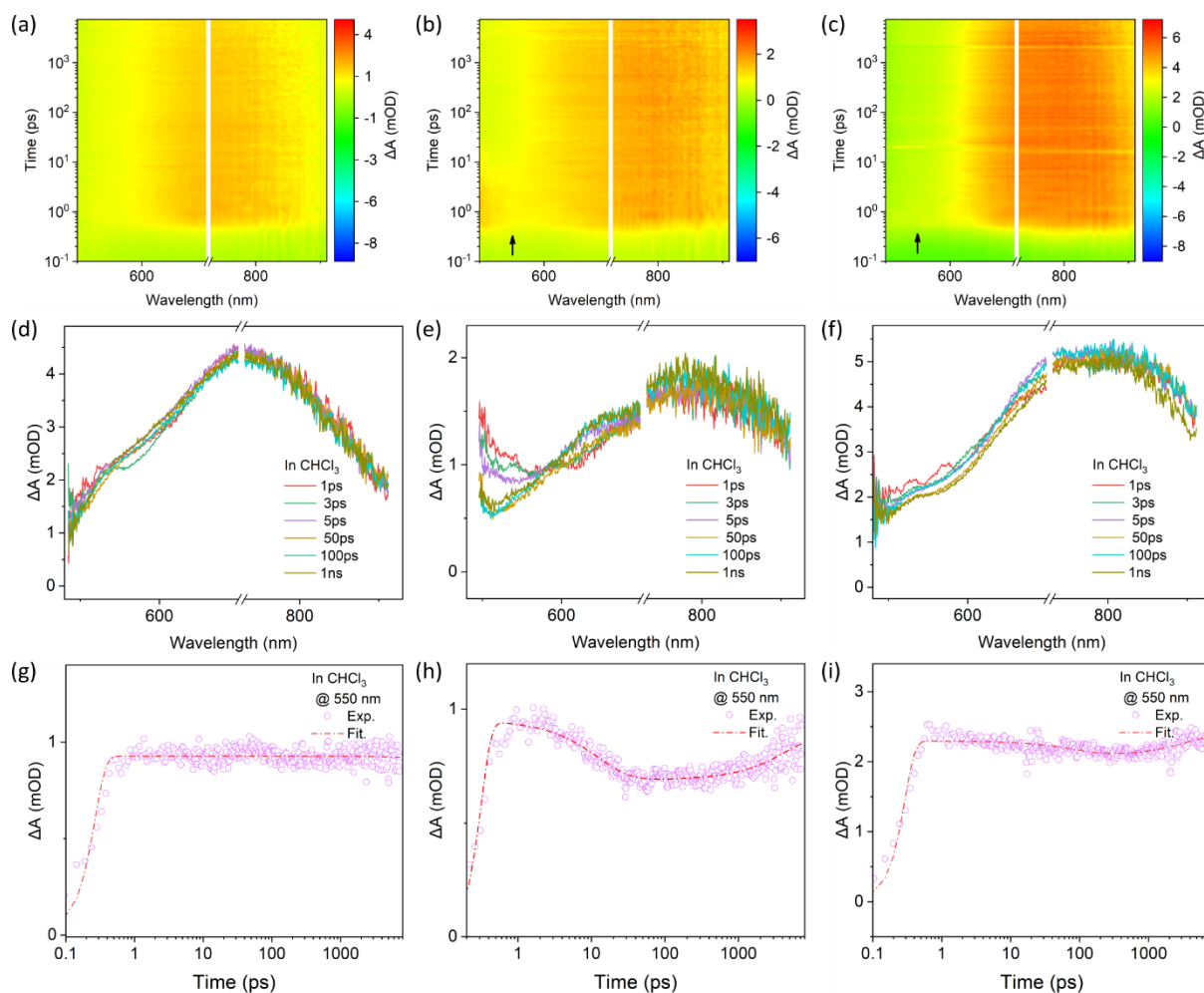


Figure 3.12 fs-TA spectroscopic characterization about the charge-transfer state for mDTCz (1st column), pDTCz (2nd column), and pDTTCz (3rd column). (a), (b), and (c) The 2D transient absorption spectra (ΔA in false colors) in CHCl_3 , excited by $50 \mu\text{W}$ laser at 360 nm. The arrow indicates the fast decay signals within the first picoseconds. (d), (e), and (f) Extracted spectra from transient spectra. (g), (h), and (i) are selected fs-TA decay at 550 nm in CHCl_3 .

Furthermore, it is found that for mDTCz, with more molecular movement feasibility, the CT state has a shorter decay lifetime. The data is summarised in **Table 3.5**. The fast CT state is only observed within the NIR range, with a lifetime of 3.91 ps at 1550 nm, as shown in **Figure 3.11g**. Comparably, the decay lifetime of the fast component is 10.45 ps and 8.32 ps for pDTCz, at 550 nm and 1550 nm, respectively, as shown in **Figure 3.11f**. For pDTTCz solution in CHCl_3 , it is 10.34 ps at 550 nm, while is it as long as 19.11 ps at 1550 nm, as shown in **Figure 3.11i**. Considering the bulky structure of the pDTTCz molecule, it is likely that the signal in the NIR range can be assigned to the through-bond CT state relaxation to the

singlet state geometry, while that observed at visible wavelength range can be assigned to the through-space CT state relaxation.

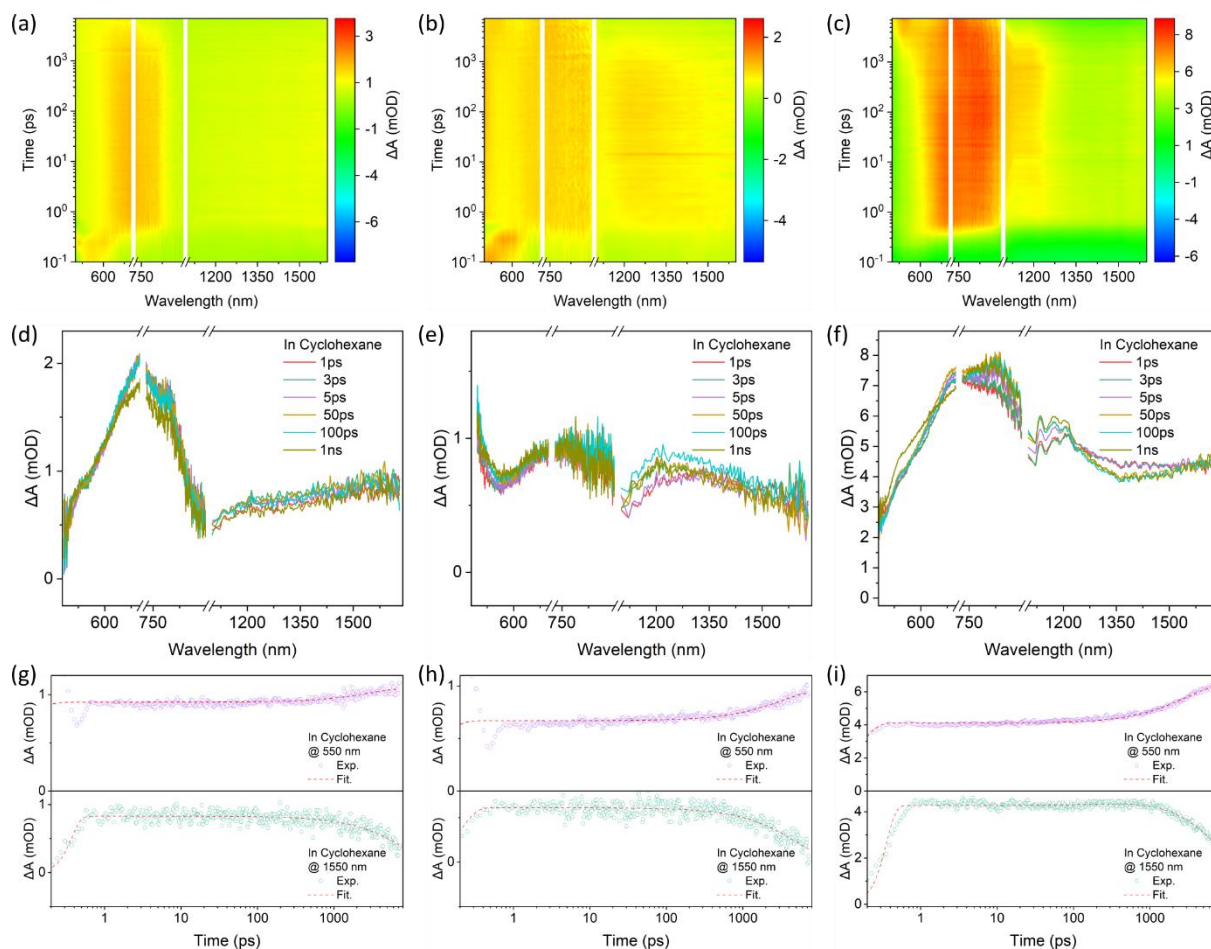


Figure 3.13 fs-TA spectroscopic characterization about the charge-transfer state for mDTCz (1st column), pDTCz (2nd column), and pDTTCz (3rd column). (a), (b), and (c) The 2D transient absorption spectra (ΔA in false colors) in cyclohexane, excited by $100 \mu\text{W}$ laser at 360 nm . (d), (e), and (f) Extracted spectra from transient spectra. (g), (h), and (i) are selected fs-TA decays at 550 nm and 1550 nm in cyclohexane.

3.6 Time-resolved anti-counterfeiting application

The fascinating photoluminescence properties of mDTCz, pDTCz, and pDTTCz in neat films show interests in applications such as time-resolved microscopy. Therefore, we explored the possibility of using them to generate anti-counterfeiting patterns through drop-coating on glass with grids. As shown in **Figure 3.14**, under the ultraviolet irradiation, the pattern "H, F, and E" shows a blue fluorescence. After stopping the excitation, blue or sky-blue RTP radiation from mDTCz, pDTCz, and pDTTCz can be seen. "F" and "E" remain

clearly visible after a duration of 3.08 s, whereas the RTP emission from “H” is gradually obscured. These results indicate that more space charge transfer in pure films favors the generation of longer RTP emission and the potential applications in the field of time-resolved encryption hold great promise.

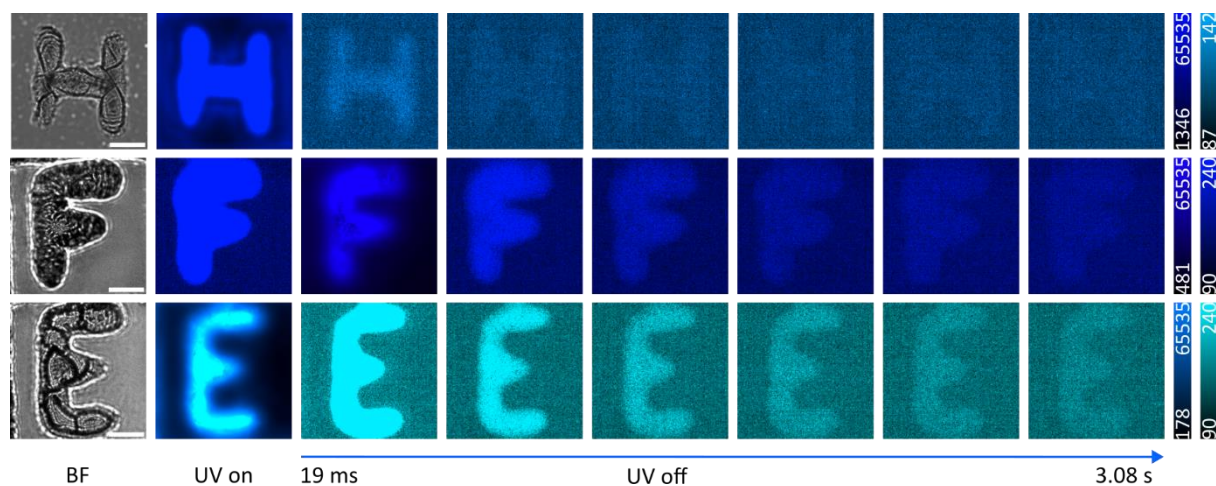
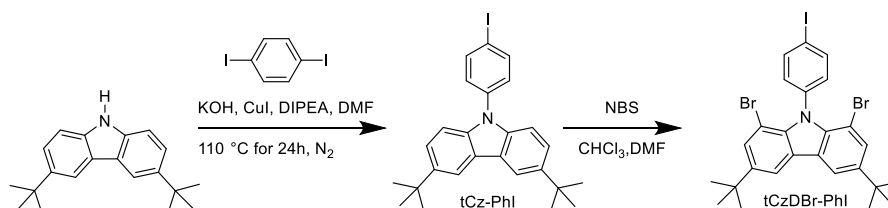


Figure 3.14 Time-resolved microscopy based on the RTP from neat materials after solvent evaporation. From top to bottom: mDTCz, pDTCz, and pDTTCz, respectively. The scale bar is 10 μm . BF indicates the bright field without excitation. Color bar: left (UV on), right (UV off).

3.7 Summary

In this chapter, we propose a design strategy to enhance the phosphorescence efficiency of neat films through space charge transfer induced via the steric hindrance effect. A series of emitters (namely mDTCz, pDTCz, and pDTTCz) were designed and synthesized to achieve efficient RTP in neat films via stepwise adjustment of the acceptor position and the size of the donor moiety. After removal of the excitation light source, the significant phosphorescence (over 42 s) was observed in crystals of mDTCz, pDTCz, and pDTTCz. In pure film, pDTTCz exhibits a phosphorescence quantum yield of 6.3% and a phosphorescence lifetime of 37.49 ms (in ambient). This is due to steric hindrance effects, leading to stronger space charge transfer, whereby the intramolecular movement of donors and acceptors in the molecule is thought to be restricted, inhibiting non-radiative decay. Notably, mDTCz, pDTCz, and pDTTCz neat films were successfully applied to time-resolved microscopy, showing great potential for anti-counterfeiting applications. The rational design strategy developed here will be important in exploring the achievement of efficient RTP materials in neat films.

3.8 Synthetic details



Scheme 3.2 Synthetic route for compound tCz-PhI and tCzDBr-PhI.

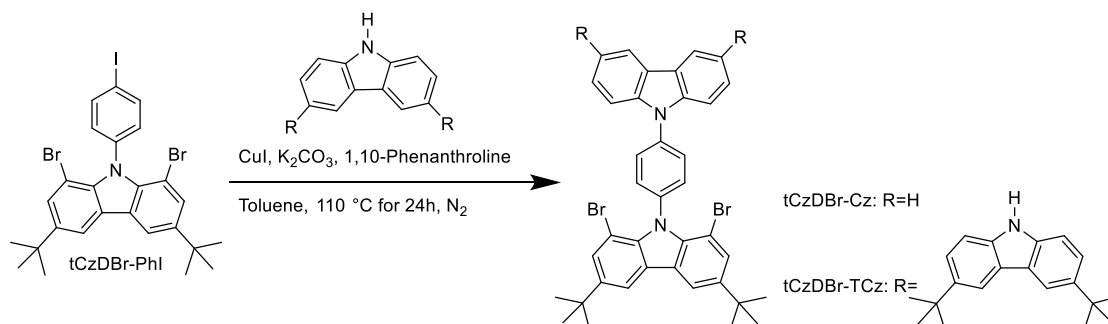
3,6-Di-tert-butyl-9-(4-iodophenyl)-9H-carbazole (tCz-PhI)

A mixture of 1,4-Diiodobenzene (0.98 g, 30 mmol), 3,6-di-tert-butyl carbazole (0.28 g, 10 mmol), copper(I) iodide (0.19 g, 1 mmol), N, N -diisopropylethylamine (0.05 g, 0.4 mmol) and potassium hydroxide (1.1 g, 20 mmol) were added in N, N-dimethylformamide (100 mL). The reaction was carried out under nitrogen atmosphere at 110 °C for 24 hours. After cooling down to room temperature, the mixture was poured into 100 mL water, and extracted with DCM three times. The organic layer was then dried over anhydrous Na₂SO₄. The crude product was purified by column chromatography to give a white solid compound (yield: 75%). ¹H NMR (400 MHz, CD₂Cl₂) δ 8.15 (dd, *J* = 2.0, 0.6 Hz, 2H), 7.95 – 7.88 (m, 2H), 7.48 (dd, *J* = 8.6, 2.0 Hz, 2H), 7.37 – 7.29 (m, 4H), 1.46 (s, 18H). ¹³C NMR (101 MHz, CD₂Cl₂) δ 143.67, 139.38, 139.25, 138.40, 128.89, 124.19, 123.86, 116.75, 109.42, 91.57, 35.04, 32.12. High-resolution mass spectrometry (HRMS) (APCI) *m/z*: calc for C₂₆H₂₈NI: 481.1266; found: 481.1266.

1,8-Dibromo-3,6-di-tert-butyl-9-(4-iodophenyl)-9H-carbazole (tCzDBr-PhI)

3,6-Di-tert-butyl-9-(4-iodophenyl)-9H-carbazole (2 g, 5.36 mmol), NBS (1.95 g, 11 mmol), DMF (60 mL) and CHCl₃ (40 mL) were added into a 250 mL flask. The mixture was stirred at 80 °C in the dark for 12 h. After cooling to room temperature, the mixture was poured into 100 mL water, and extracted with DCM for three times. The organic layer was washed with brine and then dried over anhydrous Na₂SO₄. The solution was filtered and concentrated by rotary evaporator. The crude product was purified by column chromatography to give a white solid product. (yield: 70%). ¹H NMR (400 MHz, CD₂Cl₂) δ 8.10 (d, *J* = 1,8 Hz, 2H), 7.83 – 7.75 (m, 2H), 7.62 (d, *J* = 1,8 Hz, 2H), 7.25 – 7.15 (m, 2H), 1.43 (s, 18H). ¹³C NMR (101 MHz, CD₂Cl₂) δ 145.53, 138.79, 137.60, 137.28, 134.83, 130.55,

125.99, 116.09, 104.01, 95.18, 34.98, 31.88. High-resolution mass spectrometry (HRMS) (APCI) m/z : calc for $C_{26}H_{26}NBr_2I$: 636.9477; found: 636.948.



Scheme 3.3 Synthetic route for compound tCzDBr-Cz and tCzDBr-TCz.

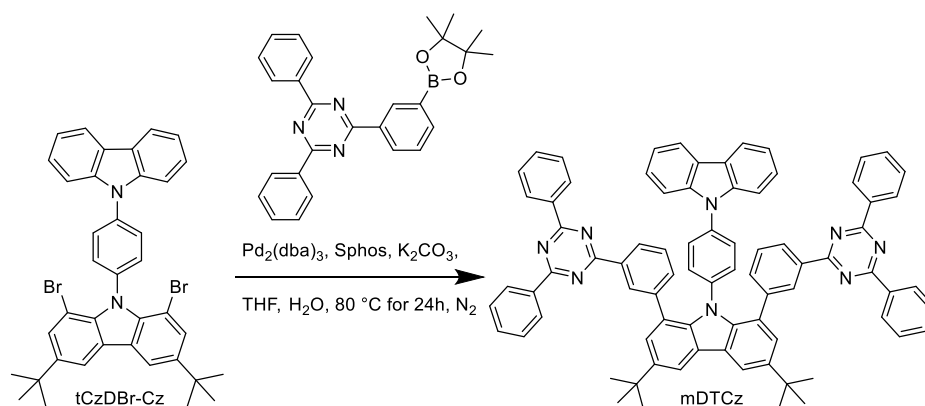
9-(4-(9H-carbazol-9-yl)phenyl)-1,8-dibromo-3,6-di-tert-butyl-9H-carbazole (tCzDBr-Cz)

1,8-Dibromo-3,6-di-tert-butyl-9-(4-iodophenyl)-9H-carbazole (0.636 g, 1 mmol), 9H-carbazole (0.183 g, 1.1 mmol), K_2CO_3 (0.152 g, 1.1 mmol), 1,10 phenanthroline (0.018 g, 0.1 mmol), CuI (0.019 g, 0.1 mmol), N, N-dimethylformamide (20 mL) were added into a 100 mL flask. The mixture was stirred at 100°C for 2 h. After cooling to room temperature, the mixture was poured into 100 mL water, and extracted with DCM for three times. The organic layer was washed with brine, and then dried over anhydrous Na_2SO_4 . The solution was filtered and concentrated by rotary evaporator. The crude product was purified by column chromatography to give a white solid product. (yield: 50%). 1H NMR (400 MHz, CD_2Cl_2) δ 8.20 (t, $J = 1.0$ Hz, 1H), 8.18 (t, $J = 1.0$ Hz, 1H), 8.17 (d, $J = 1.8$ Hz, 2H), 7.73 – 7.69 (m, 4H), 7.67 – 7.64 (m, 2H), 7.53 (dt, $J = 8.1, 1.0$ Hz, 2H), 7.48 (ddd, $J = 8.2, 6.9, 1.2$ Hz, 2H), 7.36 – 7.31 (m, 2H), 1.47 (s, 18H). ^{13}C NMR (101 MHz, CD_2Cl_2) δ 145.55, 141.20, 138.88, 137.70, 137.41, 134.51, 130.64, 126.98, 126.51, 126.02, 123.85, 120.68, 120.54, 116.18, 110.23, 104.05, 35.03, 31.92. High-resolution mass spectrometry (HRMS) (APCI) m/z : calc for $C_{38}H_{34}N_2Br_2$: 676.1089; found: 676.1093.

3,3',6,6'-Tetra-tert-butyl-9'-(4-(1,8-dibromo-3,6-di-tert-butyl-9H-carbazol-9-yl)phenyl)-9H-9,3':6',9''-tercarbazole (tCzDBr-TCz)

1,8-Dibromo-3,6-di-tert-butyl-9-(4-iodophenyl)-9H-carbazole (0.636 g, 1 mmol), 3,3',6,6'-tetra-tert-butyl-9H-9,3':6',9''-tercarbazole (0.79 g, 1.1 mmol), K_2CO_3 (0.152 g, 1.1 mmol), 1,10 phenanthroline (0.018 g, 0.1 mmol), CuI (0.019 g, 0.1 mmol), N, N-dimethylformamide (20 mL) were added into a 100 mL flask. The mixture was stirred at

100°C for 2 h. After cooling to room temperature, the mixture was poured into 100 mL water, and extracted with DCM for three times. The organic layer was washed with brine, and then dried over anhydrous Na₂SO₄. The solution was filtered and concentrated by rotary evaporator. The crude product was purified by column chromatography to give a white solid product. (yield: 65%). ¹H NMR (400 MHz, CD₂Cl₂) δ 8.33 (d, *J* = 2.0 Hz, 2H), 8.20 (dd, *J* = 4.7, 1.8 Hz, 6H), 7.85 – 7.77 (m, 6H), 7.75 – 7.68 (m, 4H), 7.50 (dd, *J* = 8.7, 1.9 Hz, 4H), 7.43 – 7.33 (m, 4H), 1.49 (s, 18H), 1.48 (s, 36H). ¹³C NMR (101 MHz, CD₂Cl₂) δ 145.68, 143.10, 140.76, 140.54, 138.46, 138.40, 137.46, 134.87, 131.42, 130.70, 127.10, 126.44, 126.11, 124.56, 124.08, 123.48, 119.71, 116.66, 116.26, 111.70, 109.54, 104.09, 35.07, 32.20. High-resolution mass spectrometry (HRMS) (APCI) *m/z*: calc for C₇₈H₈₀N₄Br₂: 1230.4750; found: 1230.4740.

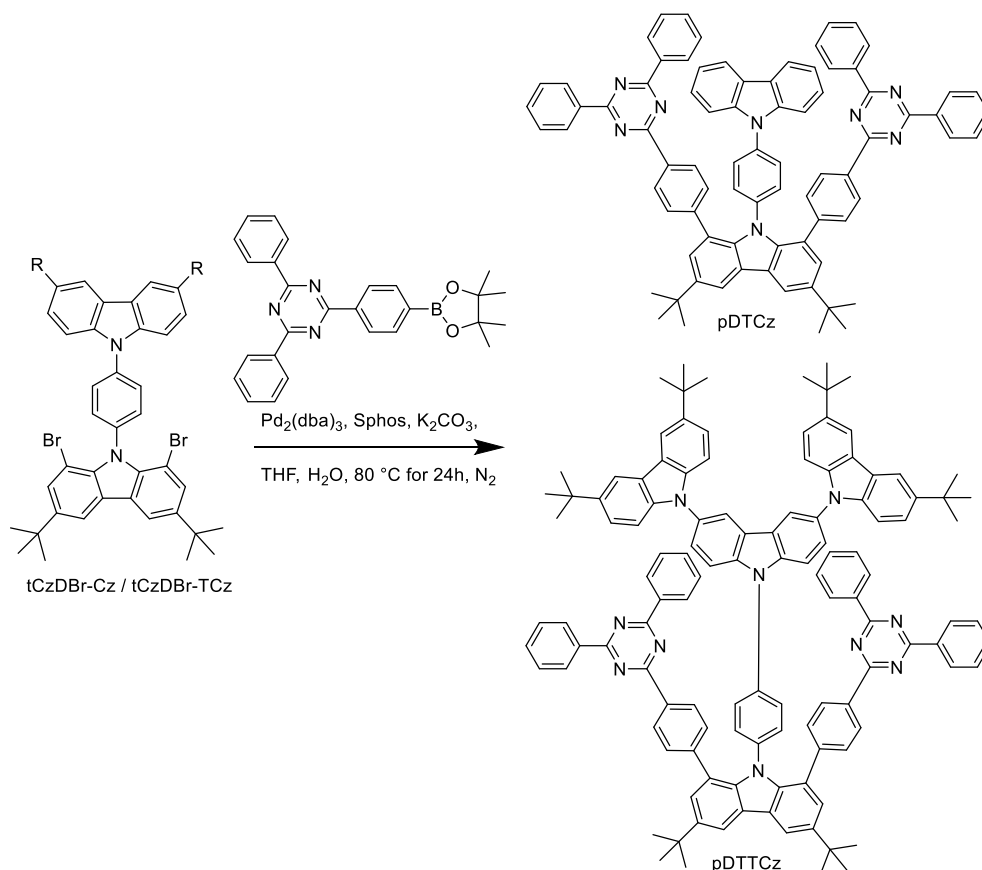


Scheme 3.4 Synthetic route for compound mDTCz.

9-(4-(9H-carbazol-9-yl)phenyl)-3,6-di-tert-butyl-1,8-bis(3-(4,6-diphenyl-1,3,5-triazin-2-yl)phenyl)-9H-carbazole (mDTCz)

A mixture of 9-(4-(9H-carbazol-9-yl)phenyl)-1,8-dibromo-3,6-di-tert-butyl-9H-carbazole (0.20 g, 0.3 mmol) and 2,4-diphenyl-6-(3-(4,4,5,5-tetramethyl-1,3,2-dioxaborolan-2-yl)phenyl)-1,3,5-triazine (0.38 g, 0.88 mmol), Pd₂(dba)₃ (0.004 g, 0.004 mmol), SPhos (0.007 g, 0.017 mmol) and K₂CO₃ (0.1 g, 0.8 mmol) were dissolved in a mixture of THF and water in an argon atmosphere. The mixture was heated to 80 °C and stirred for 24 h. After cooling to room temperature, the mixture was washed with brine and then extracted with DCM. Afterwards, the mixture was dried over anhydrous Na₂SO₄. The solution was filtered and then concentrated by rotary evaporator. The product was purified by column chromatography. (yield: 40%). ¹H NMR (400 MHz, CD₂Cl₂) δ 8.62 – 8.54 (m, 8H), 8.51 –

8.38 (m, 6H), 7.85 (s, 2H), 7.48 (dd, $J = 10.5, 4.4$ Hz, 16H), 7.29 (t, $J = 7.6$ Hz, 2H), 7.23 – 6.80 (m, 9H), 6.65 (s, 1H), 1.58 (s, 18H). ^{13}C NMR (101 MHz, CD_2Cl_2) δ 171.84, 171.63, 143.44, 141.02, 140.25, 138.37, 136.47, 136.39, 135.35, 134.00, 132.80, 131.50, 130.77, 129.17, 129.05, 128.94, 128.22, 127.64, 126.50, 126.02, 125.44, 125.15, 123.42, 120.10, 116.12, 110.30, 35.11, 32.21. High-resolution mass spectrometry (HRMS) (APCI) m/z : calc for $\text{C}_{80}\text{H}_{62}\text{N}_8$: 1134.5097; found: 1134.5133.



Scheme 3.5 Synthetic route for compound pDTCz and pDTTCz.

9-(4-(9H-carbazol-9-yl)phenyl)-3,6-di-tert-butyl-1,8-bis(4-(4,6-diphenyl-1,3,5-triazin-2-yl)phenyl)-9H-carbazole (pDTCz)

A mixture of 9-(4-(9H-carbazol-9-yl)phenyl)-1,8-dibromo-3,6-di-tert-butyl-9H-carbazole (0.20 g, 0.3 mmol) and 2,4-diphenyl-6-(4-(4,4,5,5-tetramethyl-1,3,2-dioxaborolan-2-yl)phenyl)-1,3,5-triazine (0.38 g, 0.88 mmol), $\text{Pd}_2(\text{dba})_3$ (0.004 g, 0.004 mmol), SPhos (0.007 g, 0.017 mmol) and K_2CO_3 (0.1 g, 0.8 mmol) were dissolved in a mixture of THF and water in an argon atmosphere. The mixture was heated to 80 °C and stirred for 24 h. After cooling to room temperature, the mixture was washed with brine and then extracted with

DCM. Afterwards, the mixture was dried over anhydrous Na_2SO_4 . The solution was filtered and then concentrated by rotary evaporator. The product was purified by column chromatography. (yield: 44%). ^1H NMR (700 MHz, CD_2Cl_2) δ 8.62 – 8.55 (m, 8H), 8.54 – 8.49 (m, 4H), 8.37 (d, $J = 2.0$ Hz, 2H), 7.63 – 7.54 (m, 6H), 7.49 (t, $J = 7.7$ Hz, 8H), 7.41 (d, $J = 2.0$ Hz, 2H), 7.38 – 7.33 (m, 4H), 7.10 – 7.04 (m, 2H), 7.00 – 6.90 (m, 4H), 6.67 (tt, $J = 7.6$, 3.7 Hz, 4H), 1.56 (s, 18H). ^{13}C NMR (176 MHz, CD_2Cl_2) δ 171.85, 145.26, 143.60, 140.22, 138.99, 138.74, 136.78, 136.60, 134.63, 132.74, 131.60, 130.56, 129.18, 128.90, 128.23, 127.95, 126.54, 125.85, 125.81, 125.37, 123.41, 119.90, 119.86, 116.29, 109.82, 35.09, 32.17. High-resolution mass spectrometry (HRMS) (APCI) m/z : calc for $\text{C}_{80}\text{H}_{62}\text{N}_8$: 1134.5097; found: 1134.5101.

3,3'',6,6''-Tetra-tert-butyl-9'-(4-(3,6-di-tert-butyl-1,8-bis(4-(4,6-diphenyl-1,3,5-triazin-2-yl)phenyl)-9H-carbazol-9-yl)phenyl)-9'H-9,3':6',9''-tercarbazole (pDTTCz)

A mixture of 3,3'',6,6''-tetra-tert-butyl-9'-(4-(1,8-dibromo-3,6-di-tert-butyl-9H-carbazol-9-yl)phenyl)-9'H-9,3':6',9''-tercarbazole (0.20 g, 0.16 mmol) and 2,4-diphenyl-6-(4-(4,4,5,5-tetramethyl-1,3,2-dioxaborolan-2-yl)phenyl)-1,3,5-triazine (0.38 g, 0.88 mmol), $\text{Pd}_2(\text{dba})_3$ (0.004 g, 0.004 mmol), SPhos (0.007 g, 0.017 mmol) and K_2CO_3 (0.1 g, 0.8 mmol) were dissolved in a mixture of THF and water in an argon atmosphere. The mixture was heated to 80 °C and stirred for 24 h. After cooling to room temperature, the mixture was washed with brine and then extracted with DCM. Afterwards, the mixture was dried over anhydrous Na_2SO_4 . The solution was filtered and then concentrated by rotary evaporator. The product was purified by column chromatography. (yield: 40%). ^1H NMR (400 MHz, CD_2Cl_2) δ 8.59 – 8.54 (m, 4H), 8.40 (d, $J = 2.0$ Hz, 2H), 8.23 – 8.19 (m, 8H), 8.09 (d, $J = 1.9$ Hz, 4H), 7.69 (d, $J = 2.0$ Hz, 2H), 7.44 (d, $J = 2.0$ Hz, 2H), 7.43 – 7.38 (m, 4H), 7.30 – 7.22 (m, 10H), 7.20 – 7.13 (m, 12H), 6.87 (d, $J = 6.6$ Hz, 2H), 6.78 (d, $J = 8.6$ Hz, 4H), 1.57 (s, 18H), 1.51 (s, 36H). ^{13}C NMR (101 MHz, CD_2Cl_2) δ 171.75, 171.43, 145.19, 143.52, 142.52, 140.09, 139.54, 139.22, 137.89, 136.40, 135.94, 134.72, 132.43, 131.88, 130.65, 128.80, 128.50, 128.16, 128.13, 126.19, 125.79, 125.69, 125.16, 124.01, 123.61, 123.35, 118.87, 116.35, 116.31, 111.17, 109.16, 35.00, 32.30. High-resolution mass spectrometry (HRMS) (APCI) m/z : calc for $\text{C}_{120}\text{H}_{108}\text{N}_{10}$: 1688.8758; found: 1688.8810.

Table 3.6 Crystal data and structure refinement for mDTCz, pDTCz, and pDTTCz.

	mDTCz	pDTCz	pDTTCz
Empirical formula	C ₈₃ H ₆₉ N ₈	C ₈₄ H ₇₀ N ₈ O	C ₁₂₀ H ₁₀₈ N ₁₀
Moiety formula	C ₈₀ H ₆₂ N ₈ , 0.5(C ₆ H ₁₄)	C ₈₀ H ₆₂ N ₈ , C ₄ H ₈ O	C ₁₂₀ H ₁₀₈ N ₁₀
CCDC number	2292707	2292708	2292709
Formula weight/ g/mol	1178.46	1207.48	1690.16
Temperature	120(2) K	120(2) K	120(2) K
Crystal system	Triclinic	Triclinic	Monoclinic
Space group name, number	P -1, (2)	P -1, (2)	P 2/n, (13)
a/ Å	11.6508(10)	10.0988(6)	16.2365(9)
b/ Å	14.8031(12)	17.0001(9)	16.0969(9)
c/ Å	19.2535(15)	19.2783(12)	44.636(2)
α/°	90.388(6)	101.252(5)	90
β/°	105.988(6)	93.279(5)	97.285(4)
γ/°	95.481(6)	97.677(5)	90
Volume/ Å ³	3175.7(5)	3205.2(3)	11571.7(11)
Density (calculated)/ mg/m ³	1.232	1.251	0.970
Absorption coefficient/ mm ⁻¹	0.560	0.075	0.435
Crystal size / mm ³	0.050 x 0.060 x 0.430	0.080 x 0.100 x 1.300	0.020 x 0.060 x 0.240
Wavelength, radiation type	1.54178Å, CuKα	0.71073 Å, MoKα	1.54178Å, CuKα
Theta range for data collection	2.388 to 67.991°	2.470 to 28.156°	2.745 to 67.990°
Index ranges	-12<=h<=13 -17<=h<=17 -23<=h<=22	-13<=h<=13 -22<=h<=18 -25<=h<=25	-19<=h<=19 -18<=h<=19 -49<=h<=44
Reflections collected	45317	32694	85355
Independent reflections	10910 [R(int) = 0.1899]	15480 [R(int) = 0.1129]	19987 [R(int) = 0.4244]
Goodness-of-fit on F ²	0.831	1.127	0.733
R ₁ , wR ₂ [I>2σ(I)]	0.0792, 0.1778	0.0909, 0.1953	0.0971, 0.2124
R ₁ , wR ₂ [all data]	0.1903, 0.2199	0.1509, 0.2336	0.3866, 0.3127
Largest diff. peak and hole/ eÅ ⁻³	0.362 and -0.318	0.417 and -0.374	0.472 and -0.220

3.9 References

1. Feng, H.-T. *et al.* Tuning molecular emission of organic emitters from fluorescence to phosphorescence through push-pull electronic effects. *Nat. Commun.* **11**, 2617 (2020).
2. Chen, C. *et al.* Carbazole isomers induce ultralong organic phosphorescence. *Nat. Mater.* **20**, 175–180 (2021).
3. Zhao, W. *et al.* Boosting the efficiency of organic persistent room-temperature phosphorescence by intramolecular triplet-triplet energy transfer. *Nat. Commun.* **10**, 1595 (2019).
4. He, Z. *et al.* White light emission from a single organic molecule with dual phosphorescence at room temperature. *Nat. Commun.* **8**, 1–7 (2017).
5. An, Z. *et al.* Stabilizing triplet excited states for ultralong organic phosphorescence. *Nat. Mater.* **14**, 685–690 (2015).
6. Li, D. *et al.* Amorphous metal-free room-temperature phosphorescent small molecules with multicolor photoluminescence via a host-guest and dual-emission strategy. *J. Am. Chem. Soc.* **140**, 1916–1923 (2018).
7. Zhang, Z. Y. & Liu, Y. Ultralong room-temperature phosphorescence of a solid-state supramolecule between phenylmethylpyridinium and cucurbit[6]uril. *Chem. Sci.* **10**, 7773–7778 (2019).
8. Wu, H. *et al.* Achieving Amorphous Ultralong Room Temperature Phosphorescence by Coassembling Planar Small Organic Molecules with Polyvinyl Alcohol. *Adv. Funct. Mater.* **29**, 1807243 (2019).
9. Kuila, S., Garain, S., Bandi, S. & George, S. J. All-Organic, Temporally Pure White Afterglow in Amorphous Films Using Complementary Blue and Greenish-Yellow Ultralong Room Temperature Phosphors. *Adv. Funct. Mater.* **30**, 2003693 (2020).
10. Weng, T. *et al.* A Fluorescence–Phosphorescence–Phosphorescence Triple-Channel Emission Strategy for Full-Color Luminescence. *Small* **16**, 1906475 (2020).
11. Shu, H. *et al.* Persistent room temperature phosphorescence films based on star-shaped organic emitters. *J. Mater. Chem. C* **10**, 1833–1838 (2022).
12. Yu, J. *et al.* Purely Organic Room-Temperature Phosphorescence Endowing Fast Intersystem Crossing from Through-Space Spin-Orbit Coupling. *JACS Au* **1**, 1694–1699 (2021).
13. Lv, X. *et al.* Regulating the photophysical properties of highly twisted TADF emitters by concurrent through-space/-bond charge transfer. *Chem. Eng. J.* **402**, 126173 (2020).
14. Jiang, C. *et al.* Acceptor-Donor-Acceptor π -Stacking Boosts Intramolecular Through-Space Charge Transfer towards Efficient Red TADF and High-Performance OLEDs. *Research* **2022**, 2639-5274 (2022).
15. Wang, X. *et al.* Multi-Layer π -Stacked Molecules as Efficient Thermally Activated

- Delayed Fluorescence Emitters. *Angew. Chemie* **133**, 5273–5279 (2021).
16. Li, Y. *et al.* Reduced Intrinsic Non-Radiative Losses Allow Room-Temperature Triplet Emission from Purely Organic Emitters. *Adv. Mater.* **33**, 2101844 (2021).
 17. Scholz, R. *et al.* Investigation of Thermally Activated Delayed Fluorescence from a Donor-Acceptor Compound with Time-Resolved Fluorescence and Density Functional Theory Applying an Optimally Tuned Range-Separated Hybrid Functional. *J. Phys. Chem. A* **124**, 1535–1553 (2020).
 18. Tang, X. *et al.* Highly efficient luminescence from space-confined charge-transfer emitters. *Nat. Mater.* **19**, 1332–1338 (2020).

Chapter 4. Cleverly designed molecules influence molecular stacking to eliminate charge carrier trapping

4.1 Introduction

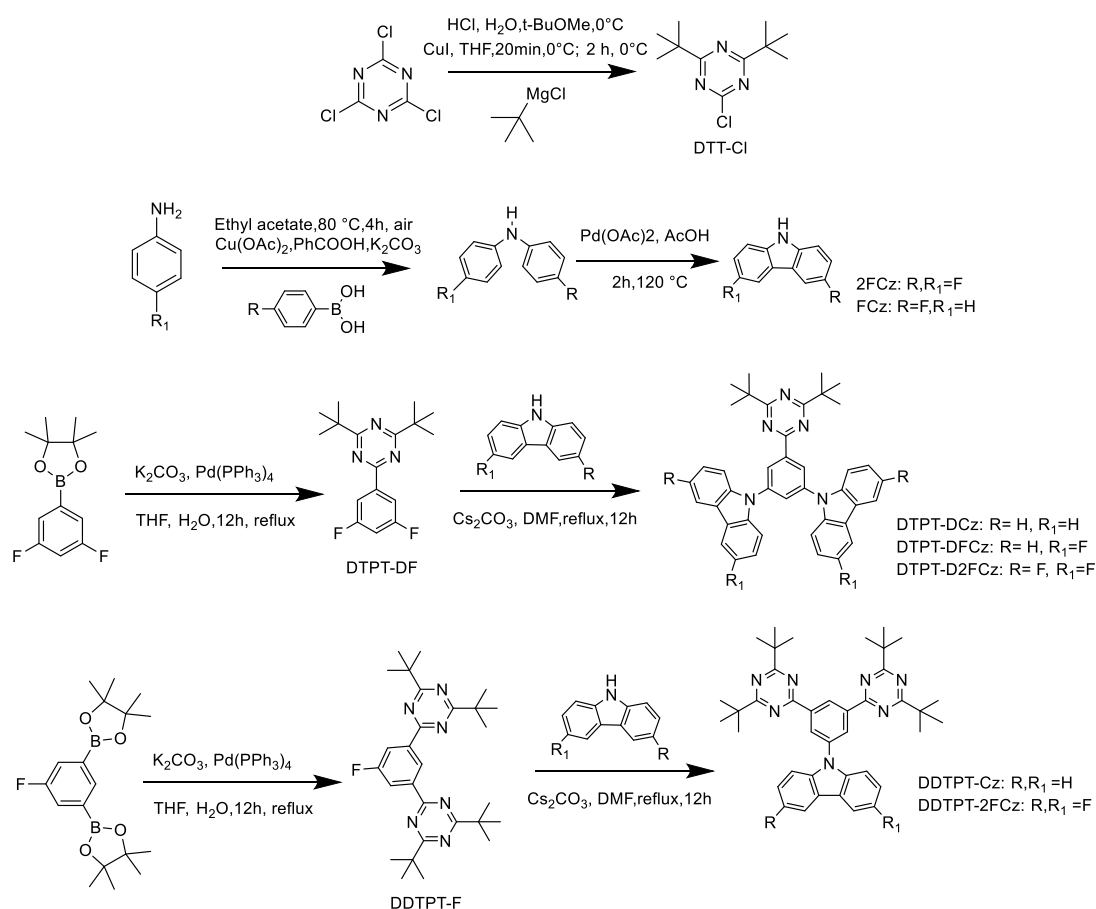
Over the last few decades, the unique advantages of organic light-emitting diodes (OLEDs) in flat panel displays and solid state lighting have attracted increasing attention.^{1,2} In the early stages of OLED development, scientists' attention has been focused on optimizing device structures and improving device efficiency. While the external quantum efficiency (EQE) of devices in green and red, now exceeds 30%.³⁻⁵ But achieving efficient and stable blue OLED devices remains a challenge. There are two fundamental reasons that limit the development of blue OLEDs. The first is the stability of the material itself, which causes OLED devices to deteriorate and have a short device lifetime. The second reason is the low carrier mobility or, even for high mobility materials, the presence of impurities trapping the charge carriers, resulting in a device in which only some of the injected carriers contribute to the charge transport. This in turn leads to an unbalanced transport of electrons and holes in the device.^{4,5}

Recently Blom et al. discovered an energy window in which trap-free bipolar charge transport can be achieved when the electron affinity (EA) of the organic material is above 3.6 eV and the ionization energy (IE) is below 6.0 eV.⁶ This means that hole and electron transport is approximately in equilibrium. Trap-free bipolar charge transport is a prerequisite for achieving efficient devices.^{7,8} But for blue emitters with a band gap larger than 2.4 eV, the possibility of achieving intrinsically trap-free transport of electrons and holes remains a challenge.⁹

In this chapter, we report the design and synthesis of five D-A type blue TADF emitters based on carbazole donors and tert-butyltriazine acceptors, 9,9'-(5-(4,6-di-tert-butyl-1,3,5-triazin-2-yl)-1,3-phenylene)bis(3-fluoro-9H-carbazole)--9,9'-(5-(4,6-di-tert-butyl-1,3,5-triazin-2-yl)1,3-phenylene)bis(9H-carbazole) (DTPT-DCz), 9,9'-(5-(4,6-di-tert-butyl-1,3,5-triazin-2-yl)-1,3-phenylene)bis(3-fluoro-9H-carbazole)--9,9'-(5-(4,6-di-tert-butyl-1,3,5-triazin-2-yl)-1,3-phenylene)bis(9H-carbazole) (DTPT-DFCz), 9,9'-(5-(4,6-di-tert-butyl-1,3,5-triazin-2-yl)-1,3-phenylene)bis(3,6-difluoro-9H-carbazole)--9-(3,5-bis(4,6-di-tert-butyl-1,3,5-triazin-2-yl)phenyl)-3,6-difluoro-9H-carbazole--9-(3,5-bis(4,6-di-tert-butyl-1,3,5-triazin-2-yl)phenyl)

-9H-carbazole (DTPT-D2FCz), 9-(3,5-bis(4,6-di-tert-butyl-1,3,5-triazin-2-yl)phenyl)-9H-carbazole (DDTPT-Cz), and 9-(3,5-bis(4,6-di-tert-butyl-1,3,5-triazin-2-yl)phenyl)-3,6-difluoro-9H-carbazole (DDTPT-2FCz). (**Scheme 4.1**), and their electron transport properties. Through the molecular design, the HOMO of the molecule is localized on the carbazole part, allowing the IE of the molecule to be located within the trap-free window. However, due to the wide band gap, the LUMO is located on the triazine entities and the EA is outside the trap-free window, and therefore electron trapping is expected to occur. For a molecule with one acceptor and two donors, reducing the number of fluorine atoms on the carbazole from two to none alters the stacking and arrangement of the molecules, resulting in an increase in electron current density by several orders of magnitude and much lower trapping of the electron transport device for the non-fluorinated carbazol. In contrast, for molecules consisting of one donor and two acceptors the absence or presence of fluorine atoms does not significantly change the electron current density.

4.2 Synthesis



Scheme 4.1 Synthetic routes for DTPT-DCz, DTPT-DFCz, DTPT-D2FCz, DDTPT-Cz and DDTPT-2FCz.

The synthesis of these five compounds is described in **Scheme 4.1**. 2-Chloro-4,6-di-tert-butyl-1,3,5-triazine (DTTCl) is obtained by the reaction of cyanuric chloride and Grignard's reagent. Fluorinated carbazoles are obtained by a two-step reaction. Firstly the coupling of aniline and phenylboronic acid gives the corresponding diphenylamine compounds, which can be used directly without purification, and the second step is a ring-closing reaction to give 3-fluorocarbazole (FCz) and 3,6-difluorocarbazole (2FCz). Both acceptors 2,4-di-tert-butyl-6-(3,5-difluorophenyl)-1,3,5-triazine (DTPT-DF) and 6,6'-(5-fluoro-1,3-phenylene)bis(2,4-di-tert-butyl-1,3,5-triazine) (DDTPT-F) were obtained by DTT-Cl and 2-(3,5-difluorophenyl)-4,4,5,5-tetramethyl-1,3,2-dioxaborolane / 2,2'-(5-fluoro-1,3-phenylene)bis(4,4,5,5-tetramethyl-1,3,2-dioxaborolane) by Suzuki reaction, respectively. DTPT-DCz, DTPT-DFCz, and DTPT-D2FCz were obtained by nucleophilic reaction between DTPT-DF and CZ/FCz/2FCz. DDTPT-Cz and DDTPT-2FCz were obtained by nucleophilic reaction between DTPT-DF and CZ/2FCz.

4.3 Optical properties

UV-vis-NIR absorption spectra of DTPT-DCz, DTPT-DFCz, DTPT-D2FCz, DDTPT-Cz and DDTPT-2FCz were recorded in toluene solutions (**Figure 4.1a**). The relevant data are summarized in **Table 4.1**. The region of 230-300 nm may be attributed to the n- π^* transitions of the molecules.^{10,11} The weak absorption bands in the range of 320–360 nm are ascribed to the intramolecular charge transfer (ICT) transition from the carbazole unit to the triazine unit. The optical gap (E_g) of the five molecules is close to 3.1 eV. The effect of solvent polarity on the emission of the five materials was systematically investigated as shown in **Figure 4.1b-f**. From room temperature photoluminescence, all materials show a dependence on solvent polarity, indicating that the emission is CT-state emission from D-A charge transfer. In the neat films, the DTPT-D2FCz and DDTPT-2FCz emission exhibit a blue shift compared to the other molecules, due to the weak electron-donating ability of the fluorinated carbazole.

Table 3.1 Photophysical properties of DTPT-DCz, DTPT-DFCz, DTPT-D2FCz, DDTPT-Cz and DDTPT-2FCz.

Sample	$\lambda_{\text{Abs.}}$ (nm) ^a	λ_{PL} (nm) ^b	λ_{PL} (nm) ^a	λ_{PL} (nm) ^c	λ_{PL} (nm) ^d	λ_{PL} (nm) ^e
DTPT-DCz	324/338	392/411	425	452	489	443
DTPT-DFCz	333/347	392/410	426	446	490	440
DTPT-D2FCz	341/356	391/410	426	447	490	433
DDTPT-Cz	324/338	394/414	430	450	491	443
DDTPT-2FCz	340/356	393/411	430	446	490	425

^a In toluene. ^b In cyclohexane. ^c In DCM. ^d In DMF. ^e In neat film.

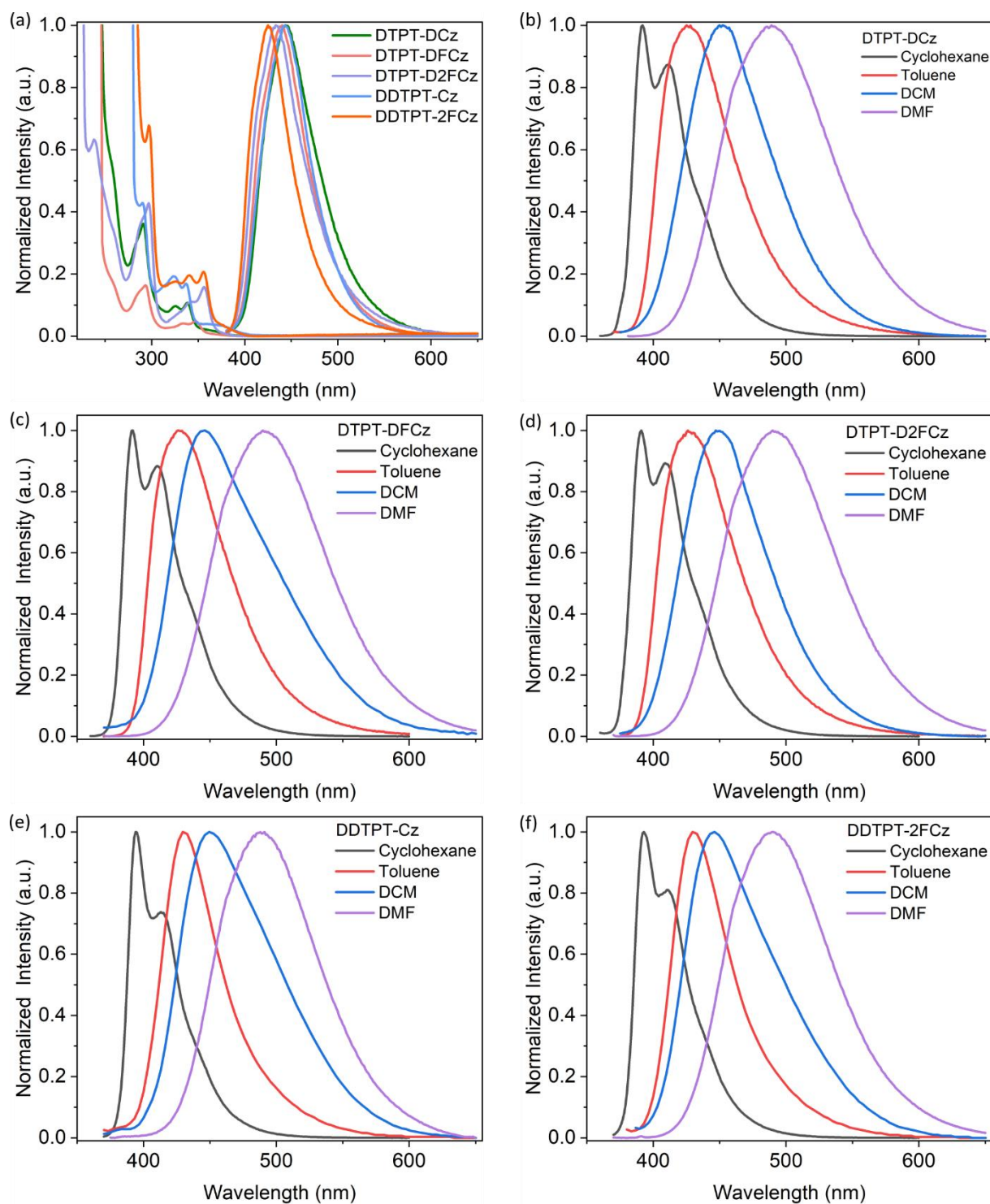


Figure 4.1 (a) UV-visible absorption spectra in toluene and steady-state PL spectra in neat film. Steady-state PL spectra in different solvents. (b) DTPT-DCz, (c) DTPT-DFCz, (d) DTPT-D2FCz, (e) DDTPT-Cz, and (f) DDTPT-2FCz.

4.4 Electrochemical properties

The electrochemical behaviour of the five compounds was determined by cyclic voltammetry (CV) as shown in **Figure 4.2a**. The corresponding data are collected in **Table 4.2**. The oxidation and reduction peaks relative to ferrocene correspond to carbazole (donor) and triazine (acceptor), respectively. Scanning to positive potentials, for three molecules containing two carbazoles the oxidation potential of DTPT-D2FCz was 1.02 eV, which was upshifted in potential by 0.33 eV and 0.08 eV compared to DTPT-DFCz and DTPT-DCz, respectively. For two molecules containing one carbazole, the oxidation potential of DDTPT-2FCz was 1.01 eV, which was shifted by 0.11 eV compared to DDTPT-Cz. In addition, the reduction potentials of all molecules containing fluorinated carbazole were upshifted compared to non-fluorinated carbazole. This is due to the low electron donating ability of fluorinated carbazole compared to carbazole, which pulls down the HOMO and LUMO of the molecules. The density functional theory (DFT) with B3LYP functional using the basis set 6-31G calculation proves it. Therefore, in summary, the HOMO levels of DTPT-DCz, DTPT-DFCz, DTPT-D2FCz, DDTPT-Cz, and DDTPT-2FCz were calculated as -5.49, -5.74, -5.82 eV, -5.70 eV, and -5.81 eV, respectively. The LUMO levels are -2.61, -2.77, -2.81, -2.74, and -2.81 eV, respectively. We obtained the ionization energies (IE) of the five compounds by ultraviolet photoelectron spectroscopy (UPS) (This was in collaboration with Sylwia Adamczyk, University of Wuppertal) which decreases with the increasing number of fluorine atoms, but also within the trap-free window,⁶ shown in **Figure 4.2b-f**. The corresponding data are collected in **Table 4.2**. The values of electron affinity (EA) for five molecules through IE and E_g are 2.82, 3.02, 2.88, 2.85, and 3.0 eV, respectively. EA is below the value of 3.6 eV, which indicates that they should be is trap-limited in electron transport.⁶

Table 4.2 Electrochemical properties of DTPT-DCz, DTPT-DFCz, DTPT-D2FCz, DDTPT-Cz, and DDTPT-2FCz.

Sample	$E_{ox}(V)^a$	$E_{red}(V)^a$	HOMO (eV) ^a	LUMO (eV) ^a	E_g (eV) ^b	IE (eV) ^c
DTPT-DCz	0.69	-2.19	-5.49	-2.61	2.88	5.70
DTPT-DFCz	0.94	-2.03	-5.74	-2.77	2.97	5.79
DTPT-D2FCz	1.02	-1.99	-5.82	-2.81	3.01	5.89
DDTPT-Cz	0.90	-2.06	-5.70	-2.74	2.96	5.81
DDTPT-2FCz	1.01	-1.99	-5.81	-2.81	3.0	6.0

^a HOMO and LUMO were estimated from the onsets of the first oxidation and reduction peaks, while the potentials were determined using ferrocene (Fc) as standard by empirical formulas $E_{HOMO/LUMO} = -$

($E_{\text{Ox/Red}}^{\text{onset}} + 4.8$) eV. ^b The E_g value : E_g (eV) = HOMO-LUMO. ^c Experimental ionization energy (IE) from ultraviolet photoelectron spectroscopy (UPS).

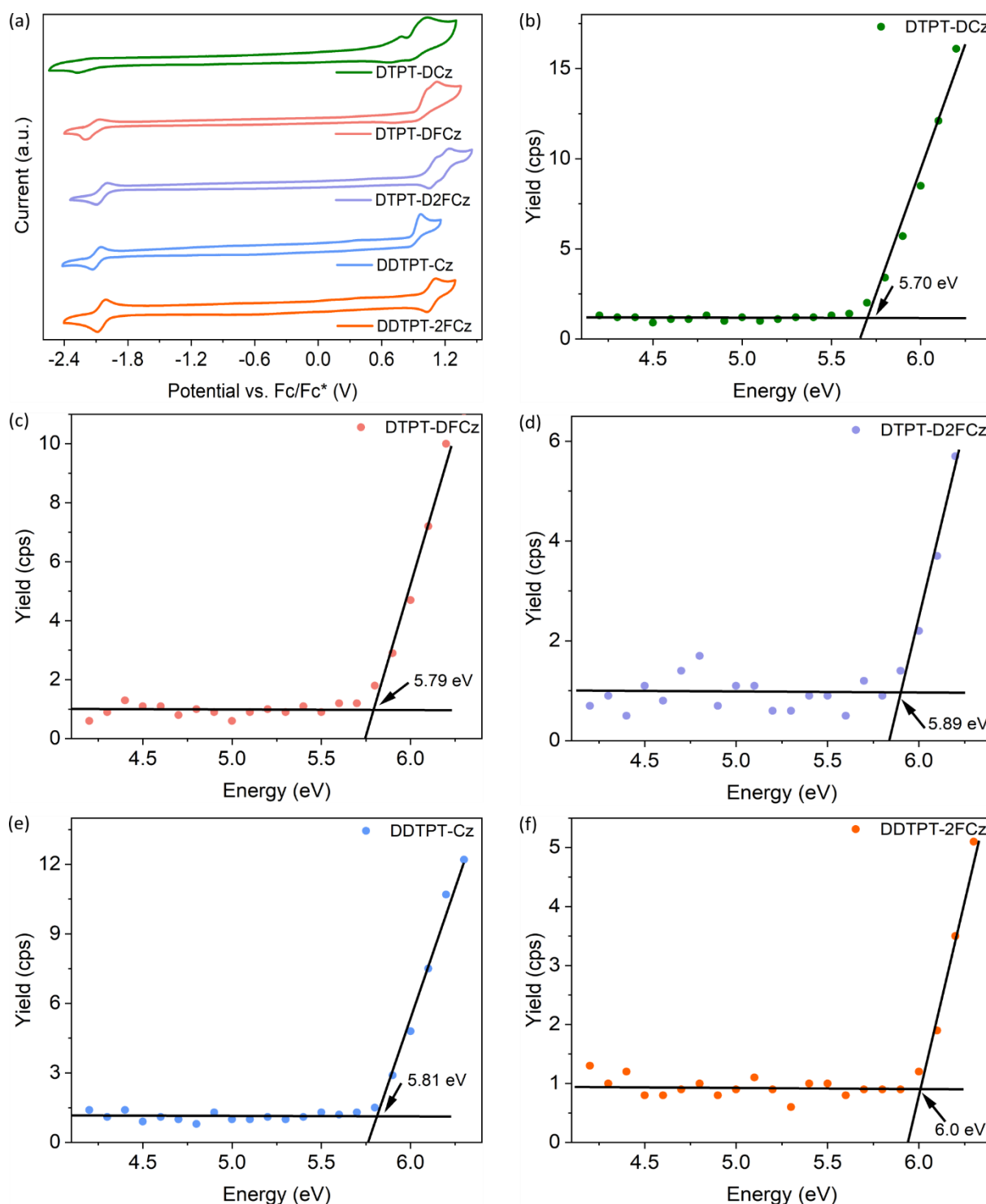


Figure 4.2 (a) Cyclic voltammograms curves of DTPT-DCz, DTPT-DFCz, DTPT-D2FCz, DDTPT-Cz, and DDTPT-2FCz in CH₃CN solutions of n-Bu₄NPF₆ (0.05 M) with a scan rate of 100 mV s⁻¹ at

room temperature under nitrogen. Photoemission yield spectroscopy in air. (b) DTPT-DCz, (c) DTPT-DFCz, (d) DTPT-D2FCz, (e) DDTPT-Cz, and (f) DDTPT-2FCz.

4.5 Density functional theory (DFT) calculations

To further understand the electronic structures and optical properties of the five compounds, density functional theory (DFT) calculations were carried out. The corresponding data are collected in **Table 4.3**. In agreement with the CV results, the HOMO and LUMO energies of the molecule decreased as the number of fluorine atoms increased. The HOMO/LUMO values of the five acceptors of DTPT-DCz, DTPT-DFCz, DTPT-D2FCz, DDTPT-Cz and DDTPT-2FCz are -5.47/-2.16 eV, -5.66/-2.31 eV, -5.85/-2.47 eV, -5.39/-2.18 eV, and -5.64/-2.34 eV, respectively.

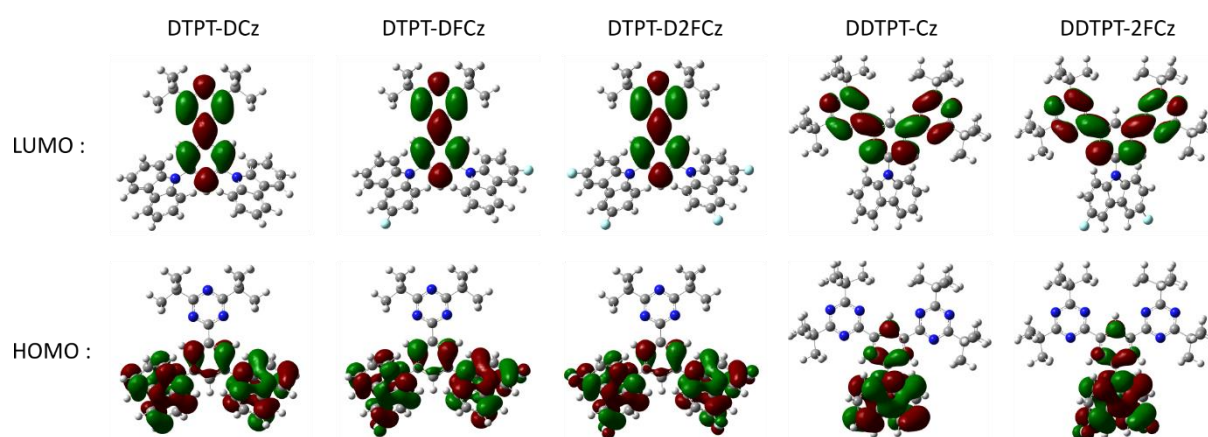


Figure 4.3 HOMO and LUMO distributions DTPT-DCz, DTPT-DFCz, DTPT-D2FCz, DDTPT-Cz and DDTPT-2FCz. DFT (B3LYP, 6-31G).

Table 4.3 The HOMO and LUMO levels of DTPT-DCz, DTPT-DFCz, DTPT-D2FCz, DDTPT-Cz and DDTPT-2FCz. Calculations were carried out at the DFT/TD-DFT//B3LYP/6-31G level.

Sample	HOMO (eV)	LUMO (eV)	E_g (eV)	S_1 (eV)	T_1 (eV)	ΔE_{ST} (eV)
DTPT-DCz	-5.47	-2.16	3.31	2.80	2.63	0.17
DTPT-DFCz	-5.66	-2.31	3.35	2.88	2.71	0.17
DTPT-D2FCz	-5.85	-2.47	3.38	2.85	2.69	0.16
DDTPT-Cz	-5.39	-2.18	3.21	2.71	2.55	0.16
DDTPT-2FCz	-5.64	-2.34	3.3	2.73	2.58	0.15

The electronic density distributions of the LUMO and HOMO of the five compounds were derived from DFT analysis as shown in **Figure 4.3**. The LUMO of the five materials is localized on the triazine group and the central benzene ring, while the HOMO is mainly distributed on the carbazole, a small amount of HOMO is distributed on the central benzene

ring. A small overlap between the HOMO and LUMO ensures that the ΔE_{ST} is less than 0.2 eV.

4.6 Crystal structure analysis

To investigate the molecular ordering of the DTPT-DCz, DTPT-DFCz, and DTPT-D2FCz, we used x-ray diffraction (XRD) of suitable crystals grown from dichloromethane and methanol. The corresponding data are collected in **Table 4.5-6**. As shown in **Figure 4.4**, the three molecules have hydrogen bonds (2.45-2.55 Å) between the triazine ring and the central benzene ring. DTPT-DCz and DTPT-DFCz crystallizes in a triclinic crystal system with space group P1, all containing two molecules in the crystal unit. For DTPT-DFCz, two molecules in a cell have a large spatial distance of about 7.13-7.14 Å (**Figure 4.4d**). Due to the repulsive effect of fluorine atoms, a big cavity can be seen in the center of the cell unit. Moreover, the carbazole units were distributed in a 50:50 antiparallel distribution. The torsion angles between the central phenyl ring and carbazole units are 53° and 48° (**Figure 4.4c**). The central phenyl ring and the triazine ring have a torsion angle of 13°. In contrast, DTPT-DCz does not have fluorine atoms, and there are no large cavities in the crystalline units, which are more closely arranged. The closest distance between two mutually parallel carbazoles is 2.61 Å (**Figure 4.4b**). The carbazole unit is spatially closer to the triazine, with the closest distance of 3.04 Å. The torsion angles between the central phenyl ring and the carbazole moieties are 77° and 51°, respectively, and are slightly larger than the same angles in DTPT-DFCz and DTPT-D2FCz. The central phenyl ring and the triazine ring have a torsion angle of 2° (**Figure 4.4a**), which means an almost planar arrangement of the two fragments. XRD analysis revealed the space group for DTPT-D2FCz to be P 21/c (monoclinic), with no co-crystallized solvent molecules. For one molecule, the torsion angles between the central benzene ring and the carbazole unit were determined to be 63° and 43° (**Figure 4.4e**). The torsion angle between the central benzene ring and the triazine ring was 20°.

As shown in **Figure 4.f**, the unit cells contains four molecules with two carbazoles of two adjacent molecules stacked arrangement in a 180° offset. At the same time there are intermolecular π - π interactions between the two carbazoles, the closest distance of F atoms is 5.39 Å, which results in weaker dipolar interactions. But the second carbazole of a molecule is different, the second carbazole ring of a molecule interacts with only one benzene unit with its nearest neighbor. The second benzene unit of the same carbazole ring is not involved in

stacking. From the molecular crystal information, we found that the molecules in compound DTPT-DCz are densely packed and for DTPT-D2FCz, the distance between the intermolecular triazine rings is larger (**Figure 4.4f**).

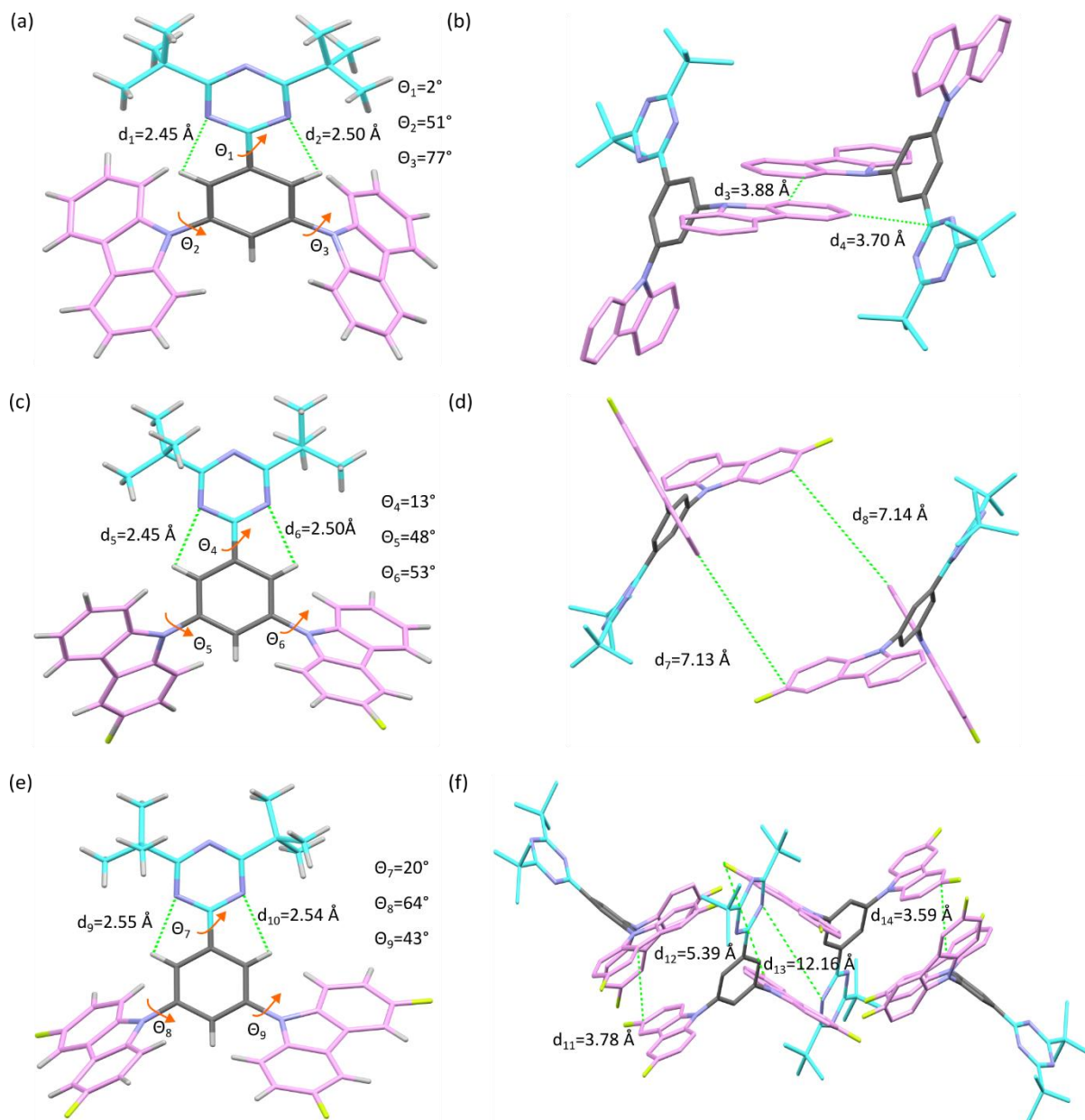


Figure 4.4 Intramolecular interactions in the single crystal. (a) DTPT-DCz, (c) DTPT-DFCz, and (e) DTPT-D2FCz. Molecular packing behavior in a unit cell. (b) DTPT-DCz, (d) DTPT-DFCz, and (f) DTPT-D2FCz.

As in the previous three molecules, hydrogen bonds (2.45-2.55 Å) are present between the triazine ring and the central benzene ring in molecules DDTPT-Cz and DDTPT-2FCz (**Figure 4.5a** and c). DDTPT-Cz, crystallized in a triclinic crystal system with space group P1,

containing four molecules in the unit cell, shows a disordered arrangement and a large intermolecular space distance of 3.59 Å (**Figure 4.5b**). The central benzene and carbazole rings of DDTPT-Cz and DDTPT-2FCz have torsion angles of 46° and 37°, respectively. The difference is that for DDTPT-2FCz, the space group of DDTPT-2FCz is P 21/c (orthorhombic). Although the crystal unit also contains four molecules, the molecules show an ordered arrangement due to the presence of fluorine atoms. For two adjacent molecules, there are intermolecular interactions between the carbazole group of one molecule and the triazine of the other (**Figure 4.5d**). These result in a smaller torsion angle for the central benzene and triazine rings of molecule DDTPT-2FCz than for molecule DDTPT-Cz.

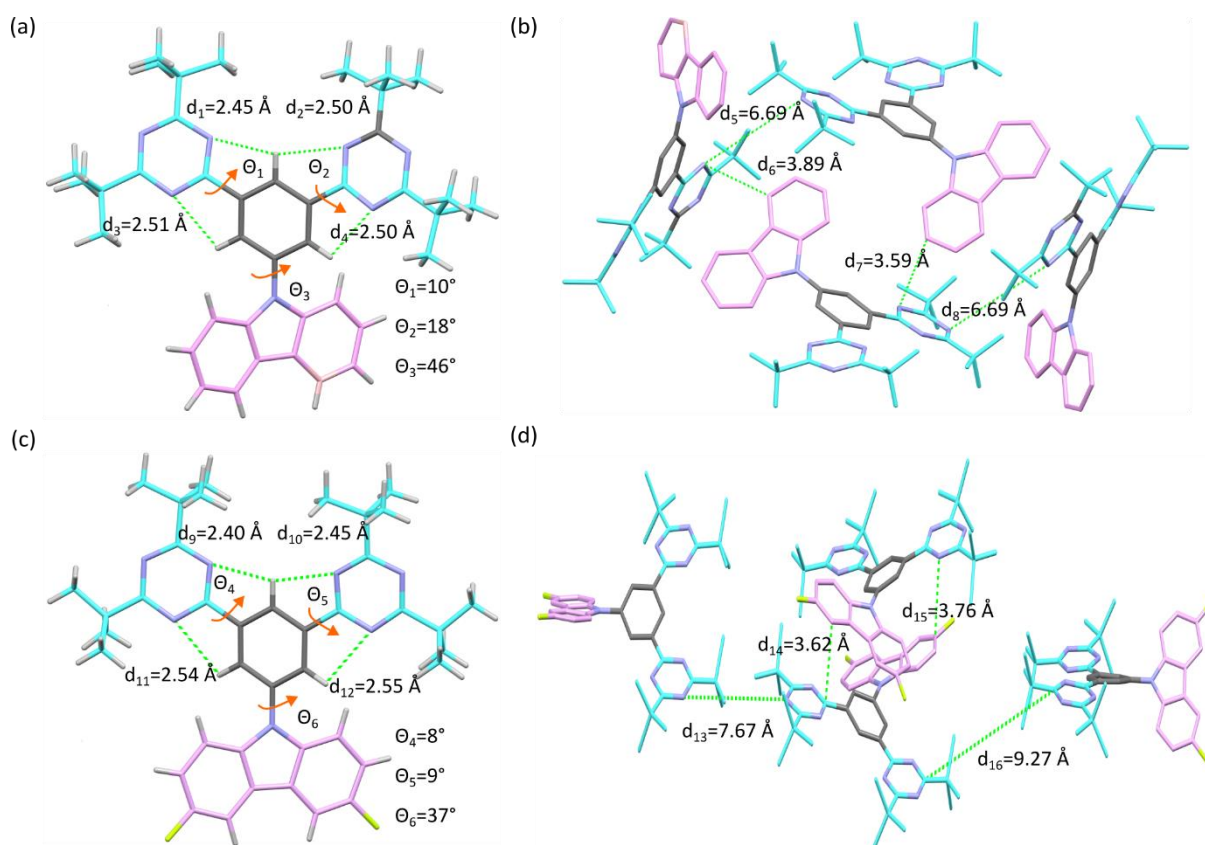


Figure 4.5. Intramolecular interactions in the single crystal. (a) DDTPT-Cz, (c) DDTPT-2FCz. Molecular packing behavior in a unit cell. (b) DDTPT-Cz, (d) DDTPT-2FCz.

4.7 Electron transport

To study the electron transport of the emitters, we prepared electron-only (EO) devices using the emitters placed between two low work function electrodes. The device structure is: Al/ active layer/ 2,2',2''-(1,3,5-Benzinetriyl)-tris(1-phenyl-1-H-benzimidazole) (TPBi) (4

nm)/Ba/Al. This was in collaboration with Xiao Tan (Max Planck Institute for Polymer Research, Mainz). As shown in **Figure 4.6a**, the thickness of the studied emitter in the device is ~100 nm. Interestingly, for the three molecules with one acceptor and two donors (DTPT-DCz, DTPT-DFCz, and DTPT-D2FCz), the measured J-V curves show that the electron current density varies by 4-5 orders of magnitude in the range 0-7 V, depending on the number of fluorine atoms on the carbazole.

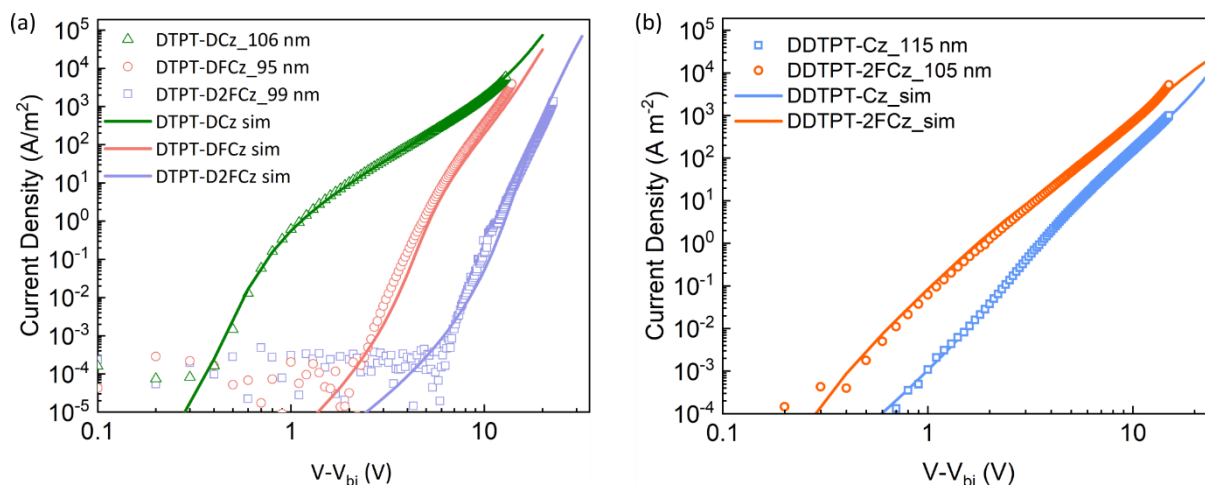


Figure 4.6 Experimental (symbols) and simulated (lines) current density (J)-voltage (V) characteristics. (a) DTPT-DCz, DTPT-DFCz, and DTPT-D2FCz. (b) DDTPT-Cz and DDTPT-2FCz.

It is worth considering that the devices with DTPT-DCz as the semiconductor still exhibit trap-free space charge-limited electron transport despite the LUMO energy of the three materials being outside the trap-free window.¹³ The other two (DTPT-DFCz, and DTPT-D2FCz) exhibit the opposite trend. Obviously, all three material acceptors are the same, while electron transport takes place through the triazine unit, so the electron current density somehow is influenced by the donor part. However, the introduction of fluorine atoms reduces the electron-donating ability of carbazole, and more fluorine atoms lead to a deeper HOMO and LUMO level of the molecule, which is closer to the trap-free window. However, the electron current did not show better performance with the decrease of LUMO and HOMO levels. The non-fluorinated carbazole exhibited better electron transport compared to the monofluorocarbazole as a donor. Further increase in the number of introduced fluorine atoms leads to more severe electron trapping. The J-V characteristics were modeled with the previously developed drift-diffusion model to quantify the trap density,¹³ results are summarized in **Table 4.4**. We observed that the trap density of molecule DTPT-DCz is $1.5 \times 10^{22} \text{ m}^{-3}$, nearly trap-free.¹³ The trap density of the molecules DTPT-DFCz and DTPT-

D2FCz are 15 and 43 times higher than those of DTPT-DCz, respectively. This is due to the denser molecular packing in the compound DTPT-DCz making it less susceptible to oxygen or other compounds that affect electrical conductivity. On the other hand, DTPT-D2FCz can act as a self-trap by exciting electrons into the acceptor (triazine) and not passing them on to the neighboring molecules due to the large distance between the respective triazine rings. As shown in **Figure 4.6b**, for the two molecules with two acceptors and one donor (DDTPT-DCz, and DDTPT-2FCz), the measured J-V curves show very similar electron current density. We observed that the trap densities of the molecules DDTPT-Cz and DDTPT-2FCz were $10 \times 10^{22} \text{ m}^{-3}$ and $12 \times 10^{22} \text{ m}^{-3}$, respectively (**Table 4.4**). This is despite the fact that DDTPT-2FCz has a more regular arrangement compared to DDTPT-Cz. However, because of the large distance between the respective triazine rings of DDTPT-Cz and DDTPT-2FCz, no electrons are passed to neighbouring molecules. The result is that their trap densities are similar.

Table 4.4 Drift-diffusion modeling parameters for electron-only devices of DTPT-DCz, DTPT-DFCz, DTPT-D2FCz, DDTPT-Cz and DDTPT-2FCz.

	DTPT-DCz	DTPT-DFCz	DTPT-D2FCz	DDTPT-Cz	DDTPT-2FCz
Trap density, N_t gauss ($\times 10^{22} \text{ m}^{-3}$)	1.5	23	65	10	12
Trap depth, E_t (eV)	0.74	0.80	0.70	0.45	0.70
Width of Gaussian trap distribution, σ_t (eV)	0.12	0.14	0.12	0.10	0.14
Lattice constant EGDM, a ($\times 10^{-9} \text{ m}$)	1.3	1.4	1.1	1.5	1.0
Density of states (DOS) variance EGDM, σ (eV)	0.12	0.14	0.12	0.10	0.14
Mobility at 295 K, μ ($\times 10^{-11} \text{ m}^2/\text{Vs}$)	3	0.63	1.5	5.4	0.69

4.8. Summary

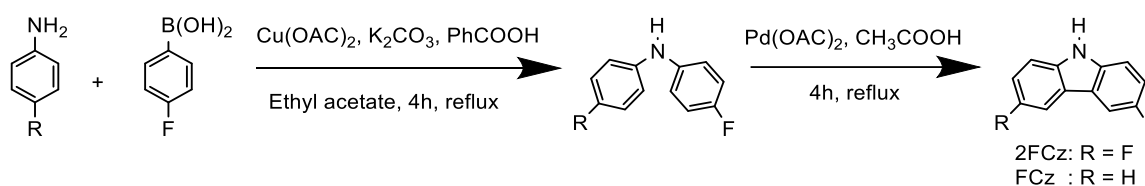
In this chapter, we present five new D-A blue emitters where the HOMO and LUMO orbitals are spatially separated by chemical design. The molecule's IE is located within the trap-free window, but the EA is located outside the trap-free window due to the wide band gap. The presence of fluorine atoms affects the stacking and alignment of the molecules, and DTPT-DFCz and DTPT-D2FCz, the weak interaction of the fluorine atoms results in a large distance between their respective triazine rings, preventing the transfer of electrons to neighbouring molecules and leading to a high trap density. In contrast, the denser molecular

packing of molecule DTPT-DCz makes it less susceptible to oxygen or contaminants that affect conductivity, resulting in a lower trap density (trap-free). However, due to the large distances between the respective triazine rings of DDTPT-Cz and DDTPT-2FCz, their trap density are similar. We have experimentally discovered the effect of molecular stacking on trap density and electron transport capacity. Dense molecular stacking can eliminate the adverse effects of external impurities in organic emitters and achieve trap-free transport. This has important implications for the realization of highly efficient and stable blue OLED devices.

4.9 Synthetic details

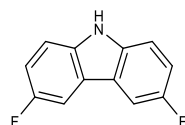
General procedure for the formation of fluorocarbazole.¹⁴

Under an argon atmosphere the $\text{Cu}(\text{OAc})_2$ (1.0 eq.) was dissolved together with (4-fluorophenyl)boronic acid derivatives (50 eq.), aniline derivatives (50 eq) and K_2CO_3 (50 eq.) in ethyl acetate. The reaction mixture was stirred 4h at 80°C . The solvent was removed with a rotary evaporator to produce a residue which was purified by column chromatography to give a sticky black liquid (bis(4-fluorophenyl)amine/4-fluoro-N-phenylaniline). Then palladium (II) acetate was added to the fluorinated diphenylamine in glacial acetic acid was heated under reflux temperature for 30 minutes. After cooling, the reaction mixture was filtered through celite, which was subsequently washed with sodium bicarbonate and ethyl acetate, removal of the solvent gave a brown residue, and purified by column chromatography (stationary phase: silica eluent, Hexane/EA:5/1).



Scheme 4.2 Synthetic routes for the FCz and 2FCz.

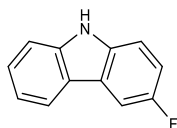
3,6-Difluorocarbazole(2FCz)



According to the general procedure to an anhydrous $\text{Cu}(\text{OAc})_2$ (0.363 g, 0.20 mmol) and (4-fluorophenyl)boronic acid (1.39 g, 10 mmol), in ethyl acetate (50 mL) was added 4-

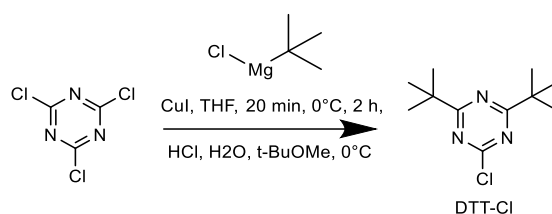
fluoroaniline (1 mL, 10 mmol) and 4-fluorophenylboronic acid (4.20 g, 30 mmol), and K_2CO_3 (1.38 g, 10 mmol) at room temperature. The resulting mixture was heated to 80°C for 4 hours. The purified product was obtained as black liquid (bis(4-fluorophenyl)amine, 1.29 g, 6.5 mmol, 65%). Then palladium (II) acetate (1.46 g, 6.5 mmol) was added to the product of the previous step in glacial acetic acid (40 mL). The purified 2FCz product was obtained in a yield of 39%. 1H NMR (400 MHz, CD_2Cl_2) δ 8.09 (s, 1H), 7.59 (ddt, $J = 9.0, 2.6, 0.7$ Hz, 2H), 7.32 (ddd, $J = 8.8, 4.3, 0.5$ Hz, 2H), 7.11 (td, $J = 9.0, 2.6$ Hz, 2H). ^{13}C NMR (101 MHz, CD_2Cl_2) δ 157.69, 137.36, 123.78, 114.66, 112.08, 106.29. High-resolution mass spectrometry (HRMS) (APCI) m/z : calc for $C_{12}H_7NF_2$: 203.0547; found: 203.0547.

3-Fluorocarbazole (FCz):



According to the general procedure to an anhydrous $Cu(OAc)_2$ (0.363 g, 20 mmol) and benzoic acid (1.221 g, 1.0 mmol), in ethyl acetate (50 mL) was added 4-fluoroaniline (1 mL, 10 mmol) and phenylboronic acid (3.66 g, 3.0 mmol), and K_2CO_3 (1.38 g, 10 mmol) at room temperature. The purified product was obtained as black liquid black liquid. (4-fluoro-N-phenylaniline, 1.12 g, 6 mmol, 60%). Then palladium (II) acetate (1.35 g, 6 mmol) was added to the monofluorinated diphenylamine in glacial acetic acid (35 mL) for the ring closure to carbazol. The purified FCz was obtained in a yield of 45%. 1H NMR (400 MHz, CD_2Cl_2) δ 8.25 – 8.06 (m, 1H), 8.04 (dq, $J = 7.9, 1.0$ Hz, 1H), 7.74 (ddt, $J = 9.0, 2.5, 0.7$ Hz, 1H), 7.50 – 7.37 (m, 3H), 7.29 – 7.14 (m, 2H). ^{13}C NMR (101 MHz, CD_2Cl_2) δ 157.84, 141.03, 136.28, 126.85, 124.14, 123.31, 120.83, 119.79, 113.86, 11.68, 111.33, 106.14. High-resolution mass spectrometry (HRMS) (APCI) m/z : calc for $C_{12}H_8NF$: 185.0641; found: 185.0640.

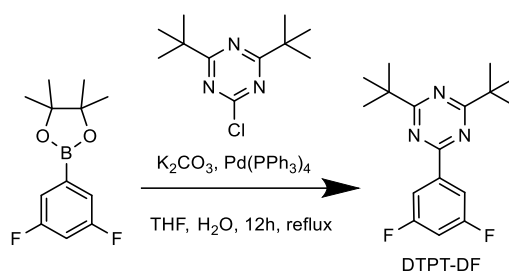
2-Chloro-4,6-di-tert-butyl-1,3,5-triazine (DTT-Cl)



Scheme 4.3 Synthetic routes for the DTT-Cl.

Following a literature report cyanuric chloride (2.7 g, 14.5mmol) and CuI (95 mg, 0,5mmol, 3.4 mol-%) was stirred in THF (10 mL) at 0 °C. Then tBuMgCl (35 mL, 1 M in THF, 35 mmol,) was slowly added to the mixture, over 20 minutes. The reaction mixture was stirred for 2 hours at 0 °C then it was diluted with tBuOMe (50 mL) and quenched with 2.4 M HCl (100 mL) and water. The organic phase was washed with aqueous NH₄Cl, aqueous NaHCO₃, water, and dried with MgSO₄, filtered and evaporated to dryness. The residue was dissolved in hexane and filtered over a column of SiO₂. The product was shortly dried under vacuum and upon standing in air for several hours (yield is 75%). ¹H NMR (400 MHz, CD₂Cl₂) δ 1.36 (s, 18H). ¹³C NMR (101 MHz, CD₂Cl₂) δ 188.12, 171.41, 40.12, 28.85. High-resolution mass spectrometry (HRMS) (APCI) m/z: calc for C₁₁H₁₉N₃Cl: 228.1268; found: 228.1273.

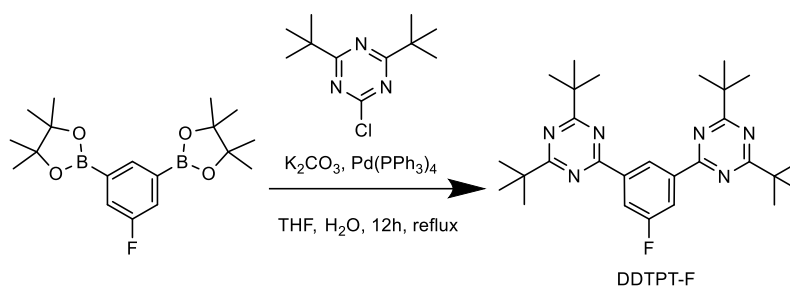
2,4-Di-tert-butyl-6-(3,5-difluorophenyl)-1,3,5-triazine (DTPT-DF)



Scheme 4.4 Synthetic routes for the DTPT-DF.

2-(3,5-difluorophenyl)-4,4,5,5-tetramethyl-1,3,2-dioxaborolane (2.5 g, 10.4 mmol) and 2,4-di-tert-butyl-6-chloro-1,3,5-triazine (1,8 g, 7.9 mmol) were dissolved in anhydrous THF. After 30 min, tetrakis(triphenylphosphine)palladium (0.41 g, 0.35 mmol) and potassium carbonate (9.93 g, 71,82 mmol) was added in above mixture continuously. The residue was extracted by methylene chloride and distilled water. Then the solvent was removed from the resulting mixture under reduced pressure. The crude product was purified by column chromatography on silica gel using n-hexane/ dichloromethane. (yield is 80%). ¹H NMR (400 MHz, CD₂Cl₂) δ 8.17 – 7.94 (m, 2H), 6.92 (tt, 1H), 1.35 (s, 18H). ¹³C NMR (101 MHz, CD₂Cl₂) δ 186.00, 168.56, 162.62, 140.99, 117.79, 107.42 39.99, 29.09. High-resolution mass spectrometry (HRMS) (APCI) m/z: calc for C₁₇H₂₂N₃F₂: 306.1782; found: 306.1784.

6,6'-(5-fluoro-1,3-phenylene)bis(2,4-di-tert-butyl-1,3,5-triazine) (DDTPT-F)

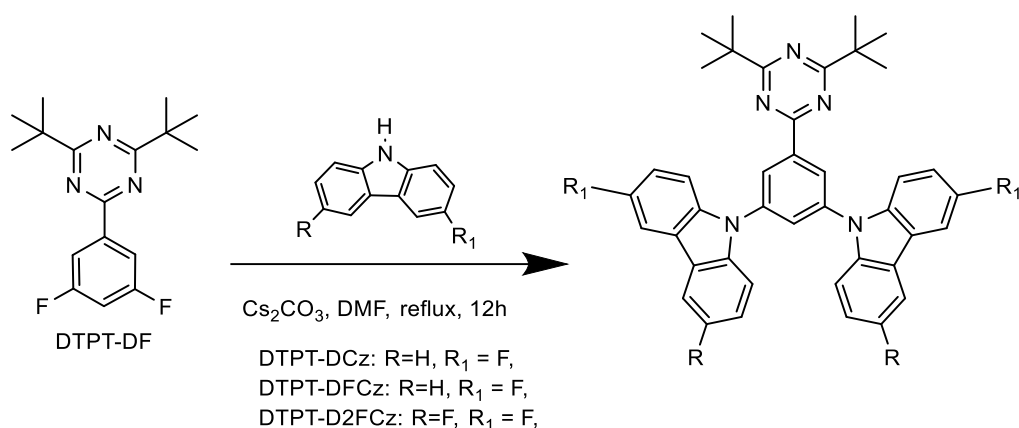


Scheme 4.5 Synthetic routes for the DDTPT-F.

2,2'-(5-fluoro-1,3-phenylene)bis(4,4,5,5-tetramethyl-1,3,2-dioxaborolane) (3.62 g, 10.4 mmol) and 2,4-di-tert-butyl-6-chloro-1,3,5-triazine (1.8 g, 7.9 mmol) were dissolved in anhydrous THF. After 30 min, tetrakis(triphenylphosphine)palladium (0.41 g, 0.35 mmol) and potassium carbonate (9.93 g, 71.82 mmol) was added in above mixture continuously. The residue was extracted by methylene chloride and distilled water. Then the solvent was removed from the resulting mixture under reduced pressure. The crude product was purified by column chromatography on silica gel using n-hexane/ dichloromethane. (yield is 60%). ^1H NMR (400 MHz, CD_2Cl_2) δ 9.69 (t, $J = 1.5$ Hz, 1H), 8.47 (dd, $J = 9.5, 1.5$ Hz, 2H), 1.47 (s, 36H). ^{13}C NMR (101 MHz, CD_2Cl_2) δ 185.92, 169.24, 139.97, 139.89, 125.46, 125.43, 118.88, 40.02, 29.07. High-resolution mass spectrometry (HRMS) (APCI) m/z : calc for $\text{C}_{28}\text{H}_{40}\text{N}_6\text{F}$: 479.3298; found: 479.3293.

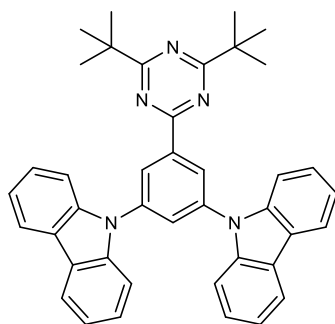
Coupling of carbazoles to 2,4-di-tert-butyl-6-(3,5-difluorophenyl)-1,3,5-triazine.

Under argon atmosphere carbazole (Cz: 2 eq., FCz: 2 eq., and 2FCz: 2 eq.), cesium carbonate(4 eq) followed by DMF (100 mL) resulted in a suspension, which was stirred for 30 min at room temperature. Afterwards 2,4-di-tert-butyl-6-(3,5-difluorophenyl)-1,3,5-triazine(1 eq) was poured in all at once and reaction mixture was stirred at 155°C for 12 hours. The black mixture was diluted with water and crude product was extracted with chloroform (3 \times 30 mL). Organic phases were dried over Na_2SO_4 and solvent was removed. The solvent was evaporated under reduced pressure and the crude product was purified by column chromatography (stationary phase: silica, eluent: hexane/DCM 4:1).



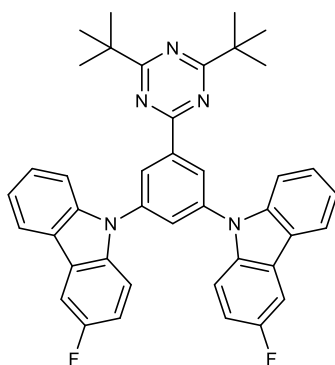
Scheme 4.6 Synthetic routes for the DTPT-DCz, DTPT-DFCz, and DTPT-D2FCz.

9,9'-(5-(4,6-di-tert-butyl-1,3,5-triazin-2-yl)-1,3-phenylene)bis(9H-carbazole) (DTPT-DCz)



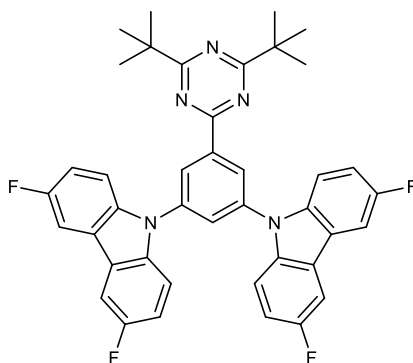
According to the general procedure carbazole (0.334 g, 2 mmol), cesium carbonate (2.6 g, 8 mmol), 2,4-di-tert-butyl-6-(3,5-difluorophenyl)-1,3,5-triazine (0.305 g, 1 mmol), were suspended in DMF (100 mL). The purified product was obtained as a white solid (yield is 64%). ¹H NMR (300 MHz, CDCl₃) δ 8.93 (d, *J* = 2.1 Hz, 2H), 8.19 (d, *J* = 7.7 Hz, 4H), 7.98 (t, *J* = 2.1 Hz, 1H), 7.59 (d, *J* = 8.2 Hz, 4H), 7.47 (ddd, *J* = 8.3, 7.1, 1.3 Hz, 4H), 7.42 – 7.29 (m, 4H), 1.42 (s, 18H). ¹³C NMR (75 MHz, CDCl₃) δ 185.87, 140.73, 139.81, 128.32, 126.43, 126.06, 123.83, 120.66, 120.61, 109.83, 39.87, 29.11. High-resolution mass spectrometry (HRMS) (APCI) *m/z*: calcd for C₄₁H₃₇N₅: 599.3049; found: 599.3042.

9,9'-(5-(4,6-di-tert-butyl-1,3,5-triazin-2-yl)-1,3-phenylene)bis(3-fluoro-9H-carbazole) (DTPT-DFCz)



According to the general procedure 3-fluoro-carbazole (0.370 g, 2 mmol), cesium carbonate(2.6 g, 8 mmol), 2,4-di-tert-butyl-6-(3,5-difluorophenyl)-1,3,5-triazine(0.305 g, 1 mmol), were suspended in DMF (100 mL). The purified product was obtained as a white solid (yield is 58%).¹H NMR (300 MHz, CDCl₃) δ 8.90 (d, *J* = 2.0 Hz, 2H), 8.12 (d, *J* = 7.8 Hz, 2H), 7.92 (t, *J* = 2.1 Hz, 1H), 7.82 (dd, *J* = 8.7, 2.6 Hz, 2H), 7.57 (d, *J* = 8.2 Hz, 2H), 7.54 – 7.44 (m, 4H), 7.33 (t, *J* = 7.5 Hz, 2H), 7.19 (td, *J* = 9.0, 2.6 Hz, 2H), 1.43 (s, 18H).¹³C NMR (75 MHz, CDCl₃) δ 185.94, 168.93, 159.81, 156.66, 141.29, 139.76, 137.06, 128.01, 127.06, 126.01, 124.48, 123.39, 120.8, 114.32, 113.99, 110.47, 110.03, 106.43, 39.89, 29.10. High-resolution mass spectrometry (HRMS) (APCI) *m/z*: calcd for C₄₁H₃₅N₅F₂: 635.2861; found: 635.2849.

9,9'-(5-(4,6-di-tert-butyl-1,3,5-triazin-2-yl)-1,3-phenylene)bis(3,6-difluoro-9H-carbazole (DTPT-D2FCz)

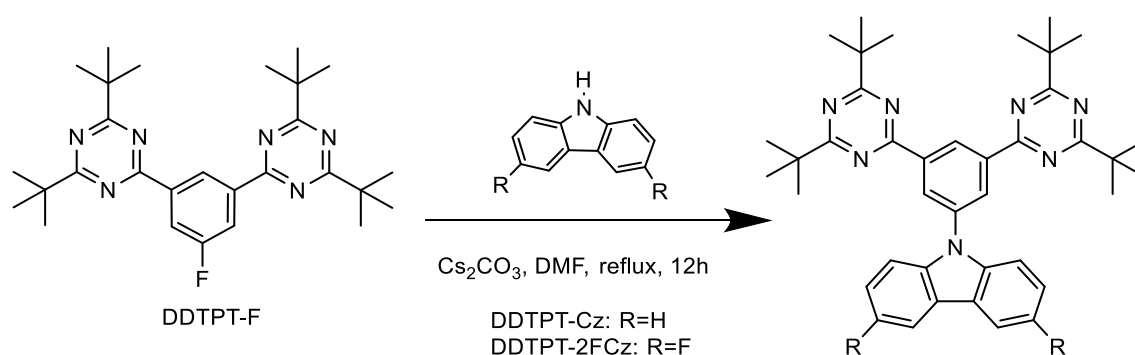


According to the general procedure 3,6-difluoro-carbazole (0.406 g, 2 mmol), cesium carbonate (2.6 g, 8 mmol), 2,4-di-tert-butyl-6-(3,5-difluorophenyl)-1,3,5-triazine (0.305 g, 1 mmol), were suspended in DMF (100 mL). The purified product was obtained as a white solid (yield is 56%).¹H NMR (400 MHz, CD₂Cl₂) δ 8.90 (d, *J* = 2.1 Hz, 2H), 7.92 (t, *J* = 2.1 Hz, 1H), 7.79 (dd, *J* = 8.7, 2.5 Hz, 4H), 7.52 (dd, *J* = 9.0, 4.2 Hz, 4H), 7.24 (td, *J* = 9.0, 2.6 Hz,

4H), 1.43 (s, 18H). ^{13}C NMR (101 MHz, CD_2Cl_2) δ): 186.19, 169.14, 158.29, 141.57, 139.89, 138.27, 128.17, 126.37, 124.10, 115.06, 111.21, 106.67, 40.04, 29.05. High-resolution mass spectrometry (HRMS) (APCI) m/z : calcd for $\text{C}_{41}\text{H}_{33}\text{N}_5\text{F}_4$: 671.2672; found: 671.2662.

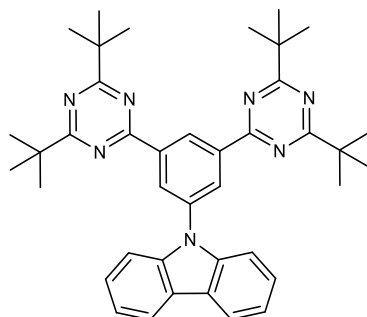
General procedure for introduction of two tert-Butyltriazine in carbazole containing fluorine.

Under argon atmosphere carbazole (Cz: 1 eq., and 2FCz: 1 eq.), cesium carbonate(3 eq) followed by DMF (100 mL) resulted in a suspension, which was stirred for 30 min at room temperature. Afterwards 6,6'-(5-fluoro-1,3-phenylene)bis(2,4-di-tert-butyl-1,3,5-triazine) (1 eq) was poured in all in once and reaction mixture was stirred at 155°C for 12 hours. The black mixture was diluted with water and crude product was extracted with chloroform (3×30 mL). Organic phases were dried over Na_2SO_4 and solvent was removed. The solvent was evaporated under reduced pressure and the crude product was purified by column chromatography (stationary phase: silica, eluent: hexane/DCM 4:1).



Scheme 4.6 Synthetic routes for the DDTPT-Cz and DDTPT-2FCz.

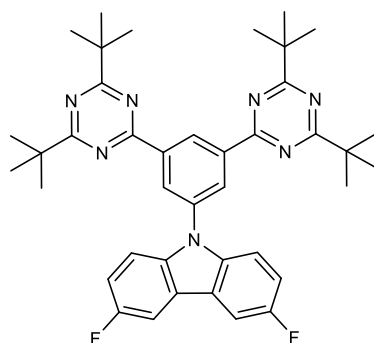
9-(3,5-bis(4,6-di-tert-butyl-1,3,5-triazin-2-yl)phenyl)-9H-carbazole (DDTPT-Cz)



According to the general procedure carbazole (0.167 g, 1 mmol), cesium carbonate (1.3 g, 4 mmol), DDTPT-F (0.478 g, 1 mmol), were suspended in DMF (100 mL). The

purified product was obtained as a white solid (yield is 51%). ^1H NMR (300 MHz, CDCl_3) δ 9.97 (d, $J = 1.7$ Hz, 1H), 8.95 (d, $J = 1.6$ Hz, 2H), 8.23 (d, $J = 7.7$ Hz, 2H), 7.56 – 7.42 (m, 4H), 7.36 (ddd, $J = 8.0, 6.8, 1.3$ Hz, 2H), 1.47 (s, 36H). ^{13}C NMR (75 MHz, CDCl_3) δ 185.66, 169.38, 141.05, 139.47, 138.63, 130.45, 128.72, 126.31, 123.67, 120.56, 120.31, 109.89, 39.85, 29.08. High-resolution mass spectrometry (HRMS) (APCI) m/z : calcd for $\text{C}_{40}\text{H}_{47}\text{N}_7$: 625.3893; found: 625.3876.

9-(3,5-bis(4,6-di-tert-butyl-1,3,5-triazin-2-yl)phenyl)-3,6-difluoro-9H-carbazole(DDTPT-2FCz)



According to the general procedure 3,6-difluoro-carbazole (0.203 g, 1 mmol), cesium carbonate (1.3 g, 4 mmol), DDTPT-F (0.478 g, 1 mmol), were suspended in DMF (100 mL). The purified product was obtained as a white solid (yield is 50%). ^1H NMR (300 MHz, CDCl_3) δ 9.94 (t, $J = 1.6$ Hz, 1H), 8.89 (s, 2H), 7.79 (dd, $J = 8.7, 2.5$ Hz, 2H), 7.43 (dd, $J = 9.0, 4.2$ Hz, 2H), 7.21 (td, $J = 9.0, 2.5$ Hz, 2H), 1.46 (s, 36H). ^{13}C NMR (75 MHz, CDCl_3) δ 185.72, 169.22, 159.53, 156.39, 139.64, 138.24, 130.02, 128.80, 123.72, 114.79, 110.89, 106.38, 39.86, 29.07. High-resolution mass spectrometry (HRMS) (APCI) m/z : calcd for $\text{C}_{40}\text{H}_{45}\text{N}_7\text{F}_2$: 661.3705; found: 661.368.

Table 4.5 Crystal data and structure refinement for DTPT-DCz, DTPT-DFCz, and DTPT-D2FCz.

	DTPT-DCz	DTPT-DFCz	DTPT-D2FCz
Empirical formula	C ₄₁ H ₃₇ N ₅	C ₄₂ H ₃₇ Cl ₂ F ₂ N ₅	C ₄₁ H ₃₃ F ₄ N ₅
Moiety formula	C ₄₁ H ₃₇ N ₅	C ₄₁ H ₃₅ F ₂ N ₅	C ₄₁ H ₃₃ F ₄ N ₅
CCDC	2299611	2299612	2299610
Formula weight/ g/mol	599.75	720.66	671.72
Temperature	120(2) K	120(2) K	120(2) K
Crystal system	Triclinic	Triclinic	Monoclinic
Space group name, number	P -1, (2)	P -1, (2)	P 21/c, (14)
a/ Å	9.7727(7)	9.8028(5)	22.5670(14)
b/ Å	12.9858(9)	11,8512(6)	19.3623(8)
c/ Å	13.9307(10)	17.0677(9)	7.8595(4)
α/°	79.017(6)	77.251(4)	/
β/°	71.369(5)	73.484(4)	95.503(5)
γ/°	78.050(6)	78.832(4)	/
Volume/ Å ³	1624.1(2)	1835.89(17)	3418.4(3)
Density (calculated)/ mg/m ³	1.226	1.304	1.305
Absorption coefficient/ mm ⁻¹	0.073	0.225	0.768
Crystal size / mm ³	0.400 x 0.400 x 0.700	0.120 x 0.310 x 0.500	0.040 x 0.070 x 0.760
Wavelength, radiation type	0.71073 Å, MoKα	0.71073 Å, MoKα	1.54178Å, CuKα
Theta range for data collection	2.539 to 27.958°	2.505 to 28.125°	3.013 to 67.819
Index ranges	-12<=h<=12 -17<=h<=15 -18<=h<=18	-12<=h<=12 -15<=h<=15 -22<=h<=22	-26<=h<=26 -21<=h<=20 -8<=h<=9
Reflections collected	14572	34061	24590
Independent reflections	7688 [R(int) = 0.0191]	8896 [R(int) = 0.0337]	6018 [R(int) = 0.0967]
Goodness-of-fit on F ²	1.050	1.041	1.635
R ₁ , wR ₂ [I>2sigma(I)]	0.0426, 0.1100	0.0511, 0.1221	0.1348, 0.3393
R ₁ , wR ₂ [all data]	0.0481, 0.1156	0.0980, 0.1429	0.1694, 0.4076
Largest diff. peak and hole/ eÅ ⁻³	0.385 and -0.197	0.659 and -0.294	0.893 and -0.670

Table 4.6 Crystal data and structure refinement for DDTPT-Cz and DDTPT-2FCz.

	DDTPT-Cz	DDTPT-2FCz
Empirical formula	C ₄₀ H ₄₇ N ₇	C ₄₀ H ₄₅ F ₂ N ₇
Moiety formula	C ₄₀ H ₄₇ N ₇	C ₄₀ H ₄₅ F ₂ N ₇
CCDC	2299609	2299608
Formula weight/ g/mol	625.84	661.83
Temperature	120(2) K	120(2) K
Crystal system	Triclinic	Orthorhombic
Space group name, number	P -1, (2)	P na21, (33)
a/ Å	13.1756(15)	a = 30.1148(11) Å
b/ Å	15.9934(18)	b = 17.0693(8) Å
c/ Å	19.326(2)	c = 7.2057(3) Å
α/°	/	/
β/°	95.503(5)	/
γ/°	/	/
Volume/ Å ³	3799.0(8)	3704.0(3)
Density (calculated)/ mg/m ³	1.094	1.187
Absorption coefficient/ mm ⁻¹	0.509	0.630
Crystal size / mm ³	0.030 x 0.050 x 0.480	0.020 x 0.030 x 0.850
Wavelength, radiation type	1.54178 Å, CuKα	1.54178 Å, CuKα
Theta range for data collection	2.427 to 67.496°	2.935 to 67.971°
Index ranges	-15<=h<=15 -18<=h<=19 -22<=h<=23	-24<=h<=35 -20<=h<=16 -7<=h<=7
Reflections collected	32057	16075
Independent reflections	12879 [R(int) = 0.1163]	6236 [R(int) = 0.0609]
Goodness-of-fit on F ²	0.955	1.066
R ₁ , wR ₂ [I>2sigma(I)]	0.1372, 0.3201	0.1119, 0.2610
R ₁ , wR ₂ [all data]	0.2050, 0.4026	0.166, 0.3268
Largest diff. peak and hole/ eÅ ⁻³	0.484 and -0.510	0.555 and -0.486

4.10 References

1. Baldo, M. A. *et al.* Highly efficient phosphorescent emission from organic electroluminescent devices. *Nature* **395**, 151–154 (1998).
2. Kim, S. Y. *et al.* Organic light-emitting diodes with 30% external quantum efficiency based on a horizontally oriented emitter. *Adv. Funct. Mater.* **23**, 3896–3900 (2013).
3. Huang, F. *et al.* Combining Carbazole Building Blocks and ν -DABNA Heteroatom Alignment for a Double Boron-Embedded MR-TADF Emitter with Improved Performance. *Angew. Chemie Int. Ed.* **62**, e2023064 (2023).
4. Nicolai, H. T. *et al.* Unification of trap-limited electron transport in semiconducting polymers. *Nat. Mater.* **11**, 882–887 (2012).
5. Haneef, H. F., Zeidell, A. M. & Jurchescu, O. D. Charge carrier traps in organic semiconductors: A review on the underlying physics and impact on electronic devices. *J. Mater. Chem. C* **8**, 759–787 (2020).
6. Kotadiya, N. B., Mondal, A., Blom, P. W. M., Andrienko, D. & Wetzelaer, G. J. A. H. A window to trap-free charge transport in organic semiconducting thin films. *Nat. Mater.* **18**, 1182–1186 (2019).
7. Van der Zee, B., Li, Y., Wetzelaer, G. A. H. & Blom, P. W. M. Efficiency of Polymer Light-Emitting Diodes: A Perspective. *Adv. Mater.* **34**, 2108887 (2022).
8. Kotadiya, N. B., Blom, P. W. M. & Wetzelaer, G. J. A. H. Efficient and stable single-layer organic light-emitting diodes based on thermally activated delayed fluorescence. *Nat. Photonics* **13**, 765–769 (2019).
9. Cui, L. S., Kim, J. U., Nomura, H., Nakanotani, H. & Adachi, C. Benzimidazobenzothiazole-Based Bipolar Hosts to Harvest Nearly All of the Excitons from Blue Delayed Fluorescence and Phosphorescent Organic Light-Emitting Diodes. *Angew. Chemie - Int. Ed.* **55**, 6864–6868 (2016).
10. Hintermann, L. *et al.* The AZARYPHOS family of ligands for ambifunctional catalysis: Syntheses and use in ruthenium-catalyzed anti-markovnikov hydration of terminal alkynes. *Chem. - A Eur. J.* **15**, 7167–7179 (2009).
11. Shih, P. I. *et al.* Novel carbazole/fluorene hybrids: Host materials for blue phosphorescent OLEDs. *Org. Lett.* **8**, 2799–2802 (2006).
12. Koster, L. J. A., Smits, E. C. P., Mihailetchi, V. D. & Blom, P. W. M. Device model for the operation of polymer/fullerene bulk heterojunction solar cells. *Phys. Rev. B - Condens. Matter Mater. Phys.* **72**, 1–9 (2005).
13. Sachnik, O. *et al.* Elimination of charge-carrier trapping by molecular design. *Nat. Mater.* **22**, 1114–1120 (2023) doi:10.1038/s41563-023-01592-3.
14. Woon, K. L., Nadiah, Z. N., Hasan, Z. A., Ariffin, A. & Chen, S. A. Tuning the singlet-

triplet energy splitting by fluorination at 3,6 positions of the 1,4-biscarbazoylbenzene. *Dye. Pigment.* **132**, 1–6 (2016).

Chapter 5. Conclusion and Outlook

Organic optoelectronic materials have been developed for decades, and fluorescent materials have been widely used in bio-imaging, information storage, sensing devices, and organic light-emitting diodes (OLEDs). However, in OLEDs, the blue OLED devices still have problems such as instability and low efficiency. On the one hand, the large bandgap of the blue emitters leads to material instability, and on the other hand, it is due to the existence of traps in the device. Therefore, in order to achieve efficient and stable blue OLED devices, in addition to good stability of the material, it is also crucial to have no traps in the device.

The development of phosphorescent materials (especially pure organic RTP) has lagged far behind that of fluorescent materials due to their effect on external factors such as water and oxygen. Although some progress has been made in recent years, there are still some challenges to overcome in order to make phosphorescent materials as successful as fluorescent materials for commercial applications. To date, most reports on organic room-temperature phosphorescence have been characterized by low quantum yields and short lifetimes. Therefore it is imperative to achieve efficient and stable organic room temperature phosphorescence.

In this thesis, firstly, high quantum yield RTP molecules were obtained based on TADF molecules. Secondly, RTP was achieved in a neat film through space charge transfer and steric hindrance effects. Thirdly, by introducing fluorine atoms, which affect the way the molecules are arranged and stacked, the blue molecules are achieved without traps in the electron transport device. The main conclusions are conceived and summarized as follows:

1. The key factor for achieving efficient RTP molecules is the fast ISC process. It is well known that the TADF molecules have a small ΔE_{ST} between the singlet and triplet states so the ISC process is fast. However, due to the presence of the RISC process in the TADF molecule, this will inevitably compete with the phosphorescence emission and making it difficult to achieve efficient RTP. In chapter 2, we present three-model emission in which the energy levels in the two triplet states (T_1 and T_2) are lower than in the singlet state (S_1). Specifically, the model emitter 1,8-mDTAZ-PhtCz exhibits fluorescence, delayed fluorescence and phosphorescence emission. It has both fluorescence and phosphorescence emission in the blue region. We have confirmed experimentally and theoretically that another

upper triplet state (T_2) is also involved in the emission process. Through Förster resonance energy transfer, after doping different fluorescent materials, all the energy of 1,8-mDTAZ-PhtCz is transferred to the fluorescent molecules, achieving transient emission of fluorescent molecules on the time scale from nanoseconds to seconds. Based on the model molecule 1,8-mDTAZ-PhtCz, the emitter 1,8-pDTAZ-PhtCz with only fluorescence and RTP emission was obtained by adjusting the relative energy difference between T_2 and T_1 and S_1 , while the RTP quantum yield can reach more than 30%.

2. For pure organic RTP molecules, it is difficult to observe phosphorescence emission in neat films, due to the dense build-up of the molecules in neat films, which tends to generate annihilation of triplet state excitons, resulting in a short lifetimes. In chapter 3, we present a strategy to improve the phosphorescence efficiency of neat films through steric hindrance induced space charge transfer. The higher efficiency of ISC that can be obtained through space charge transfer and bond charge transfer between donor and acceptor has been demonstrated in TADF. Meanwhile larger steric hindrance can effectively suppress molecular rotation and non-radiative decay. Based on the above, we designed a series of emitters (namely mDTCz, pDTCz, and pDTTCz). Through the stepwise adjustment of acceptor positions and donor molecule sizes, efficient RTP was achieved in neat films. All molecules emit blue fluorescence and phosphorescence in neat films. Our experimental data show that lifetimes up to 40 ms and phosphorescence quantum yields of 6.3% are achievable in neat films. All molecules have a lifetime of over 30 ms under ambient conditions. The strategy developed here provides important insights into the realization of highly efficient organic phosphorescent materials in neat films.

3. The main cause of poor devices performance apart from the stability of the materials itself, is the unbalanced transport of electrons and holes. Specifically for blue emitters the electron affinity (EA) is generally outside the trap-free window, and it remains a challenge to achieve intrinsic trap-free transport of holes and electrons. In chapter 4, we present five materials they are DTPT-DCz, DTPT-DFCz, DTPT-D2FCz, DDTPT-Cz, and DDTPT-2FCz. Contrary to expectations, for DTPT-DCz, DTPT-DFCz, and DTPT-D2FCz, the electron current density instead decreases by several orders of magnitude as the LUMO of the molecule gets closer to the trap-free window. This is due to the fact that the introduction of fluorine atoms changes the stacking and arrangement of the molecules. For DDTPT-Cz and

DDTPT-2FCz, the fluorine atom on the carbazole does not significantly change the electron current density.

This thesis demonstrates the three-mode emission rule and successfully designs the efficient room-temperature phosphorescent materials, deepening the understanding between room-temperature phosphorescence and TADF (chapter 2). Even room temperature phosphorescence emission in neat films via molecular design is possible (chapter 3). Not only that, but we also designed molecules to reveal the effect of molecular arrangement and stacking on the density of traps in electron transport devices (chapter 4). In the future we should endeavor to address the issues and challenges facing photoelectronic materials.

Appendix

Appendix-I Experimental section and analytical techniques

Chemicals and solvents

All chemicals and reagents were used as received from commercial sources (Sigma-Aldrich, and BLD Pharmatech) without further purification. Solvents for chemical synthesis were used as received from Sigma-Aldrich and Acros Organics, unless stated otherwise.

Chromatography

The column chromatography was performed using silica gel (60–120, 100–200 and 230–400 mesh). For thin layer chromatography, aluminium sheets pre-coated with silica gel (Merck, Kieselgel 60, F254) were employed.

NMR spectroscopy

^1H and ^{13}C NMR spectra were recorded in $\text{CDCl}_3/\text{CD}_2\text{Cl}_2$ solvent on a 400/700 MHz spectrometer (Bruker DPX) using tetramethylsilane (TMS) as the internal standard. The measurements were carried out at room temperature (293 K), unless stated otherwise.

Mass spectrometry

The high-resolution electrospray ionization mass spectrometry (HR-ESI-MS) was performed at the Max Planck Institute for Polymer Research, on an ESI-Q-TOF system (maXis, Bruker Daltonics, Germany).

Photophysical properties measurement

Steady state UV-Vis absorption spectra were measured on a Perkin-Elmer Lambda 900 spectrophotometer at room temperature. Steady-state PL spectra were recorded with a HORIBA Jobin-Yvon Fluorolog 3-22 Tau-3 using a photomultiplier tube (PMT) as detector, using 356 nm excitation. Time-resolved emission spectra were measured by using a 4Picos gated-iCCD camera (Standford Computer Optics) with a Ti-sapphire laser (Coherent, Astrella, 5 mJ, 800 nm, 1 kHz). The time-resolved PL intensity decay was obtained by means of TCSPC setup (Picoquant) with a pico-second laser at 375 nm (Picoquant). The laser was modulated in pulse mode to measure the prompt (1 MHz) and delayed fluorescence decay (10 KHz), while the laser was working in burst mode to measure the long-lived RTP decay. During the burst mode, firstly 100 laser pulses in a repetition rate of 1 MHz was used to get

enough long-lived triplets from the accumulation from different pulses, followed with the longest measurement time window of ~ 4.3 s defined by the setup. The ns-TA spectra were measured by using an EOS pump-probe setup (Ultrafast Systems) paired with an amplified 1030 nm fs laser (Pharos, Light Conversion, 200 fs, 200 μ J) with an effective laser repetition rate of 1 kHz. The probe white light was generated via a sub-nanosecond pulsed light source and a photonic crystal fiber, yielding broadband probe light across the UV-VIS-NIR regions. The pump pulse at 360 nm was generated with an optical parametric amplifier (Orpheus-F, Light Conversion). The pump energy was 200 μ W/cm². Samples were dissolved in degassed toluene as 4 mg/mL and measured in 2 mm path length cuvettes.

Time-resolved microscopy

The doped films were prepared with materials mixed in PMMA as described above. All films and crystal for microscopy were prepared with oxygen plasma-treated gridded glass coverslip (ibidi Grid-50) performed in a nitrogen glove box and finally been sealed. The time-resolved phosphorescence images were performed using the Thunder system (Leica) equipped with a sCMOS camera (Leica DFC9000). A 390 nm LED was selected for illumination, which equipped with a quadband filter cube (the excitation filter 375-407 nm, 462-496 nm, 542-566 nm, 622-654 nm; the dichroic beam splitter 415, 500, 572, 660 nm and the emission filter 420-450 nm, 506-532 nm, 578-610 nm, 666-724 nm). Here, we chose the same LED and corresponding quadband filtercube for the fluorescence and phosphorescence channels, except that the LED for phosphorescence channel was turned off. For the crystal, the phosphorescence images were acquired with camera exposure time of 6 s for each frame after illuminated by 390 nm LED with 100% power. After the crystal was continuously excited by the LED for 200 ms, after another 19 ms, the phosphorescence images were began to be recorded with an 11 ms interval between each phosphorescence image. HC PL FLUOTAR 10X/0.32 DRY objective was selected, pixel size is 1.291 μ m. For the fluorescence images of doped films, power of LED was set to 1%, 1%, 100%, and 16% for TBPe, TTPA, SYPPV, and DCJTB, separately. The phosphorescence images were acquired with camera exposure time of 100 ms for each frame after illuminated with 390 nm LED. After the films was continuously excited by the LED for 10 ms, after another 550 ms, the phosphorescence images were beginning to be recorded with a 400 ms interval between each phosphorescence image. HC PL APO CS2 63X/1.40 OIL objective was selected, pixel size is 0.205 μ m. It should be noted that the time switched the fluorescence channel to the phosphorescence

channel and the time switched the phosphorescence channel to the next phosphorescence channel is different, which we specifically marked in the picture. For each sample, the brightness/intensity range of all phosphorescence images was set to the same as that of the first phosphorescence image.

Cyclic voltammetry

Cyclic voltammetry (CV) was carried out on a computer-controlled GSTAT12 in a three-electrode cell in anhydrous acetonitrile solution of Bu_4NPF_6 (0.05 M) with a scan rate of 100 mV/s at room temperature under argon. A Pt wire, a silver wire, and a glassy carbon electrode were used as the counter electrode, the working electrode, and the reference electrode, respectively.

Computational methods

Density functional theory (DFT) and time dependent density functional theory (TD-DFT) were standardly performed with B3LYP hybrid functionals and 6-31g or 6-311g basis set implemented in gaussian09.¹ (chapter 3 and chapter 4) The geometry optimization of the molecule was performed in Qchem6.5 using DFT at range-separated hybrid functionals LC- ω PBE08/6-311g(d,p) level of theory² in combination with DFT-D3(BJ) dispersion correction from Grimme et al.³ and a polarizable continuum model (PCM), where the toluene as solvent is used. The lowest lying singlet (S_1) and triplet (T_1) excited states are calculated with the spin-restricted open-shell Kohn–Sham method (ROKS)^{2,3} in combination with DFT-D3(BJ) and PCM (toluene as solvent). For the second lowest lying triplet (T_2) excited state, the same level of theory is applied, however, instead of using the Geometric Direct Minimization (GDM)⁴ algorithm, the Square Gradient Minimization (SGM)⁵ is used for optimizing the excited state orbitals. Note that, the emission spectra, i.e. S_1 , T_1 , and T_2 energies, are calculated at the optimized S_1 geometry. Hole–electron analysis was displayed using the visual molecular dynamics (VMD) software package.⁶ For comparison, the results of B3LYP/6-311g (d,p), the ω tuned CAM-B3LYP/6-311g (d,p) and the ω tuned ω B97XD/6-311g (d,p).(chapter 2)

Transport devices fabrication and measurements

Electron-only devices were fabricated on glass substrates. The substrates were cleaned with detergent solution and were ultrasonicated in acetone and isopropyl alcohol. The substrates were heated to 140 °C for 10 min and subsequently treated with ultraviolet–ozone

for 20 min. The substrates were transferred into a nitrogen-filled glove box, and 30 nm of Al was thermally evaporated, followed by the organic layer (~100 nm) and a 4 nm TPBi layer. For completion, a 5 nm Ba and 100 nm Al layer was evaporated on top. Electrical characterization was carried out under N₂ atmosphere with a Keithley 2400 source meter.

X-ray diffraction

The single crystal X-ray data were collected by Dr. Dieter Schollmeyer at Institute for Organic Chemistry, Johannes-Gutenberg-University of Mainz. The structures were solved by direct methods (SIR-2004) and refined by SHELXL–2014 (full matrix). The neat films X-ray data were collected by Zhitian Ling at Max Planck Institute for Polymer Research. The one-dimensional X-ray diffraction patterns of the thin films were recorded in the 2θ between 3° and 50°, with a step of 0.01° and a speed of 10 degrees per minute, using a Rigaku SmartLab HR-XRD equipment in the ambient condition.

References

1. M. J. Frisch, et al. Gaussian 09, Revision D.01, Gaussian, Inc. 340 Quinnipiac St., Bldg. 40, Wallingford CT 06492, 2013.
2. Weintraub, E., Henderson, T. M. & Scuseria, G. E. Long-range-corrected hybrids based on a new model exchange hole. *J. Chem. Theory Comput.* 5, 754–762 (2009).
3. Grimme, S., Ehrlich, S. & Goerigk, L. Effect of the damping function in dispersion corrected density functional theory. *J. Comput. Chem.* 32, 1456–1465 (2011).
4. VAN VOORHIS, T. & HEAD-GORDON, M. A geometric approach to direct minimization. *Mol. Phys.* 100, 1713–1721 (2002).
5. Hait, D. & Head-Gordon, M. Excited State Orbital Optimization via Minimizing the Square of the Gradient: General Approach and Application to Singly and Doubly Excited States via Density Functional Theory. *J. Chem. Theory Comput.* 16, 1699–1710 (2020).
6. Humphrey, W., Dalke, A. & Schulten, K. VMD: Visual molecular dynamics. *J. Mol. Graph.* 14, 33–38 (1996).

Appendix-II NMR spectra

Chapter 2

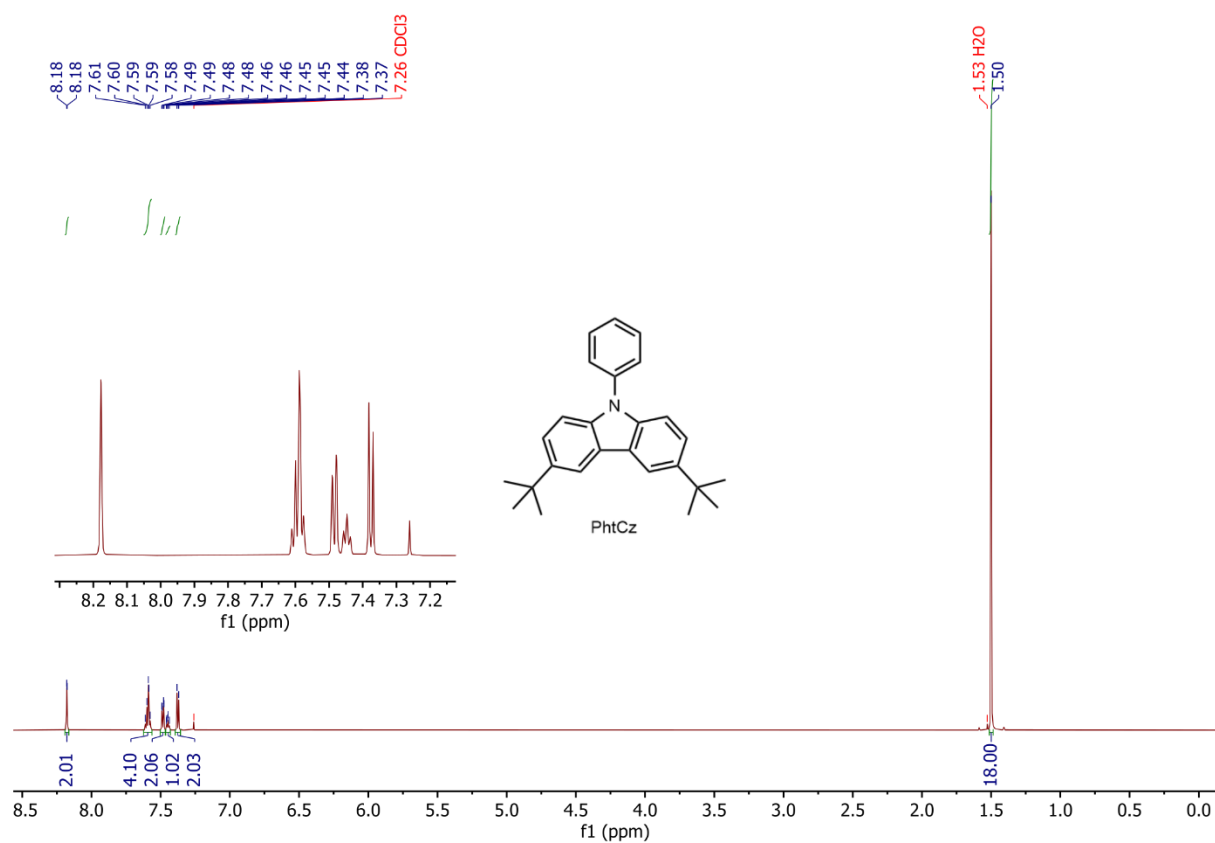


Figure appendix-II-1 ^1H NMR spectrum of compound PhtCz (700 MHz, CDCl_3).

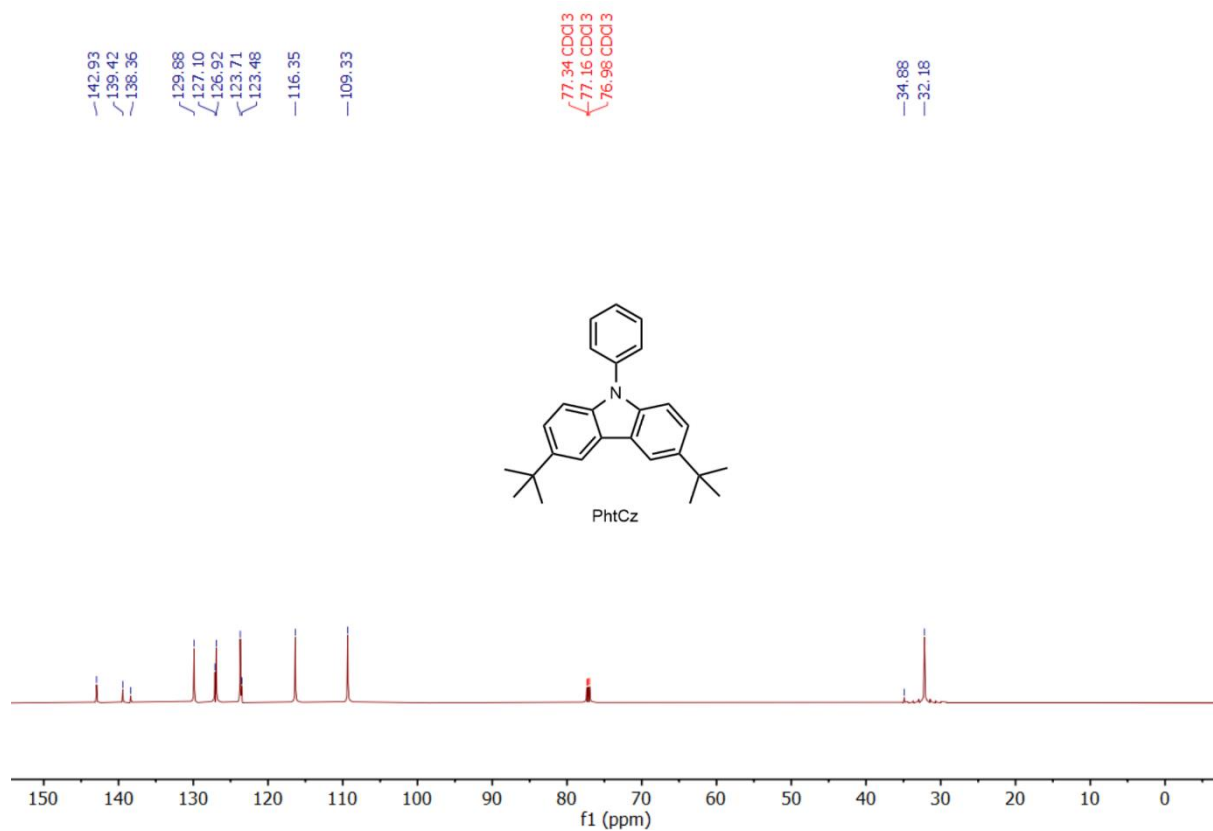


Figure appendix-II-2 ¹³C NMR spectrum of compound PhtCz (176 MHz, CDCl₃).

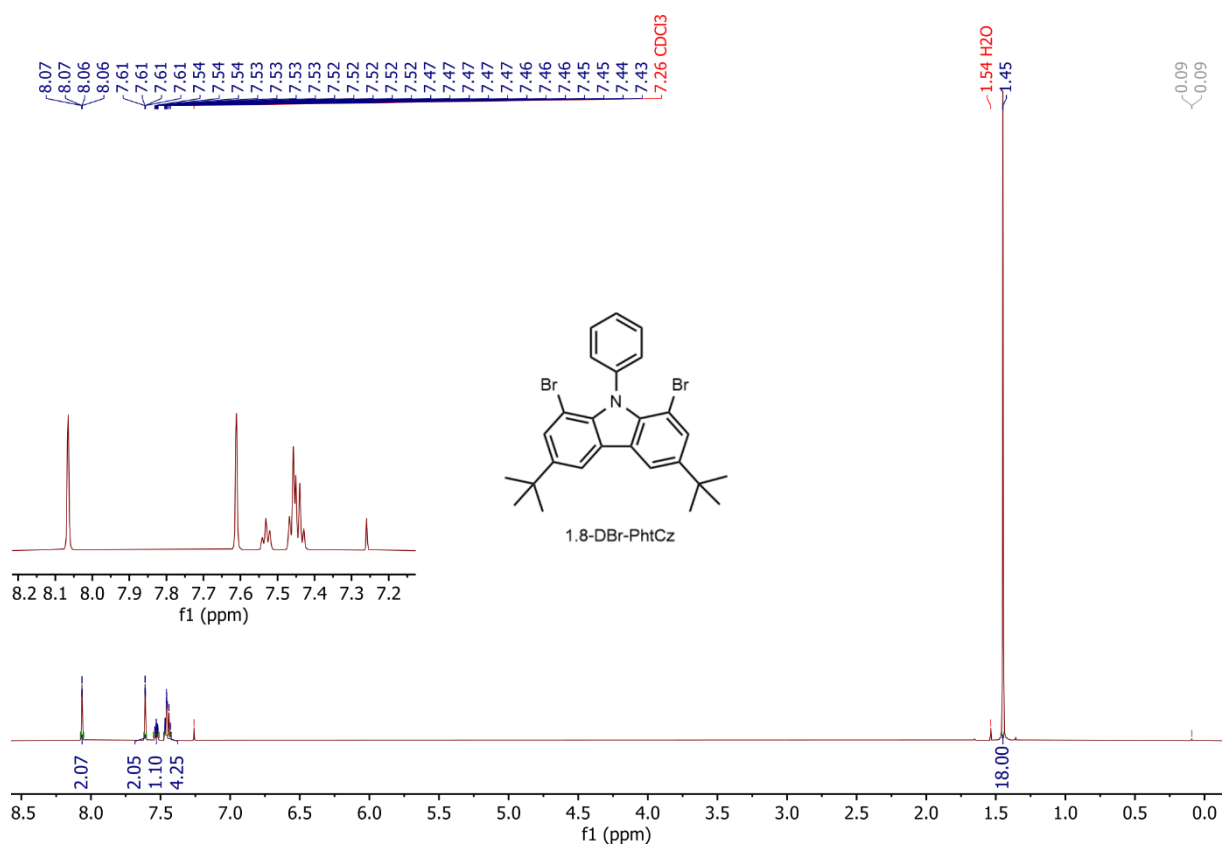


Figure appendix-II-3 ¹H NMR spectrum of compound 1,8-DBr-PhtCz (700 MHz, CDCl₃).

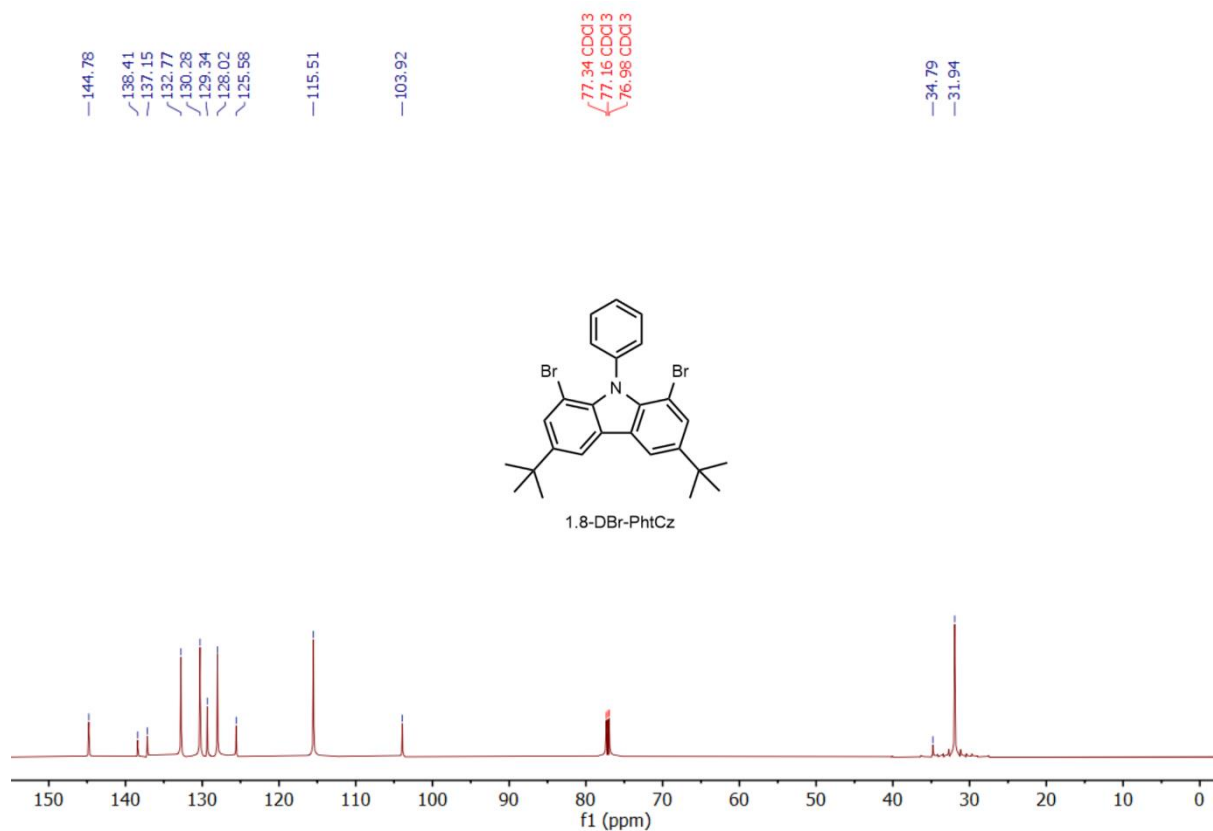


Figure appendix-II-4 ^{13}C NMR spectrum of compound 1,8-DBr-PhtCz (176 MHz, CDCl_3).

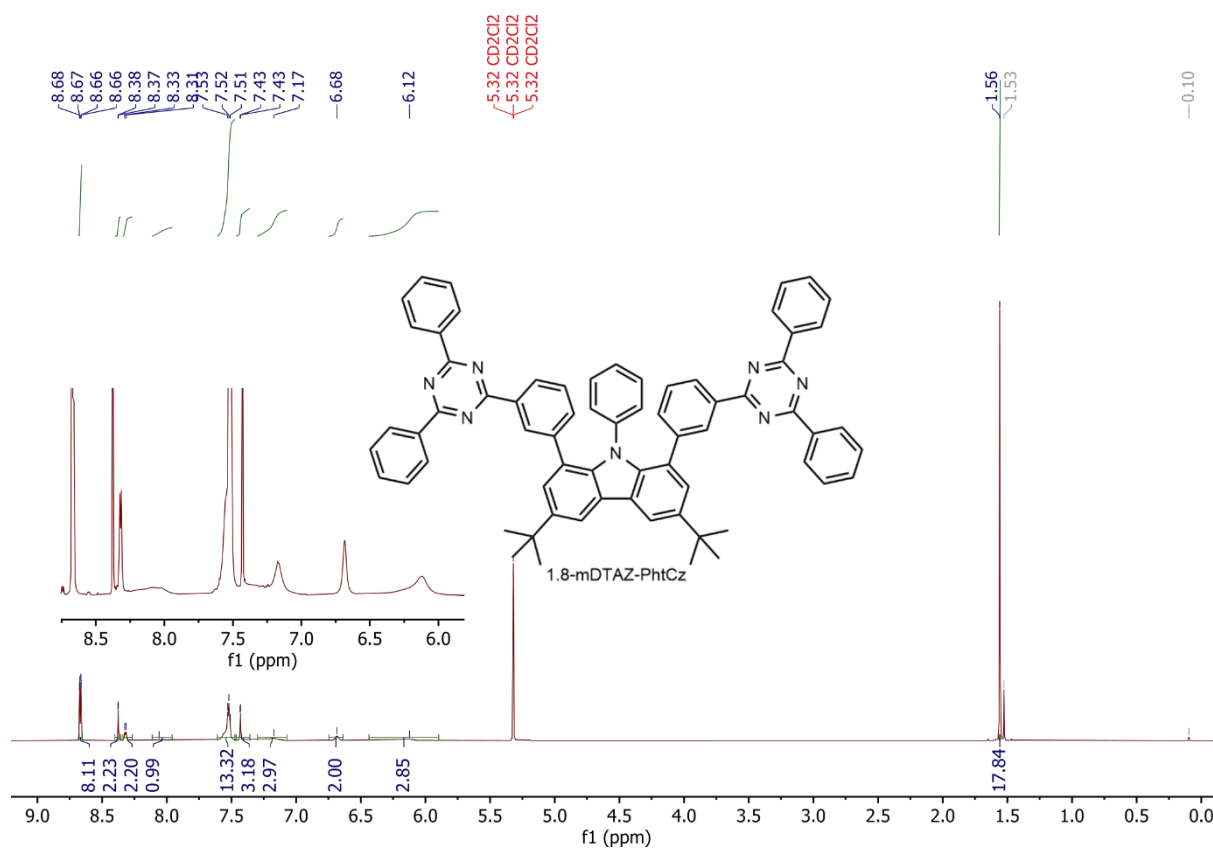


Figure appendix-II-5 ^1H NMR spectrum of compound 1,8-mDTAZ-PhtCz (700 MHz, CD_2Cl_2).

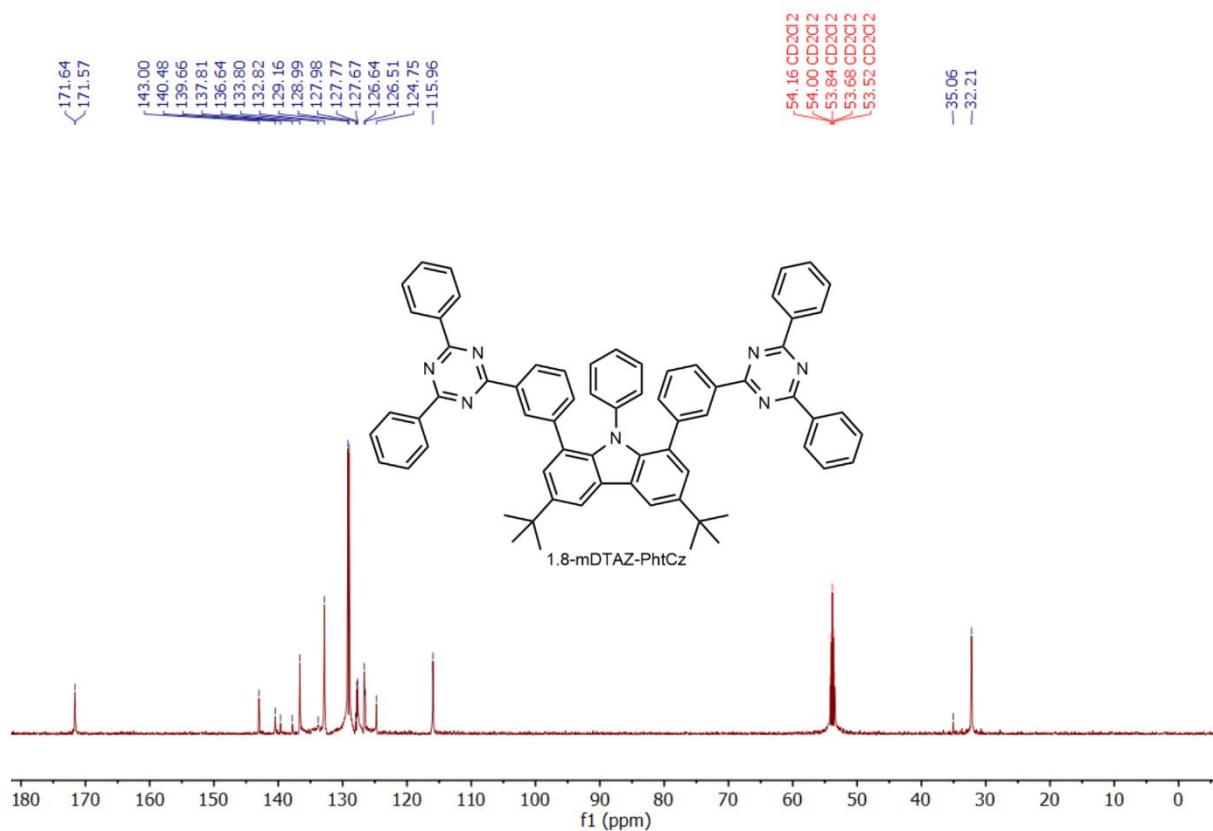


Figure appendix-II-6 ¹³C NMR spectrum of compound 1,8-mDTAZ-PhtCz (176 MHz, CD₂Cl₂).

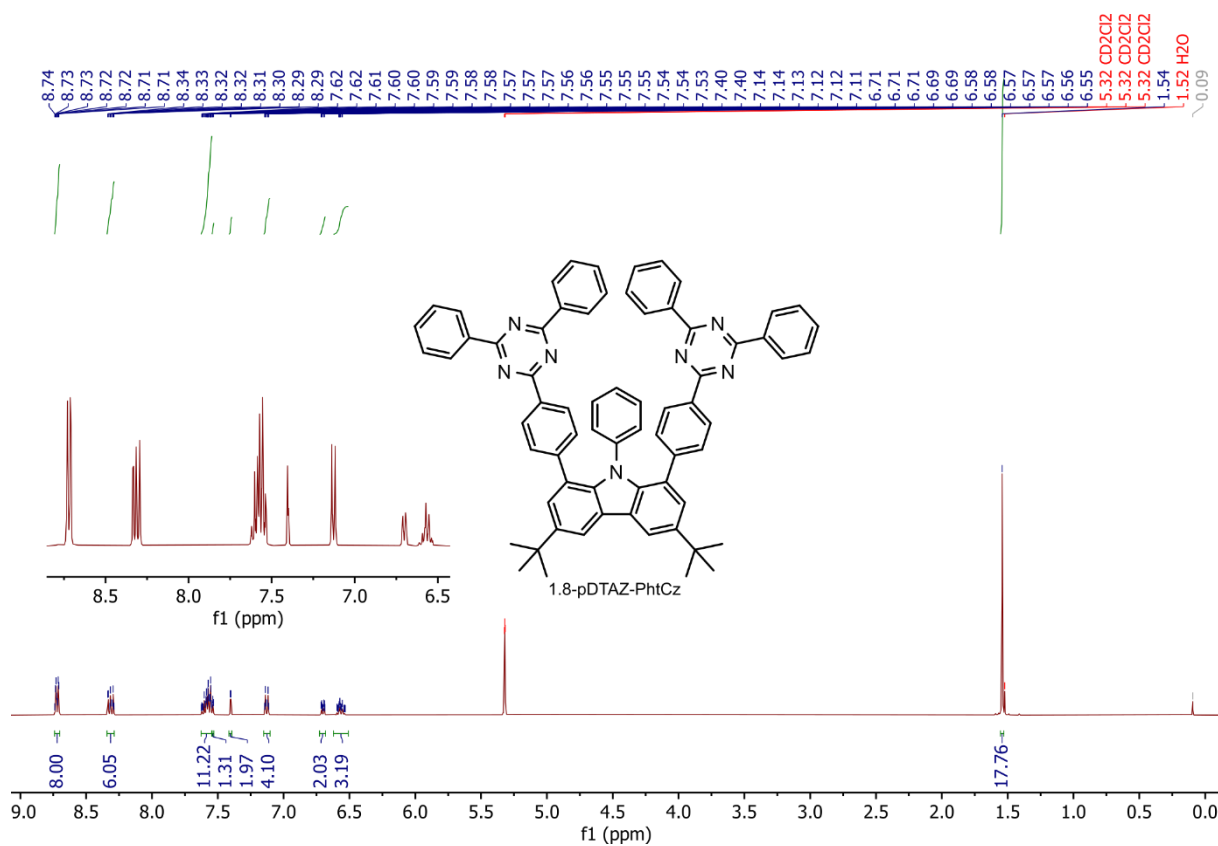


Figure appendix-II-7 ¹H NMR spectrum of compound 1,8-pDTAZ-PhtCz (400 MHz, CD₂Cl₂).

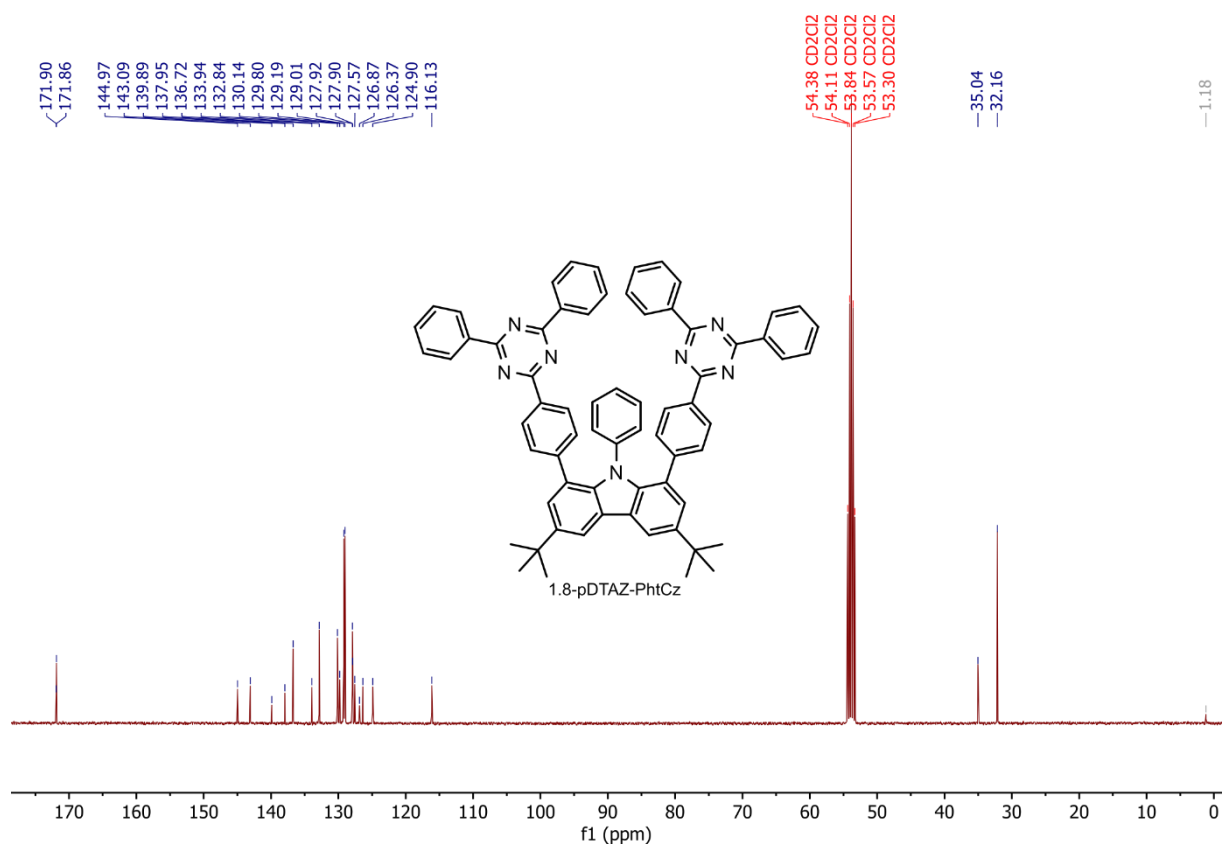


Figure appendix-II-8 ^{13}C NMR spectrum of compound **1,8-pDTAZ-PhtCz** (101MHz, CD_2Cl_2).

Chapter 3

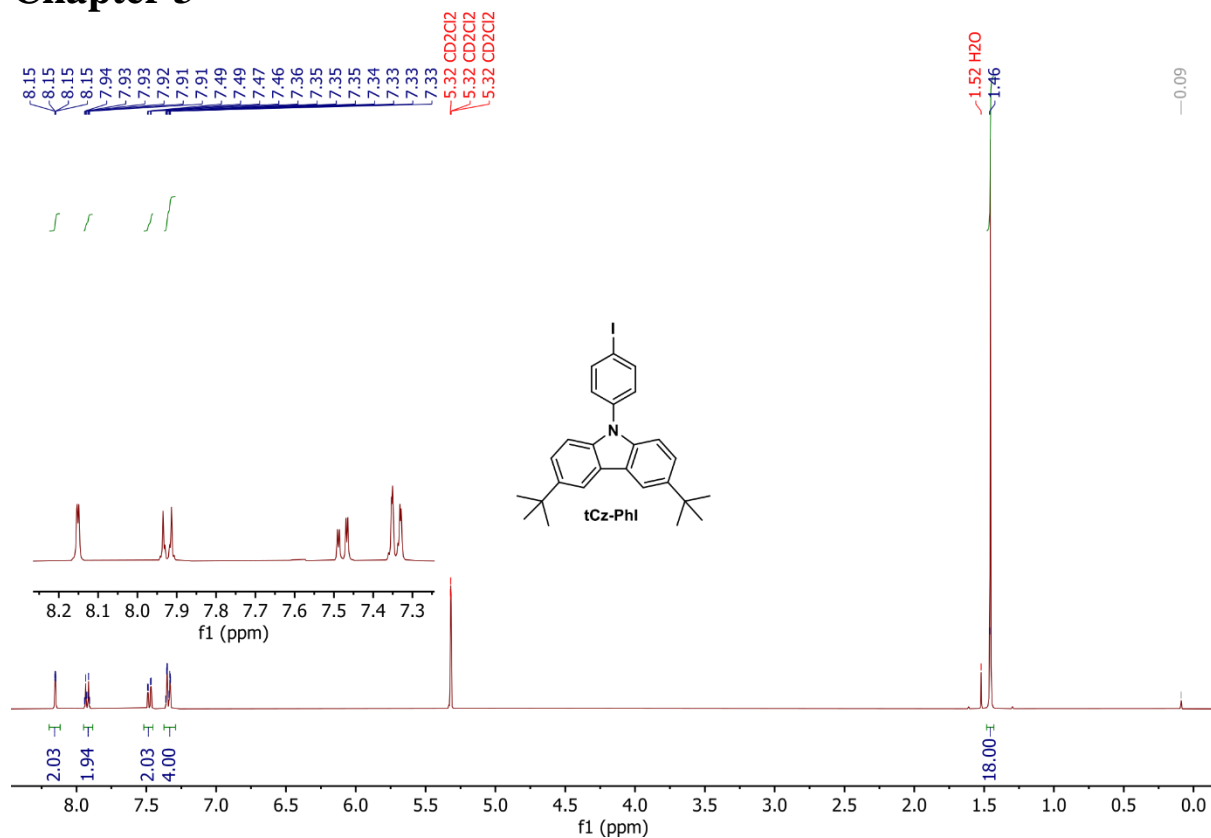


Figure appendix-II-9 ¹H NMR spectrum of compound tCz-PhI (400 MHz, CD₂Cl₂).

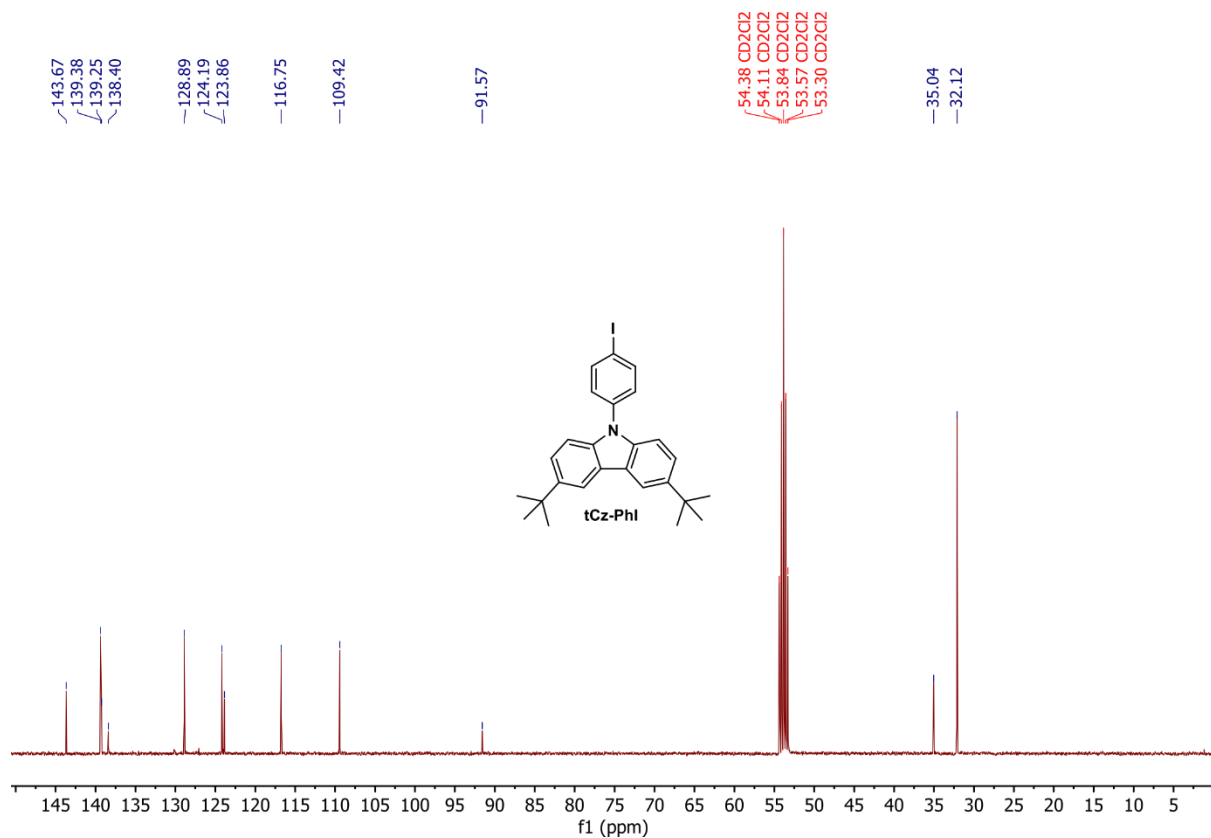


Figure appendix-II-10 ¹³C NMR spectrum of compound tCz-PhI (101 MHz, CD₂Cl₂).

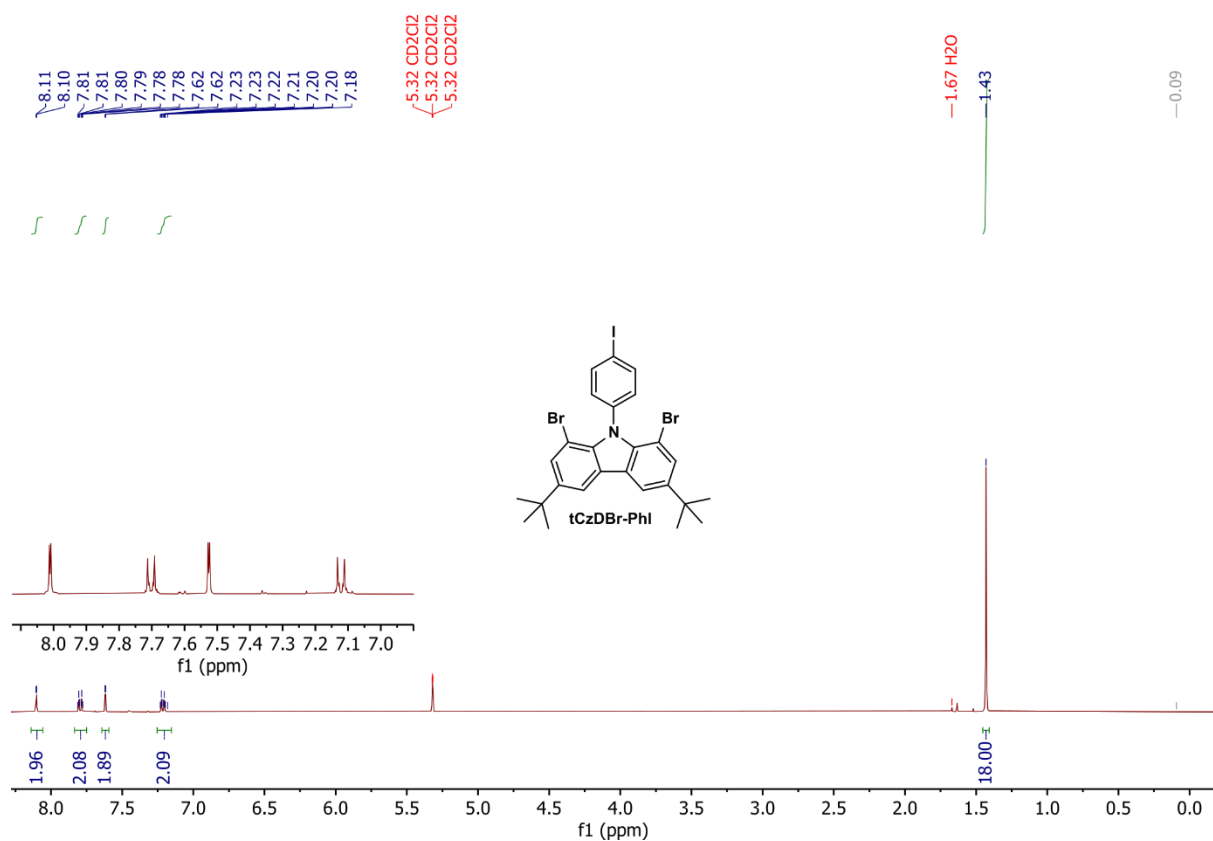


Figure appendix-II-11 ¹H NMR spectrum of compound tCzDBr-PhI (400 MHz, CD₂Cl₂).

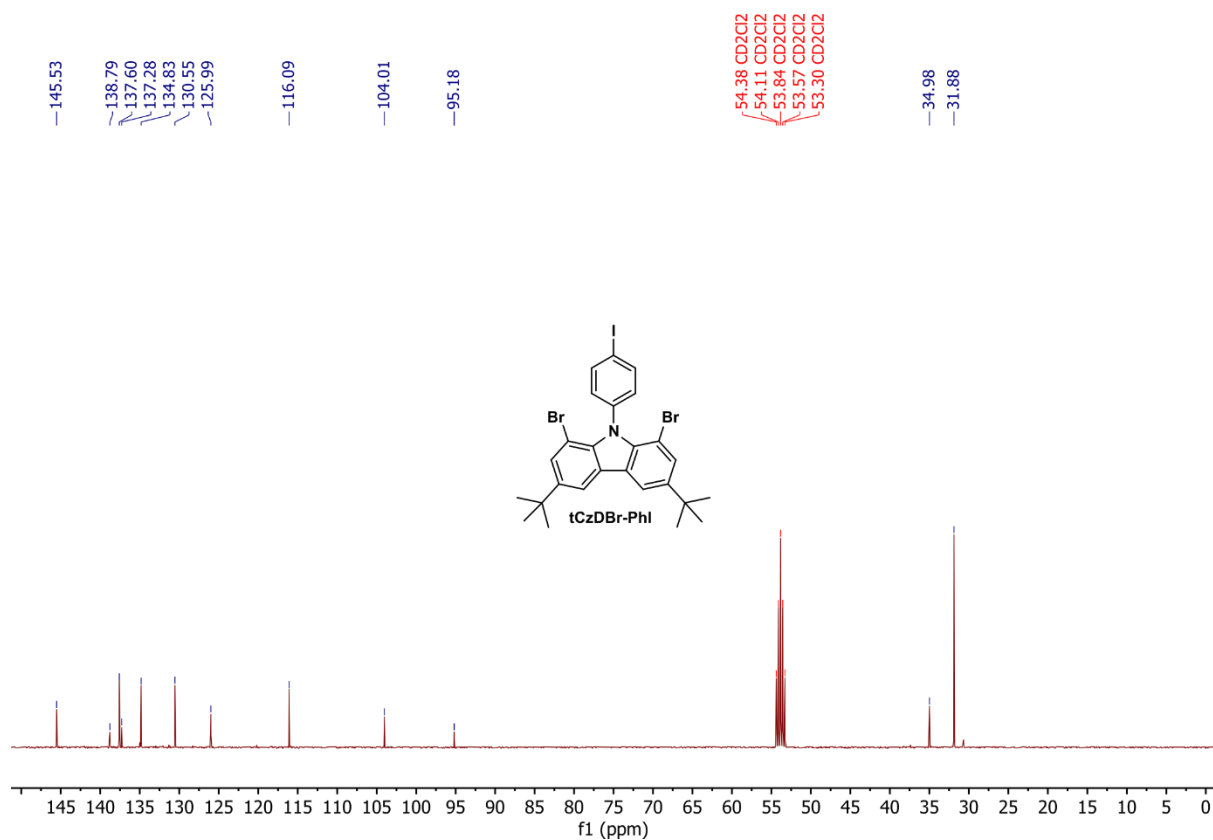


Figure appendix-II-12 ¹³C NMR spectrum of compound tCzDBr-PhI (101 MHz, CD₂Cl₂).

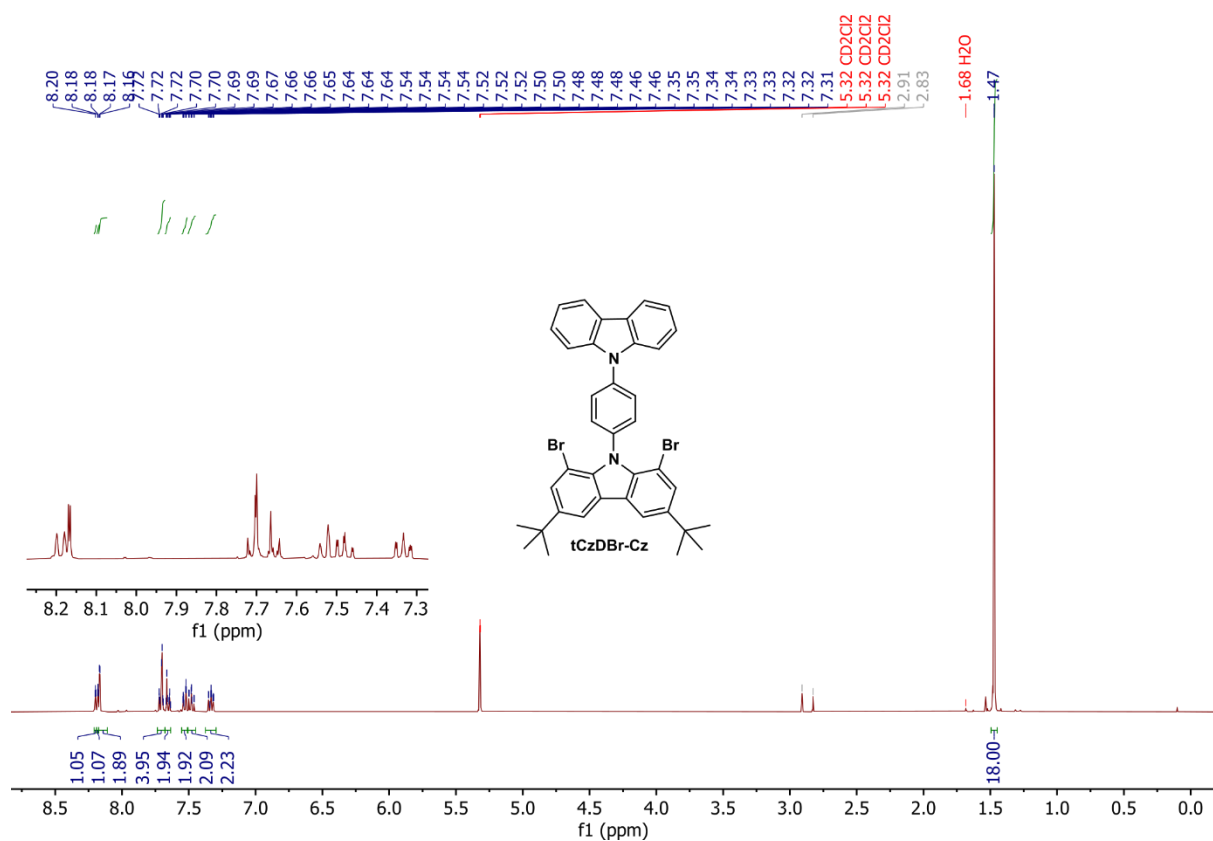


Figure appendix-II-13 ¹H NMR spectrum of compound tCzDBr-Cz (400 MHz, CD₂Cl₂).

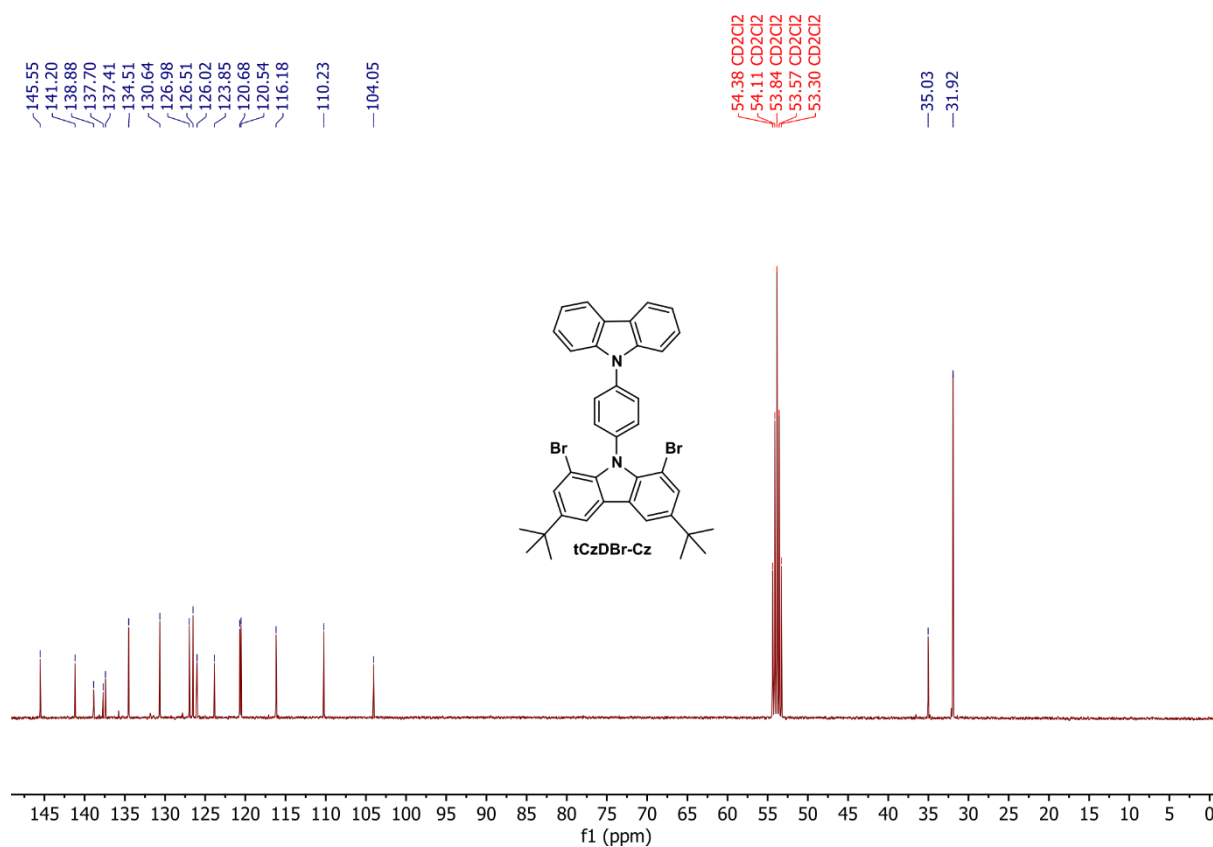


Figure appendix-II-14 ¹³C NMR spectrum of compound tCzDBr-Cz (101 MHz, CD₂Cl₂).

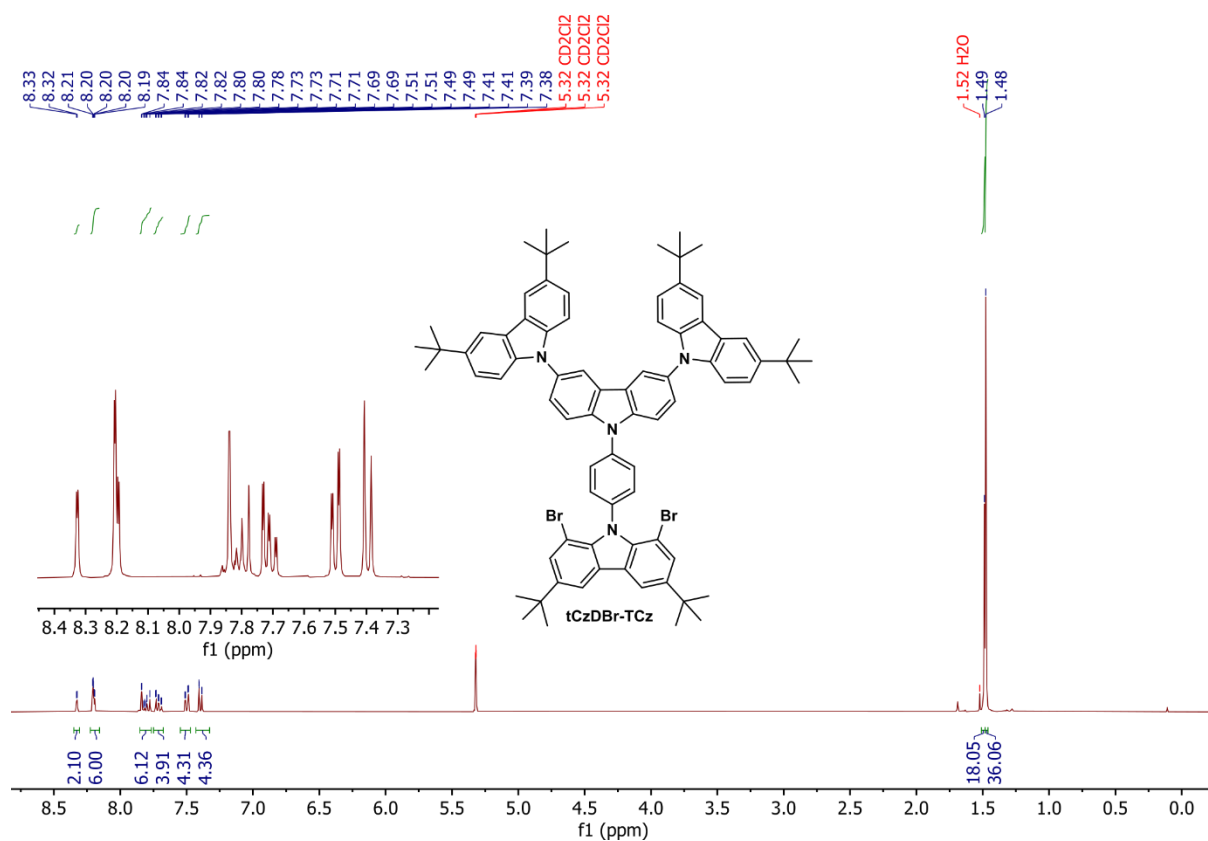


Figure appendix-II-15 ¹H NMR spectrum of compound tCzDBr-tCz (400 MHz, CD₂Cl₂).

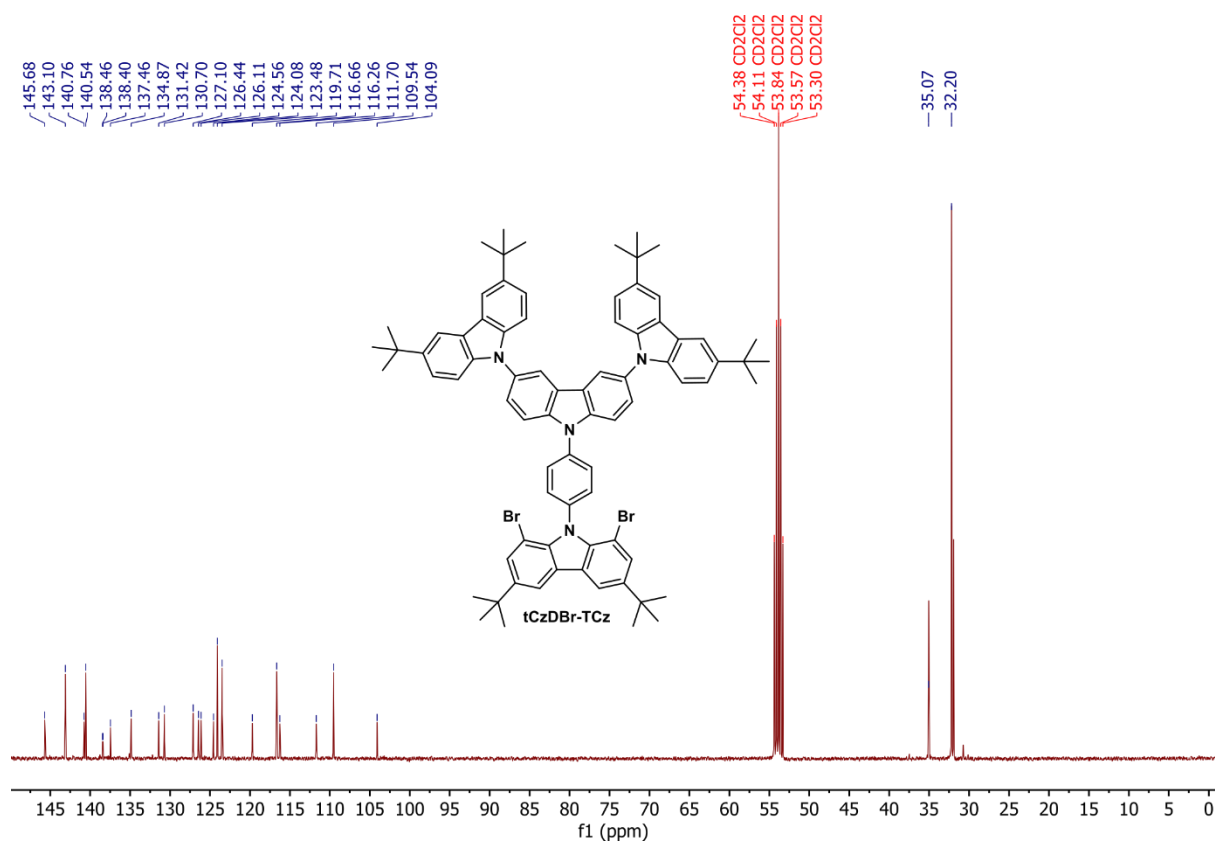


Figure appendix-II-16 ¹³C NMR spectrum of compound tCzDBr-tCz (101 MHz, CD₂Cl₂).

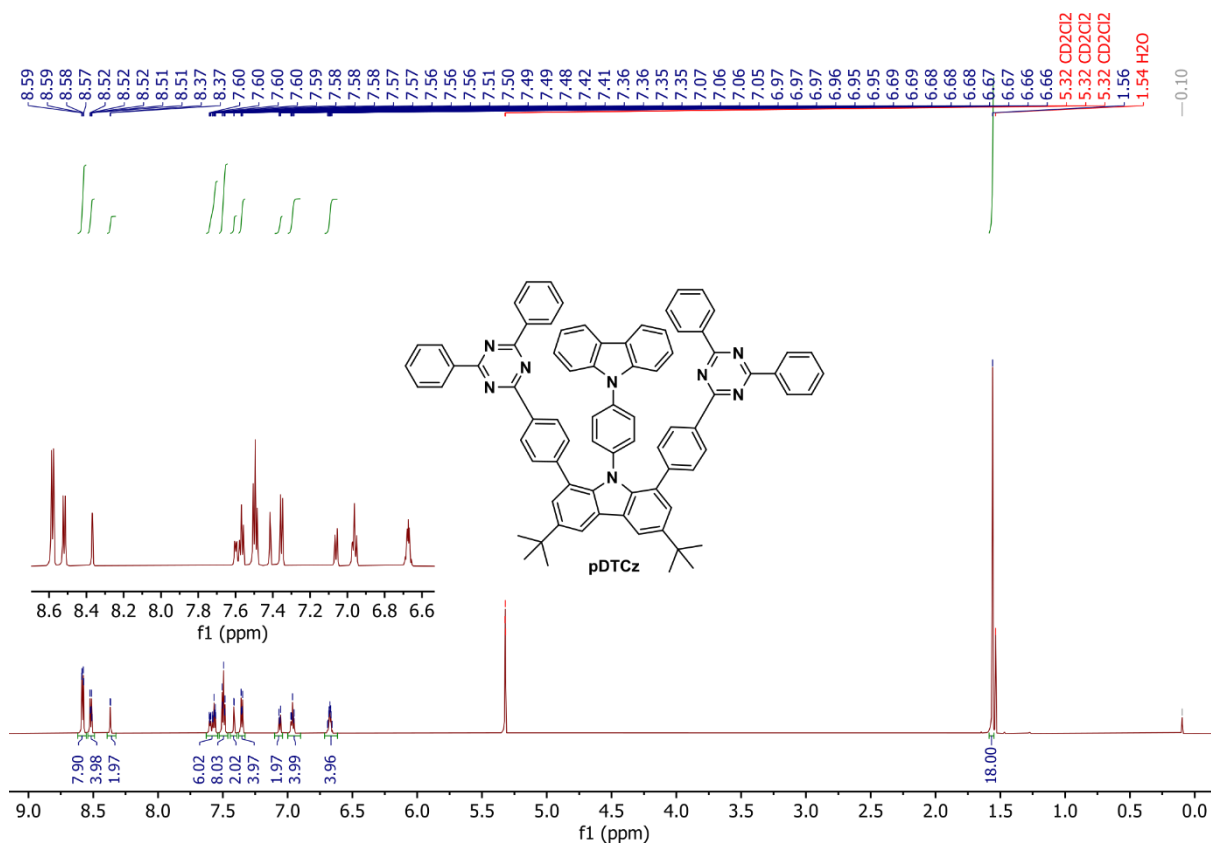


Figure appendix-II-19 ¹H NMR spectrum of compound pDTCz (700 MHz, CD₂Cl₂).

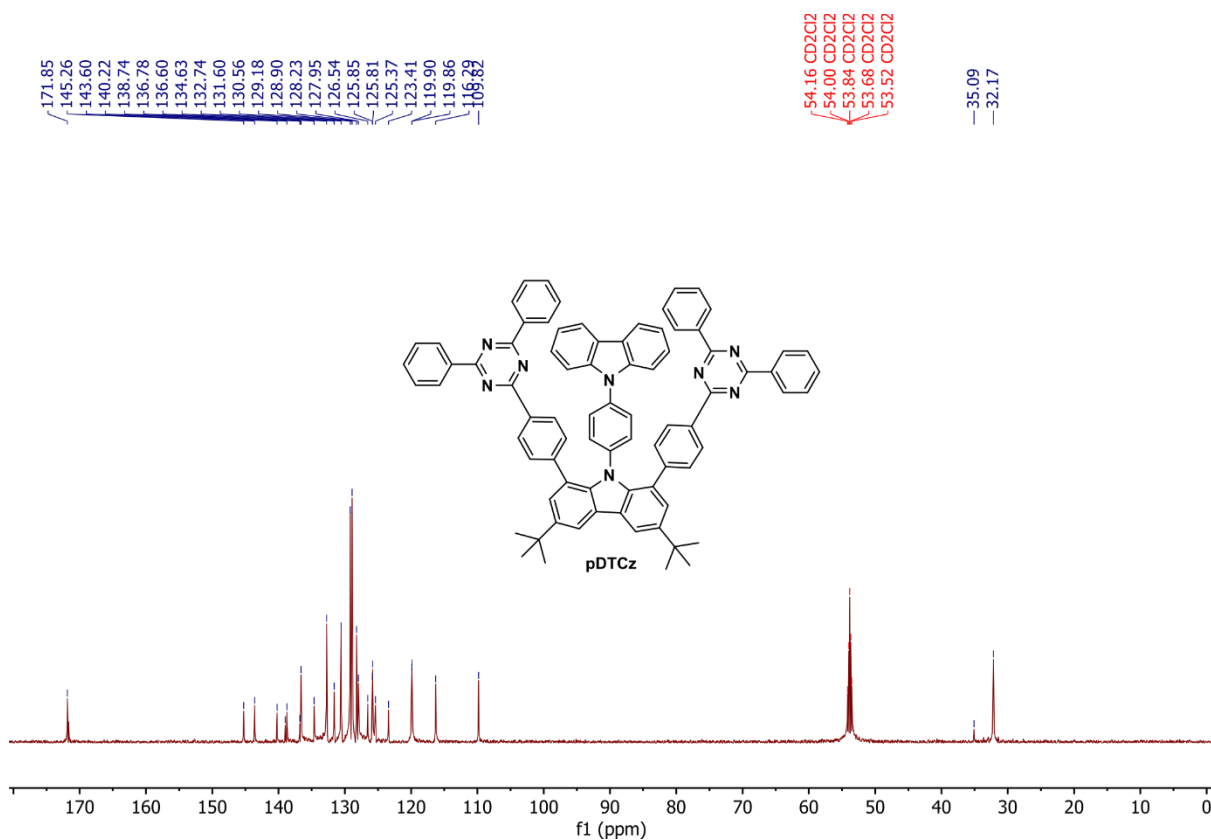


Figure appendix-II-20 ¹³C NMR spectrum of compound pDTCz (176 MHz, CD₂Cl₂).

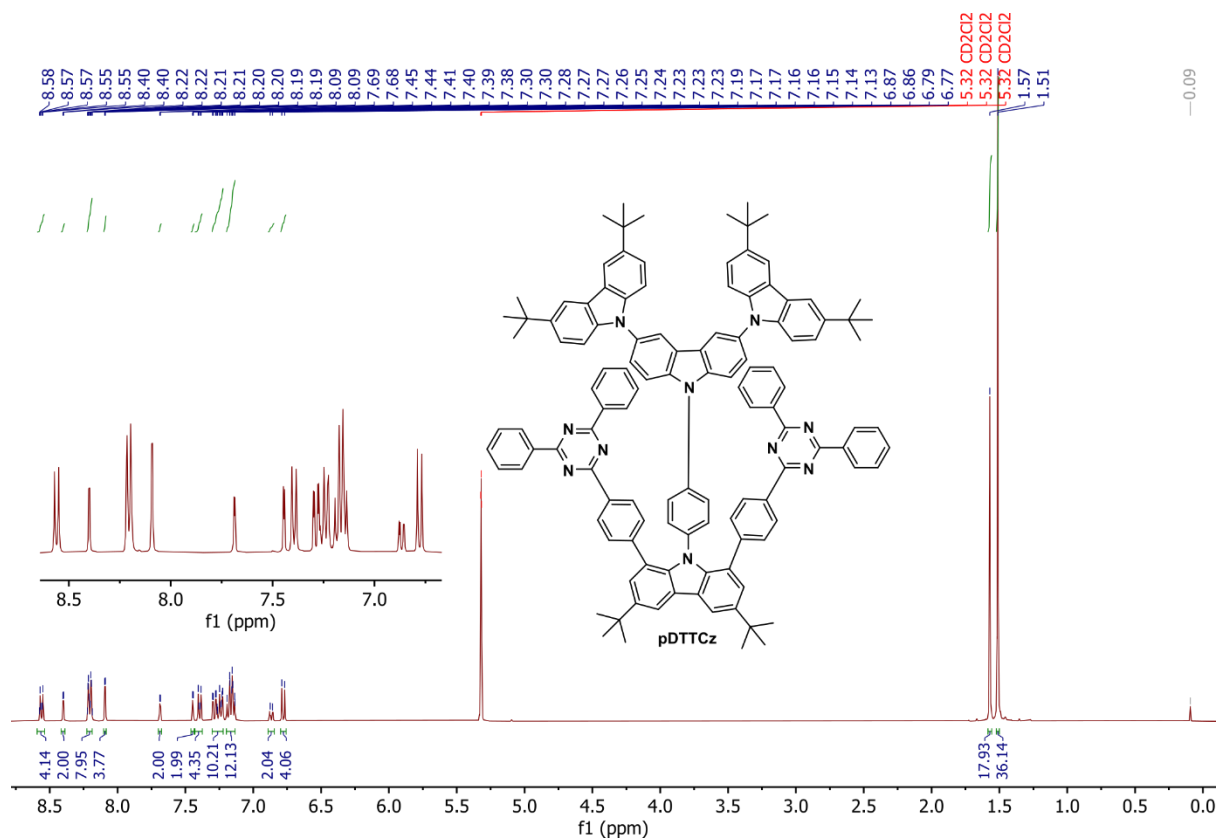


Figure appendix-II-21 ^1H NMR spectrum of compound pDTTCz (400 MHz, CD_2Cl_2).

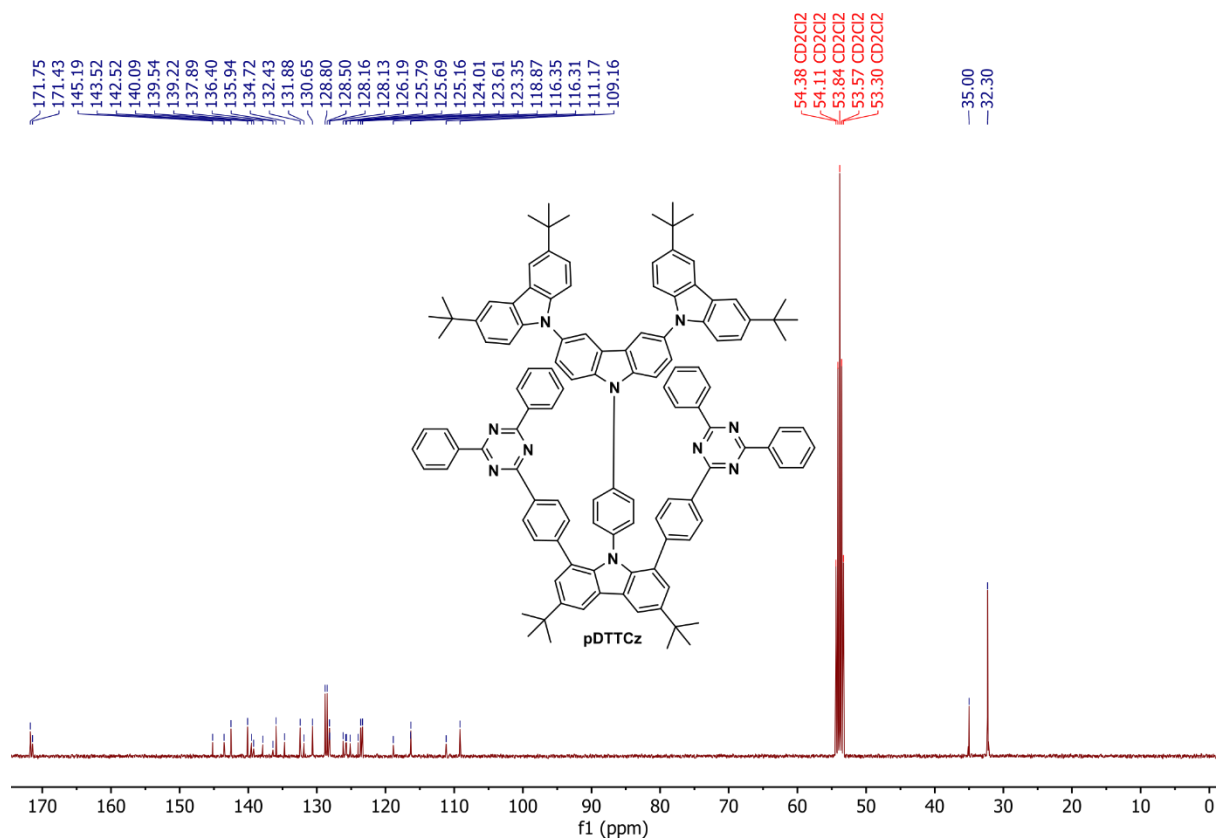


Figure appendix-II-22 ^{13}C NMR spectrum of compound pDTTCz (101 MHz, CD_2Cl_2).

Chapter 4

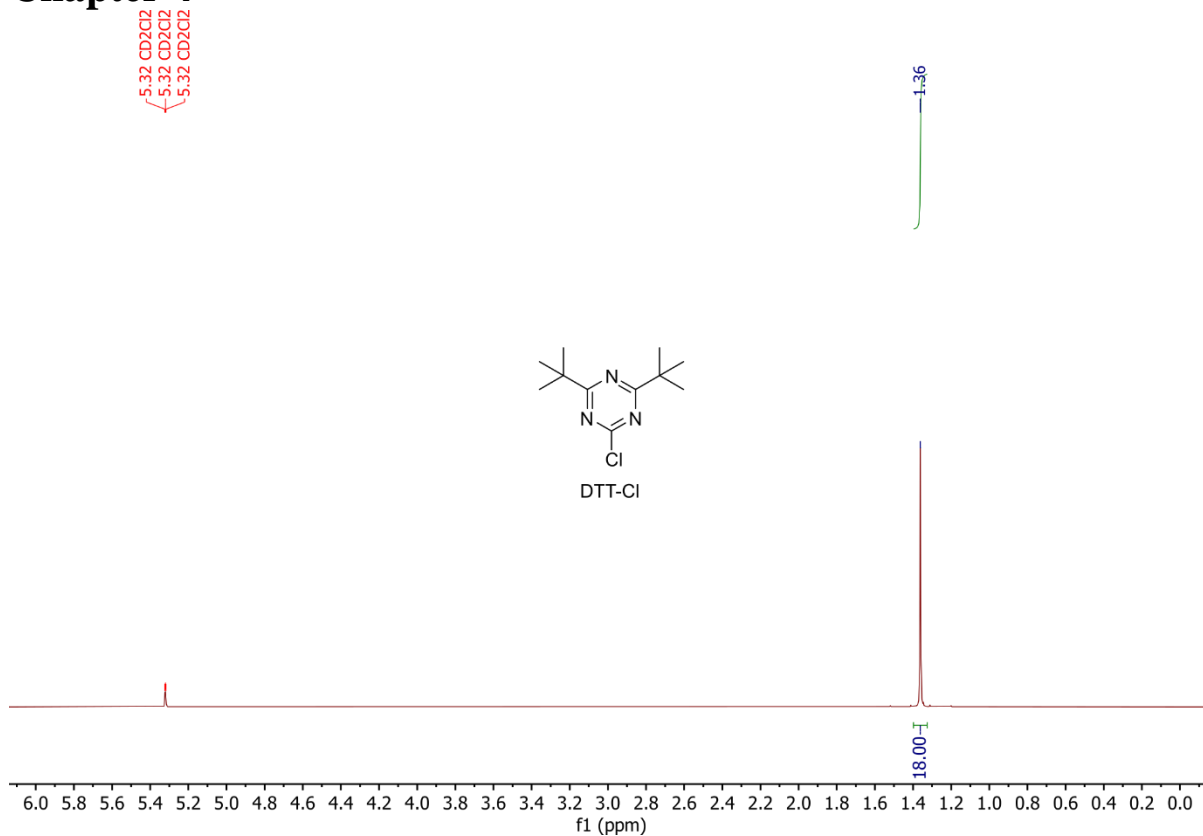


Figure appendix-II-23 ^1H NMR spectrum of compound DTT-Cl (400 MHz, CD_2Cl_2).

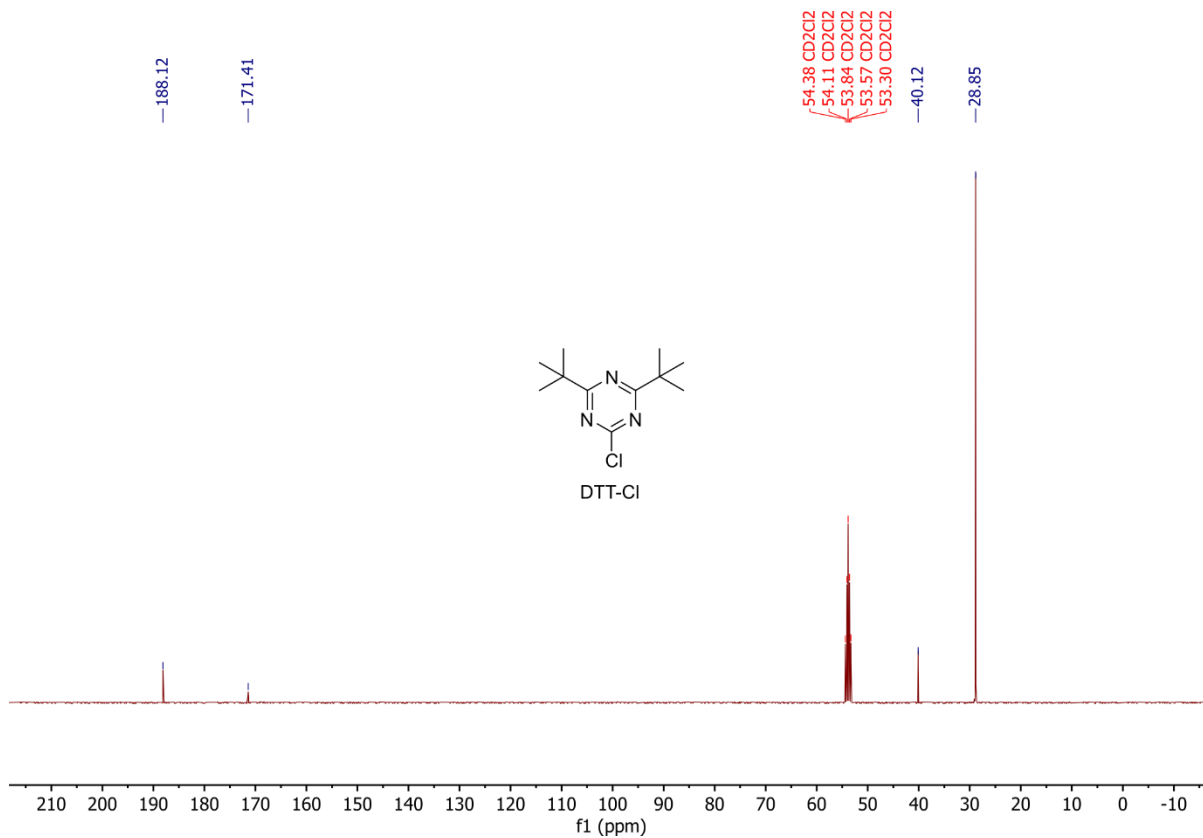


Figure appendix-II-24 ^{13}C NMR spectrum of compound DTT-Cl (101 MHz, CD_2Cl_2).

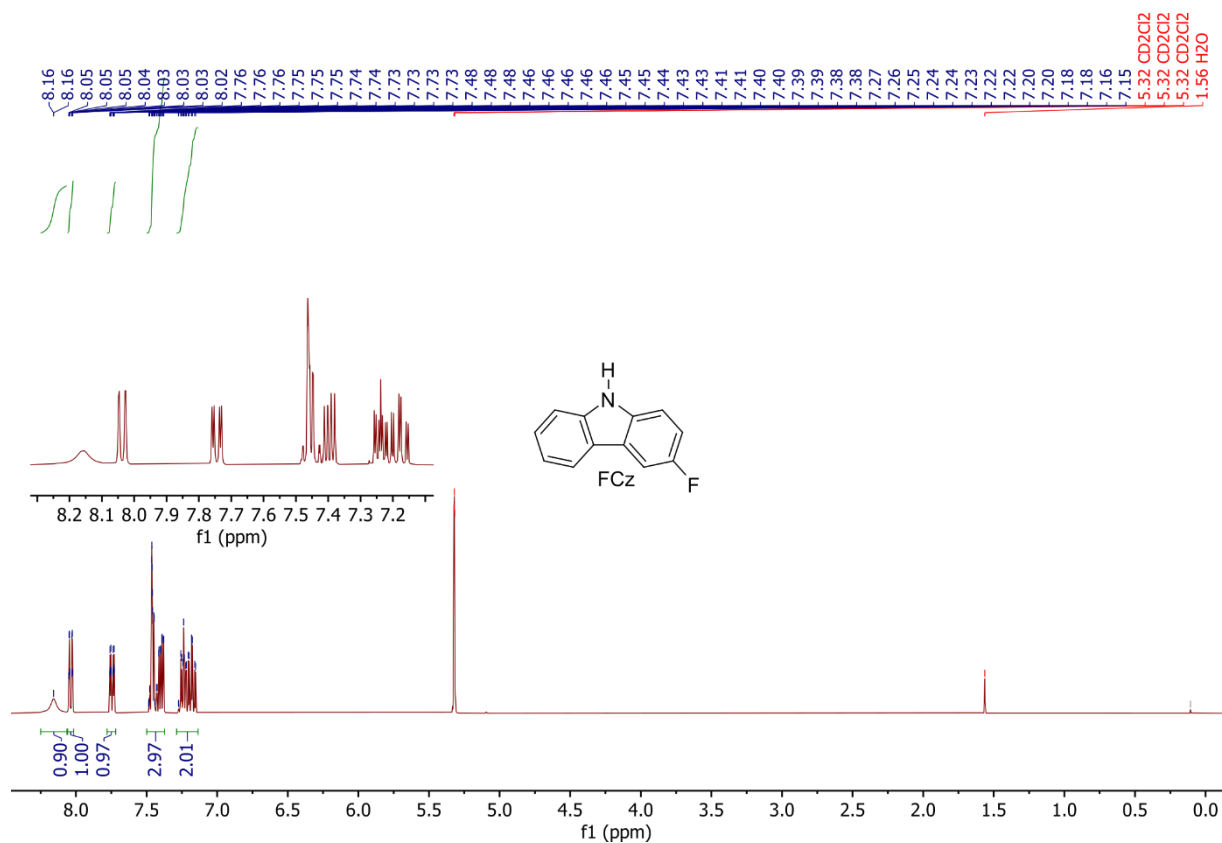


Figure appendix-II-25 ^1H NMR spectrum of compound FCz (400 MHz, CD_2Cl_2).

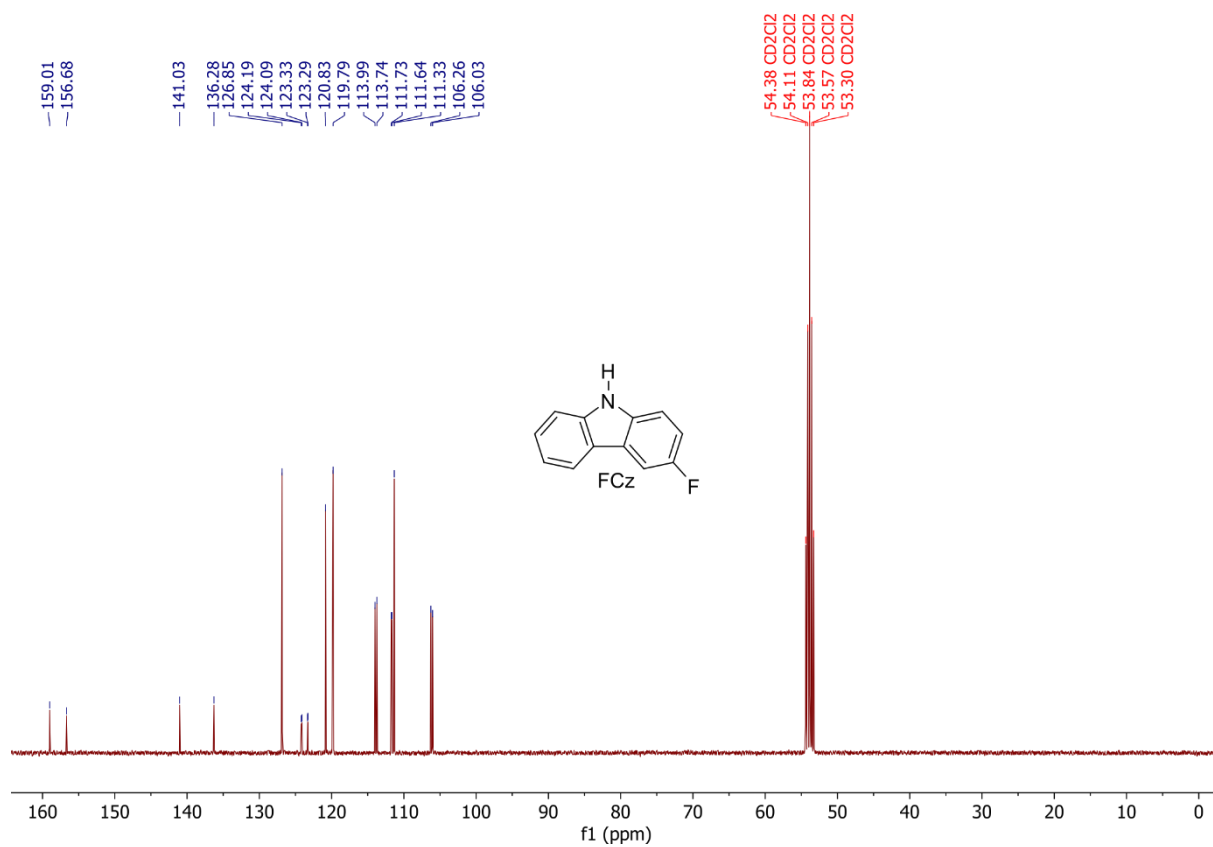


Figure appendix-II-36 ^{13}C NMR spectrum of compound FCz (101 MHz, CD_2Cl_2).

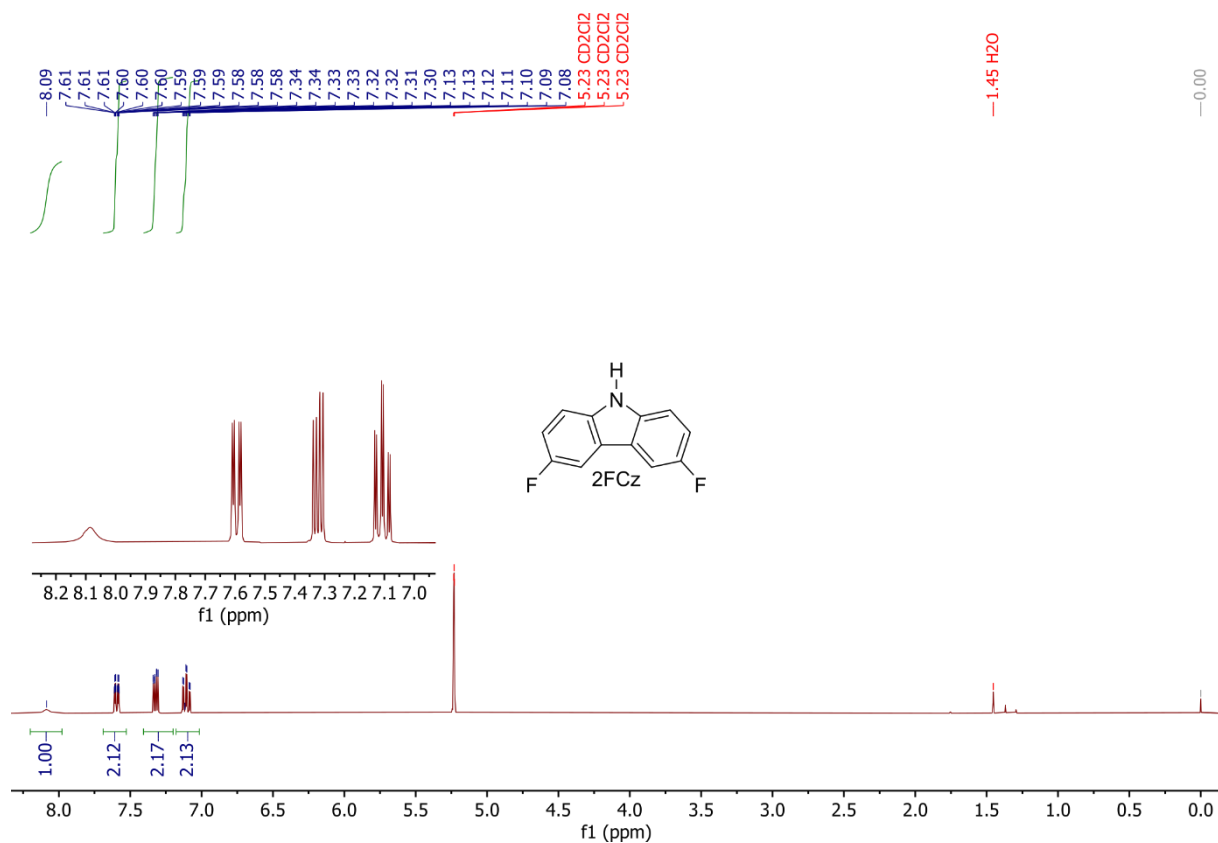


Figure appendix-II-27 $^1\text{H NMR}$ spectrum of compound 2FCz (400 MHz, CD_2Cl_2).

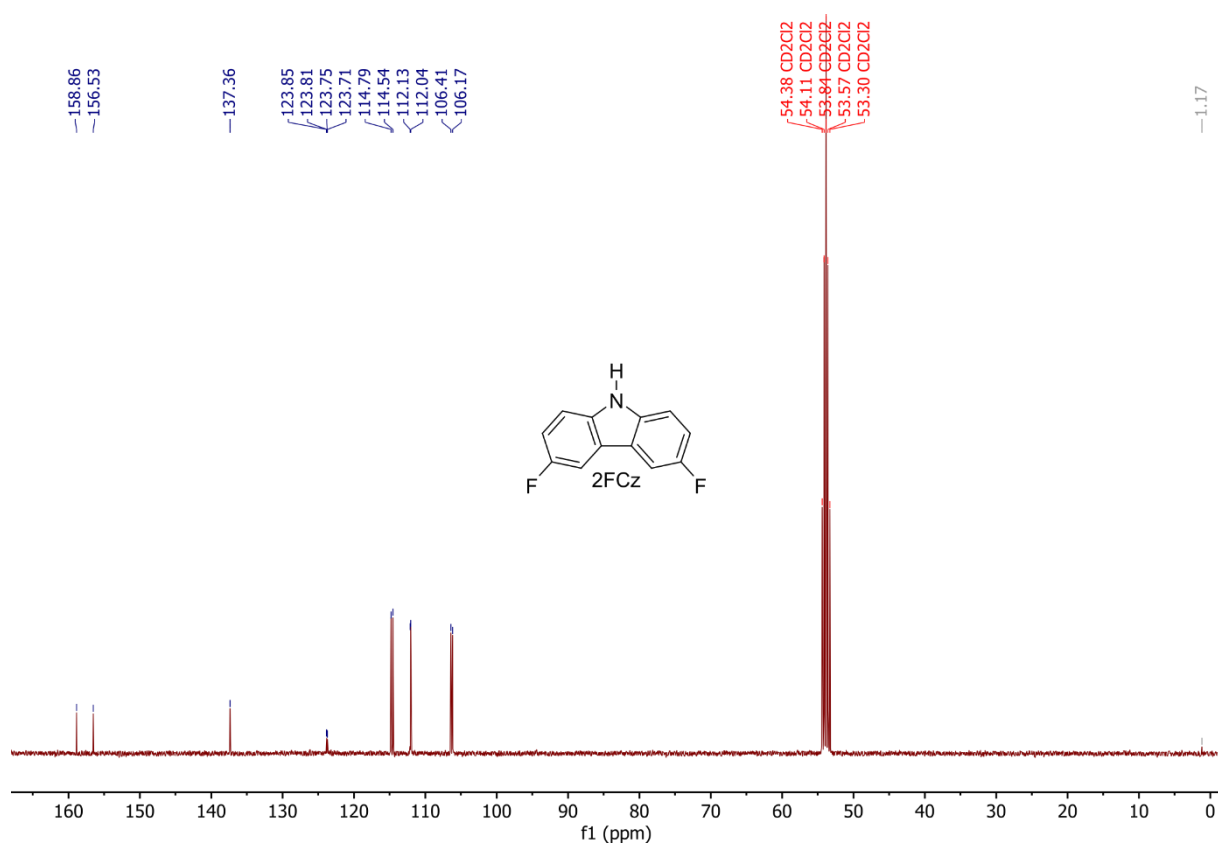


Figure appendix-II-28 $^{13}\text{C NMR}$ spectrum of compound 2FCz (101 MHz, CD_2Cl_2).

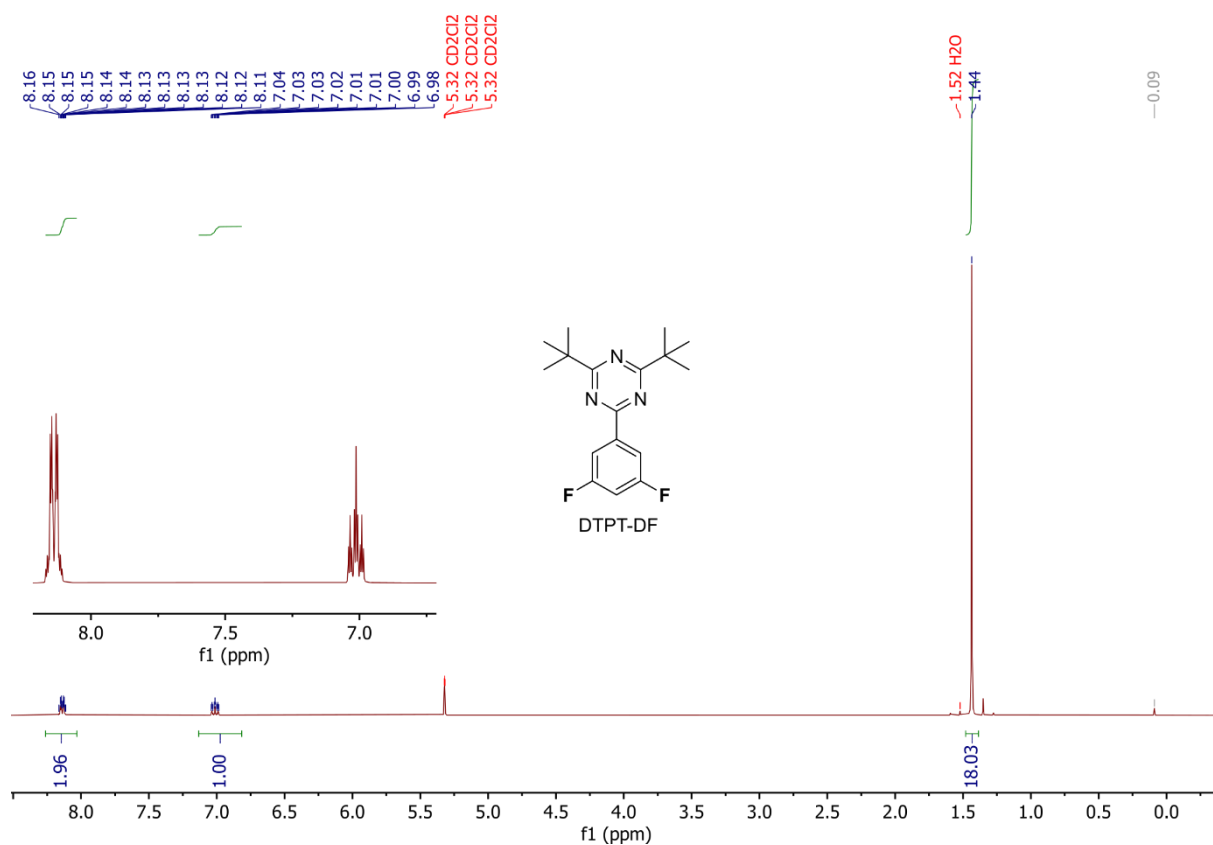


Figure appendix-II-29 ^1H NMR spectrum of compound DTPT-DF (400 MHz, CD_2Cl_2).

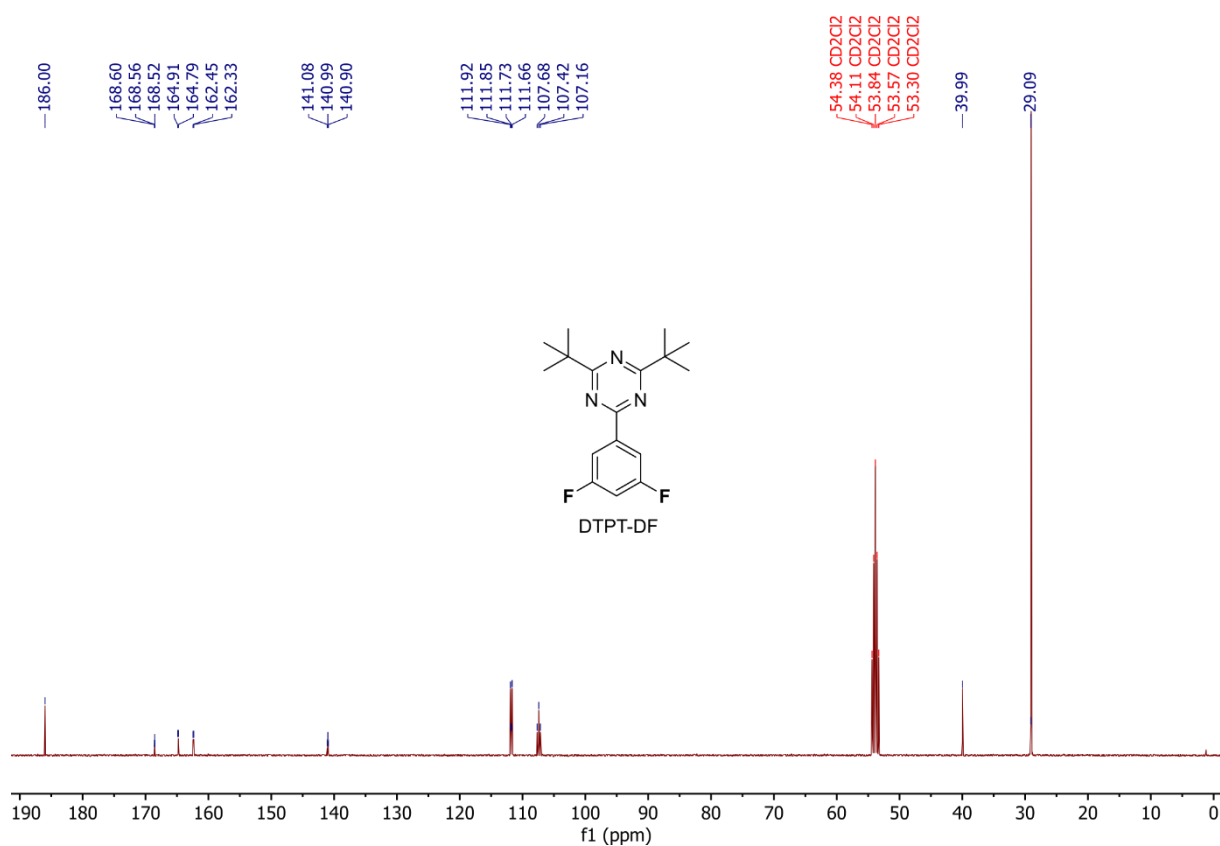


Figure appendix-II-30 ^{13}C NMR spectrum of compound DTPT-DF (101 MHz, CD_2Cl_2).

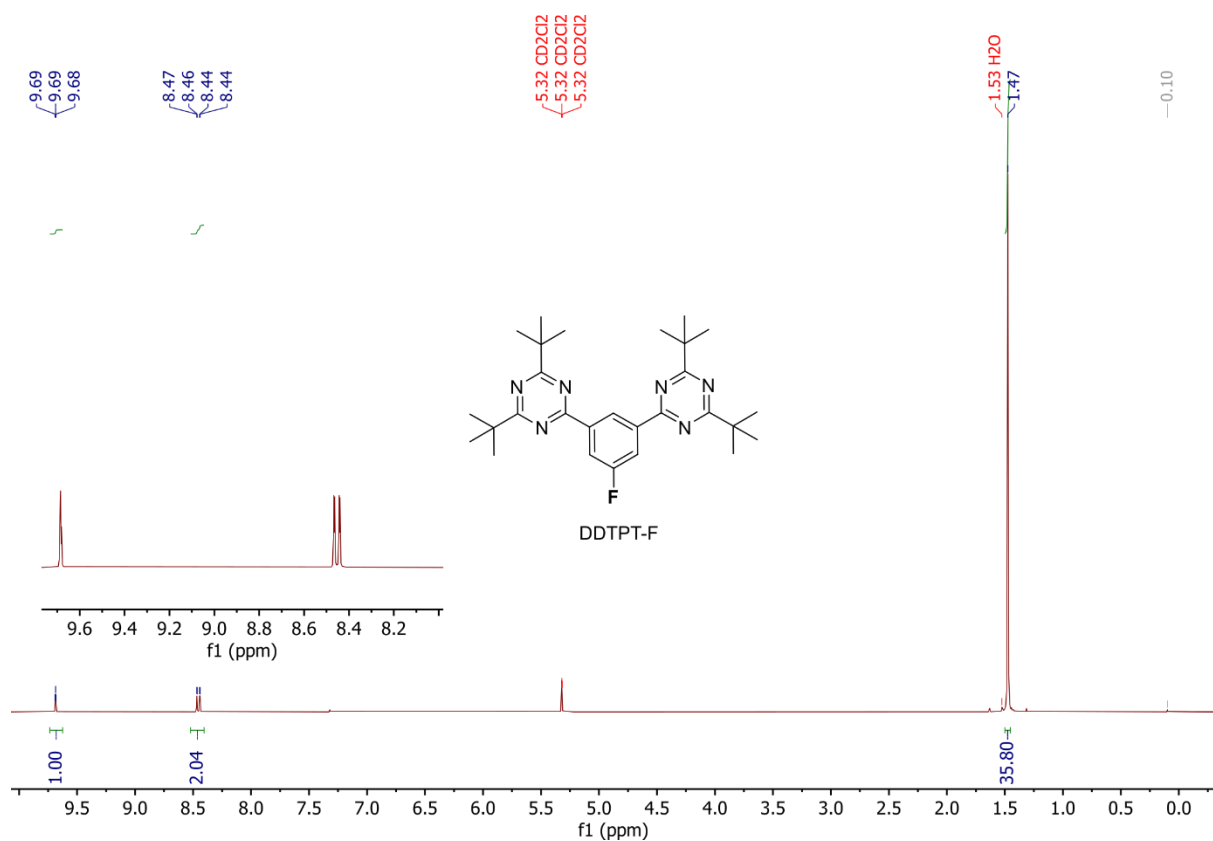


Figure appendix-II-31 ¹H NMR spectrum of compound DDTPT-F (400 MHz, CD₂Cl₂).

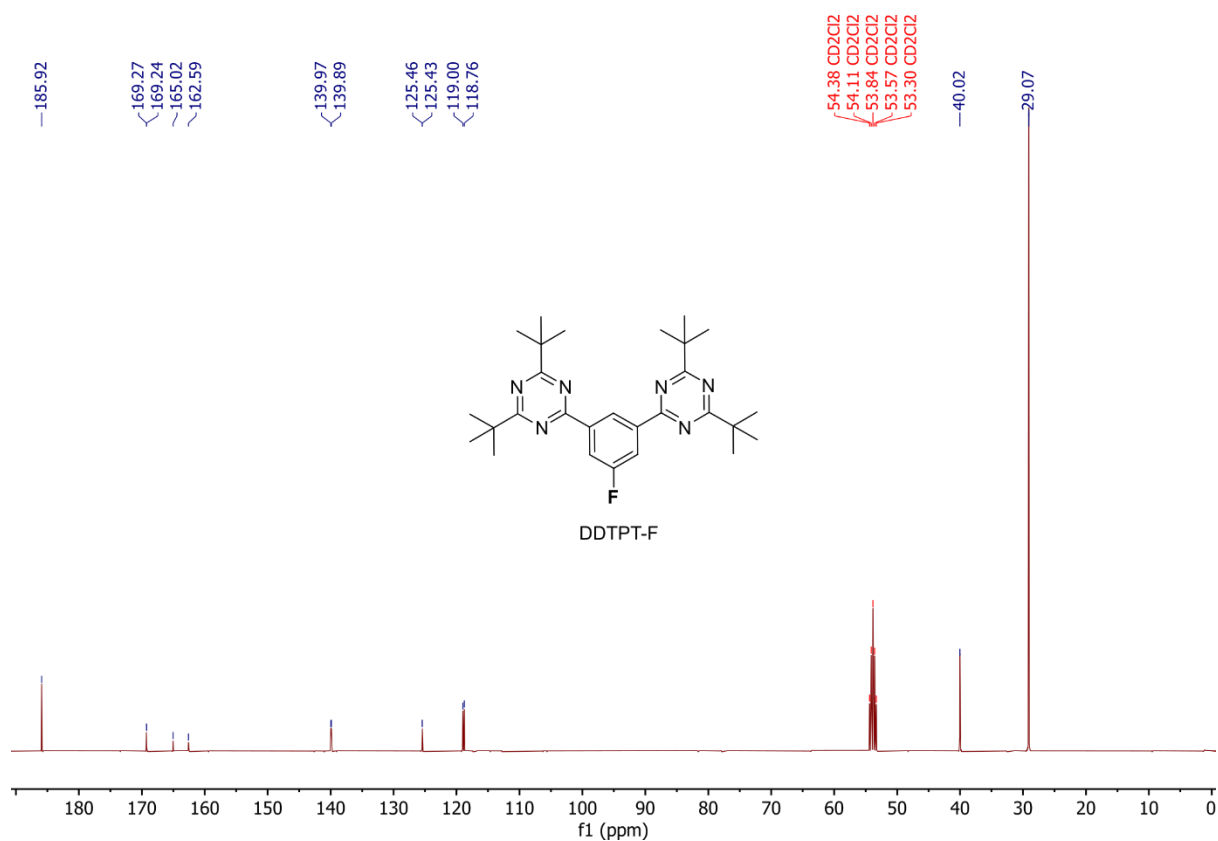


Figure appendix-II-32 ¹³C NMR spectrum of compound DDTPT-F (101 MHz, CD₂Cl₂).

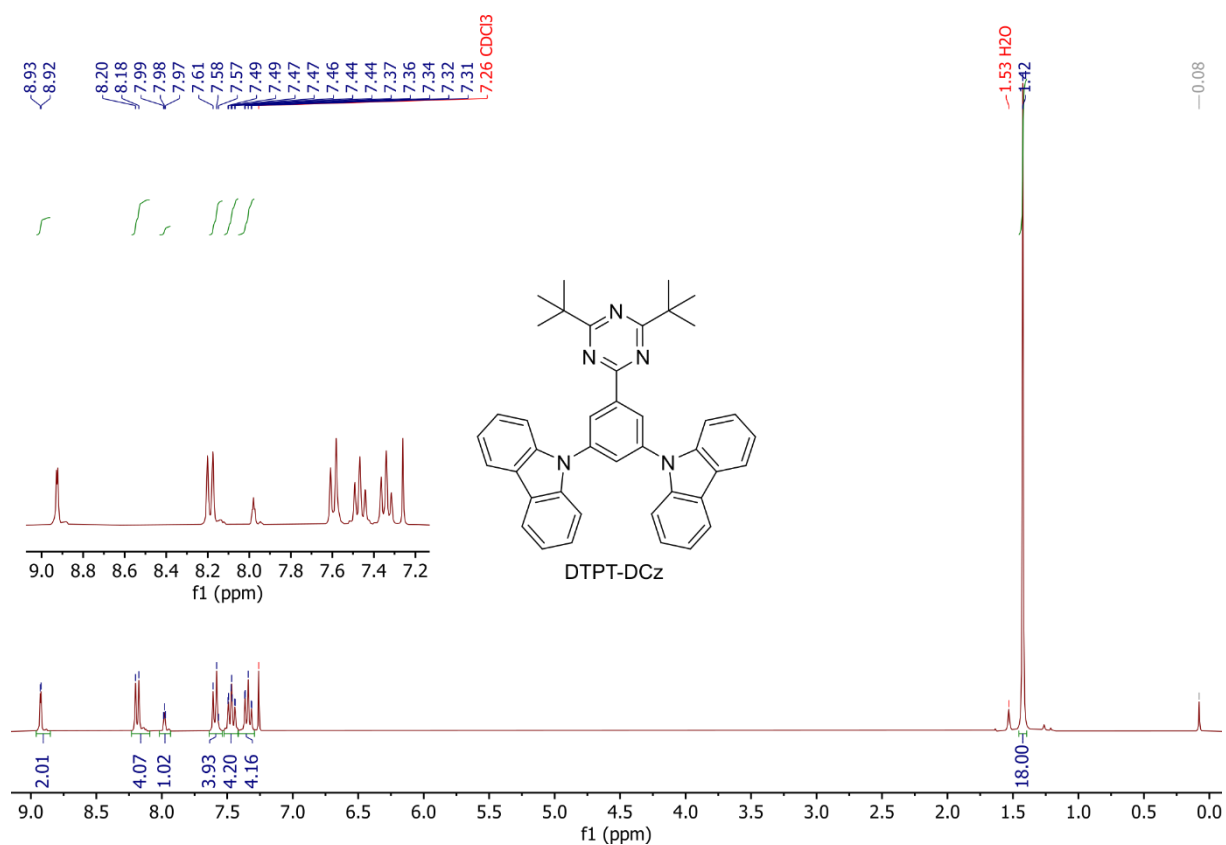


Figure appendix-II-33 ^1H NMR spectrum of compound DTPT-DCz (400 MHz, CDCl_3).

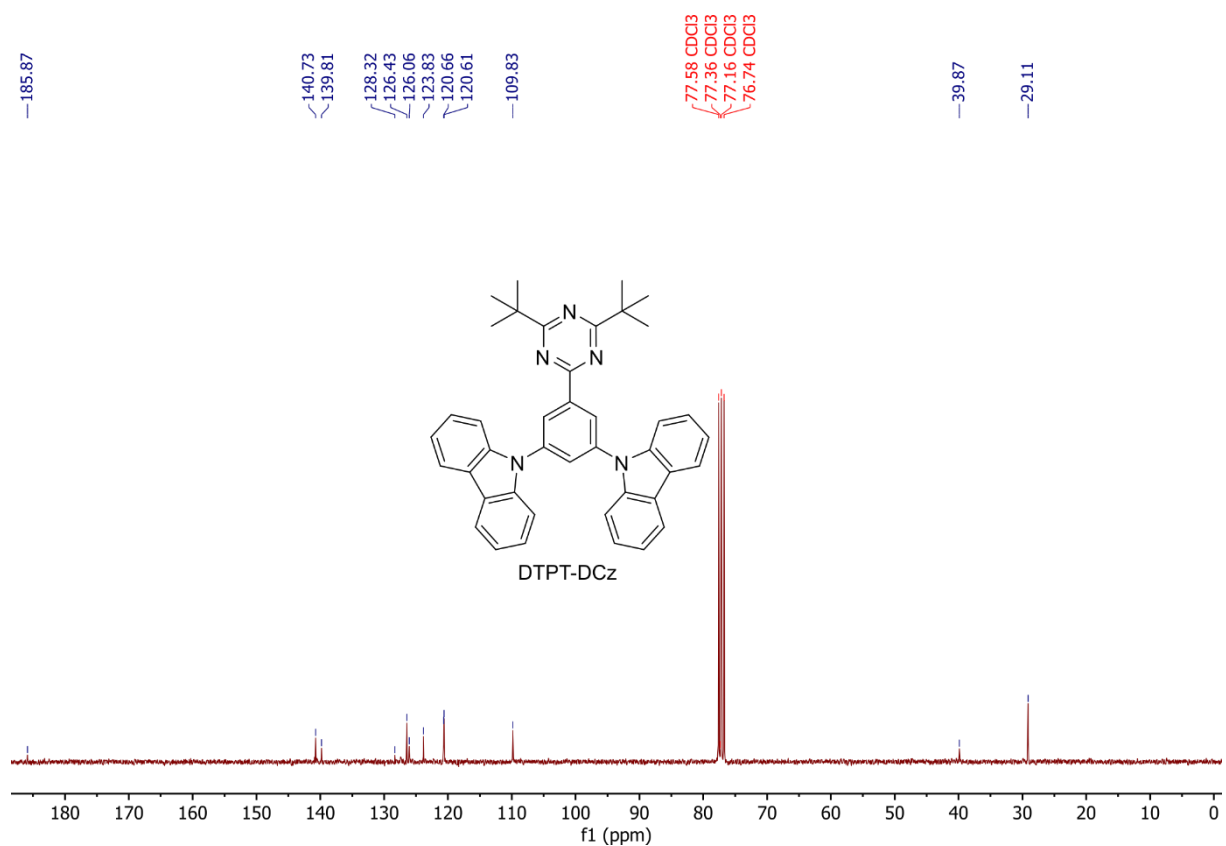


Figure appendix-II-34 ^{13}C NMR spectrum of compound DTPT-DCz (101 MHz, CDCl_3).

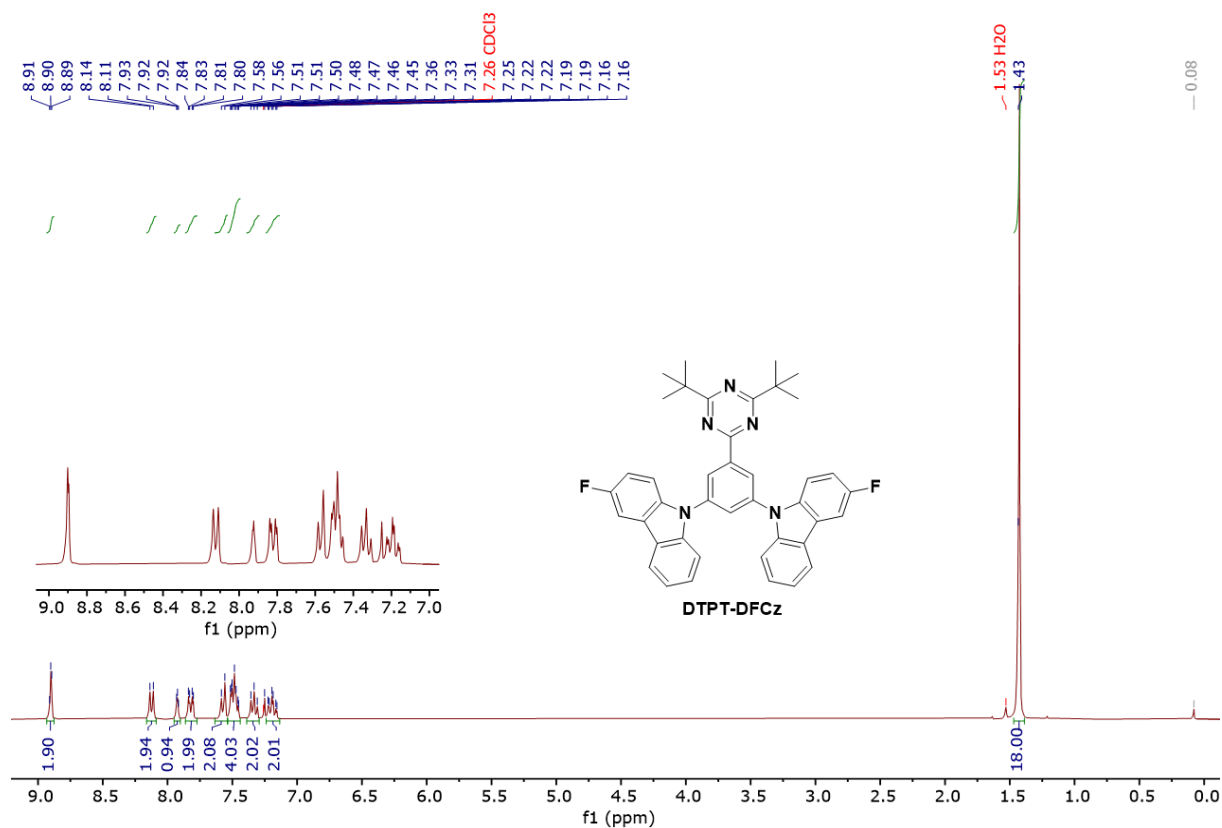


Figure appendix-II-35 ¹H NMR spectrum of compound DTPT-DFCz (400 MHz, CDCl₃).

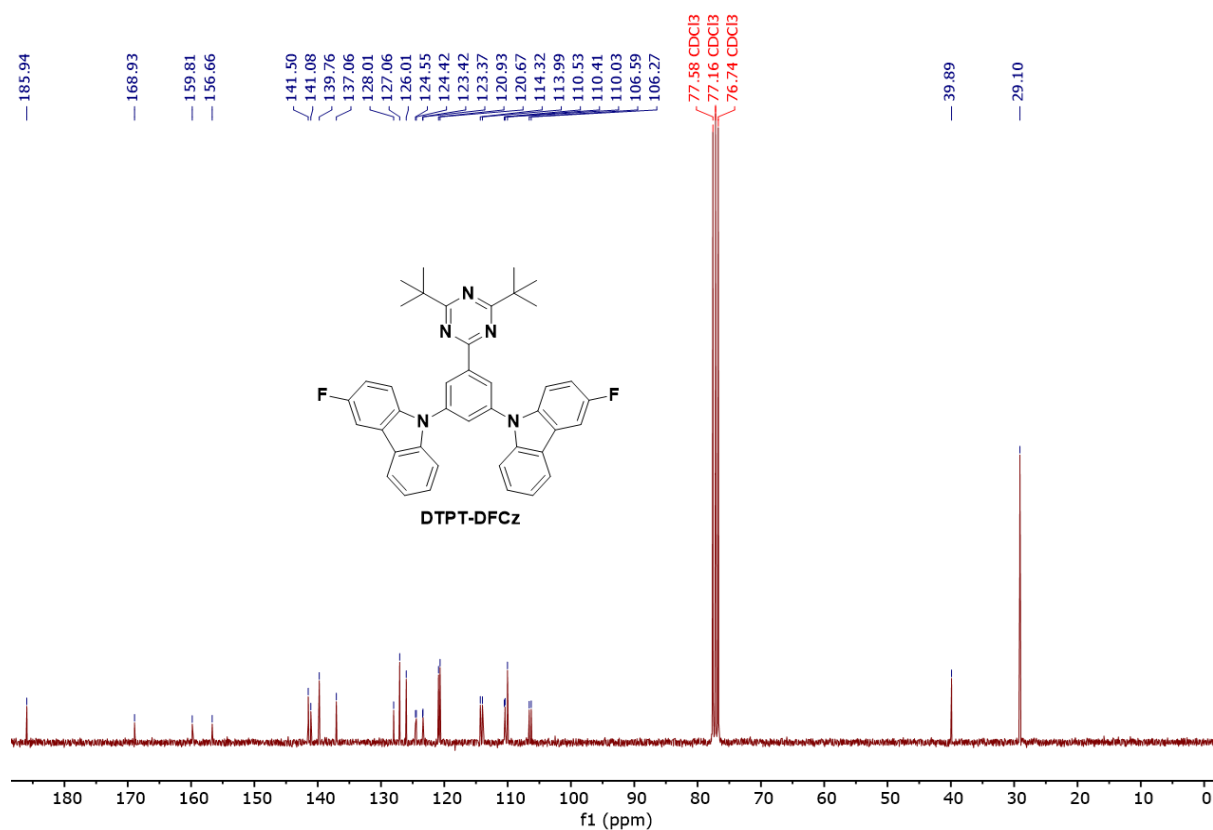


Figure appendix-II-36 ¹³C NMR spectrum of compound DTPT-DFCz (101 MHz, CDCl₃).

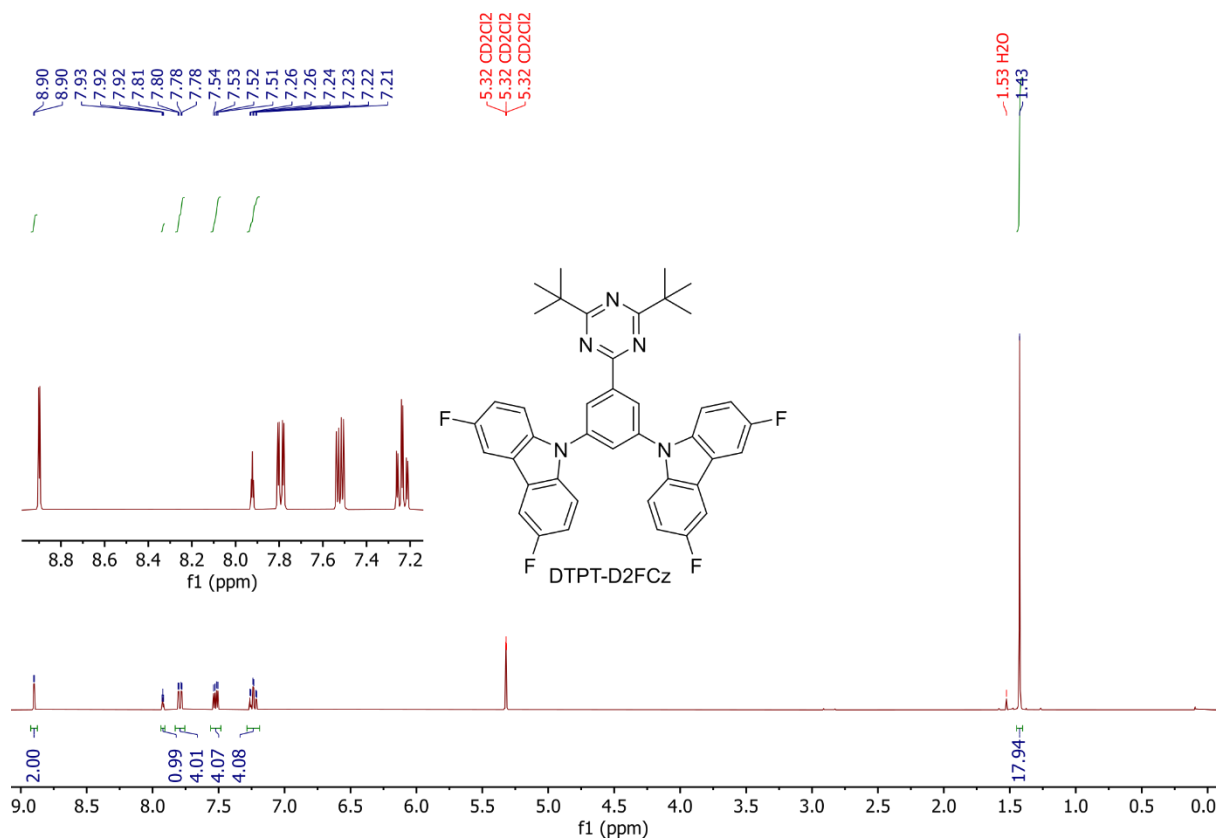


Figure appendix-II-37 ^1H NMR spectrum of compound DTPT-D2FCz (400 MHz, CDCl_3).

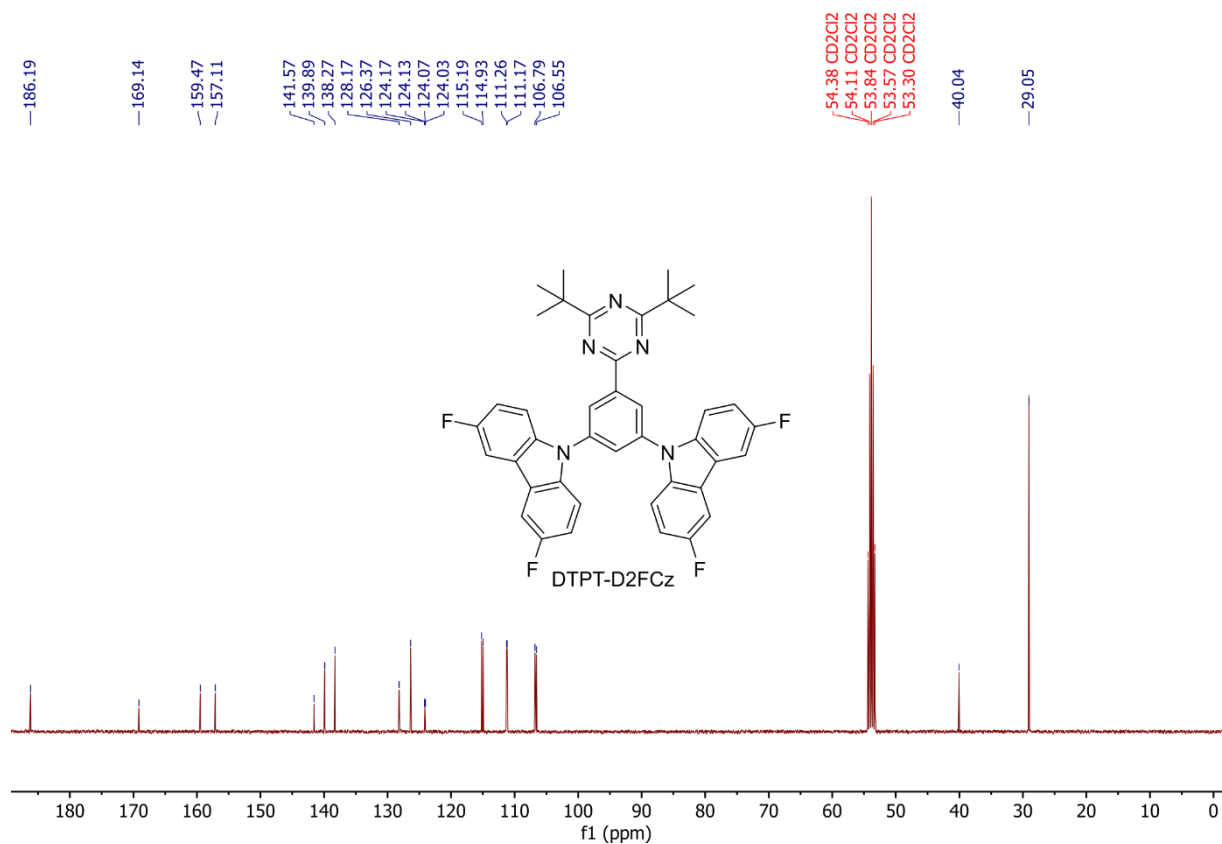


Figure appendix-II-38 ^{13}C NMR spectrum of compound DTPT-D2FCz (101 MHz, CDCl_3).

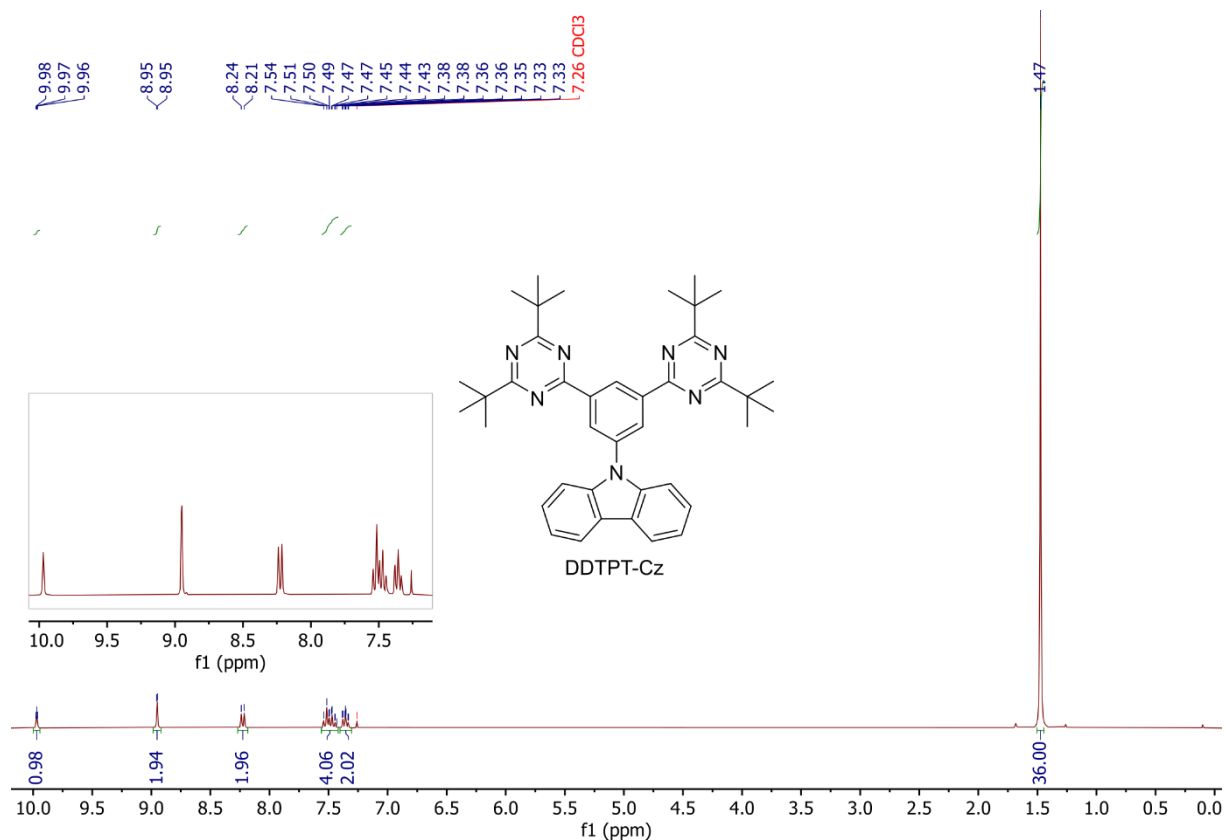


Figure appendix-II-39 ¹H NMR spectrum of compound DDTPT-Cz (400 MHz, CDCl₃).

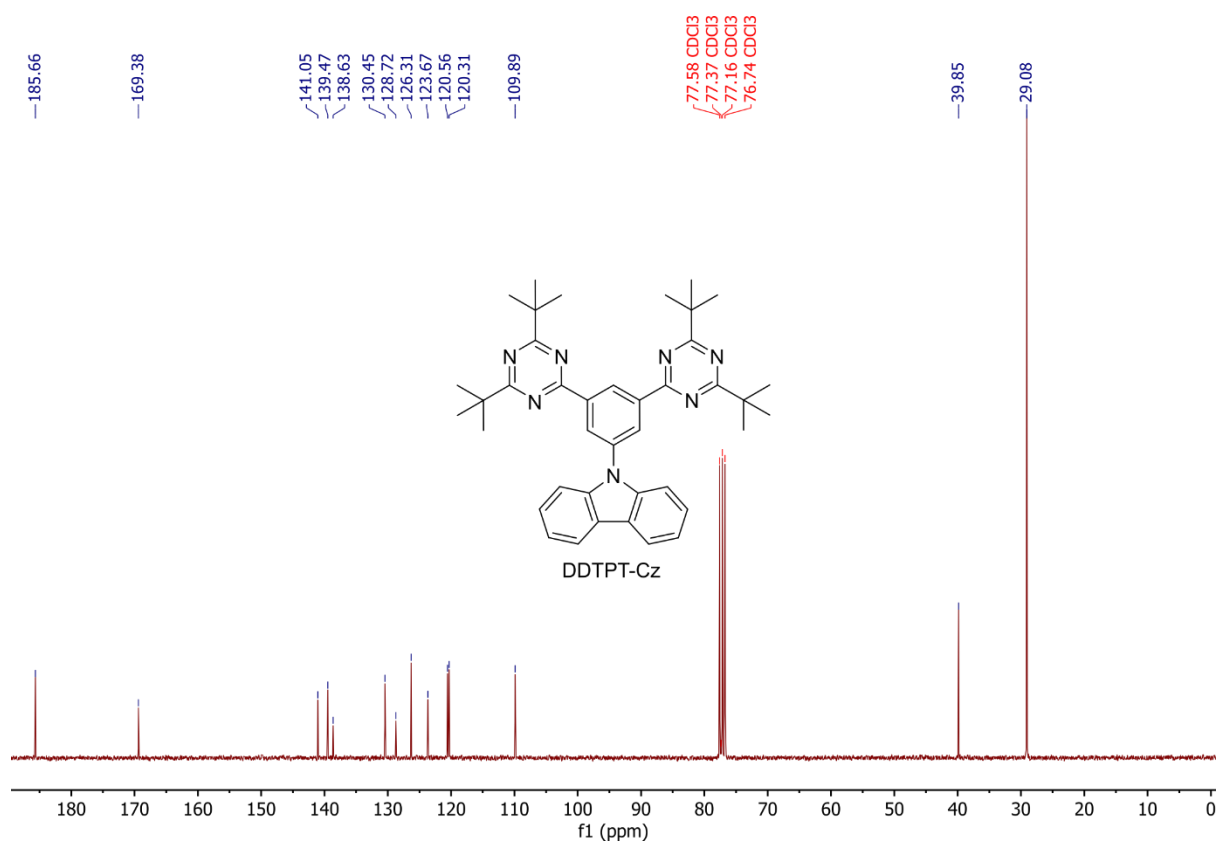


Figure appendix-II-40 ¹³C NMR spectrum of compound DDTPT-Cz (101 MHz, CDCl₃).

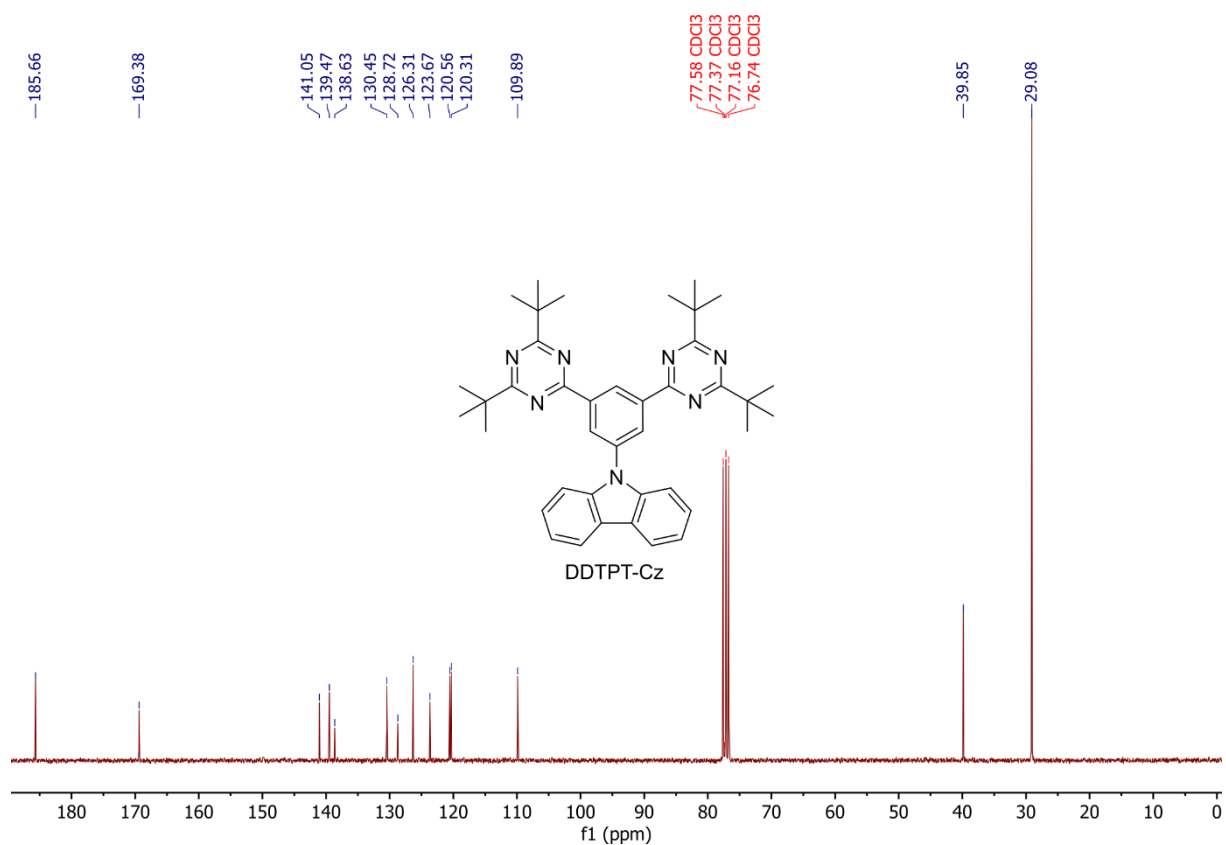


Figure appendix-II-41 ^{13}C NMR spectrum of compound DDTPT-2FCz (400 MHz, CDCl_3).

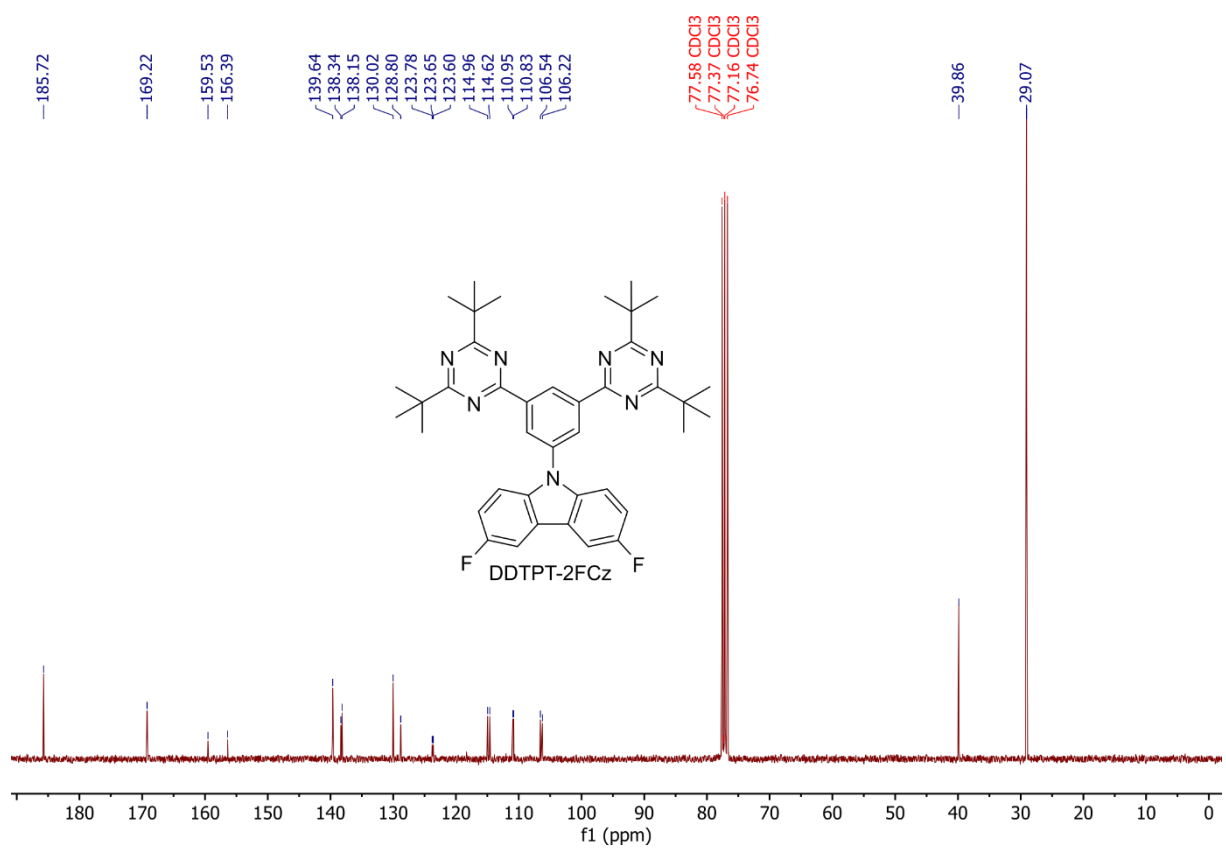


Figure appendix-II-42 ^{13}C NMR spectrum of compound DDTPT-2FCz (101 MHz, CDCl_3).

List of Publication

1. Z. Zheng, **D. Dou (Co-first)**, R. Xia, P. Wu, E. Spuling, K. Wang, J. Cao, B. Wei, X. Li, J. Zhang*, S. Bräse* and Z. Wang*, Efficient deep-blue luminescence based on dual-channel intra/intermolecular exciplexes. *Sci. Adv.* **9**, 4060 (2023)
2. O. Sachnik, X. Tan, **D. Dou**, C. Haese, N. Kinaret, K-H. Lin, D. Andrienko, M. Baumgarten, R. Graf, G. Wetzelaer, J. Michels and P. W. M. Blom*, Elimination of charge-carrier trapping by molecular design. *Nat. Mater.* **22**, 1114-1120 (2023).
3. J. Guo, Z. Zheng, P. Wu, J. Zhu, **D. Dou**, Z. Liao, R. Xia, K. Wang and Z. Wang*, Co-deposited copper(I) complexes integrating phosphorescence and TADF properties for highly efficient OLEDs. *J. Lumin.* 239, 118354 (2021).
4. R. Xia, Z. Zheng, J. Guo, **D. Dou**, K. Wang, J. Cao, and Z. Wang*, Tuning the position of methyl groups to realize highly efficient deep-red PhOLEDs. *Dye. Pigment.* 195, 109738 (2021).
5. **D. Dou**, P. Wu, Z. Liao, J. Hao, J. Zhang and Z. Wang*, A thermally activated delayed fluorescence exciplex to achieve highly efficient and stable blue and green phosphorescent organic light-emitting diodes. *RSC Adv.* **9**, 23810–23817 (2019).
6. Z. Wang, H. Wang, J. Zhu, P. Wu, B. Shen, **D. Dou**, and B. Wei, Manipulation of Thermally Activated Delayed Fluorescence of Blue Exciplex Emission: Fully Utilizing Exciton Energy for Highly Efficient Organic Light Emitting Diodes with Low Roll-Off. *ACS Appl. Mater. Interfaces.*, **9**, 21346–21354 (2017).

Curriculum Vitae

Personal Details

Name: Dehai Dou

Date of birth: 15/01/1994

E-mail: shd.161016@gmail.com

Place of birth: Anhui, China

Nationality: China

Education

03/2020 – 12/2023: PhD studies, Max Planck Institute for Polymer Research,
Mainz, Germany.

Research adviser: Prof. Dr. Martin Baumgarten

Group Director: Prof. Dr. Paul W.M. Blom

09/2016 – 06/2019: M.Sc. in Organic Chemistry, Department of Chemistry,
Shanghai University, Shanghai, China.

Research adviser: Associate Prof. Dr. Zixing Wang

09/2012 – 06/2016: B.Sc. in Chemistry, Department of Chemistry,
Huaibei normal University, Anhui, China

Thesis adviser: Prof. Dr. Lei Wang

Doctoral Thesis: Design and mechanism of thermally active delayed fluorescence (TADF)
and efficient room temperature phosphorescent (RTP) molecules

Master Thesis: The characterization and photoelectric properties of thermally active delayed
fluorescent exciplexs compounds

Acknowledgments

Time always flies and my nearly four years of PhD training at the Max Planck Institute for Polymer Research is coming to conclusion. First and foremost, I want to thank my supervisor Prof. Dr. Martin Baumgarten, who provided me many precious opportunity and constant support during my PhD studies. There are many things Martin taught me, we often discussed subjects, and he told me I should learn to think. Secondly, a similar gratitude belongs to Prof. Dr. Paul W. M. Blom for his supportive supervision. I have benefited from a lot of valuable advice on my project. Thirdly, I am very grateful to Dr. Yungui Li for his help in the room temperature phosphorescence project. Thanks to Ms. Petra Pausch for all her help. Special thanks to Prof. Dr. Mischa Bonn for financial support and Ms. Laurie Gangloff for all her help.

Many thanks to Xiao Tan, Xin Zhou, Zhitian Ling, Yanwei Gu, Qiqi Yang, Xingfu Zhu, Naz Ugur for their support of my thesis and project. I would also like to thank all my colleagues and friends at the AK-Blom group. They have created a good research atmosphere, which has made my PhD very enjoyable.

Of course, I'd like to thanks my family for their best to support and encourage me to do what I want to do. Without their canstant support I would never have had a chance to start and finish a PhD or even to come to study and life in Germany.

Finally, I would like to thank my fiancee, Xiaomin Sheng. Even though China and Germany are very far away from each other, her trust and support have always given me the courage to face difficulties and challenges. Being with her is the luckiest and most wonderful thing that has ever happened to me.

Dehai Dou

Mainz, Germany

November 2023